PHD

Cycloidal Rotor Systems

Worthing, Robert

Award date:
2023

Awarding institution:
University of Bath

Cycloidal Rotor Systems

Prepared by: Robert Worthing

Volume 1 of 1

A Thesis Submitted for the Degree of Doctor of Philosophy

University of Bath

Department of Mechanical Engineering

May 2022

Signature of Author…………***R Worthing*** (May 2022)……………………………

Robert Worthing

Authorship

I declare that the work in this thesis was carried out in accordance with the requirements of the University's Regulations and Code of Practice for Research Degree Programmes and that it has not been submitted for any other academic award. Except where indicated by specific reference in the text, the work is the candidate's own work. Any views expressed in the dissertation are those of the author.

Signature of Author and Date…………***R Worthing*** (May 2022)…………………

Robert Worthing

Declaration of Previous Submission

The material presented here for examination for the award of a higher degree by research has not been incorporated into a submission for another degree.

Signature of Author and Date…………***R Worthing*** (May 2022)…………………

Robert Worthing

Declaration of Authorship

I am the author of this thesis, and the work described therein was carried out by myself personally.

Signature of Author and Date…………***R Worthing*** (May 2022)…………………

Robert Worthing

Dedications

To my maternal Granddad Emrys Pewtner, who helped me greatly in my formative years, and paternal Granddad Ivor Worthing, who I never had the pleasure to meet. I hope, in some way, I have made you both proud.

Cycloidal Rotor Systems

Robert Worthing

Abstract

Historically the development of the cycloidal rotor into a viable propulsion concept has been hampered compared to more conventional approaches due to limitations in computational modeling capability and availability of low mass high stiffness materials. However, advancements in these areas have improved the viability of the cycloidal rotor over recent years, which has renewed interest in the cycloidal rotor in the quest to develop more efficient propulsion technologies. The cycloidal rotor is a novel thrust generation technology suitable for crewed and uncrewed flight. Thrust generation is created via blades rotating parallel to the rotor's global rotation axis, pitching cyclically. Precise thrust vectoring is achieved by controlling the blade cyclic pitch phase angle, enabling the cycloidal rotor to operate with a wide operational envelope in pure thrusting and forward flight applications.

To date, all cycloidal rotor research has concentrated on mean rotor performance, which is essential in the preliminary design stage, but its applicability is limited during detailed design. Standard rotorcraft are often subject to high levels of vibration emanating from a number of sources, with the rotor being a significant contributor. Rotorcraft rotor blades operate in a highly unsteady aerodynamic environment, subject to fluctuating aerodynamic and inertial loading, generating large vibratory blade and hub loads, leading to problems such as component fatigue and passenger discomfort. In comparison to standard rotorcraft, the vibratory response of the cycloidal rotor is little researched and understood.

The current thesis presents the development of reduced-order computational aerodynamic models and computational fluid dynamic models (CFD) to characterize the vibratory response of a cycloidal rotor in hover with increasing blade cyclic pitch amplitude and varying rotor speed. Experiments with a new four-blade cycloidal rotor test rig were undertaken to investigate the efficacy of the reduced-order computational and CFD models in predicting the mean and vibratory hub loads.

A method of rotor force sensor dynamic calibration was developed to take account of the test rig dynamic response and characterize the cycloidal rotor vibratory response fully for the first time. The reduced-order computational model and 2D CFD analysis showed good agreement with experimental data in calculating mean rotor performance. It was found that the rotor vibratory loads were dominated by the rotor 4/Rev vibratory response, which saw increased modulation with increasing blade cyclic pitch amplitude. The correlation of computational model vibratory loads with experimental data improved with model fidelity, with both models showing broad agreement with the experimental data. The computational models provided insight into the physical mechanisms behind rotor vibration, with blade wake interactions identified as having a strong influence on the overall rotor vibratory response.

With high levels of cycloidal rotor vibration identified from initial tests, rotor vibration reduction was identified as a critical factor in cycloidal rotor optimization and further development in the future. One such vibratory response reduction methodology is higher harmonic control (HHC). The thesis describes the first known investigation into the use of HHC for mitigating cycloidal rotor vibration, providing a robust demonstration of the efficacy of HHC both computationally and experimentally, identifying that the inclusion of HHC successfully reduced the cycloidal rotor vibratory response in all cases. Furthermore, it is shown that faithfully modeling the blade vortex shedding and stall behavior is key to accurate simulation of the rotor and rotor vibration control.

Acknowledgements

I want to thank Dr. Jonathan du Bois, Dr. David Cleaver, and Dr. Pejman Iravani for allowing me to pursue this Ph.D. In particular, Dr. Jonathan du Bois for his supervision, reassurance, and guidance from the start, even during the tough times and unusual working arrangements. This thesis would not have been possible without your input.

Thanks must also be given to my colleagues at Quadratec Ltd, past and present, for their encouragement in the current endeavour. In particular, Mark Thatcher for his guidance and for allowing me unlimited access to workshop facilities for testing.

Gratitude must also go to the Whitworth Awards Panel, whose financial support and encouragement of this research have made the project possible through the IMechE Whitworth Senior Scholarship. Also, I would like to thank Prof. Brian Clayton for coming out of retirement to follow me through my journey and provide mentorship as part of the Scholarship process.

My good friends Matthew Toyer and Geoff Harris have provided assistance and distraction throughout, and I am sure that I have bored them in the continual pursuit of my research but have always been willing to listen.

Finally, I would like to thank my parents and sister, Emma. Not only for support from the start of this project but also for support through life in general, and without them, I would not be at the stage I am today. I will always be grateful for everything they do for me and for encouraging me to continue with the research in sometimes difficult personal circumstances over the last few years.

Contents

3. Experimental Test Rig Design and Analysis

4. Experimental Test Procedure, Results Processing, and Analysis

7. Dynamic Hub Loading of a Cycloidal Rotor

8. Higher Harmonic Control of Cycloidal Rotor Vibration

9. Conclusion

10. Bibliography

11. Appendices

List of Figures

List of Tables

Nomenclature

c	=	Blade chord (m)
e	=	Eccentricity point position (m/s)
n	=	Rotor harmonic (n/Rev)
k	=	Reduced frequency
k	=	Single stream tube model inflow correction factor
q	=	Blade pitch rate (rad/s)
s	=	Non-dimensional distance traveled by the airfoil in semi-chords
t	=	Static temperature (K)
t	=	Pitch link offset (m)
D	=	Rotor diameter (m)
L	=	Theoretical distance between eccentric offset position pitch pin (m)
N	=	Rotor rotational speed (RPM)
P	=	Rotor power (W)
Q	=	Rotor torque (Nm)
R	=	Universal gas constant (J/kg K)
R	=	Rotor radius (m)
S	=	Rotor span (m)
T	=	Rotor thrust (N)
V	=	Flow velocity (m/s)
X	=	X-measurement direction
Y	=	Y-measurement direction
Z	=	Z-axis measurement direction
$\mathrm{A_n}$	=	Amplitude of the HHC control input (°)
$\mathrm{A_B}$	=	Blade planform area ($\mathrm{m^2}$)
$\mathrm{A_R}$	=	Rotor planform/Swept area ($\mathrm{m^2}$)
$\mathrm{C_L}$	=	Coefficient of lift
$\mathrm{C_D}$	=	Coefficient of drag
$\mathrm{C_{L_{3D}}}$	=	3D lift curve slope
$\mathrm{C_{L_\alpha}}$	=	2D thin aerofoil theory lift curve slope

C_L^c	=	Circulatory lift coefficient
C_L^{nc}	=	Non-circulatory lift coefficient
C_C	=	Blade lift coefficient parallel to the blade chord
C_{D_p}	=	Blade profile drag coefficient
C_{D_i}	=	Bade induced drag coefficient
C_{Li_α}	=	Non-circulatory lift impulse component due to angle of attack
C_{Li_q}	=	Non-circulatory impulse component due to pitch rate
C_{mc}	=	Rotating cylinder moment Coefficient
C_T	=	Coefficient of Thrust
C_P	=	Coefficient of Power
C_{T_x}	=	Coefficient of Thrust in the X-direction
C_{T_y}	=	Coefficient of Thrust in the Y-direction
DL	=	Disc loading (N/m^2)
D_{α_n}	=	Unsteady aerodynamic model circulatory deficiency functions for attached flow for angle of attack
D_{q_n}	=	Unsteady aerodynamic model circulatory deficiency functions for attached flow for pitch rate
F_R	=	Resultant mean rotor thrust (N)
F_x	=	X-measurement direction rotor thrust (N)
F_y	=	Y-measurement direction rotor thrust (N)
F_L	=	Blade lift force (N)
F_D	=	Blade Drag force (N)
F_{x_R}	=	Rotor X-measurement direction instantaneous rotor force (N)
F_{y_R}	=	Rotor Y-measurement direction instantaneous rotor force (N)
F_{R_R}	=	Rotor resultant instantaneous rotor force (N)
F_T	=	Blade tangential force relative to rotor base circle (N)
F_o	=	Aerodynamic force amplitude (N)

F_{tan}	=	Lag hinge tangential force (N)
F_{in}	=	Instantaneous lag hinge tangential force component (N)
$\|F\|$	=	Magnitude of the output force sensor signal
$\|G\|$	=	Magnitude of the input force sensor signal
$\|H(\omega)\|$	=	Transfer function magnitude
$\|F_n\|$	=	Test rig output vibratory response non-dimensional magnitude at n/Rev
$\|G_n\|$	=	Test rig input vibratory response non-dimensional magnitude at n/Rev
$\|H_n(\omega)\|$	=	Transfer function magnitude at the required dynamic calibration test point.
$\angle F$	=	Output force signal phase angle (°)
$\angle G$	=	Input force signal phase angle (°)
$\angle H$	=	Phase difference between the input and output signals (°)
$\angle F_n$	=	Test rig output vibratory response phase at n/Rev(°)
$\angle G_n$	=	Test rig input vibratory response phase at n/Rev(°)
$\angle H_n$	=	Phase difference at the required dynamic calibration test point (°)
k_i	=	Non-circulatory time constant
Mn	=	Mach number,
N_b	=	Blade number
PL	=	Power loading (N/W)
P_i	=	Induced lower (W)
P_0	=	Profile lower (W)
P_p	=	Parasitic lower (W)
P_b	=	Blade pivot point position (m)
P_B	=	Individual blade power (W)
P_R	=	Instantaneous rotor power (W)
q_e	=	Unsteady effective blade pitch rate (rad/s)
R_e	=	Reynolds number
Re_ϕ	=	Rotational Reynolds number

δs	=	The distance traveled by the wake over the time increment dt
dt	=	Wagner indicial response time increment
T_i	=	Non-circulatory time constant [105]:
T_B	=	Individual blade torque (Nm)
T_E	=	End plate outer face frictional torque (Nm)
T_q	=	End plate end face frictional torque (Nm)
V_i	=	Induced velocity (m/s)
V_T	=	Blade tangential velocity component (m/s)
V_N	=	Blade normal velocity component (m/s)
V_R	=	Blade resultant velocity (m/s)
V_a	=	Rotor advance velocity (m/s)
X_α, Y_α	=	Unsteady aerodynamic model circulatory deficiency functions for angle of attack
X_q, Y_q	=	Unsteady aerodynamic model circulatory deficiency functions for pitch rate

Greek Symbols

θ_{BL}	=	Baseline blade cyclic pitch input (°)
θ_n	=	Higher harmonic control-blade cyclic pitch input (°)
θ_s	=	Blade total cyclic pitch angle (°)
θ_{ns}	=	HHC control input sine component (°)
θ_{nc}	=	HHC control input cosine component (°)
Ψ	=	Azimuth angle (°)
ρ_a	=	Air density (kg/m^3)
ω	=	Rotor angular velocity (rad/s)
α	=	Blade quasi-steady angle of attack (°)
α_e	=	Blade unsteady effective angle of attack (°)
ϕ	=	Resultant thrust phase angle (°)
$\phi(s)$	=	Wagner function
σ	=	Rotor solidity
μ	=	Advance ratio

ω_b	=	Rotor burst speed (rad/s)
σ_H	=	Mean hoop stress (MPa)
σ_{UTS}	=	Ultimate tensile stress (MPa)
ϕ_n	=	Phase angle of the HHC control input (°)
$\dot{\theta}_S$	=	Blade pitch rate angular velocity (rad/s)
γ	=	Ratio of specific heats

Acronyms

ACSR	=	Active Control of Structural Response
ANN	=	Artificial Neural Network
AOA	=	Angle of Attack
AR	=	Aspect Ratio
BDC	=	Bottom Dead Centre
BET	=	Blade Element Theory
BVI	=	Blade Vortex Interaction
CBS	=	Cycloidal Blade System
CFD	=	Computational Fluid Dynamics
DAQ	=	Data Acquisition
DBD	=	Dielectric Barrier Discharge
DES	=	Direct Eddy Simulation
DMST	=	Double Multiple Stream Tube
DOF	=	Degree of Freedom
DS	=	Dynamic Stall
FEA	=	Finite Element Analysis
FFT	=	Fast Fourier Transform
FRF	=	Frequency Response Function
FSI	=	Fluid Structure Interaction
HCF	=	High Cycle Fatigue
HHC	=	Higher Harmonic Control
IBC	=	Individual Blade Control
LCF	=	Low Cycle Fatigue
LE	=	Leading Edge

LES	=	Large Eddy Simulation
LSB	=	Laminar Separation Bubble
LTA	=	Lighter than Air
LRTA	=	Large Rotor Test Apparatus
MAV	=	Micro Air Vehicle
MDART	=	McDonnell Douglas Advanced Rotor Technology
NI	=	National Instruments
OoB	=	Out of Balance
PPR	=	Pulse Per Revolution
RANS	=	Reynolds Averaged Navier Stokes
SLS	=	Selective Laser Sintering
TDC	=	Top Dead Centre
TE	=	Trailing Edge
TIR	=	Total-Indicator Run-Out
TVA	=	Tuned Vibration Absorbers
UAM	=	Urban Air Mobility
UAV	=	Unmanned Aerial Vehicle
UD	=	Unidirectional
URANS	=	Unsteady Reynolds Averaged Navier Stokes
VAWT	=	Vertical Axis Wind Turbine
VC	=	Virtual Camber
VI	=	Virtual Incidence
VTOL	=	Vertical Take-off and Landing

This page intentionally left blank

Chapter 1 – Introduction

1.1. Introduction

This chapter first outlines the motivation for the current cycloidal rotor research and the concept to be investigated. Secondly, the research background and significance of the cycloidal rotor are outlined, and how the cycloidal rotor may be employed to meet the current and future requirements of the crewed and uncrewed flight aviation industry. The current problems associated with cycloidal rotors have also been outlined, which has hampered their early development. Addressing the challenges associated with cycloidal rotor design forms the basis of the current research question. Finally, the main aims and objectives of the current research are defined.

1.2. Research Motivation

Following the development of the helicopter, considerable effort was devoted to the design of craft that had the hover, vertical take-off, and landing ability of a helicopter combined with cruise speed comparable to standard aircraft, now commonly called the Vertical Take-Off and Landing (VTOL) rotorcraft. Numerous VTOL conceptual designs were developed during this period with varying degrees of success, with the notable exception being the Hawker AV-8A Harrier [1]. However, poor performance and handling hampered early VTOL development efforts, with power plants typically limited to piston engines and gas turbines. In addition, craft development was often challenging due to the limited testing capability suitable for VTOL-specific applications.

Over recent times interest in the electrification of propulsion systems has increased and seen renewed interest in the design of a wide range of efficient propulsion systems for crewed and uncrewed flight, one area being VTOL craft. The VTOL capabilities remove the need for a craft launcher or runway, allowing operation in almost any location unaided.

With increased research and development into Urban Air Mobility (UAM) and an ever-expanding Unmanned Aerial Vehicle (UAV) market, there is still much scope to develop new propulsion technologies to be used in conjunction with or replace existing approaches. The new propulsion technologies would seek to improve the craft's overall operating efficiency, operational range, payload, forward flight speed, and rotor hovering efficiency. The new technologies could be used for all-electric propulsion and hybrid-electric concept optimization, where improved endurance and operational capability are still sought. In addition, the continual drive to reduce the environmental impact of the aerospace sector at all levels and scales to reduce CO_2 emissions by 75% by 2050 [2,3] adds considerable pressure to develop other technologies to address the shortfalls of traditional propulsion approaches.

Uses for UAV systems are numerous, including but not limited to emergency surveillance, crowd control, and observation. The increasing trend of system miniaturization in UAV development has seen that the scaling of conventional crewed flight propulsion concepts often results in lower aerodynamic efficiencies when compared to their crewed counterparts, a direct result of the low Reynolds number flow effects [4]. In addition, the performance requirements of UAV systems vary greatly depending on whether their operation requires endurance, hover, and or maneuverability.

The American Helicopter Society characterizes VTOL aircraft into three main categories [5]: vectored thrust, lift and cruise, and wingless. Vectored thrust VTOLs use a wing for efficient forward flight and one propulsion system for VTOL and forward flight manoeuvers. Examples include the Lilium Jet and Aurora LightningStrike. The lift and cruise VTOLs incorporate a wing for efficient forward flight performance but use two separate propulsion systems for hover operation and forward flight. Crewed flight examples include the Kitty Hawk Cora and the Aurora Flight Sciences eVTOL. Uncrewed examples include the SkyEye Sierra VTOL, which is a fixed-wing electric eVTOL UAV, and the Tango VTOL UAV. Finally, wingless VTOLs are single or multi-rotor craft efficient in hover but less so in forward flight due to the lack of fixed-wing and are typically used for short-range operation. Examples include the E-Hang 184 and Volocopter.

The blending of propulsion technologies in the vectored thrust, lift, and cruise categories has resulted in increased demand for craft more commonly known as fixed-wing VTOL in military and civil operations. This is due to the fixed-wing VTOL ability to incorporate the forward flight efficiency of fixed-wing aircraft with the vertical landing and hovering efficiency of a conventional rotorcraft.

1.3. Research Background and Significance of Cycloidal Rotors

The cycloidal rotor is an innovative propulsion design concept that is scalable for crewed and uncrewed flight. The origin of the cycloidal rotor is unknown, but it is widely accepted that Kirsten [6,7], during the 1920s, was the first to recognize its potential in aeronautical and marine applications. However, despite further developing a physical and analytical model [8], it was concluded that although the concept showed promise for hover and low-speed forward flight, with an overall efficiency lower than that of propeller technology of the day, sadly, the concept saw little further development. Coupled with the lack of understanding of the flow physics of oscillating aerofoils, structural challenges of the design, and no way of analyzing it with sufficient accuracy, the cycloidal rotor is one of the most researched propulsion concepts never to have flown in crewed flight.

Although cycloidal rotor research is still embryonic, the increase in efficient flight research within the last decade has seen a renewed interest in cycloidal rotor propulsion. As a result, many of the problems and challenges associated with cycloidal rotor propulsion are still unknown or little researched. With the development of high-speed computing and numerical analysis techniques in recent years, many of the barriers to furthering the development of the cycloidal rotor have been reduced.

The cycloidal rotor differs from standard rotorcraft, whereby a series of blades rotate parallel to the global rotor rotation axis, as shown in figure 1.1. The ability of the rotor to change the phase angle and amplitude of the rotor blade cyclic pitch angle enables thrust to be vectored in any direction almost instantaneously, with thrust magnitude controlled via blade cyclic pitch angle and or rotor rotational speed.

Meaning the cycloidal rotor can be used in VTOL-only applications and UAM applications as a fixed-wing VTOL variant. The transition from hover to forward flight is vital for VTOL applications. Precise control of thrust magnitude and direction of the cycloidal rotor allows an easy transition from hover to forward flight manoeuvers without any detrimental effect on aircraft performance and control.

The resultant thrust generated by a cycloidal rotor blade can be broken down into a lateral (propulsive) and vertical (lifting) thrust force component. The coordinate system used for all measurements throughout the current research is shown in figure 1.2. Where the lateral (propulsive) force is defined as F_x acting parallel to the velocity-free stream in forward flight. The vertical (lifting) force is defined as F_y and acts perpendicular to the velocity-free stream in forward flight. Positive torque T_z acts counterclockwise (CCW) in the direction of rotor rotation.

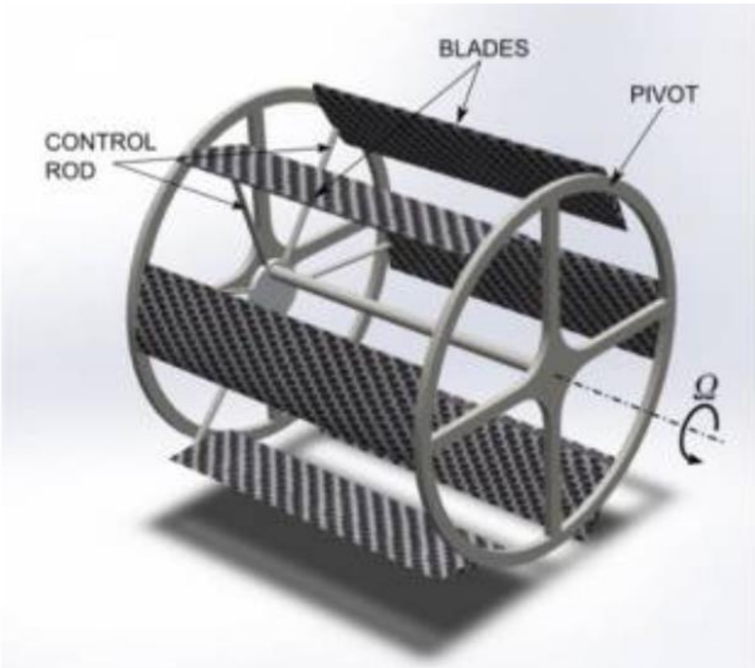

Figure 1.1 – 3D CAD model representation of a cycloidal rotor with six NACA 0012 blades and a maximum blade cyclic pitch angle of 40° [9]

Control of vectored thrust increases gust tolerance due to the rotor's ability to react quickly to rotor air loads and operating environment changes. Tight control of the thrust vectoring provides more precise maneuverability, agility, and the ability to fly in any direction in confined spaces, which is a key advantage over many competing technologies. This makes the cycloidal rotor an attractive proposition that addresses many of the drawbacks of current propulsion systems at varying scales, with the ability to operate over a wide range of operational regimes.

The cycloidal rotor can be used in isolation as a stand-alone propulsion system or simultaneously with other, more conventional forms of propulsion. An example is helicopter tail rotors and Lighter than Air (LTA) vehicle propulsion concepts [10,11]. Scalable for crewed and uncrewed flight, a comparison of the cycloidal rotor power loading for a six-blade rotor with data available on other conventional crewed rotorcraft configurations is shown as Cycloidal Blade System (CBS) in figure 1.3, illustrating the concept's promise. The cycloidal rotor power loading data presented in figure 1.3 is derived from experimental test data forming part of a larger research project by Seoul National University [12] to develop a 0.8m diameter, six-blade, simply supported rotor to be developed into a rotorcraft for crewed flight applications. Cycloidal rotor research to date has concentrated on fully electric-powered craft, but they can equally be used in hybrid-powered systems.

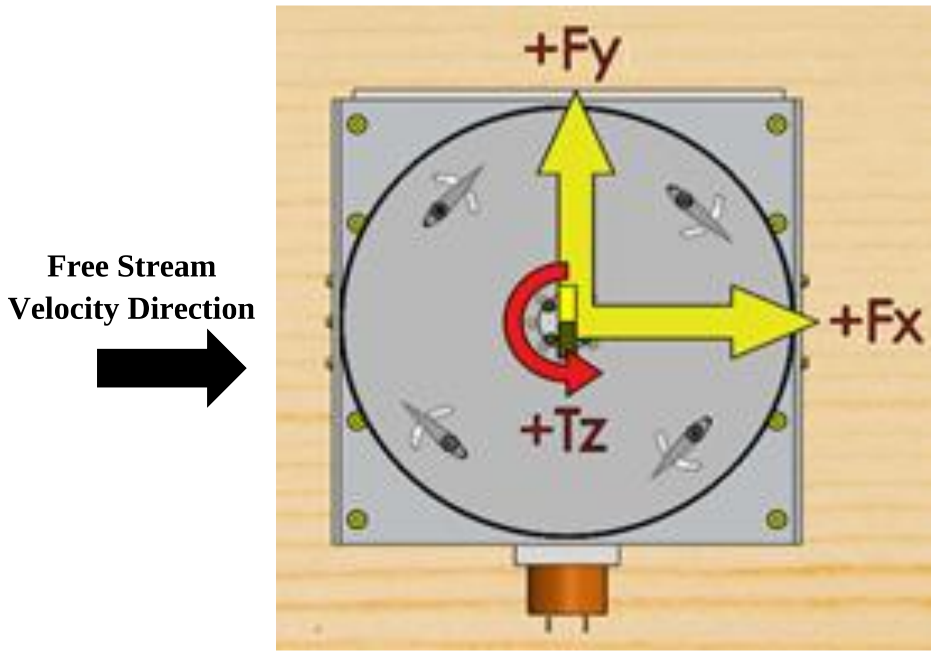

Figure 1.2 – Cycloidal rotor positive force and torque measurement coordinate system convention used throughout the computational and experimental studies in the current research.

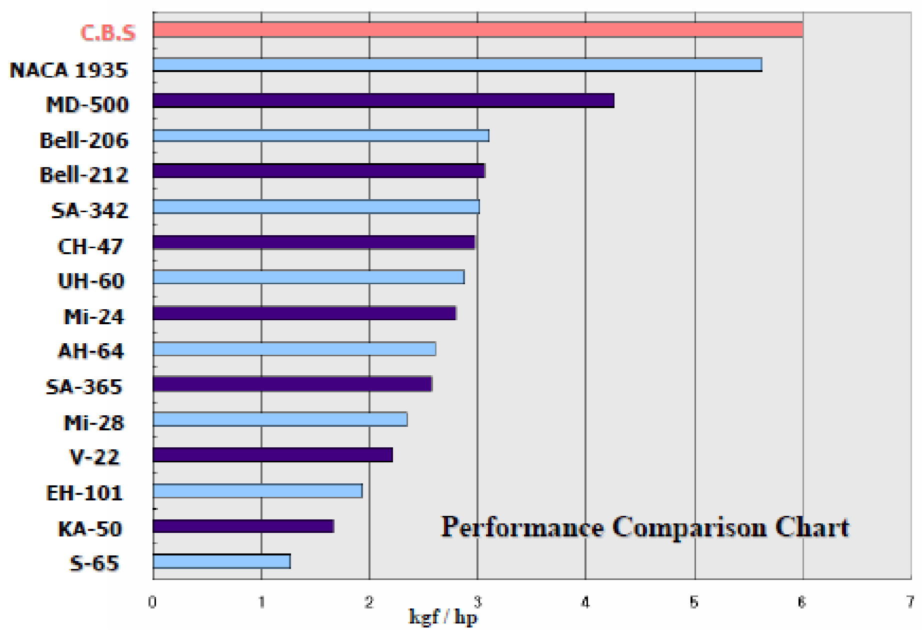

Figure 1.3 – A comparison of a six-blade cycloidal rotor power loading derived from experimental data with the power loading of other crewed craft [12]

1.4. Open Research Questions

A major challenge of using the cycloidal rotor for craft propulsion is that rotor rotation generates a transverse centrifugal load on the rotor blades, which act to bend the blades, whereas, for a conventional rotorcraft, the centrifugal load stiffens them. Research into new high stiffness-to-weight ratio materials will enable the issues associated with the blades and supporting structures to be addressed, utilizing the latest advanced composite material and innovative manufacturing methods.

One of the significant factors limiting the performance of UAV systems is the mass of the propulsive system, and the cycloidal rotor at this stage is no exception. Typically a UAV has a propulsive system mass of 60% compared to 20% for birds [13]. However, optimization and sufficient development could improve operating efficiency over other, more conventional approaches. The pitching of the blades is fundamental to cycloidal rotor operation from both a steady and dynamic load perspective, with all of the lateral and vertical thrust force generated as a direct result.

Surprisingly the blade pitching schedule in hover and forward flight is little researched and analyzed, with only one known optimization study to date [14].

UAV scale cycloidal rotor research has concentrated on a rotor in hover [4], with only limited studies considering the performance in forward flight [15,16]. A number of studies have considered the change in rotor performance with rotor and blade geometry changes. Still, only the sinusoidal low-pitch blade pitching schedule has been considered for both hover and forward flight operation. The forward flight operation utilizes the hovering blade kinematics rotated through a 90° phase angle.

There is still much to be learned about the cycloidal rotor. Through further optimization and understanding, additional improvements in thrust generation during hover and increased efficiency in forward flight will raise awareness and competitiveness of the design. Efficiency improvements will be achieved by optimizing the blade pitching kinematics and utilizing advanced computational and experimental techniques. Although analyzed for flight applications in this instance, applications for cycloidal rotors are numerous, including a novel Vertical Axis Wind Turbine (VAWT).

1.5. Aims, Objectives, and Research Questions

Despite the many proposed benefits associated with the cycloidal rotor, one problem that inhibits its operation associated with blade pitching is high levels of rotor vibration, exaggerated by the large rotating rotor structure. These vibratory loads can deteriorate passenger and pilot comfort and equipment operation. Additionally, increased loading levels increase the complexity of component design and can lead to the loss of the structural integrity of components in the rotating and nonrotating frame.

Since the inception of the helicopter, the measurement and reduction of rotor vibration have been a considerable challenge. The cycloidal rotor is no exception. This thesis develops methods for assessing the cycloidal rotor steady-state and dynamic vibratory aerodynamic load response to devise reliable predictive capabilities for a rotor under hovering conditions. The current research seeks to answer the following two questions:

Question 1 –

'What are the computational and experimental model requirements to accurately capture the higher-order dynamic response of a cycloidal rotor?'

And

Question 2 –

'Can the cycloidal rotor higher-order dynamics be manipulated through Higher Harmonic Control (HHC) blade pitch control to improve the performance and vibratory loading generated by the rotor?'

The main objectives can be broken down into the following:

1. To analyze, design, and build an integrated low-pitch cycloidal rotor test rig that is reconfigurable to allow different blade pitching schedules to be considered during hover.

2. Conduct a thorough experimental investigation under hover test conditions to investigate the effect of changes in blade cyclic pitch angle and rotor rotational speed on steady-state and dynamic aerodynamic loads.

3. Develop an experimental methodology to calculate the dynamic response of force measurement sensors to correct measured dynamic loads to account for the test rig dynamic response.

4. Develop and implement reduced-order computational aerodynamic code and 2D Computational Fluid Dynamic (CFD) models to analyze the current test rig geometry in hover and understand the mechanisms behind rotor unsteady load generation.

5. Validate the computational models with one another and with results from independent experimental and computational data where available.

6. Develop a computational methodology for rotor vibratory load optimization.

7. Use the optimization approach developed and investigate novel blade pitching kinematics to improve the efficiency of the rotor in hover to determine whether HHC can be implemented during cycloidal rotor operation.

8. Experimentally investigate the use of the HHC and the resulting correlation with the different computational model approaches.

9. To use the current studies to inform the development of future cycloidal rotor research questions and procedures.

1.6. Thesis Structure and Contributions

The context and scope of the research have been outlined in the current chapter. An extensive literature review of cycloidal rotors and conventional rotorcraft vibration reduction techniques is summarised in Chapter 2. The review discusses the change in cycloidal rotor performance with changing geometry and an overview of previous cycloidal research. The review gives an overview of conventional rotorcraft vibration measurement techniques and identifies techniques that can be used for conventional rotorcraft rotor vibratory load suppression. A summary of competing propulsion technologies is also given.

Chapter 3 discusses the experimental test rig design, analysis, and build. The test rig is used as the basis for all testing programs in the current research.

Chapter 4 sets out the proposed testing framework and methodology, including the control and instrumentation of the test rig. The development and evaluation of a sensor dynamic calibration procedure are also presented to account for the force measurement instrumentation dynamic response. Finally, initial test rig testing results are given, with shortfalls highlighted prior to test rig modification. Final steady-state results are presented and validated against independent studies.

Chapter 5 outlines the development of a reduced-order unsteady Blade Element Theory (BET) aerodynamic code that takes account of rotor blade unsteady aerodynamics. Validation of the BET code to independent experimental and computation studies is also provided.

Chapter 6 describes the 2D CFD modeling approach used throughout the research, outlining the choice of solver and the geometry used to take account of the multiple sliding mesh interfaces used to account for blade and rotor rotation. Independent validation of the CFD modeling approach is also shown.

Chapters 7 and 8 contain the main contributions of this thesis, covering both the computational and experimental aspects of the research. Chapter 7 presents the first known computational and experimental study to characterize the vibratory response of the cycloidal rotor with increasing blade cyclic pitch angle amplitude at different rotor rotational speeds.

In Chapter 8, a linear and non-linear optimization methodology is developed computationally and validated through experimentation with the inclusion of a single higher harmonic blade cyclic pitch angle input. The resulting change in cycloidal rotor vibratory response and performance are analyzed and discussed, following the first known inclusion of an HHC input for cycloidal rotor vibration suppression.

Chapter 9 draws the thesis to a close with conclusions, forming an overall summary of the computational modeling and experimental results. The focus is on the strengths and limitations of the techniques used and the overall change in cycloidal rotor operation highlighted. Finally, suggestions for future work are made, informed by the current research.

Chapter 2 – Literature Review

2.1. Introduction

This section provides an overview of the literature concerned with cycloidal rotors, finishing with an emphasis on rotor vibration suppression techniques and rotor vibration measurement. Firstly, a brief historical overview of the cycloidal rotor is given, followed by an explanation of the cycloidal rotor operating principle. Next, a review of cycloidal rotor operation characteristics with changing geometry is given, followed by an overview of previous cycloidal research. The review provides an overview of conventional rotorcraft vibration measurement techniques and identifies techniques that can be used for cycloidal rotor vibratory load suppression, which may produce the benefits required. A brief overview of rotorcraft that operate within the same markets as the cycloidal rotor is given, where the cycloidal rotor can provide additional advantages. Finally, emphasis is given to Higher Harmonic Control (HHC), a technique used for rotor vibratory load suppression evaluated computationally and experimentally in this thesis.

2.2. Brief Cycloidal Rotor Historical Overview

Kirsten [6] was the first to notice the potential of the cycloidal rotor and the first to identify its key advantage, the ability to vector thrust in any direction. With initial qualitative test results showing promise, and with the aid of Boeing, the Kirsten-Boeing propeller was developed and subsequently used by Voith-Schneider for marine applications, the only known application of the cycloidal rotor to date.

Strandgren [17] developed a simple quasi-steady aerodynamic analysis of the cycloidal rotor to determine how thrust is generated from the pitching of the rotor blade, with the study concluding that the thrust magnitude and direction could be controlled solely by the blade pitching kinematics. Almost simultaneously, Wheatley [8] developed a simplified blade element momentum theory model to analyze the performance of the cycloidal rotor under forward flight, concluding that the cycloidal rotor should be capable of hover, vertical flight, and autorotation, but the design required excessive power for forward flight operation. The latter is partly due to the fact that a low-pitch cycloidal rotor was being tested at higher advance ratios greater than one, a technicality that was not realized until recently.

With little understanding of oscillating aerofoil aerodynamics at that time, no cycloidal rotor development ensued in the following decades until its revival by Boschma in 1998 [18]. However, interest in cycloidal propulsion has surged in the last decade due to potential new applications, with Levy [19] being the first to analyze a UAV scale rotor.

2.3. Cycloidal Rotor General Overview

The cycloidal rotor consists of a number of blades rotating around an axis parallel to the blade span, similar to an H-Darrieus VAWT, usually positioned with a span position of 90° to the direction of forward flight. The blades are pitched cyclically with rotor rotation, as shown in figure 2.1, with the thrust-producing capability of the cycloidal rotor coming solely from the unsteady pitching of the blades, often using common aerodynamic surfaces and profiles [20].

The unique ability of the cycloidal rotor to vector thrust in any direction within the rotor plane has given rise to the cycloidal rotor's ability to perform VTOL, hover, and forward flight movements, giving high agility and maneuverability. The vector thrusting is achieved by changing the blade pitch magnitude and phase angle, which is controlled via a blade pitch control mechanism, usually an eccentric cam or novel four-bar mechanism [4], as shown in figure 2.2.

More recently, passive cam mechanisms have been developed, allowing several blade pitching schedules to be implemented in a single geometry for both hover and forward flight operation [21]. In addition, the use of the blade pitch mechanism allows the phase and amplitude of the blade pitch to be changed independently of one another, thus giving control of the rotor thrust in any direction within the full 360° of azimuth.

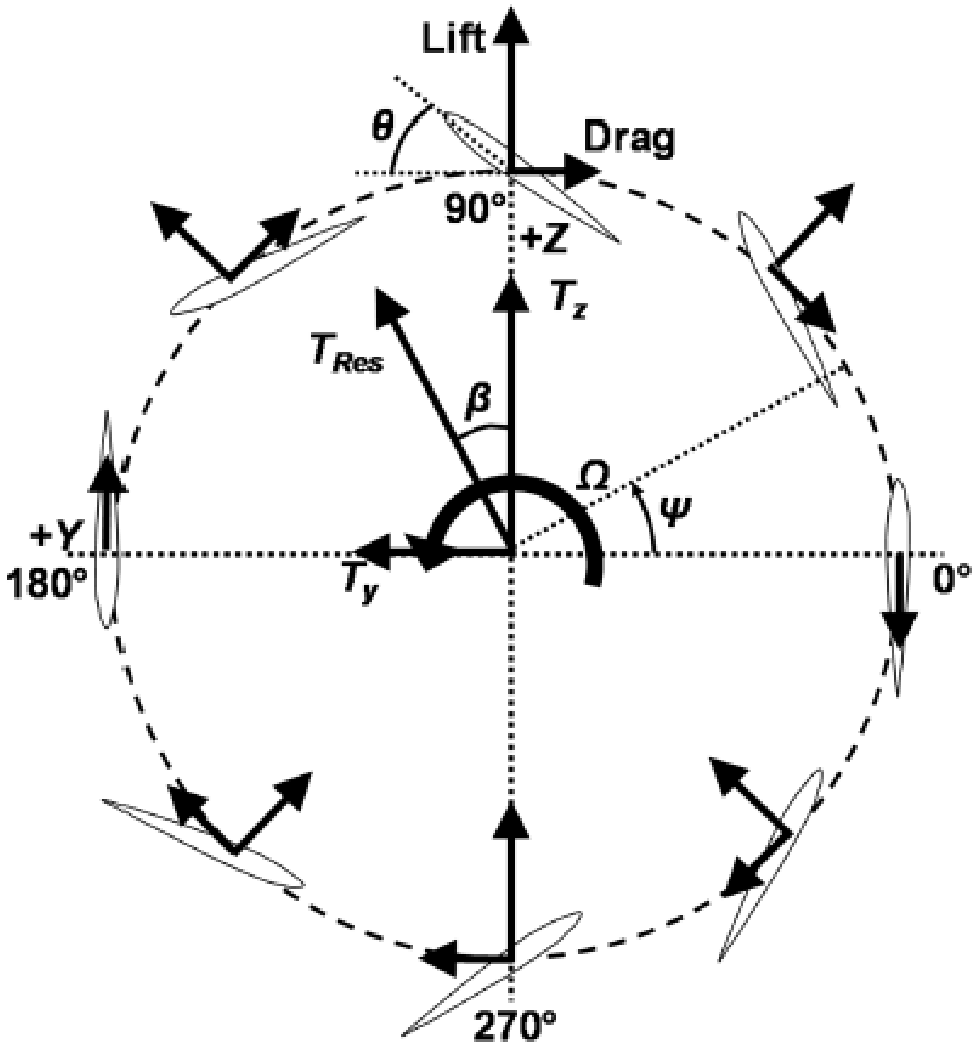

Figure 2.1 – Low pitch cycloidal rotor blade pitching profile [4]

There are three forms of the cycloidal rotor that are suitable for flight applications, differentiated by their respective blade pitching schedule [22], as shown in figure 2.3. The respective configurations are known as the Pi-pitch, low-pitch, and high-pitch systems. Their applicability is determined to a degree by the rotor advance ratio μ required, where

$$\mu = \frac{V_a}{\omega R} \tag{2.1}$$

V_a defines the rotor speed of advance relative to the air, ω the rotor angular velocity, and R is the rotor radius. During hover, the blades travel in a circular arc, with a rotor advance ratio of zero, while during forward flight, the blades trace out a cycloid.

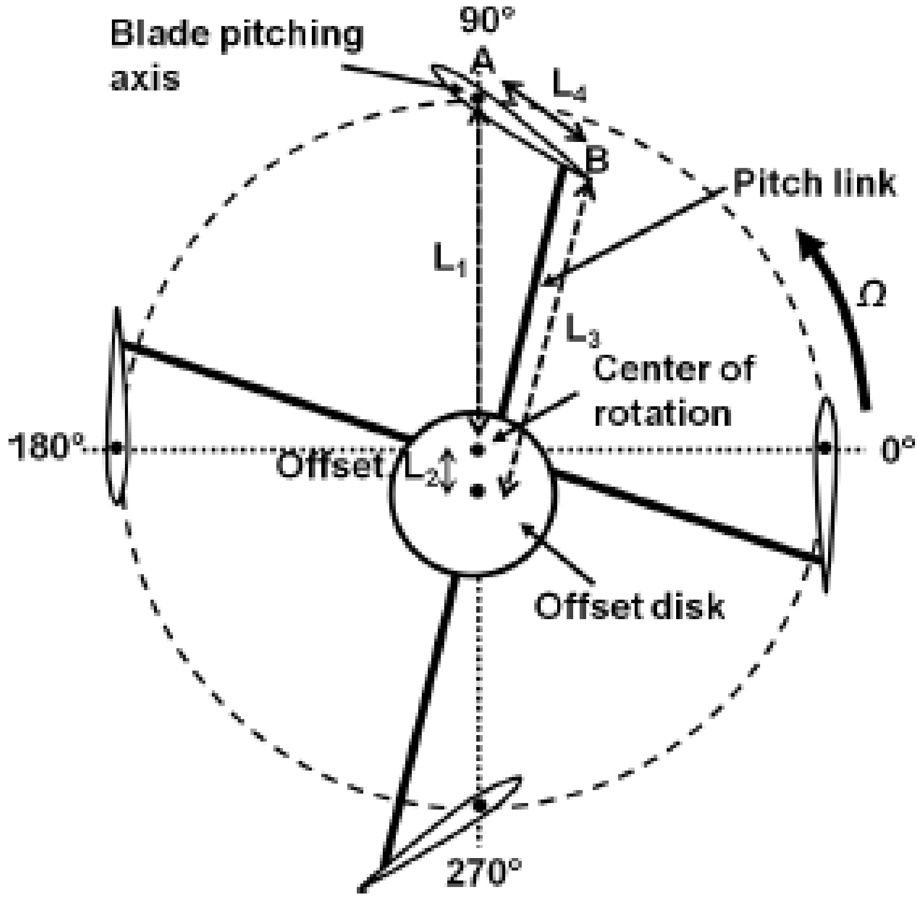

Figure 2.2 – Low pitch cycloidal rotor pitch mechanism with four-bar linkage [4]

Research conducted by Kirsten [6] was performed on a fixed or Pi-pitch system. The blade's trailing edge becomes the blade's leading edge once per rotor revolution, meaning that the blade pitch period is half that of the rotor rotational speed.

Wheatley [8] was the first to recognize the benefit of utilizing a low-pitch system for a hovering rotor, with the blades pitching in a sinusoidal manner via a double cam mechanism. The blades follow a curtate cycloid path during forward flight, as shown in figure 2.3. The blades effectively oscillate but do not complete full rotations about their own axis with respect to the rotor axis.

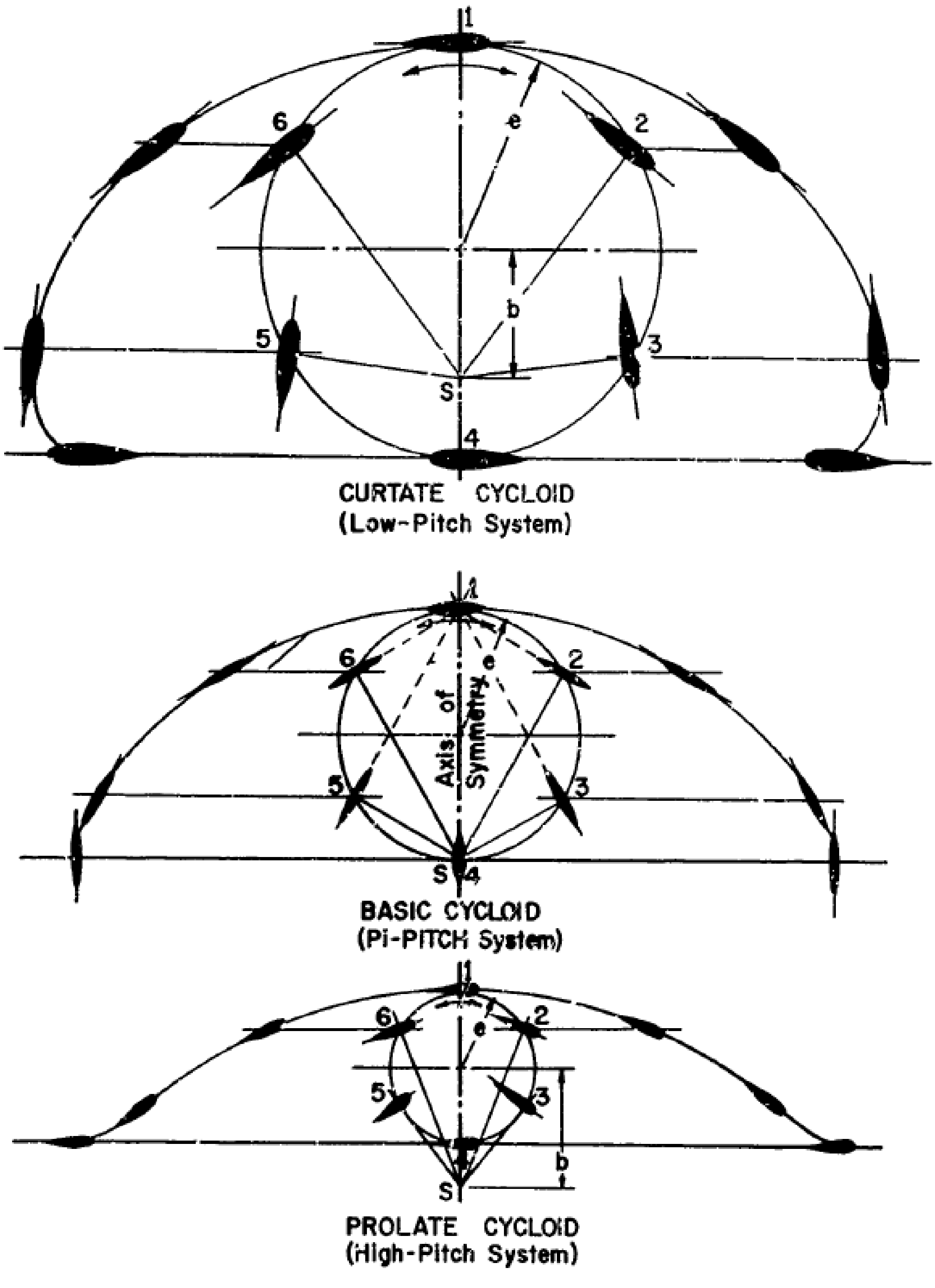

Figure 2.3 – Forms of cycloidal motion [22]

The sinusoidal low-pitch configuration, as shown in figure 2.1, is the most efficient for hover and low-speed forward flight. Unlike the Pi-pitch variant, the blade's leading edge remains at that position throughout the 360° of rotor rotation. Hence the period of blade pitching is the same as the rotor rotational speed. The low-pitch mechanism is only acceptable up to advance ratios of one; at this point, the relative velocity seen by the blade approaches zero [22]. Zero relative velocity is of particular interest at blade position 4 in figure 2.3 for the low-pitch system at the blade Bottom Dead Centre (BDC) position. At the BDC position, the blade needs to be rotated through a 180° phase so that the leading edge becomes the trailing edge, changing the low-pitch into a high-pitch cycloidal system.

In a high-pitch system, the blades follow a prolate cycloid path. Illustrating that the high-pitch system is suited to high-speed forward flight instead of hovering, typically for advance ratios greater than one [22]. Changing the blade pitching schedule shows that the cycloidal rotor can operate as a pure lifting (no lateral rotor force) or propulsive thrusting device. The rotor falls somewhere between these two extremes in most practical applications.

The transition through an advance ratio of one is not straightforward, with a difficult transition region typically between advance ratios of 0.8 and 1.2. At present, this transition region is not fully understood or analyzed, with the possibility of transitioning between the two unknown. As the advance ratio approaches one, the blade at the BDC position needs to be subjected to high angular accelerations to give an almost instantaneous inversion; this appears unrealistic in practical applications. As the advance ratio approaches infinity, the rotor blade remains in the horizontal plane with respect to rotor rotation, meaning the cycloidal rotor is approaching a fixed-wing craft. A key challenge in cycloidal rotor development is designing and analyzing a universal pitch mechanism that allows a smooth transition through the Pi-pitch region with a rotor advance ratio of one.

Blades in a low-pitch cycloidal rotor experience a maximum geometric angle of attack (AOA) diametrically opposite, as illustrated in figure 2.4, at the 6 and 12 o'clock blade positions. The relative position in relation to the azimuth angle is dependent on the pitch mechanism phase angle, ε, as indicated in figure 2.4. The rotor notation and sign convention used within the current research are shown in figure 2.4.

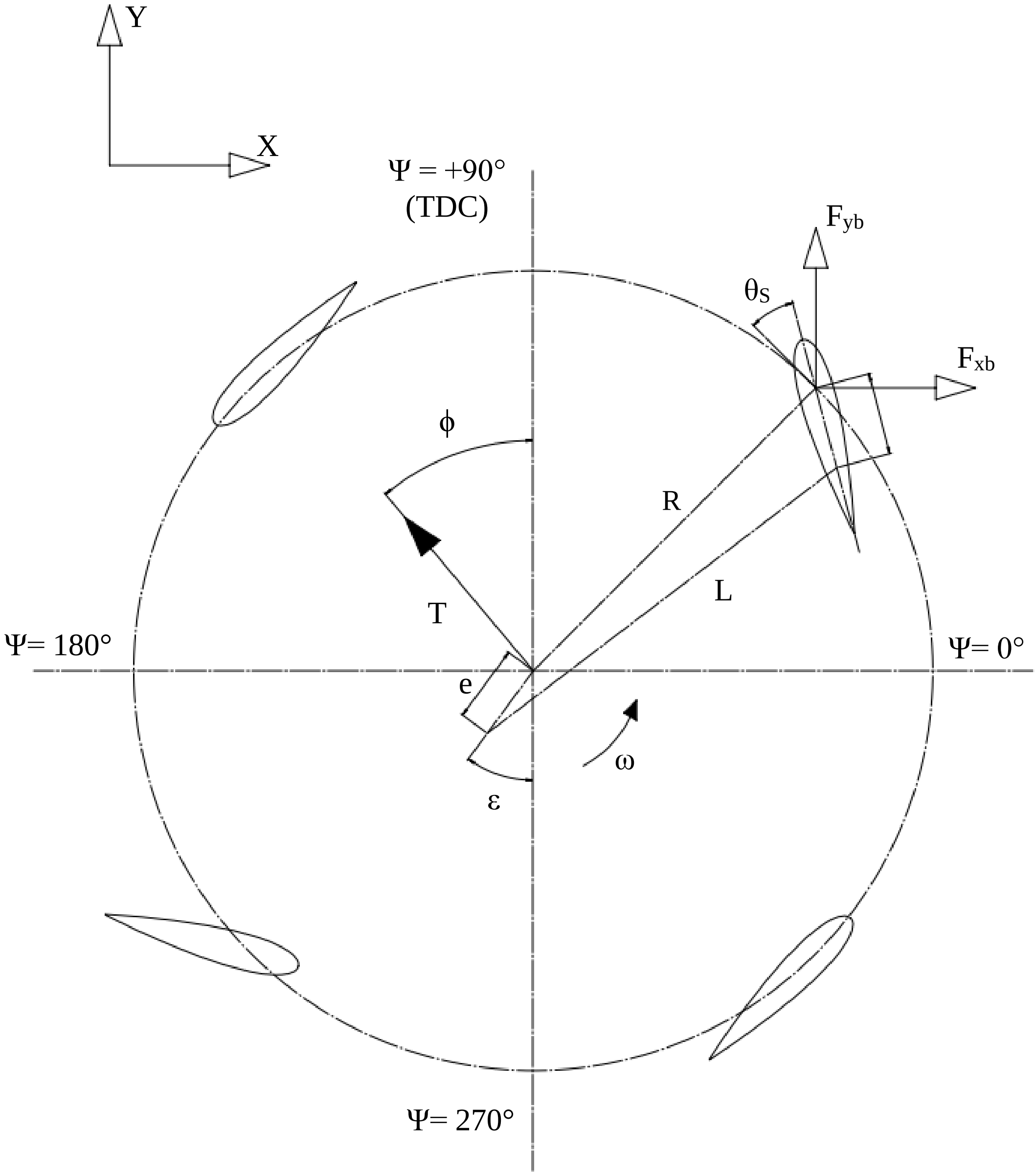

Figure 2.4 – Cycloidal rotor notation, sign convention, and nomenclature used throughout the current research for a hovering rotor

The pitch schedule of a sinusoidal low-pitch rotor conforms closely to an ideal sinusoid at low blade cyclic pitch amplitudes. The pitch angle moves further away from the ideal sinusoidal motion as the amplitude increases. An example of the deviation between the ideal and prescribed blade pitching motion is shown in figure 2.5 for a blade cyclic pitch amplitude of 40°.

The standard approach of Disk (DL) and Power loading (PL) can be used to allow comparison of the cycloidal rotor to other rotorcraft concepts, defined as

$$\mathrm{DL} = \frac{\mathrm{T}}{\mathrm{A_R}} \tag{2.2}$$

and

$$\mathrm{PL} = \frac{\mathrm{T}}{\mathrm{P}} \tag{2.3}$$

Where T is the rotor thrust, $\mathrm{A_R}$ is the rotor planform or swept area, and P is the rotor power. A high power loading coupled with a low disc loading for VTOL craft is desirable for the most efficient hover performance. VTOL craft with a lower effective disk loading requires lower power per unit thrust generated, thus making them more efficient. Cycloidal rotors have higher DL than conventional rotorcraft and have a DL comparable to a heavily loaded helicopter [4].

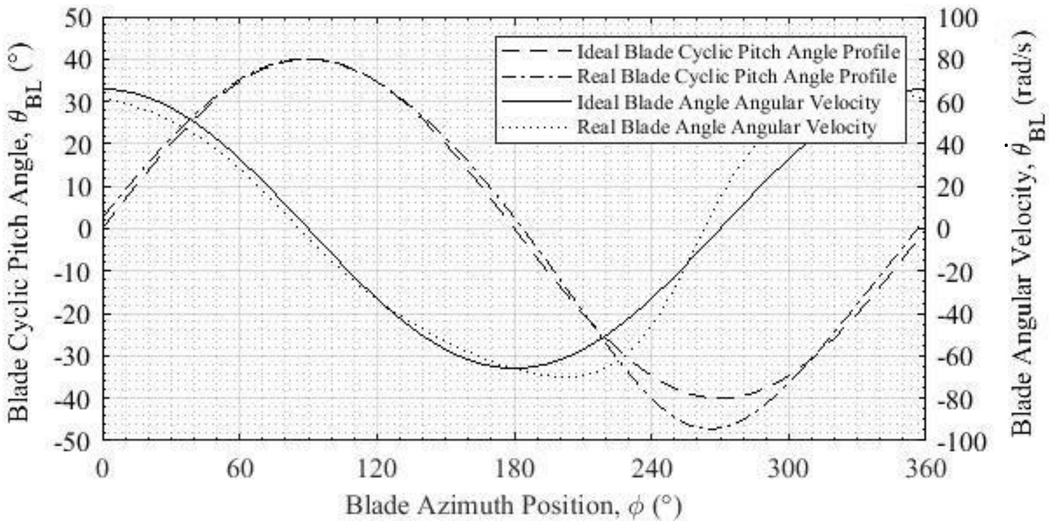

Figure 2.5 – Geometric blade pitching kinematics (blade cyclic pitch angle 40°)

This means that a larger rotor swept area is required to improve hover efficiency, but this cannot be considered in isolation; large swept areas often mean longer and more slender blades, which come with their challenges in design and analysis. Unlike conventional rotors, where centrifugal loads help stiffen the blades, the centrifugal load acts to bend the blade in a cycloidal rotor. Therefore cycloidal rotor blade design must have sufficient bending stiffness to bear this load. For the case of the cycloidal rotor, all operating states of the rotor need to be considered simultaneously to develop the design and concept further.

2.4. Recent Cycloidal Rotor Research

Research on the conventional cycloidal rotor design has been covered in section 2.3. The present section outlines the main research to date covering the optimization of the cycloidal rotor and proposals to modify it from its conventional form.

Pascoa [23] investigated whether the superposition of additional blade cyclic pitch angle input frequencies onto the baseline sinusoidal blade cyclic pitch profile could be used to increase cycloidal rotor performance. Initially, for a single blade, followed by a six-blade 1.2m diameter cycloidal rotor analysis. The analysis was undertaken through the use of a 2D CFD Unsteady Reynolds Averaged Navier Stokes (URANS) model. The CFD models were initially used to study the vortex dynamics around a single oscillating blade and extended to the full cycloidal rotor. The vortex behavior in both geometries was analyzed through Takens Reconstruction Theorem to determine whether the flow was chaotic or periodic with the inclusion of an arbitrary additional blade cyclic pitch input.

Takens Reconstruction Theorem converts time series data into phase space to visualize any changes in the system's dynamic variables and reconstruct qualitative features of the system. The change of the blade lift coefficient with time was analyzed in this instance [23]. Takens Reconstruction Theorem generates a phase diagram to see how the desired variables evolve with time, where the phase diagram shape describes the qualities of the system. A phase diagram that overlaps during subsequent loops is said to be steady. Where no discernable pattern is identified, the system is described as chaotic.

In all, sixty combinations were considered to cover changes in input frequency, phase, and amplitude, to determine the effect on system performance for the single blade and full cycloidal rotor geometries. Finally, the mean thrust coefficients were calculated and compared with the baseline case without the additional frequency input. For the single oscillating blade, five input amplitudes were considered between 0.1° and 2°, at phase angles 90° apart. Three arbitrary frequency values were selected, 1 Hz, 10 Hz, and 100 Hz, for a blade oscillation of approximately 3 Hz. The additional frequency input increased blade performance by up to 8% at 10 Hz with an amplitude of 2° and phase of -180°. Conversely, performance decreased by 15.5% at 10 Hz with an amplitude of 1.5° and phase of 90°.

The cycloidal rotor geometry was analyzed at a rotational speed of 200 RPM (3.33 Hz) at two harmonics, 80 Hz and 160 Hz, representing frequencies of 24/Rev and 48/Rev. The amplitude and phase were constant at 1° and 0°, respectively. The analyses concluded that the superposition of a higher harmonic blade cyclic pitch input increased the cycloidal rotor thrust and power levels, but the PL of the rotor reduced as the thrust increased.

Andrisani et al. [9] undertook an analysis using a simplified aerodynamic model to define a hovering rotor's optimal blade pitching schedule to minimize the mean power at a given mean thrust. The study made several simplifying assumptions, the main being that the thrust and power generated by each blade are independent. Compared to the original pitching profile, the same thrust level can be obtained with an optimized blade pitching profile, with a 10% reduction in rotor rotational speed. This equates to a 14% increase in thrust for a given power.

Transient 2D CFD analyses were undertaken with an incompressible Reynolds Averaged Navier Stokes (RANS) solver to validate the simplified model. The optimal pitching schedule CFD results are in good agreement with the reduced-order model. For a given power, the resultant thrust increases up to 25% in some cases, with a rotor speed reduction of 10%. The phase of the resultant thrust from the CFD is markedly different from the reduced-order model.

The instantaneous rotor forces analysis showed that the optimal pitching schedule induced increased resultant force un-steadiness compared to the baseline blade pitching schedule. Such an effect could significantly impact the validity of this approach in a physical system by inducing increased levels of rotor vibration, which may be challenging to accommodate structurally.

To improve the performance of cycloidal rotors in forward-flight and vertical lift operation, Habibnia and Pascoa [24] proposed an optimization methodology incorporating 2D CFD and Artificial Neural Network (ANN) to calculate an optimum blade pitch schedule for each operating state. CFD simulations were undertaken for a wide range of blade operating conditions at a number of rotor speeds for forward and vertical flight. Simulations were used to produce a numerical database and used in conjunction with the ANN algorithm for subsequent optimization analyses to dynamically analyze the cycloidal rotor and provide a blade pitching schedule for optimum efficiency.

The study identified three key sequential flow areas to the cycloidal rotor hovering operation, considering the six-blade rotor used in this instance. The '*inhaling* region' is where the air is drawn into the rotor from the free stream, typically from and extending past the rotor's top half, as identified by region 1 in figure 2.6. Secondly, as the flow progresses through the rotor for a hovering rotor, it flows vertically downward through the rotor cage, depicted by region 2. Finally, as the flow exhausts or *'exhales'* from the lower half of the rotor and is inclined to the right, assuming the rotor is rotating in a counter-clockwise (CCW) manner and resembles a free jet, characterized as '*downwash jet flow.'* as shown by region 3. The analysis also concluded that the *'inhaling'* and '*exhaling*' regions in vertical flight are similar to that of a hovering rotor. The proposed approach to actively control cycloidal rotor blade pitching was successful in rotor optimization.

Like an oscillating aerofoil at high-pitch angles, the cycloidal rotor can operate under dynamic stall conditions. To enhance the aerodynamic efficiency of cycloidal rotors, Xisto et al. [25] have considered using Dielectric Barrier Discharge (DBD) plasma actuators for active flow control on the leading edge of a single pitching aerofoil to delay dynamic stall.

DBD, compared to other flow control techniques, consume low power and has the added benefit of not having any moving parts. Two forms of DBD were considered using single and multiple DBDs. The DBD actuators were included in a NACA0012 aerofoil and analyzed with a URANS solver with the k-ω shear stress transport (SST) transition model to capture the occurrence of dynamic stall [25].

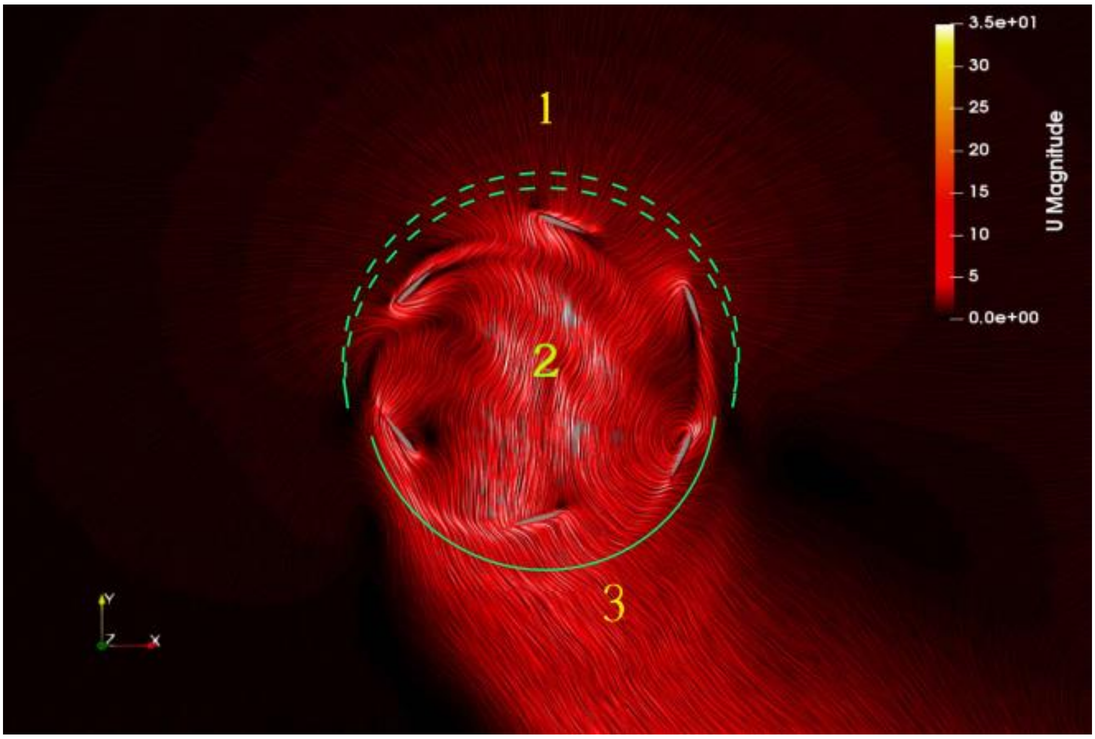

Figure 2.6 – Flow structure in a hovering cycloidal rotor at 300 RPM, 20° blade cyclic pitch angle, and a rotor diameter of 0.8 m [24]

Cycloidal rotor flow is highly unsteady, coupled with the blade pitch angle continually changing; using a single DBD was insufficient to provide adequate flow control. A blade configuration with multiple DBD actuators was also considered to improve flow control. The design's success was sensitive to the position of the chordwise actuator positions, as the optimal position will change with changing blade cyclic pitch angle and rotor rotational speed. In *'steady actuation mode,'* the DBD actuators remained on throughout and reduced the aerodynamic efficiency in the downstroke of the single aerofoil. The DBD actuators should be used with a control algorithm to operate at key positions in the cycle to minimize losses [25].

2.5. Effects of Rotor Design on Performance

The following section reviews the main cycloidal rotor geometrical parameters for low-pitch cycloidal rotors in hover to aid and guide the analysis and design of the test rig outlined in Chapter 3. Although outside the scope of the current research, studies that consider the analysis of a low-pitch rotor in forward flight have also been considered, two examples being [14, 15]. In addition, no studies to date focus on high-pitch cycloidal rotors in hover or forward flight for crewed and uncrewed flight applications.

2.5.1. Blade Pitching Schedule and Amplitude

During operation, all of the thrust and blade control forces are generated purely by the motion of the blades, which is a combination of pitching and oscillatory motion [22]. Early designs used fixed cyclic pitch mechanisms, where only the thrust vectoring capability of the cycloidal rotor was used [8]. As a result, changes in thrust magnitude could be developed only by changes in rotor rotational speed.

For a standard low-pitch cycloidal rotor, the blade geometric pitch angle is sinusoidal motion with respect to the azimuth angle, suggested to be optimal for a rotor in hover by Wheatley [8]. Most recent designs use a four-bar mechanism to pitch all blades from one eccentric point. The analysis of the four-bar mechanism shows that pure cycloidal motion is impossible with such a device due to all of the blade's trajectories being identical. Consequently, the blade geometric pitch angle change with azimuth position is not quite a pure sine wave. Due to the asymmetric blade pitching, there is a difference between the blade pitch angle in the upper and lower rotor halves, resulting in a larger blade geometric AOA at the BDC position [26].

At low-pitch angles, the deviation from ideal motion is not significant. However, as the maximum blade cyclic pitch angle increases to greater than 20°, the variation is noticeable with the geometric blade pitch angle overshooting the ideal sinusoidal motion, as shown in figure 2.5. Furthermore, the blade angular velocity and acceleration also change as a result [26], as both are functions of changes in blade cyclic pitch angle with azimuth. Hence, the actual blade pitching kinematics need to be included to analyze the cycloidal rotor correctly.

The blades need to operate at a high peak geometric AOA to improve cycloidal rotor efficiency, where the maximum blade cyclic pitch angle is known to impact rotor performance significantly [27, 28]. As the blade cyclic pitch angle increases, rotor thrust and power loading also increase as a direct result, with the best power loading achieved at a peak blade pitch angle of 40° for a four-bladed rotor in hover [29]. In addition, higher blade cyclic pitch angles enable the rotor to run at lower rotational speeds for a given thrust requirement without any detrimental effect on other aspects of the rotor operation.

Blade pitching gives rise to rapid changes in the boundary layer around the blade's Leading Edge (LE) and Trailing Edge (TE), which is more pronounced in the lower half of the rotor [30] for a rotor in hover. As the blade cyclic pitch angle increases, stall is delayed compared to a static aerofoil due to the blade oscillation, which can be used to augment thrust.

A large downwash is generated within the rotor during operation, estimated to be between 60-70% of the rotational speed of the blades [31]. Added to the non-uniformity of the flow within the rotor, this acts to reduce the effective blade AOA and deplete blade thrust generation. However, despite the effective AOA reduction in the lower half of the rotor, the generated thrust is still higher in the lower half of the rotor than the upper, under hovering status [4]. This is attributable to the increase in blade cyclic pitch angle at the BDC position due to the asymmetric pitching of the blade, helping to maintain the blade's effective AOA, and due to unknown induced velocity and virtual camber (VC) effects. A thorough explanation of virtual camber is provided in section 2.5.15.

During hover, the rotor draws in air from both above and from the sides of the rotor [31]. When coupled with the large inflow generated within the rotor, this gives rise to lateral or side force generation, which is of a similar magnitude to the vertical (lifting) force component at certain geometric blade cyclic pitch angles. Where the lateral or side force thrust component, as defined in figure 1.2 as F_x acts parallel to the velocity-free stream in forward flight. For purely VTOL operations, it is important to eliminate or reduce the side force component, which for a cycloidal rotor remains a significant task [32]. The phase angle required to minimize the lateral force component is a function of blade pitch angle only and independent of rotational speed [33] for a rotor in hover. In some instances, the resultant thrust leads the maximum blade pitch angle by approximately 10 to 20 degrees [19], with the phase lead angle reducing with an increase in thrust.

The pitching of the blades has only been considered to be sinusoidal or approaching sinusoidal via the use of a four-bar mechanism. McNabb [34] and Adams et al. [21] suggested that the pitching schedule of the blades can be optimized for all flight operating conditions, including hover and forward flight at various advance ratios, where the optimal blade pitching kinematics is a function of rotor advance ratio, μ. Little analysis has been undertaken to establish an optimal blade pitching schedule, but Adams et al. [21] have shown that different blade pitching schedules are required for efficient hover and forward flight to optimize both DL and PL simultaneously.

2.5.2. Rotor Diameter

Yun and Park [35] found that a larger diameter improved rotor efficiency. As the rotor diameter increases in hover, the rotor rotational speed reduces inversely for a given thrust. This is a direct result of keeping the relative blade velocity constant with the rotor radius. As the rotor diameter increases, the swept area will also increase, and the rotor scaling ratio effect will reduce the DL for a given thrust. A trade-off needs to be made between the rotor rotational speed reduction and the rotor structural mass increase due to the larger diameter.

2.5.3. Blade Loading

The resultant thrust generated by a cycloidal rotor blade can be broken down into a lateral (propulsive) and vertical (lifting) thrust component, as defined by F_{xb}

and F_{yb} in figure 2.4. The blades are subject to centripetal, aerodynamic, and torque loading due to rotor rotation and blade oscillation, with rotor efficiency driven by their design. High transverse blade loading is inherent in the rotor design, with blade centripetal loading estimated to be several orders of magnitude higher than the blade aerodynamic loads from recent analyses. Designing purely for centripetal loads due to a lack of understanding has led to typically over-dimensioned structures.

Blade centripetal loading is nearly constant with changes in azimuth angle and directly proportional to blade mass and the square of the rotor rotational speed ω. Aerodynamic loads vary cyclically and reverse twice per rotor revolution, generating a dynamic flap-wise and edge-wise bending moment on the blade, a source of blade fatigue, and increased airframe vibration. A definition of the blade loading directions used is shown in figure 2.7. The blade inertial and aerodynamic loads are responsible for blade deformation in the flap-wise, edge-wise, and torsional directions. As blade stiffness reduces, the aerodynamic load contribution is more pronounced [36], making it more important to distinguish between blade inertial and aerodynamic loading.

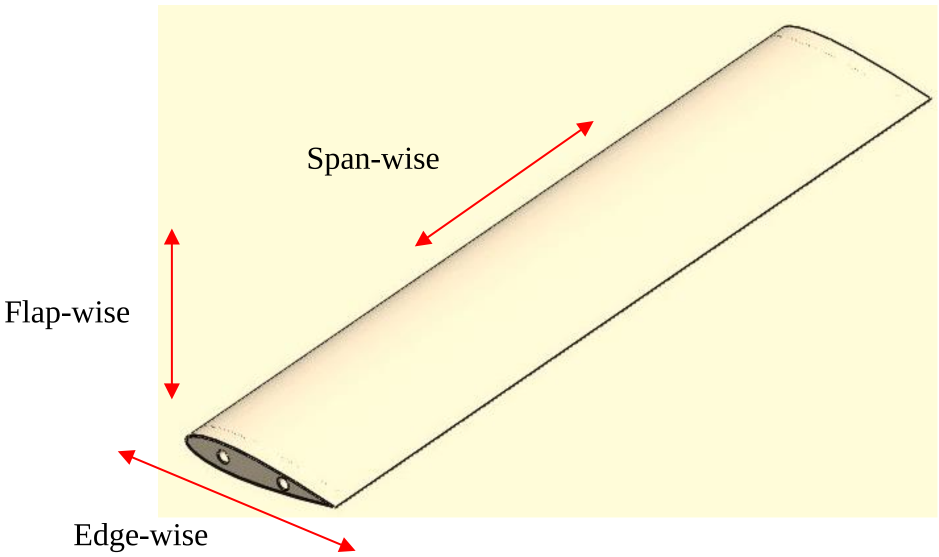

Figure 2.7 – Cycloidal rotor blade loading direction definition

Carbon fiber is the material of choice in all recent blade advancements due to the ability to tailor the material properties to achieve the high strength-to-weight ratios required. Finite element software has been used to optimize blade material layup.

Maine [37] developed a carbon fiber blade with isotropic material properties to account for the variation of blade loading with azimuth angle. In reality, an orthotropic material layup is required to ensure optimal properties in the flap-wise direction to negate the transverse loading effects whilst keeping mass to a minimum.

The control forces required to oscillate the blades in the given pitch schedule are developed purely by the pitch mechanism [33]. The blade loads induce a pitching moment about the blade pitch axis that is reacted at the control rod attachment point. Its magnitude is dependent on the blade pitch angle and position of the blade pitch axis relative to the LE of the blade. Many designs [20, 38] pitch the blade from the in-board rotor side, meaning that the blade is only restrained at one end; this can lead to excessive blade twist at high blade loadings, leading to a nose-down deflection of the blade, which is more pronounced under dynamic stall (DS) conditions.

The aerodynamics of the cycloidal rotor is unsteady due to the pitching of the blades. The degree of unsteadiness is a function of rotor rotational speed and blade chord and is given as the Reduced Frequency k:

$$k = \frac{\omega c}{2V_a} \tag{2.4}$$

where c is the blade chord. k values greater than 0.05 show the onset of unsteady aerodynamics. At low blade AOA, the flow is still transient in nature but can remain attached, resulting in unsteady aerodynamic loads that ultimately vary about a mean value. As the blade cyclic pitch angle of the blades is increased beyond the static stall angle of the blade, this can lead to dynamic stall. This results in phase variations in the unsteady air loads, leading to increased blade load hysteresis, giving higher than static lift values generated by the pitching of the blades. The hysteresis's magnitude depends on whether the flow is reattaching or separating, which is a function of the blade pitch mechanism offset, phase angle in forward flight, and the degree of unsteadiness in the flow.

Instantaneous blade lift and drag loads depend on local dynamic pressure, effective blade AOA, and the blade's orientation in relation to the free-stream velocity in forward flight. The effective blade AOA is also a function of the rotor advance ratio in forward flight [34]. The blade relative flow velocities change in direction and magnitude with changes in rotor azimuth angle, leading to blade vertical and horizontal force components that vary continuously and cyclically with rotor rotation. Under forward flight conditions, the retreating side of the rotor is moving in the same direction as the free stream velocity, which reduces the blade's tangential velocity [14].

2.5.4. Rotor Rotational Speed

The rotor rotational speed is dependent on the net thrust levels required and the rotor outer diameter. As the rotor rotational speed increases, higher forces are produced due to the higher relative velocities at the blades for a given rotor diameter in hover. For a constant blade tip speed and blade pitch amplitude, the rotor power and torque vary as defined by [4], where

$$P \propto \omega^3 \tag{2.5}$$

$$T \propto \omega^2 \tag{2.6}$$

where ω is the rotor rotational speed, P is the rotor power, and T is the rotor thrust.

2.5.5. Rotor Span

Strandgren [17] and McNabb [34] identified the importance of the rotor aspect ratio, the ratio of span to rotor diameter, with both recommending that the rotor be made with an aspect ratio of one for optimum efficiency. Benedict et al. [39] suggest that the cycloidal rotor blade and span should be easily optimized because the relative blade velocity, AOA, and Reynolds number are relatively constant in the rotor spanwise direction. Research by Yang [40] contradicts this and suggests that there is a wake contraction or Vena Contracta along the blade span that changes the blade spanwise flow regime, inducing 3D flow effects. However, it is worth noting that shorter blade spans produce higher PL in hover [41].

The aerodynamic efficiency of the cycloidal rotor, similar to an H-Darrieus VAWT, increases at lower aspect ratios for both hover and forward flight. Adams et al. [14] predict that the thrust-producing ability of the cycloidal rotor in forward flight reduces with span increase almost linearly for a given RPM.

The power per unit span for a rotor in hover increases almost linearly; as the rotor span increases, the thrust force goes up proportionally as a direct result [4]. For a given thrust, the rotational speed of the rotor will reduce with an increase in span. If a longer span is used, consideration must be given to the blade's unsupported length and stability. It is known from VAWT analyses [42] that at lower aspect ratios, the performance of the rotor is more susceptible to blade tip losses and 3D flow effects. However, this is not proven yet for a cycloidal rotor.

2.5.6. Rotor Support

One of the main drawbacks of the cycloidal rotor design is the relatively large rotating structure [43]. Flow rotation or swirl within the rotor cage and other rotational losses, including support structure parasitic drag, accounts for between 10-15% of the aerodynamic power loss under hovering status for a UAV scale rotor [4]. This suggests that the rotor's circulatory flow may lie with the blades' motion combined with the rotation of the overall support structure for a rotor during hover.

Flow circulation is defined as a measure of the total rotation contained in the flow field. At the surface of the rotating cylinder, or the rotor support structure in this instance, the fluid will rotate at the tangential velocity component of the cylinder or rotor end disc outer radius due to the no-slip condition at the boundaries. A rotating cylinder with no imposed parallel free-stream flow will result in pure circulatory flow, which will give a flow pattern of concentric circles, as shown in figure 2.8, where the inner circle defines the rotor. A thorough explanation of the rotor circulatory flow is provided in section 2.5.13, during the discussion of the Magnus effect during cycloidal rotor operation.

A high structural mass results in a lower rotor natural frequency for a given stiffness. A factor that must be included in the rotor design to avoid any potential resonance issues. Increased dimensions and mass increase the rotor polar and tangential mass moments of inertia relative to the rotational axis, thus increasing the parasitic torque and reducing the available acceleration assuming the power is constant. Another contributor to the parasitic torque is the power train frictional losses. The support and pitching mechanism can contain numerous components, including pins and bearings, and if not designed correctly, it can have a detrimental effect on the overall design.

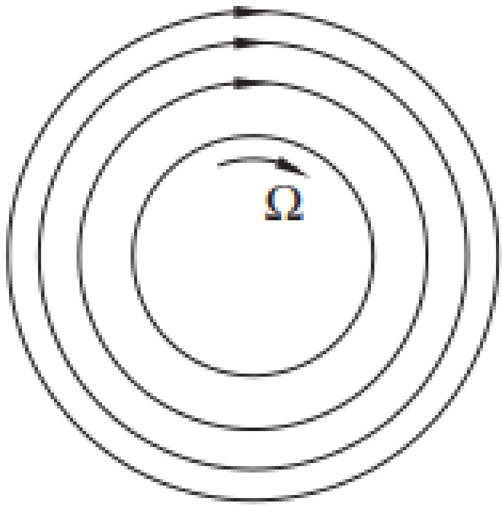

Figure 2.8 – Flow patterns for a rotating circular cylinder with no imposed parallel free-stream flow

To date, Hwang et al. [43] is the only analysis available to consider the airframe and/or rotor support influence. Most of the smaller UAV designs use a cantilevered rotor supported at the inboard side only. The larger variants [34] tend to utilize a simply supported configuration. There are a number of advantages to simply supporting the rotor, mainly from a rotor deflection, balancing, and rotor dynamics perspective. In theory, a simply supported rotor is easier to configure to meet the design's critical speed and vibration requirements due to possible resonances at multiple frequencies of the speed of rotation [43]. Although the cantilevered design is more challenging, it does have the advantage of reduced mass, which is important from an overall rotor design perspective.

The rotor support is subject to unsteady torsional and bending loads radially and tangentially and is designed to resist high levels of transverse blade loading and possible aerodynamic harmonic vibration. Thus consideration needs to be given to reducing the static and fatigue loads imparted onto the rotor support. In addition, unsymmetrical pitching of opposing blades at high pitching amplitudes can give rise to aerodynamic out-of-balance at multiple frequencies of rotational speed, which is a function of rotational speed and blade number. This can be more pronounced at lower solidities due to the higher individual aerodynamic blade loadings and increased risk of inertial loading out of balance.

Larger-scale rotors use spherical bearings at the supports, putting the support arms into tension and minimizing any bending moments [43]. The support of the blades is important not only from a blade pitching perspective but blade supports can also be used to reduce the bending stresses within the blades at the in and outboard blade sections.

Most analyses to date [38, 39] have utilized spoked endplates to reduce the overall rotating mass. No one has considered in detail the effect of solid endplates. But due to their increased mass, inertia, and parasitic drag, it would suggest that solid end plates would reduce the PL of the rotor during hover, but this needs further analysis. On small-scale rotors, the blades can be designed to have sufficient stiffness, to resist the required bending moments, but the support structure is difficult to design with the same level of stiffness at low mass. Hwang et al. [43] found the rotor end supports to be the driving factor in their initial rotor modal analysis due to their low effective stiffness. There is limited scope for centripetal stiffening effects within both the blade and support design with UAV scale rotors unless flexible blades are used, but this is not necessarily the case as the rotor dimensions increase, where the blades become more flexible and slender.

2.5.7. Blade Aspect Ratio

The rotor blade aspect ratio is defined as the ratio of the blade span to the chord. High-aspect ratio wings have long spans, while low-aspect-ratio wings have either short spans or large chords. 3D vortices shed at the blade tips induce an additional velocity term that changes with the blade aspect ratio. The effect of a finite aspect ratio is to give rise to induced drag, which is inversely proportional to the blade aspect ratio. The higher the wing aspect ratio, the lower the induced drag. The further the distance between the blade tip vortices, the less their effectiveness in producing induced drag. Hence the lower the aspect ratio, the stronger the 3D flow effects. For small aspect-ratio blades, the blade tip vortices roll up at the blade ends and dominate the flow field [44]. The induced velocity also varies in the blade chordwise direction. The assumption of a high-aspect-ratio permits the chordwise velocity variation to be neglected [44].

For a blade with a high-aspect ratio, it can be assumed that the flow around each blade is approximately 2D. Therefore, blade efficiency will improve with aspect ratio and for a given blade aspect ratio with an increase in end plate size, where end plates change the blade tip vortex characteristics. The effect of end plates is considered further in section 2.5.14.

Figure 2.9 shows the lift vs. incidence curve for an arbitrary aerofoil section in a 2D and 3D flow, illustrating the influence of 3D flow end effects on the aerofoil lift curve slope. With 3D flow effects included, the gradient of the lift curve slope reduces, confirming the blade efficiency improvement with aspect ratio for a given angle of incidence.

Gosselin et al. [45] conducted a parametric analysis of a single-blade vertical axis wind turbine (VAWT) with and without end plates for an aspect ratio of 7, 14, and 72, using a k-ω SST RANS CFD model. At an aspect ratio of 7, the overall turbine efficiency was 40% of the theoretical 2D efficiency. The efficiency increased to 70% of the theoretical 2D efficiency when the aspect ratio was increased to 14. Increasing the blade aspect ratio to 72 enabled 95% of the 2D efficiency to be realized, illustrating the reduction in the contribution of 3D flow effects with an increase in blade aspect ratio.

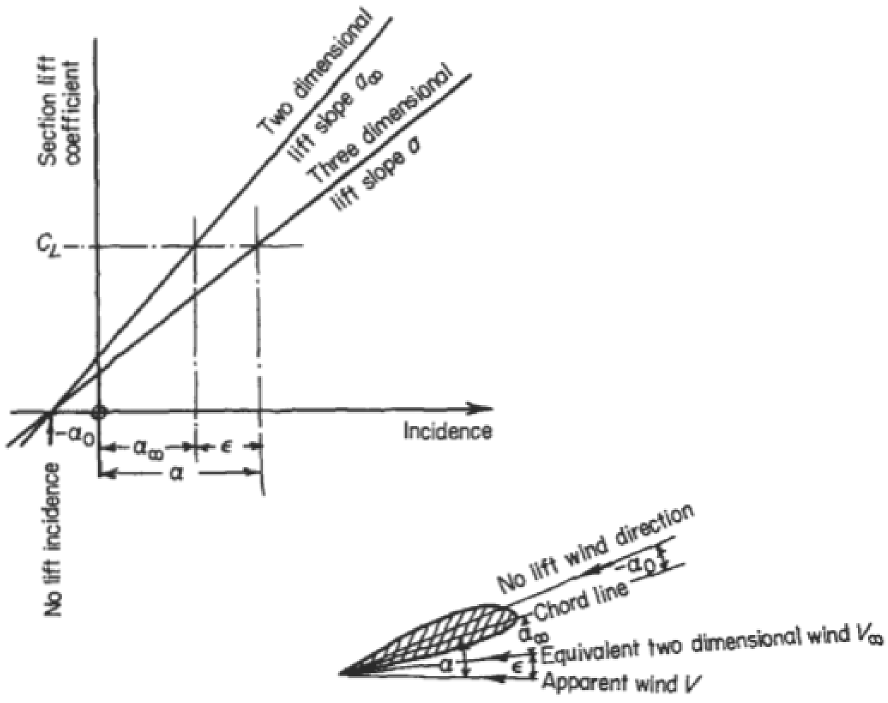

Figure 2.9 – Lift-versus-incidence curve for an arbitrary aerofoil section working two-dimensionally and working in a three-dimensional flow regime influenced by end effects [44]

2.5.8. Blade Profile

The blades used to date have been a combination of flat plates with no or small leading-edge radii [30, 46] to the use of more conventional NACA 4-digit series aerofoil in the majority of cases [43]; due to their ability to work equally well at a positive and negative AOA. There have been no studies to date to develop aerofoil sections specifically for cycloidal rotors and, more importantly, at low Reynolds number flows in UAV scale applications. For low Reynolds number flows, special attention must be given to the viscous flow effects [4]. A Blade that is a flat plate generates blade loads from drag only, while aerofoil sections derive some of their force from lift. A lift force is more efficient at generating thrust in forward flight, which ultimately improves the thrust generation ability of the rotor.

Benedict [4] has considered a number of blade sections, from NACA 0006 to NACA 0015 profiles. The NACA 0015 profile produced the highest PL for all analyses, and the NACA 0006 was the lowest for a hovering rotor. With a symmetric blade cyclic pitch amplitude of +/- 35° on a 4-bladed rotor, the NACA 0006 still produced a significantly lower PL than the NACA 0015 profile, suggesting that the overall performance of the aerofoil section and the rotor is very sensitive to blade thickness and LE radii [46].

Typically at low Reynolds numbers, thinner aerofoils perform better in rectilinear flow [29], but this does not translate to cycloidal motion. A blade with low profile drag needs to be developed for cycloidal motion, with good stall and lift characteristics. Standard aerofoils typically have low C_L/C_D ratios at low Reynolds numbers, which is something that needs to be addressed. A blade with a high lift coefficient and reduced profile power will enable a rotor with a lower solidity and lighter structural mass to be developed. A blade with a low pitching moment would help minimize blade torsional moments and potentially vibration and keep control loads on the pitching mechanism to a minimum.

There have been no cambered aerofoil-based studies based on a cycloidal rotor. However, it has been attempted on H-Darrieus VAWT [47] to improve the turbine's self-starting ability. However, in preliminary studies, Yang [40] found that using cambered blades on a cycloidal rotor reduced the PL. Another contributing factor to the reduction in performance could be the increased profile drag of a cambered aerofoil compared with that of an un-cambered blade.

2.5.9. Blade Thickness

As the thickness of the blade increases, the recirculation zone at the leading edge and hence flow separation reduces, with the thicker symmetrical profiles having better stall characteristics than the thinner alternatives. Xisto et al. [20] found that as the thickness of the blade increases, it is less susceptible to flow separation, with the flow staying attached at the leading edge for longer and at a higher blade AOA. For symmetric NACA 4-digit series profiles, as the blade thickness increases, the PL increases for all values of DL [29], a direct result of a decrease in power with an increase in blade thickness, attributable to a lower profile drag and lower recirculation region at the leading edge due to blade pitching.

With an increase in aerofoil thickness, there is a reduction in the strength of the Blade Vortex Interaction (BVI), suggesting that BVI is dependent on the blade section to a degree, which in turn is dependent on flow separation at the blade LE [20]. As the NACA 4-digit blade thickness increases, smaller aerodynamic forces are generated, resulting in smaller unsteady aerodynamic force fluctuations, lower thrust generation, and blade deflection. This results in smoother operation, lower fatigue loading on the blades, and a lighter support structure.

As the thickness of the NACA 4-digit aerofoil section increases, the maximum lift coefficient reduces, which gives a compromise between the high aerodynamic efficiency of a slender aerofoil and the increased structural stiffness and safety of the thicker section. Safety has been one of the overarching issues to date and one of the reasons why a NACA 0018 aerofoil has been used more often than not in cycloidal rotor design [48].

Due to the unsteady pitching of the blade, LE radii have a prominent effect on the efficiency of the rotor design [46]. As the blade thickness reduces, flow separation occurs sooner and at a lower blade AOA as a result of the smaller LE radius. This means that even at relatively low blade AOA, once flow separation occurs, there is an increase in the profile drag on the blade section and a reduction in rotor efficiency.

2.5.10. Blade Number

The cycloidal rotor is not limited to any number of blades per se, with the minimum being two. A two-bladed rotor, during operation, generates most thrust at the 90° (12 o'clock) and 270° (6 o'clock) azimuth position in hover [28]. With three blades, one blade is still generating most of the lift at any given moment, which can result in larger blades being required [4]. As the blades pitch and rotate about the azimuth, they generate periodic impulses at frequencies multiples of the rotor rotational speed, which is dependent on the number of blades used. These periodic impulses, in turn, generate torque and blade force fluctuations with rotor rotation [30] and can result in a high level of out-of-balance vibration and accompanying levels of unsteady force and torque ripple.

The strength of the periodic impulse is dependent on blade number. As the blade number increases for a given solidity, the operation of the cycloidal rotor appears to smooth out. Kim et al. [28] suggest that for a rotor with two blades, the periodic impulse vibration becomes 'severe,' with the operation of the cycloidal rotor becoming noticeably smoother when six rotor blades are used. This is a direct result of fewer blades generating thrust at any one time as the number reduces. The blade inertial loads are balanced for a two-bladed rotor during operation, but the unsteady aerodynamic loads are not.

Although an increase in blade number is beneficial from a vibration perspective, as the number of blades increases, the profile drag of the blades also increases, with profile drag being highly reliant on rotor speed. There is a significant increase in rotor inflow and blade interference with an increase in blade number. The interference is a consequence of the increased interaction between the stronger wakes of blades in both the upper and lower half of the rotor [28]. As the rotor downwash increases with blade number, this reduces the blade AOA, particularly in the lower half of the rotor, and results in less lift per blade being generated.

Intuitively doubling the blade number would double the resultant thrust generation, but this is not seen. The performance of the cycloidal rotor is much reduced when six blades are used [20] compared to using three blades, with rotor thrust not increasing linearly with an increase in blade number [49]. A peak blade cyclic pitch angle input change from 25° to 40° results in a distinct change in the flow regardless of blade number for a constant rotor solidity [29]. This suggests that rotor inflow and blade wake interactions are also a function of the blade geometric peak cyclic pitch angle and blade pitching schedule.

As the number of blades reduces, for a given thrust, the rotational speed of the rotor needs to increase accordingly; alternatively, to achieve the same level of thrust, a blade with a larger chord could also be used. For a constant solidity, a two-bladed rotor produces a higher lift and PL than a three and four-bladed rotor in hover [29], with the four-bladed rotors producing the lowest lift, attributed to the changes in rotor inflow and interference effects with blade number [28, 29]. Xisto et al. [20] also concluded that a three-bladed rotor has a higher PL than the four-bladed variant. The four-bladed configurations generate higher thrust levels than the three-bladed rotor, assuming a 40° and 20° peak blade pitch amplitude.

2.5.11. Blade Pitch Axis Location

For an oscillating aerofoil in a rectilinear free stream, pitch axis location is not important from a lift generation perspective. However, for a cycloidal rotor, the pitch axis location relative to the blade LE has a strong impact on the efficiency of the rotor [15]. Ideally, the blade pitch axis should be coincident with the center of gravity position of the blade, as this remains unchanged with the blade's geometric pitch angle. As opposed to the center of pressure, this varies with blade geometric pitch angle changes. Invariably there is a difference between the pitching axis, aerodynamic center, and center of gravity position, generating a moment about the pitch axis. Therefore, during the design of the cycloidal rotor, it is beneficial to reduce the distance between the pitching axis, aerodynamic center, and center of gravity to reduce fluctuating blade loads, which will directly affect the blade fatigue life. Typically for a NACA 4-digit series aerofoil, the position of the aerodynamic center is around the 25% chord position.

The thrust generated reduces for a given rotor rotational speed as the pitching axis moves away from the blade's LE in hover [29]. During hover, the optimum pitch axis location is between the 25 and 35% chord position, with the PL steadily increasing up to the 25 and 35% chord position. After this, the PL reduces for the two, and four-bladed rotors considered in [29]. The highest power consumption typically occurs around the 50% chord position [50]. At advance ratios less than 0.4, moving the pitching axis away from the LE results in reduced thrust levels. However, thrust increases as the pitch axis moves away from the blade LE for higher advance ratios between 0.94 and 1.25 [6].

Little research has been undertaken to establish the effect of pitch axis location in forward flight. But the thrust again decreases, almost linearly, as the pitch axis moves away from the blade LE [15]. The closer the pitch axis to the LE of the blade, the increased thrust production efficiency, even in forward flight, with the optimum pitch axis location dependent on the rotor advance ratio [14]. A study comparing the rotor PL and DL needs to be undertaken to find the optimum pitch axis location for a hovering rotor.

2.5.12. Rotor Solidity

Rotor Solidity σ is the ratio between the lifting area of the blades and the swept area of the rotor, given by

$$\sigma = \frac{N_b c}{2\pi R} \tag{2.7}$$

where N_b represents the total blade number. There are essentially two ways to change the rotor solidity. Firstly by keeping the blade number constant and increasing the chord length, and secondly, by keeping the blade chord constant and increasing the number of blades, keeping the chord to radius (c/R) ratio constant. Another option would be to increase the rotor diameter.

Benedict [4] suggests that it is better to keep the same number of blades and increase their chord instead of increasing the number of blades with the same chord to achieve a given rotor solidity. Changing solidity by increasing the blade chord produces large improvements in power loading [29], with power loading increasing up to a rotor solidity of approximately 0.25 in some cases. If the key objective is to maximize thrust, it is beneficial to have fewer blades with a larger chord [29] than the inverse.

A rotor with high solidity can achieve a higher thrust value at a lower rotational speed than a rotor with low solidity. Benedict [4] shows that the profile drag at higher rotational speeds is dominant over the increase in profile drag due to the increase in blade number and planform area, but this depends on the individual aerofoil profile used.

As solidity increases, the total thrust and torque also increase in hover, but the thrust and torque per blade reduce if the solidity is increased by increasing blade number. Additionally, the higher the rotor solidity, the more the rotor behavior will be affected by the Magnus effect. The total number of blades based on a given chord length can increase drastically at high solidities. This tends to reduce rotor inflow and changes the rotor blade wake interactions. Rotational speed will also play a part in governing rotor inflow at high solidities; as such, with an increase in blade number, the efficiency of the rotor could be adversely affected [20]. The optimum solidity of the rotor is determined by the rotor c/R ratio for a given pitch amplitude in hover and advance ratio when forward flight operation is considered [15, 49].

2.5.13. Rotor Magnus Effect

For the case of a stationary cylinder in cross flow, flow separation occurs at the rear of the cylinder, which creates a recirculating flow in the downstream wake of the body, as shown in figure 2.10. The flow separation results in a drag force being created parallel to the free stream, but due to the flow being approximately symmetric about the horizontal centreline outlined in figure 2.10, the measured lift force is essentially zero [51].

When the cylinder in figure 2.10 spins in a clockwise direction, the streamlines are no longer symmetrical, as shown in figure 2.11. In this case, the stagnation points shift to the lower half of the cylinder and can move off the surface of the cylinder if the rotational speed is high enough [52]. Frictional effects between the surface of the cylinder and fluid entrain the flow near the cylinder surface in the direction of rotation. The flow entrainment generates a higher velocity at the upper surface of the cylinder than at the lower. As the velocity increases in the upper half, the pressure decreases, producing a pressure imbalance between the rotor's upper and lower half, producing a lift force normal to the flow direction. This is known as the Magnus effect, and it is dependent on the cylinder rotational speed, fluid free-stream velocity, the viscosity of the fluid, and the size of the cylinder [53].

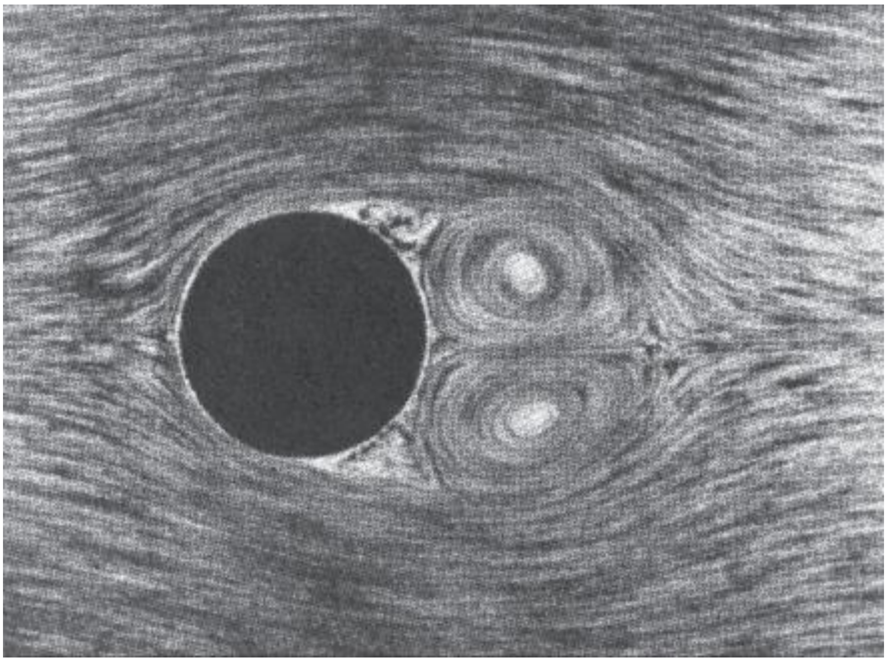

Figure 2.10 – Flow field images obtained in water to show the direction of the streamlines for a flow from left to right for the nonspinning cylinder [51]

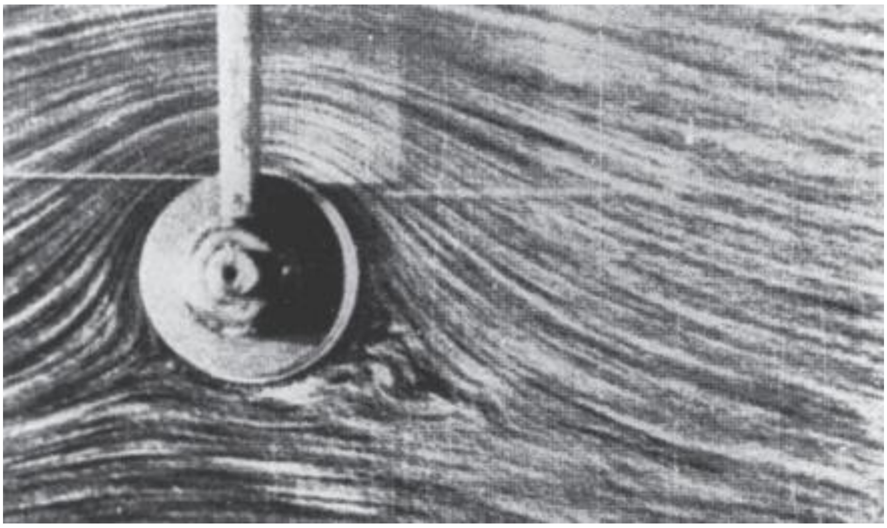

Figure 2.11– Flow field images obtained in water to show the direction of the streamlines for a flow from left to right for the spinning cylinder with a peripheral surface velocity of $3V_\infty$ [51]

The Magnus effect can be explained by a superposition of a non-lifting freestream flow over a cylinder and a circulation, Γ about the cylinder, representing the strength of the vortex. The vortex is positioned at the center of the cylinder, as illustrated in figure 2.12. The lift per unit span of the cylinder can be calculated from

$$L = \rho V_{\infty} \Gamma \tag{2.8}$$

which is known as the Kutta-Joukowsky Theorem, showing that the lift per unit span is directly proportional to the circulation. From equation 2.8, ρ is the fluid density, V_{∞} is the fluid free-stream velocity, and Γ is the circulation about the rotating cylinder. In the case of a spinning cylinder in a viscous fluid, the circulation can be defined as

$$\Gamma = \oint v.\,dl \tag{2.9}$$

once integrated this gives

$$\Gamma = v.\,2\pi R \tag{2.10}$$

where v defines the velocity at a point on the surface, which is the angular velocity for a cylinder given by

$$v = \omega R \tag{2.11}$$

ω is the cylinder rotational speed, and R is the cylinder radius. The circulation around the cylinder can then be calculated from

$$\Gamma = 2\pi\omega R^2 \tag{2.12}$$

The magnitude of the Magnus effect is strongly related to the velocity ratio between the angular velocity of the rotor and the fluid free-stream velocity, defined as α [53]. Depending on the velocity ratio, the magnitude of the lift and drag forces is also sensitive to the free-steam flow Reynolds number, where the characteristic dimension is defined as the cylinder diameter, particularly at low-velocity ratios [54].

The variation of lift and drag forces was more pronounced at a Reynolds number greater than 60,000 [54], with a slight reduction in both lift and drag forces noted with a reduction in the Reynolds number.

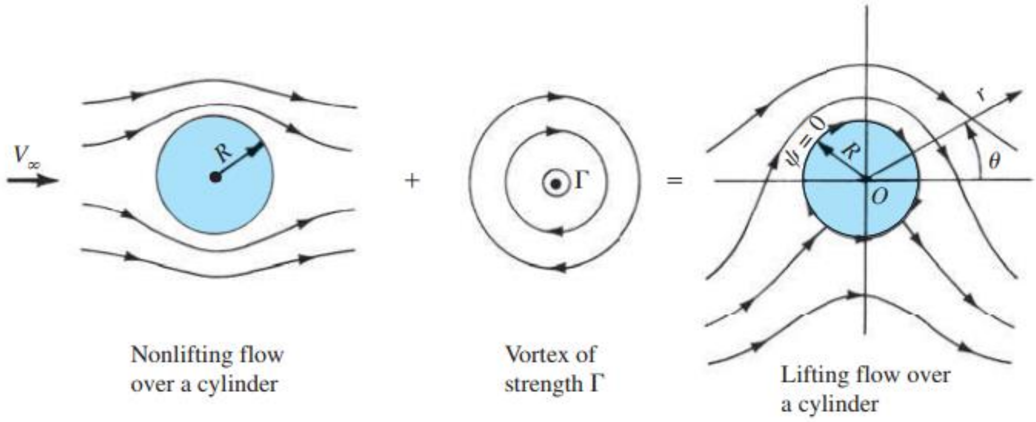

Figure 2.12 – An illustration of the flow components to calculate the lifting force over a rotating cylinder via the addition of a non-lifting flow and a vortex of strength Γ [52]

Research by Swanson concluded that a reduction in cylinder aspect ratio also resulted in a reduction in the maximum lift measured, which coincided with a reduction in the velocity ratio where the maximum lift was measured [55]. The aspect ratio effect is attributable to leakage flow and tip losses a the cylinder ends [53].

An early study by Prandtl [56] proposed that for an infinite cylinder that is approaching two-dimensional flow conditions, the maximum coefficient of lift generated by a spinning cylinder in a uniform cross-flow is limited to 4π. Three-dimensional equipment used by Swanson [55] aimed to determine if the coefficient of lift limit estimated by Prandlt could be exceeded with changes in rotor aspect ratio. It was shown that the maximum coefficient of lift achieved was 4.55π at a velocity ratio of 17. The study concluded that a higher coefficient of lift could be generated with an increase in the rotor aspect ratio [55].

The sensitivity of the cycloidal rotor design to the Magnus effect for forward flight operation in low-speed and high-speed forward flight where there is a free stream flow velocity component at this stage is unresearched. With the focus of the current research being on a rotor in hover, there is no free stream velocity component to consider in the traditional sense. The Magnus effect is usually associated with high solidity geometries at a high rotational speed. A solid cylinder is typically used in applications such as the Flettner rotor [53]. The solidity of the cycloidal rotor is typically much lower than a solid cylinder, with a solidity of up to 0.25 to 0.35 being used, depending on the rotor configuration [4].

With the solidity of the current test rotor and the range of rotor rotational speeds being tested being low compared to typical Magnus effect rotors, and coupling this with the fact that the rotor is not being tested under forward flight conditions, the Magnus effect is not considered in the current work. The Magnus effect should be reconsidered for future analyses with a change in focus.

2.5.14. End Plate Effects

It is well established in the design of vertical axis wind turbines (VAWT), which are geometrically similar to the cycloidal rotor in that blades with open ends generate tip loss effects that reduce the overall power output of the device [57]. Therefore, in VAWT design, additional winglets at the blade tips are sometimes added along with devices such as endplates to increase system performance by reducing tip losses. The addition of the winglets and endplates helps to reduce the spanwise flow caused due to the pressure delta between the pressure and suction sides of the blade, to improve blade aerodynamic performance [58,59]. The implementation of endplates was shown to improve the overall performance of a VAWT in all configurations researched by Amato et al. [60].

Simulations on a single-bladed NACA 0015 VAWT with two aspect ratios of 7 and 15 were performed by Gosselin et al. [61]. The larger aspect ratio had a greater coefficient of performance of 62.5%, indicating that the shorter blades are more susceptible to blade tip losses and 3D flow effects, as a larger percentage of the blade span is affected by the tip vortices. It is suggested that the inclusion of end plates in the design should also be undertaken in conjunction with the optimization of the rotor aspect ratio. A trade-off must be made to account for the additional surface area of the endplates, as this will introduce more drag [61], which could ultimately exceed the increase in efficiency seen with a reduction in tip vortex strength.

Ramkissoon [62] conducted experiments with and without end plates attached to an MI-VAWT1 aerofoil and showed that adding blade endplates increased the lift coefficient at all angles of attack, up to a maximum of 14% over the case without end plates included.

The effects of endplates on a rotating cylinder were undertaken experimentally by Badalamenti [54] to assess the impact of endplate size on aerodynamic performance for Reynolds numbers between 1.6×10^4 and 9.5×10^4. Analysis showed that endplates significantly enhanced the lift generated by the cylinder and improved the lift-to-drag ratio, with a limiting lift coefficient reached in all geometries considered. Furthermore, measurements of the total pressure variation in the wake showed that the force generated by the cylinder depended on the formation and development of vortices at the cylinder tips modified by end plate geometry.

2.5.15. Virtual Camber Effect

A key feature of the cycloidal rotor is the effect of virtual camber (VC) and virtual incidence (VI), as shown in figure 2.13. During operation, the path of each blade is curvilinear, resulting in only one point along the blade chord moving in a circular arc, the pitch point. The flow of a symmetric aerofoil profile in curvilinear motion is very different from a symmetric aerofoil profile in rectilinear motion; this phenomenon is known as the VC effect. Most aerodynamic theories assume that the blade's relative velocity and AOA are constant along the chord. For a cycloidal rotor, these vary along the blade with changes in chord [28], with the AOA essentially being unique at each chord position as each point along the chord experiences a different flow velocity magnitude and direction, resulting in a chordwise variation of the AOA.

A symmetric geometric aerofoil profile in curvilinear flow can be approximated as an aerofoil with VC and VI [14], mimicking a cambered aerofoil in a rectilinear flow. For example, a symmetric blade at 0° geometric pitch angle in a curvilinear flow is shown in figure 2.14, illustrating that the aerofoil can be viewed to behave like a cambered blade with an angle of incidence [4]. This angle of incidence is defined as the virtual incidence (VI), and the VI acts to create a phase shift in the aerofoil lift curve slope [4]. One of the first to introduce the principle of virtual camber was Migliore et al. [64], who using conformal mapping, proved that a symmetric aerofoil in a curvilinear flow at a given geometric AOA could be analyzed as an equivalent virtual airfoil having camber and incidence.

VC is highly dependent on rotor c/R ratio, blade pitch axis location, and solidity. As the c/R ratio increases, the VC effect also increases and becomes more pronounced, improving rotor hover performance. Consequently, larger chord blades with a small rotor radius are optimal during hover. Pitching the blade away from the 50% chord position also introduces a VI. For example, a blade pitched at the 25% chord position with a 6-inch diameter rotor introduces a VI of approximately 6.1° and a VC of 5.3% [39]. This essentially brings about a phase shift in the blade's lift and drag coefficient curve. For a given c/R ratio moving the pitch axis closer to the LE increases the VI in hover, with the VC also increasing as a result. In forward flight, the contribution of VC and VI depends not only on pitch axis location and c/R but also on the free stream velocity.

The VC can be positive or negative depending on the blade's azimuthal position. During hover operation, the VC is negative at the Top Dead Centre (TDC) position and positive at the Bottom Dead Centre (BDC) position, reducing and increasing the effective blade AOA at the TDC and BDC rotor positions, respectively. This results in the majority of the lift generated in the lower half of the rotor in hover, due to the large local air loads, with the vertical force component at the TDC position nearly half that of the BDC position in some cases [4], dependent on rotor c/R and blade pitch amplitude. Conversely, at a low effective blade AOA, the negative camber in the upper half of the rotor can result in a negative AOA, producing a downward force.

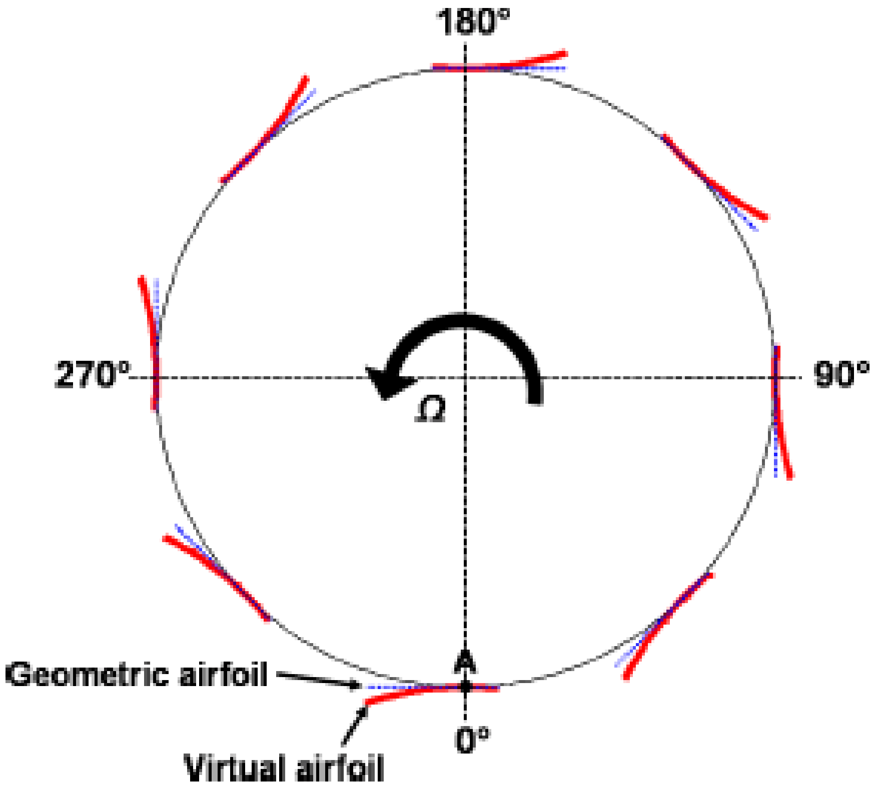

Figure 2.13 – Cycloidal rotor virtual camber in forward flight [4]

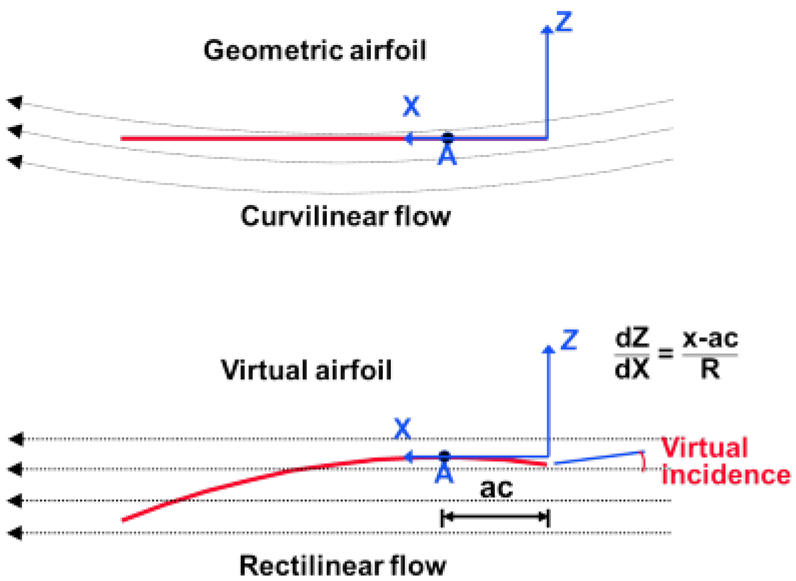

Figure 2.14 – Cycloidal rotor virtual incidence definition [63]

All forward flight cases considered to date use the hover pitching kinematics rotated through 90 degrees [14]. The negative camber in the frontal rotor region can cause the blade to stall in some instances, generating a negative lateral or propulsive thrust component and lowering the rotor's propulsive efficiency. In contrast, the aft half of the rotor has a positive VC generating most of the rotor thrust [14], which ultimately depends on the rotor advance ratio. The effect of VC is also another factor why the blades do not contribute equally to lift generation in both rotor halves.

Under symmetrical pitching, the blade's geometric pitch angle is zero degrees at the 90 and 270° azimuth (side) positions, as shown in figure 2.13, resulting in no lateral thrust force component. However, due to the VC effect, the side blades generate a small thrust due to the low effective AOA, a further reason why a side force is generated during hover. Therefore, to adequately capture the flow physics of the cycloidal rotor, any aerodynamic analysis should capture the VC flow curvature effects.

In forward flight, the thrust force per unit rotor swept area drops with an increasing c/R ratio, conflicting with the requirements of a hovering rotor. Fortunately, the rotor's propulsive lateral thrust force-generating capability is less susceptible than the vertical or lifting thrust-generating capability to changes in c/R ratio [6]. One contributor to this reduction could be the negative thrust produced in the fore region of the rotor under certain advance ratios and blade pitch amplitudes. With increasing free stream velocity, rotor power decreases with increasing c/R ratio at 3.5 and 7 m/s [14] for a given solidity. During forward flight operation, power loading improves with increasing c/R and increasing advance ratio, up to a c/R ratio of approximately 0.63. The optimum c/R ratio is unique for each advanced ratio required [14].

2.5.16. Advance Ratio

The rotor advance ratio dominates the blade's resultant velocity during forward flight, changing the effective blade AOA. An additional velocity component in the horizontal direction to account for the free stream needs to be considered during analysis [14]. The net rotor thrust is highly dependent on the blade pitching schedule and advance ratio. In forward flight operation, certain rotor regions negate thrust generation [14], not only due to geometric effects. All forward flight studies to date have assumed the hover blade pitching kinematics are rotated through 90°, where the peak positive blade cyclic pitch angle now occurs at the 9 o'clock position, as opposed to 12 o'clock in hover.

Under certain advance ratios, the flow velocity decreases to below the free-stream velocity in the rotor's upper (retreating) half. Suggesting power is being extracted by the blades in the upper rotor region in forward flight, shown to be the case at an advance ratio of 0.73, resulting in a loss of lift on the upper region of the rotor [14]. This difference becomes more pronounced with increasing advance ratio [14] due to the lower resultant blade velocities on the upper rotor region. Conversely, the flow is accelerated through the lower (advancing) rotor region, which operates at higher dynamic pressures and higher resultant blade velocities, with this being the main region of thrust generation [22].

During forward flight, the lift (vertical) force generation efficiency of the cycloidal rotor increases with an increasing advance ratio. Conversely, the propulsive (horizontal) force generation efficiency decreases with an increasing advance ratio for a given lift force component [6]. But this needs to be traded against the decrease in rotor power with advance ratio increase [15].

2.6. Competing Propulsion Systems and Technologies

As alluded to in Chapter 1, the broad operational envelope of the cycloidal rotor means that it has many contemporaries in both crewed and uncrewed flight applications. The following section outlines some current novel propulsive technologies where the cycloidal rotor would be looking to compete.

The Lilium Jet is a reconfigurable system for cargo or crewed flights for up to six passengers. The design uses distributed ducted electric fans built into the wing trailing edge flaps. The integration of the propulsive device into the wing allows for thrust vectoring through lift-off and hover flight via the control of the relative angle of the fan to the main wing.

Another crewed flight craft that uses distributed propulsion is the Aurora Lightning Strike. A total of 24 ducted fans are incorporated into both wings, powered through a hybrid propulsion system. Both wing systems rotate as one unit to enable thrust to be vectored for take-off and forward flight manoeuvers. During high-speed forward flight, each wing's upper and lower surfaces provide lift due to the wings forming a box-like structure.

Kitty Hawk has developed the Cora with reduced seating to cater to the urban air mobility market for the more personal flight mode of operation. The Cora is a two-seater autonomous eVTOL powered by 12 distributed electric propellers attached to the 11 m wings. Taking off vertically removes the need to use a runway or vehicle launcher in tight environments.

A smaller craft also developed for the urban air mobility market is the E-Hang 184, which is a single-seater craft. The design uses brushless DC motors in conjunction with coaxial propellers at four positions, above and below each motor.

At the uncrewed craft scale, typically UAV, a contemporary is the SkyEye Sierra UAV, which utilizes four conventional rotors in conjunction with a fixed-wing design. It is similar in appearance to a glider, with the addition of rotors for take-off and landing. The craft has a 3 kg payload and an overall range of 320 km, where the propulsive system is electric. The Tango VTOL UAV is similar in design approach to the SkyEye Sierra, with an increased payload of up to 5 kg; it is typically used for scientific research and surveillance applications. The design is available as a purely electric or hybrid-powered device.

2.7. Rotor Vibration Suppression Techniques

Much effort has been made to improve conventional rotorcraft vibration levels in recent times. However, they are still a significant issue due to the ever-expanding rotorcraft operational envelope, such as increased forward flight speed, which increases vibration levels due to retreating blade recirculation.

Since their early development, high levels of rotor vibration have been a parasitic feature of rotorcraft operation [65]. Consequently, much attention is being paid to optimizing vibration levels experienced in the fuselage, particularly at the pilot seat [66] for crewed flight. For example, figure 2.15 shows the change in pilot seat vertical vibration magnitude with and without higher harmonic control (HHC) [67]. Coupled with the increased expectations of passengers and crew [65], it puts additional emphasis on research to reduce overall vibration levels, which is compounded by efforts to improve the life and functionality of equipment in both crewed and uncrewed flight applications.

Rotorcraft vibration reduction measures to date have been implemented with both passive and active vibration reduction techniques, with examples being [68, 69]. Each vibration suppression method will be summarised in turn in relation to conventional rotorcraft. Finally, the ability of the chosen methodology for implementation on a cycloidal rotor will be discussed.

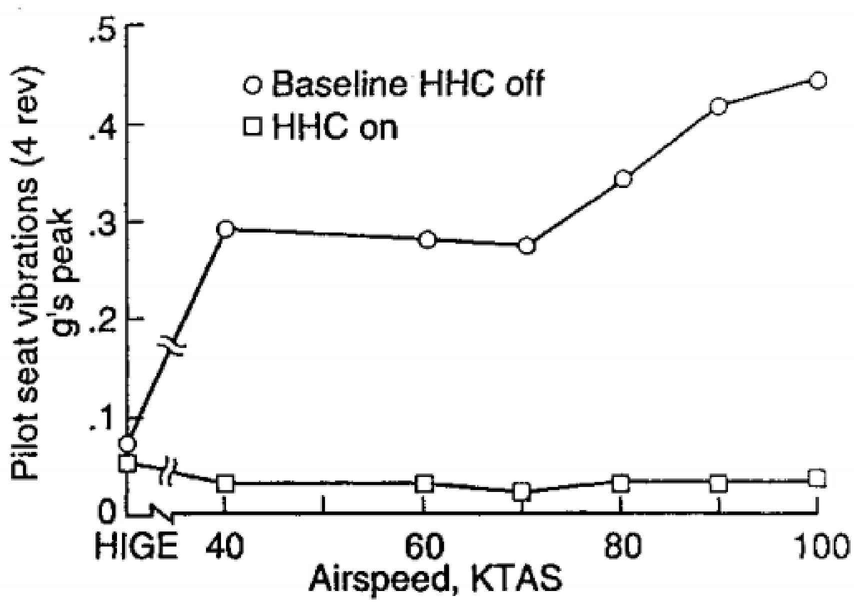

Figure 2.15 – Vertical vibration reduction at the pilot seat with HHC [67]

2.7.1. Passive Vibration Techniques

Three common methods used for passive vibration reduction are vibration absorbers, isolators, and actual rotor design. Vibration absorbers are designed to reduce vibration at the source by canceling the rotor system's exciting forces before transmission to the non-rotating frame, to control vibration levels throughout the airframe. Similarly, rotor vibration isolators are also typically used between the rotor and fuselage to reduce the vibratory loads passed from the rotating to the non-rotating frame. Rotor design traditionally attempts to reduce vibration by designing the blades and, in some cases, support structure with modes away from forcing harmonics to avoid resonant vibration.

Passive methods have the advantage that multiple technologies can be used simultaneously. In addition, they do not require additional actuation, eliminating the additional mass and power requirements when actuation is needed, typically associated with active vibration suppression techniques. However, passive methods do have the disadvantage of not being adjustable when in operation. They are usually designed for optimal use over a narrow operating envelope, which could be an option for a rotor that spends most of its operation in hover. All three passive vibration reduction methods are outlined in the following sections.

2.7.1.1. Vibration Absorbers

The most common form of rotorcraft passive vibration technique is vibration absorbers, effectively tuned mass dampers more commonly known as tuned vibration absorbers (TVA). The absorber is specifically designed to match the natural frequency of the main airframe structure to which it is mounted. As a result, the peak airframe vibration amplitude is reduced during operation. Vibration absorbers are often used to add damping to a difficult or expensive system to damp directly, making them ideal for rotorcraft applications. TVA comes in many forms, and many configurations have been analyzed. Examples include pendulum-type absorbers and magnetic dynamic absorbers that use eddy currents to provide damping.

The design of vibration absorbers is typically much lighter and simpler than comparable active vibration reduction techniques. It has the advantage that existing parts of the craft design can be used as the absorber mass element under certain circumstances. A common example is the use of a helicopter battery [70]. Although they have the advantage of low mass, their design limits optimal performance over a very small operating band. Their off-design point effectiveness varies depending on the overall design configuration. A few representative examples are outlined below.

Han and Smith [71] analyzed the feasibility of reducing lag-wise bending moments in a hingeless rotor by embedding elastomer vibration absorbers distributed within the blade's leading edge. Results show a decrease in the first and second-order lag-wise bending moments by 50% and 90%, respectively, when the absorber is placed in the blade chordwise direction, confirming that significant vibration damping can be achieved under high loading conditions. However, it did have the disadvantage of increasing blade tip lag-wise bending moments.

The study confirmed that the technique could be used over multiple rotor harmonics through careful design and showed that adding a chordwise absorber at the blade tip is more suitable for higher harmonic load control. In all cases considered, the absorber mass was kept to 6 kg, representing 10% of the overall blade mass.

An analytical design procedure for designing a simple pendulum absorber to minimize blade root and shear reactions was developed by [72] through systematic variation of the pendulum geometric parameters. Pendulum vibration absorbers are a TVA used to attenuate the amplitude of torsional vibrations in rotating machines. They contain masses constrained to move along a particular path to generate a centripetal restoring force. The study found that a flapping pendulum can attenuate the root out-of-plane force and moment if appropriately designed. But a lead-lag pendulum is required to attenuate root in-plane reactions.

The inclusion of the pendulum caused a spanwise redistribution of the structural loads, resulting in an attenuation of the reactions at the rotor hub. The pendulum causes a decrease in the inboard and an increase in the loads outboard of the pendulum position. The results generated [72] show that an optimized pendulum reduced the hub vertical shear by 98.7%.

A bifilar absorber can also be used as an additional means of vibration reduction; an example is shown in figure 2.16 [73]. The bifilar assembly is mounted directly above the rotor hub and is tuned to provide a centrifugal restoring force, typically only to attenuate vibration at one frequency to reduce in-plane vibration [73].

It is commonly used to attenuate the N/Rev main rotor vibration. The bifilar assembly consists of a mass restrained by two pins mounted into the main rotor structure, where the pins, along with the holes in the bifilar masses, define the motion of the absorber. It is possible to tune the response of the absorber by modifying the restraining pins and the overall bifilar mass. Bifilar absorbers have been successfully used on the Sikorsky H-60 and S-76 helicopters but can increase the total profile drag of the rotor system [73]

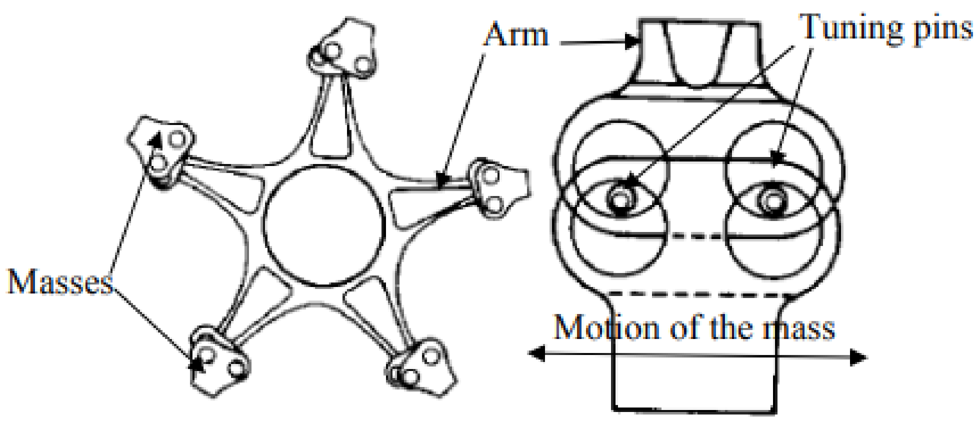

Figure 2.16 – An example of a bifilar absorber used in conjunction with a helicopter rotor [73]

2.7.1.2. Vibration Isolators

Rotor vibration isolators can be used between the rotor and fuselage to reduce the vibratory loads passed from the rotating to the non-rotating frame; an example is shown in figure 2.17, which is known as the dynamic antiresonant vibration isolator. Typically, such a system is challenging to design to capture the low-order frequency modes whilst minimizing system deflection [74]. The dynamic antiresonant vibration isolator overcomes this via the inclusion of a stiff spring to reduce static deflection levels within the system and is tuned via modification of the tuning mass at the end of the assembly arm. Such absorbers are not limited to the rotor-to-fuselage interfaces but have been used to reduce vibration at the pilot's seat by the Kaman company [75].

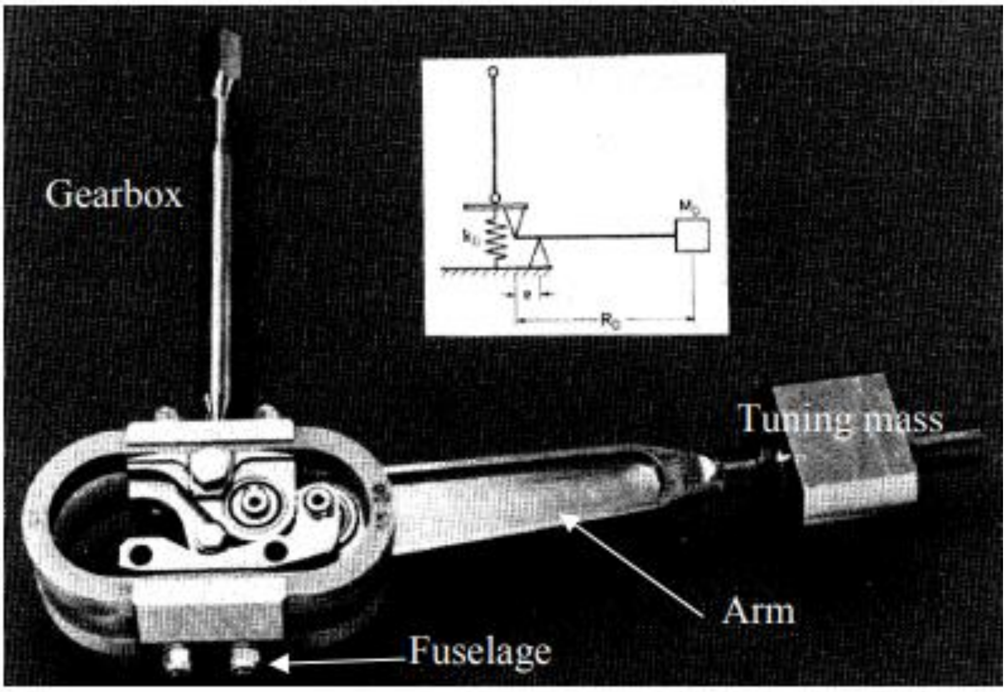

Figure 2.17 – An example of a vibration isolator designed to be used between the helicopter's main rotor gearbox and fuselage [74]

2.7.1.3. Rotor Design

In conventional rotorcraft, the rotor significantly contributes to overall vibration levels. As a result, the blade design has been the emphasis of many optimizations. Typically this has included the modification of blade spanwise mass and stiffness along with blade material layup, tip geometry, and blade form to achieve the required blade natural frequencies through frequency placement. Historically the optimization process was decoupled from the overall blade design.

An example of blade tailoring is the BERP IV blade [76]. The modification of the blade design to achieve vibration reduction was typically considered in isolation, with varying levels of success, where the emphasis was on avoiding excessive resonant vibration by giving sufficient margin on integer harmonics of rotor vibration. The BERP IV design process attempted to couple the blade design to integrate the aerodynamics, dynamic, composite design, manufacturing, and stress analysis processes [76] to ultimately ensure the forward flight performance of the BERP IV blade was maintained. The forward flight performance was maintained by ensuring attached flow at high angles of attack, maximizing the retreating blade performance. However, adding mass at the blade tip resulted in chordwise Centre of Gravity (CoG) changes and increased control loads.

The BERP IV blade was designed using a combination of structural optimization and aeroelastic tailoring techniques to counter the estimated increases in control loads. This is a direct result of the modified blade frequency requirement and the revised tip geometry. To reduce vibration through blade optimization requires the fuselage dynamic response to be characterized., enabling the calculation of the fuselage transfer function at several locations. The fuselage characterization was then used to determine the objective function for the blade optimization, which was airframe vibration reduction [76]. Optimizing the blade layup by analyzing the shear and unidirectional (UD) layers enabled an increase in the third harmonic flap mode frequency from 4.9/Rev to 5.8/Rev.

A method of vibration reduction was proposed in [77] to minimize helicopter blade and rotor vibration by optimizing the size and location of tuning masses through the application of three optimization methodologies, as opposed to physical blade design modification. The objective function minimized the blade root vertical shear while avoiding excessive additional blade mass. The analysis minimized the shear load of the first flapping mode by modifying the blade mode shape to reduce vibratory load response. Additional masses were concentrated at the blade tip.

The first optimization method [77] optimized the vertical shear for a single frequency mode and single harmonic. However, the approach was not always effective when the method was used over more than one frequency mode. The second method aimed to reduce the vertical shear amplitude over several harmonics for several frequency modes. In this case, the shear force associated with the 5/Rev harmonic was reduced from -39.48 lbf to -0.12 lbf. The final optimization methodology aimed to reduce the vertical shear force as a function of time during one rotor revolution and was deemed the most effective. The peak shear amplitude reduced from -78.00 1bf to -0.576 lbf, with up to a 12% mass penalty.

2.7.2. Active Vibration Techniques

With rotor vibration being a significant source of overall craft vibration, active vibration techniques have concentrated on rotor vibration suppression. Despite the predicted ability of active vibration techniques to reduce rotor vibration, their use in rotorcraft has been limited. However, compared with passive vibration reduction techniques, they have the advantage that they can be optimized over a wide operating envelope, often through the use of closed-loop control, where sensors monitor overall rotorcraft or rotor vibration levels.

Typically, active vibration methods are more complex and need a method of actuation in the rotating or non-rotating frame to induce the blade or airframe motion required. Active vibration techniques come with the additional penalty of actuation power requirements, which can be high compared to overall rotorcraft mass [78]. A more significant concern that has stalled their progression has been rotorcraft safety and system redundancy in a failure [79]. A summary of some recent advancements is outlined below.

2.7.2.1. Individual Blade Control

Conventional HHC is implemented in two ways, using actuators below the swashplate in the non-rotating frame and secondly in the rotating frame, with actuators between the swashplate and rotor blade [80]. The rotating frame actuation approach is more commonly known as Individual Blade Control (IBC). IBC works on the same principle of rotor vibration suppression as HHC by creating higher harmonic aerodynamic loads that suppress the original blade loads by actuating each blade individually. IBC can be implemented via blade actuation through pitch link control or 'on-blade' via trailing edge flaps.

Tests to implement IBC through pitch link actuation are limited. Jacklin [81] was one of the first to perform full-scale tests on a Sikorsky UH-60 IBC system. Hydraulic actuators generated motions in place of rigid pitch links to produce motions up to ±6.0° at 2/Rev. Two advance ratios, 0.1 and 0.175, were considered with a fixed rotor speed. As expected for a four-bladed rotor, rotor vibratory loads were dominated by the 4/Rev harmonic.

4/Rev vibration was reduced by 70% with the inclusion of a 1.0°, 3/Rev IBC input at 315° phase. From 0° to 0.75° amplitude, the vibration reduction was linear with IBC input but was nonlinear after that. Additional tests with multiple harmonic inputs were undertaken to determine whether increased vibration suppression could be achieved. A combined 3 and 4/Rev input harmonic reduced the overall vibration level less than a 3/Rev IBC input alone by 6%

Implementing IBC via active flaps requires the use of deformable features that are actuated, and designed into the blade structure, to generate the change in aerodynamic loads required for vibration suppression. This approach reduces safety concerns associated with HHC and traditional IBC as they are not incorporated into the main structure and are controlled by a separate control loop, separated from the main craft control system, increasing system redundancy. However, actuated flaps can compromise aspects of the blade design by introducing flow discontinuities into the blade surface, potentially increasing turbulence, vorticity, and BVI in some instances. A significant challenge to the use of active flaps is designing an actuator that can be incorporated into the space of the rotor blade [82].

Straub et al. [82] installed a trailing edge active flap on each blade of a five-bladed rotor, as shown in figure 2.18. Each flap was placed at a 25% blade chord position with a flap deflection amplitude of up to ±3° at 2, 3, and 5/Rev. Testing was undertaken under hover conditions and forward flight up to 124 knots. The effectiveness of the trailing edge flap was demonstrated, with a reduction in blade vortex interaction (BVI) identified, with an 80% reduction in the overall rotor vibratory response.

Actively controlled, partial span, trailing edge flaps [83] were analyzed using quasi-steady aerodynamics to calculate aerodynamic loads, used in conjunction with a quadratic cost function to minimize vibration. Vibration reduction with actively controlled flaps was compared with conventional IBC, and it was found that actively controlled flaps reduced vibration similar to that achieved with traditional IBC, but the actuation power requirements are between 70-90% lower.

The study concluded that the size of the control flap had little effect on overall vibration suppression but had a significant impact on actuator power requirements. Vibration reduction and actuator power requirements were sensitive to changes in flap spanwise location. An increase in blade torsional stiffness reduced the effectiveness of the control flap and increased actuator power.

Milgram [84] analyzed a four-blade Sikorsky S-76 rotor at frequencies 3, 4, and 5/Rev, with trailing edge blade flaps, and predicted significant reductions in 4/Rev hub loads cyclic inputs around 1-2°. The conclusion is that changes in performance due to changes in flap length, chord, and location could be offset successfully by adjusting control input amplitude and phase. He proposed a flap with the smallest chord and largest deflection to be optimal. Overall the trailing edge flap was found to reduce vibration significantly at all advance ratios considered between 0.15 and 0.30.

Figure 2.18 – IBC actively controlled flap [82]

2.7.2.2. Higher Harmonic Control (HHC)

Higher Harmonic Control (HHC) has received the most attention in the last two decades compared with other vibration reduction techniques, with some typical examples summarised below. HHC works by modifying the blade vibratory aerodynamic loads before transmission through to the rotor hub and airframe by actuation of the swashplate in the non-rotating reference frame.

During HHC, the swashplate is typically excited at N_b/Rev, where N_b represents the blade number, resulting in blade pitch oscillations of N_b - 1 and N_b + 1/Rev in the rotating frame [85]. Typical conventional rotorcraft require a small HHC blade cyclic pitch angle input amplitude of between 0.5° to 1.5° [86], supporting the theory that a linear, frequency-domain representation of the helicopter response to control can be utilized. The higher harmonics induce unsteady aerodynamic loads that suppress the original blade loads. The success of HHC implementation lies in the design of the actuators that must have low mass and power requirements, coupled with a robust controller with capability over a wide frequency range.

HHC is typically implemented using closed-loop control. The vibratory output is measured, and control inputs are updated at set time intervals when steady-state outputs are achieved. When the system reaches a steady-state vibratory response, amplitude and phase are measured and used to update the amplitude and phase of the HHC inputs for vibration suppression. The closed-loop control effectively acts as an online optimization process to find the optimal HHC input operating point. With HHC included, a closed-loop controller assuming linearity over the range of HHC control from 0° to 3° amplitude was implemented by Robinson [87] and effectively reduced the vibratory 4/Rev response of a hingeless rotor from their baseline values without HHC input by up to 99% at a forward flight speed of 100 knots.

Hammond [88] conducted wind tunnel tests on a four-bladed helicopter rotor, considering several control algorithms, and concluded that vibration reduction of between 70% and 90% was possible for a range of advance ratios when HHC was implemented with an optimized controller.

Nguyen et al. [89] performed HHC investigations on a full-scale, isolated XV-15 rotor under two forward flight test conditions to reduce the 3/Rev rotor vibratory loads. The HHC control input for both test cases was approximately 0.9°. The controller reduced the rotor vibratory footprint by 50%, with the pitch link control loads ultimately limiting the forward flight speed with HHC included.

It is essential that HHC does not degrade rotor performance significantly, and the effects of a 2/Rev HHC pitch input on rotor performance were analyzed by Cheng et al. [90]. It showed that an optimized 2/Rev HHC input could reduce the helicopter rotor power by up to 16%. The primary mechanism behind the power reduction was the change in the distribution of the profile drag coefficient over the rotor disk.

Nixon et al. [91] performed wind tunnel experiments on a 1/5 scale three-bladed V-22 tilt-rotor model in the Langley Transonic wind tunnel. Results show that the implementation of HHC successfully reduced 3/Rev rotor vibration by 75% and concluded that simultaneous reduction of multiple harmonics should be possible through the superposition of multiple HHC inputs. Despite the significant differences between helicopter and tilt-rotor operation, the study found that much of the helicopter HHC development could be used in tilt-rotor design.

Analysis by Kottapalli [92] was undertaken prior to testing a 44 ft diameter Sikorsky S-76 articulated rotor to establish the effect of HHC on push rod loads with changes in airspeed. Separate tests were performed with a 3, 4, and 5/Rev HHC input, with an amplitude of 1°. In all cases, the pushrod loads were highly sensitive to the phase of the HHC input. Pushrod loads are seen to increase with increasing forward flight speed. The inclusion of the optimum 3 and 5/Rev HHC input increased the pushrod loads by up to 20% compared to the baseline configuration. Conversely, the optimum 4/Rev HHC input reduced the pushrod loads for all flight speeds considered.

Payne [93] investigated the use of a 2/Rev HHC input to feather the rotor blade in an attempt to eliminate retreating blade stall, to improve helicopter forward flight performance. An analytical investigation concluded that a 2/Rev HHC input alone would not significantly delay retreating blade stall but concluded that the superposition of several higher harmonics should enable the retreating blade stall to be pushed beyond current limits.

2.7.2.3. Active Control of Structural Response (ACSR)

Another vibration reduction method is ACSR, one of the most widely-used active vibration control systems in operation. ACSR differs from HHC as the input forces for vibration reduction are applied directly to the airframe through actuation. It does not attempt to modify the vibratory load path through rotor modification. Instead, force input requirements are calculated based on resultant vibration data obtained from airframe accelerometers. A controller monitors vibration from the accelerometers and determines the force and timing requirements of the force input at harmonics of the main rotor frequency to reduce vibration for the changing flight conditions.

Staple and Welsh [94] showed that for a pilot system, the performance of ACSR was superior to passive techniques analyzed at the time, with fuselage vibration reduced by between 72 to 84%. On average, the 5/Rev fuselage vibration levels were reduced by 75% at 140 knots.

Pearson [95] developed an adaptive controller to implement ASCR to reduce helicopter structure vibration and highlighted that the overall vibration reduction is sensitive to the control strategy used. Computational simulations were validated against experimental results and estimated that a 90% reduction in the blade pass frequency vibration amplitude was achievable.

2.8. Rotorcraft Vibration Testing and Analysis

Accurate measurement of rotor vibratory hub loads is critical in any rotor system development. However, it has always remained a significant challenge in rotorcraft design and testing. Rotor vibration testing is fundamental to rotor development and has been typically performed on standard rotorcraft concepts in their early development stages. A shake test must be performed to calculate a dynamic calibration matrix of the rotor force and moment for the test rig itself. The rotor balance is usually installed below the rotor hub in the non-rotating frame and measures both the steady and the vibratory rotor hub loads. A dynamic calibration identifies the transfer functions relating the actual applied vibratory hub loads to the balance readings to calculate the vibratory loads in the rotating frame.

Kreshock et al. [96] found that force balance manufacturing errors and strain gauges installation resulted in coupling between balance measurement degrees of freedom, which was compensated for by performing a static calibration. Balances are often 'soft' relative to the rest of the system and contribute to system resonances. Static calibration only corrects for amplitude. A dynamic calibration accounts for amplitude and phase changes to account for balance stiffness.

An early shake test was performed on the large-scale dynamic rig as part of the McDonnell Douglas Advanced Rotor Technology (MDART) program, utilizing the NASA Ames Rotor Test Apparatus [97,98,99]. A hydraulic actuator was used to apply random excitation from 0 to 64 Hz to the hub during the shake test at input force levels up to 600 lb. The system output vibratory force and moments were measured to calculate the hub vibration modes and rotor balance dynamic calibration matrix. The dynamic calibration matrix was calculated using a least-squares error method to correct the 5/Rev vibratory balance readings for both magnitude and phase in the principal loading directions for the five-bladed rotor operating in forward flight. The results showed that the blade pass harmonics dominate the rotor vibratory response.

Calibration results outlined the influence of frequency bandwidth, hub mass, rotor speed, and thrust preload. The frequency response functions (FRF) showed that hub mass variation had the most significant effect. The dynamic calibration reduced the side loading magnitude by 66%, increased the axial force magnitude by 50%, and reduced the magnitudes of the rolling and pitching moments by 50%.

An experimental four-bladed hub was manufactured as part of the ARES testbed [96]. Burst-random excitation with a 0-200 Hz frequency range was used, with excitation force levels typically ±10 lbf, but loads from 2 lbf to 15 lbf were investigated to calculate system nonlinearity. It was noted that the system response in the normal and axial directions was highly dependent on the excitation frequency. Hence, using static calibration values alone would result in vibratory loads being incorrect by as much as one order of magnitude [96], confirming that the use of dynamic calibration can significantly improve the correlation between predicted and measured force balance outputs. Furthermore, the study determined that the ARES testbed exhibited several natural frequencies near the 4/Rev rotor frequency. As a result, the FRF had large amplification factors at these points. In addition, the system response was very sensitive to model changes, significantly reducing the accuracy of the dynamic calibration in these areas.

Further tests were carried out in the NASA Ames Wind Tunnel on the Large Rotor Test Apparatus (LRTA) [100]. An example setup is shown in figure 2.19. To undertake a shake test to characterize the oscillatory response of the test rig and provide a dynamic calibration matrix of the balance to measure vibratory hub loads accurately. Several loading scenarios used a shaker to excite the system with a random signal from 0 to 80 Hz at 800 lb force. Force measurements were taken in each orthogonal loading direction, with balance gauge interactions and cross-coupling between the principal loading directions not considered. As a result, the dynamics calibration matrix considers only one-dimensional transfer functions.

Figure 2.19 – NASA AMES test rig shake test installation [100]

The shake tests provided frequency response data at frequencies up to approximately 35 Hz, or 8/Rev for the UH-60A rotor. However, the study showed that the shaker setup was insufficient to generate enough energy to excite the test rig over 40 Hz. This illustrated the complexity of dynamic testing and confirmed that it would be challenging to create an accurate dynamic calibration for the system over the entire frequency range of interest based on obtained shake test data. It was concluded that normal modes measured at the balance are only minimally affected by hub mass up to 7/Rev and can be corrected successfully based on the method of experimental dynamic calibration adopted. However, a vibration mode at 4/Rev was highly sensitive to changes in hub mass. As a result, it resulted in high variability in the mode, making it difficult for the dynamic calibration to be based purely on experimental data.

An alternative approach countered the shortcomings of the shake test data [100]. Data collected simultaneously from accelerometers were used to determine the mode shapes of the system at various resonant frequencies to validate a Finite Element Analysis (FEA) model. The model was then tuned to represent the physical behavior of the test rig, and transfer functions were calculated based on simulation results data.

Russell et al. [101] proposed an alternative method to obtain additional information about the system's dynamic response by using measured bending and torsion moments using strain gauge bridges on the blades in the rotating frame. However, it was concluded that this approach could not measure the exact shear forces in the blades. The more conventional method of dynamic calibration was then used and noted to be very time-consuming if high levels of coupling between axes and nonlinearities in the system occur.

A significant drawback with the design of multi-component measurement balances is the coupling between axes. Flexible beams were used between the strain gauge and the piezoelectric cells [102] to overcome this. Unfortunately, preliminary analytical investigations were not good enough to calculate the exact transfer functions. The balance was excited by a shaker in each loading direction component individually, but this approach contained a few significant errors. The main source was the inability to use only one input to excite all frequency modes in one test. This was overcome by undertaking multiple tests with different input amplitudes at the same test conditions.

2.8. Chapter Review

With increased interest in Urban Air Mobility (UAM) and an ever-expanding Unmanned Aerial Vehicle (UAV) market, the quest to develop more efficient propulsion technologies continues. The cycloidal rotor is a promising thrust generation technology with a broad range of operational capabilities. However, there is still much to be learned about the cycloidal rotor and its operation.

Since the inception of the helicopter, it has suffered from high levels of rotor vibration at harmonics of the blade pass frequency, which ultimately inhibits rotor and fuselage performance. As a result, helicopter research has continually tried to improve rotorcraft operational performance through vibration reduction, but the measurement and reduction of rotor vibration have been a considerable challenge. In this regard, the cycloidal rotor is similar, as the cycloidal rotor also operates with high levels of rotor vibration due to the rotating structure and the blade's unsteady aerodynamics. Coupled with the fact that one of the significant factors limiting the performance of uncrewed UAV systems is the mass of the propulsive system [12], rotor vibration assessment and reduction is seen as a crucial factor in the advancement of the cycloidal rotor concept. Vibration reduction will allow for smoother operation and enable the design of lighter rotors due to reduced dynamic loading.

To the author's knowledge, all experimental and computational models to date focused on cycloidal rotor research have concentrated on evaluating mean rotor performance. While this is important, the ability to measure experimentally and computationally the rotor vibratory response is seen as a key new area to provide further insight into the cycloidal rotor operation. In addition, the investigation of the rotor vibratory loading benefits from maximizing the potential of the current research output. The thesis is the first to investigate the development of reliable experimental and computational predictive capabilities to assess both the cycloidal rotor steady-state and dynamic vibratory response for a rotor under hovering conditions.

The current research initially concentrates on modeling a conventional cycloidal rotor under changing blade cyclic pitch amplitude and rotational speed to benchmark all experimental and computational models. A computational methodology for rotor vibratory load optimization is developed to investigate novel blade pitching kinematics to improve the efficiency of the rotor in hover and to determine whether HHC can be successfully implemented during cycloidal rotor operation. Finally, an experimental study investigates the use of the HHC and the resulting correlation with the different computational model approaches determined to confirm the efficacy of the models in fulfilling the objectives defined in section 1.5.

The proposed experimental system involves the use of a novel cam arrangement, a variant of which was used successfully in [21] for forwards flight Micro Air Vehicle (MAV) research, as shown in figure 2.20. The cam use eliminates the need for actuation via active pitch links and the containment of high control loads as they are self-contained within the cam mechanism. The containment of control loads is achieved via a pitching bearing that is connected to one end of the rotor blade. The bearing runs within the cam profile, and the cam dictates the motion of the blade. The principle behind the blade pitching is shown in figure 2.21, highlighted by region 2. An additional benefit is the high levels of control input repeatability as the cam profile is fixed. It reduces the need for complex actuation systems and can operate over an unlimited range of rotor speeds.

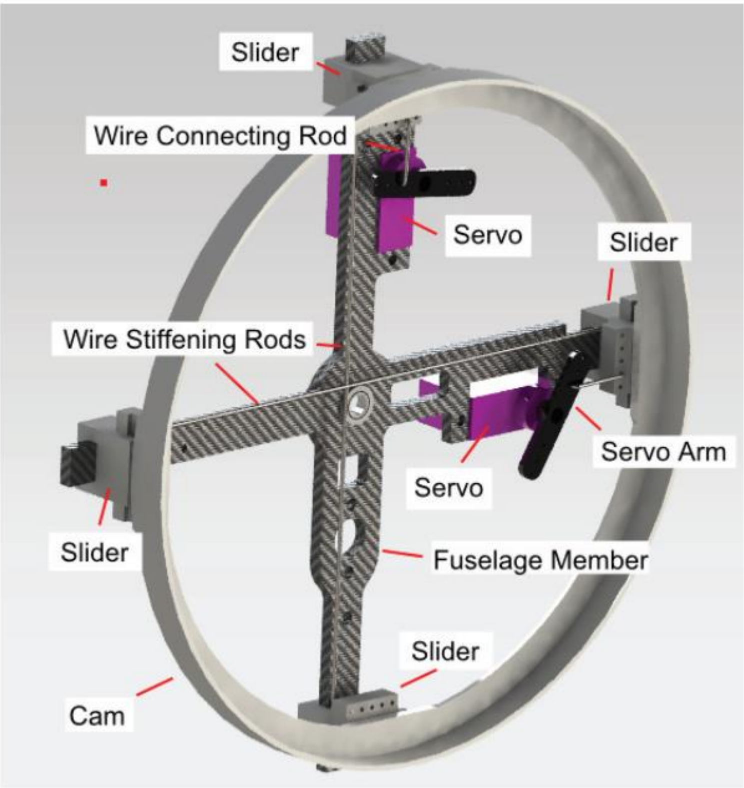

Figure 2.20 – Original cam-based mechanism used for blade cyclic pitch and input during forward flight analysis of cycloidal rotors by Adams [21]

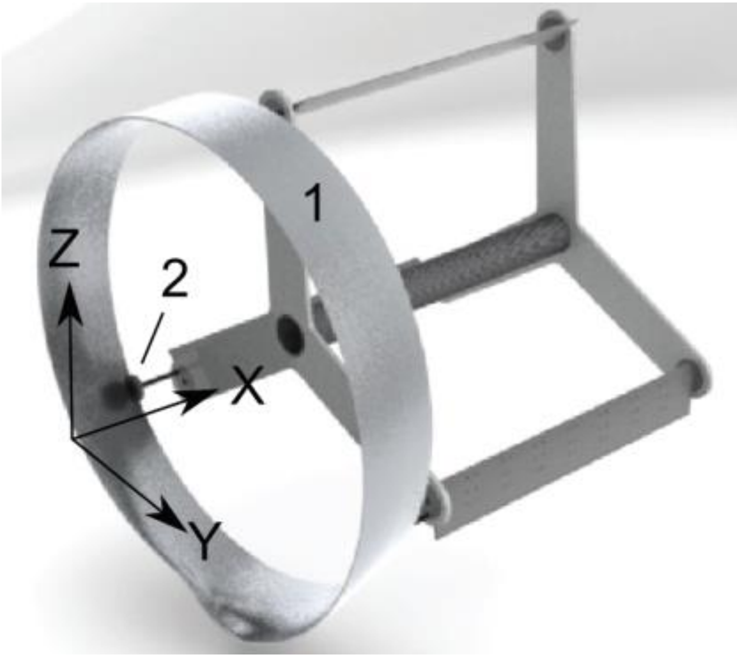

Figure 2.21 – Close up view of cam mechanism bearing face as used by Adams [13]

Chapter 3 – Experimental Test Rig Design and Analysis

3.1. Introduction

This chapter provides an overview of the design principles, methods, and processes behind the design and manufacture of the test rig shown in figure 3.1, as used in all experimental studies. The limited availability of cycloidal rotor test equipment drove the need to design the test equipment from the ground up at the University of Bath for testing a hovering rotor and rotor in forward flight in various configurations if required. It also allows for benchmarking the developed computational modeling outlined in subsequent chapters.

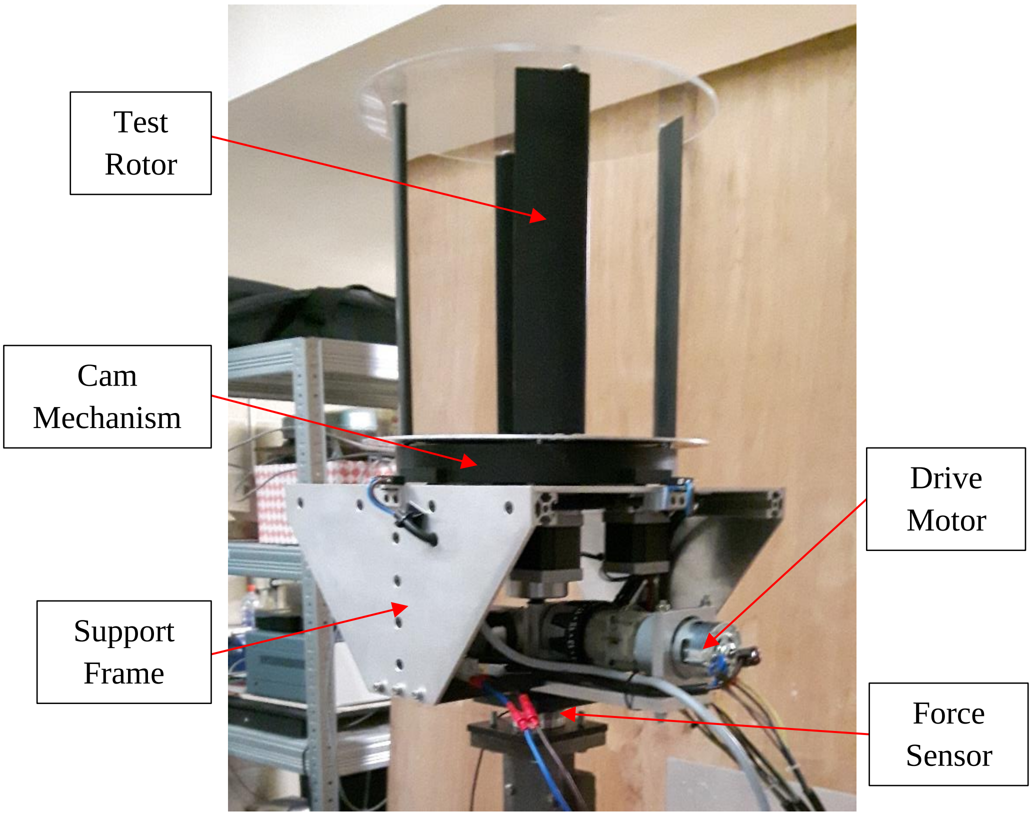

Figure 3.1 – Design and manufactured four-blade cycloidal rotor test rig with NACA 0018, 50 mm chord blades used throughout the current research

The test rig design contains many aspects, including the rotor, rotor blade, pitching mechanism, and main support design. Reasons for the design choices and overall rotor scale are given. It is worth noting that the overarching emphasis throughout was one of safety in design while using a blade geometry and blade pitch axis location that was near-optimal for a hovering rotor. It is suitable for ground tests and wind tunnel tests, but developing the current test rig into a rotor capable of flight requires further structural optimization.

The test rig design methodology is iterative and divided into a number of key areas to cover rotor load cases, blade structural design, and blade fabrication. Each of these areas is covered in detail in the following sections. The leading dimensions of the test rig shown in figure 3.1 are outlined in figure 3.2, covering the main rotor, cam mechanism, and support frame. The support frame provides the base to which all other components are mounted, which includes the rotor force measurement sensor, the rotor bearing arrangement, and the main drive motor. A summary of the test rig's key operational parameters is given in table 3.1. Detailed component drawings and a general arrangement of the test rotor are provided in Appendix A.

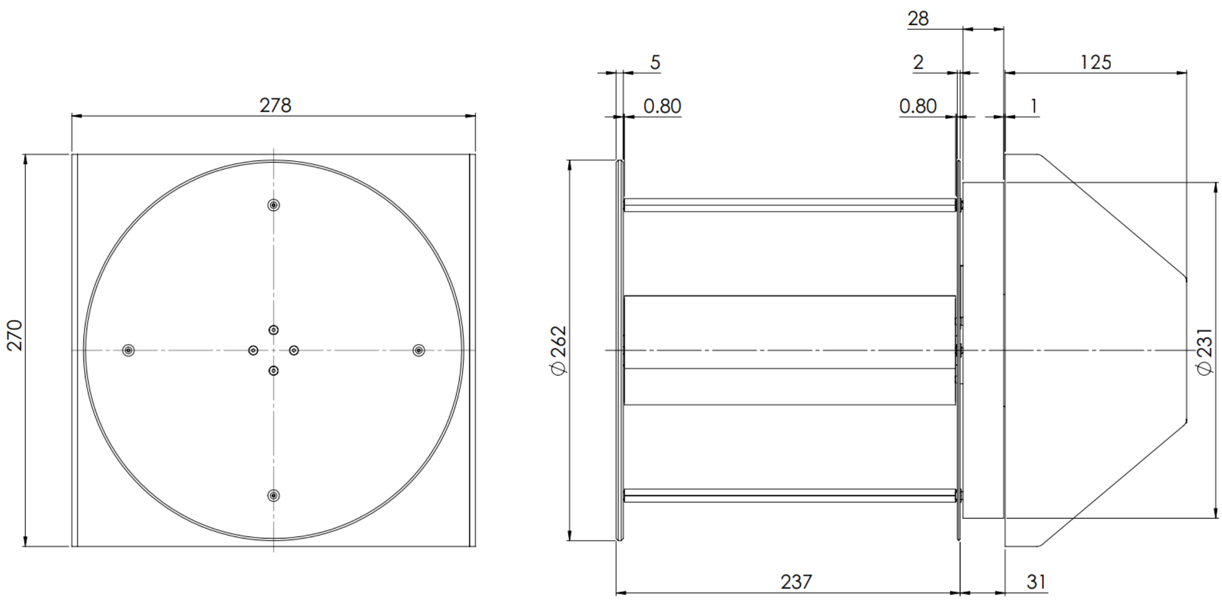

Figure 3.2 – Cycloidal rotor test rig overall design envelope dimensions

Table 3.1 – Low-pitch cycloidal rotor test rig operational parameter summary

Parameter	Value
Rotor diameter, D	200 mm
Rotor blade number, N_b	4
Rotor span, S	230 mm
Blade chord, c	50 mm
Blade cyclic pitch angle, θ_{BL}	+/- 45°
Phase input, ε	0 - 360°
Rotor rotational speed, N	0 - 2000 RPM
Blade Pivot Point	0.25c
Pitch Control System Pivot Position	0.65c
Aerofoil Profile	NACA0018

3.2. Design Approach

The cycloidal rotor concept can be designed on any scale, from UAV to crewed flight. Previous studies [4,21] have presented rotor mean performance results from cycloidal rotor parametric studies, but the chosen geometry and overall rotor configuration appear to have been arbitrary. Several design constraints were set at the outset of the current investigation based on the available test facilities at the University of Bath and an optimal configuration designed from there. To future-proof the project for forward flight study, the geometry of the University of Bath Open Jet Wind Tunnel was considered, which has a nozzle exit diameter of 0.6 m. Based on work by Pope [103], the blockage, which is the ratio of model frontal area to test-section area, is to be kept in the range of 1% to 10%, with 5% being used for the rotor blockage in the current study, which is typical. Another constraint was the potential availability of force transducers with adequate measurement range and resolution to capture small blade cyclic pitch input changes, with requirements varying depending on rotor geometry.

A NACA 0018 symmetric aerofoil was chosen for several reasons. Firstly cycloidal rotor blade loading is dominated by a transverse load generated by the rotor rotation, predominantly in the blade flap-wise direction. The flap-wise direction is the direction orthogonal to the chord for an aerofoil, essentially the minor aerofoil axis. Conversely, the edge-wise direction is parallel to the blade chord and is the major aerofoil axis. Finally, the span-wise direction acts along the length of the blade. The three principal axis directions are defined in figure 3.3.

The NACA 0018 aerofoil, with its increased flap-wise second moment of area, will reduce radial deflection and blade twist, reducing blade span-wise geometric AOA variation. Secondly, safety, with the increased blade thickness and adequate cross-section, depending on the blade chord, more area will be available for blade attachment points. The attachment points form a vital part of the blade design and could result in a catastrophic failure if not dimensioned correctly. Finally, as the thickness of the blade increases, it is less susceptible to flow separation, with the flow staying attached at the leading edge [21] at higher blade AOA, which is an advantage at high blade cyclic pitch inputs.

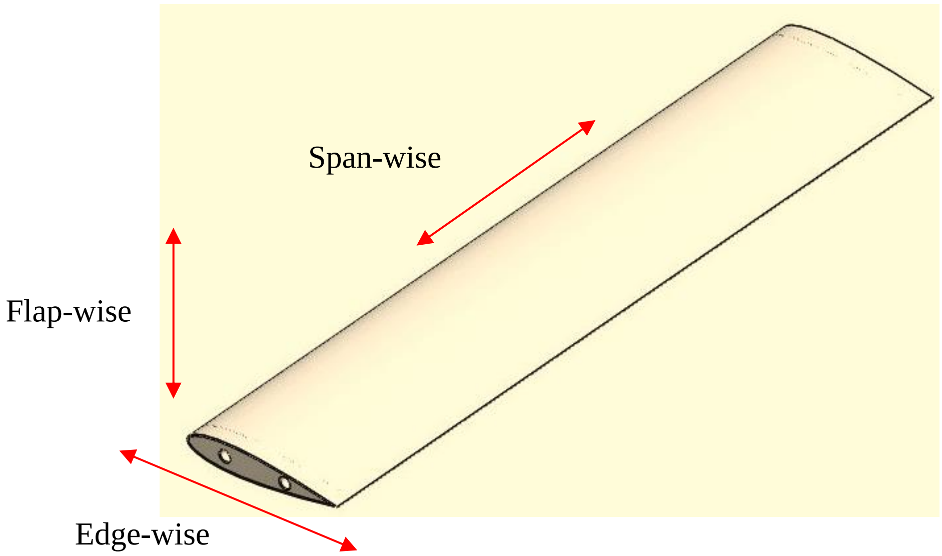

Figure 3.3 – Rotor blade principal axis directions and definitions

The optimum blade pitch axis location for a hovering rotor was estimated to be between the 25 and 35% chord position [4]. Therefore, for the current studies, the blade was pitched at the 25% chord position in all cases. With a reduction in blade number increasing the levels of rotor vibration [28], a four-bladed rotor was assumed to provide a compromise between the 'severe' vibration of the two-blade rotor and noticeably smoother operation when six blades were used [28]. Depending on testing requirements, a four-blade rotor can run at two blades if necessary.

Rotor solidity can be increased by increasing the blade number or blade chord. Changing solidity by increasing the blade chord produces significant improvements in PL [29], up to a rotor solidity of approximately 0.25. A value of 0.25-0.3 has been chosen for the current rotor design. Figure 3.4 shows the change in wind tunnel blockage with rotor diameter and span, compared with the 5% blockage threshold. Considering the blockage requirements and Open Jet Wind Tunnel geometry, a rotor with an aspect ratio of one, with the same rotor diameter and span, would be preferred, reducing nozzle boundary layer effects and non-uniformity of flow close to the tunnel walls. The diameter and span were set at 200 mm and 230 mm, respectively, to allow for a constant clearance around the rotor in relation to the wind tunnel nozzle diameter.

Consideration of the rotor calculated thrust levels for varying rotor diameters concluded that a 200 mm diameter would be the smallest diameter possible based on the instrumentation available while not degrading performance substantially. Levy [19] estimated that the thrust-producing area of the rotor is approximately 50% of the planform area. Consequently, the largest rotor dimensions were chosen within the constraints.

The rotor span was checked via a scaling analysis using the BET code developed in Chapter 5, as shown in figure 3.5. It is important to note that the BET code developed works well at low rotor solidity and at lower rotor rotational speeds, where the Magnus effect can be neglected. For configurations at very high rotational speeds in forward flight an inflow model will be required to account for the viscous Magnus effects. The impact of the rotor Magnus effect is not considered in the current analyses due to the rotor solidity and rotor rotational speed range tested up to 2,000 RPM. As the rotor span increases, the thrust force goes up proportionally as a direct result. For a 200 mm diameter rotor, the thrust at a span of 200 mm is 8.5% lower than a 600 mm span, which is justified by the decrease in mass and complexity with the reduced span design.

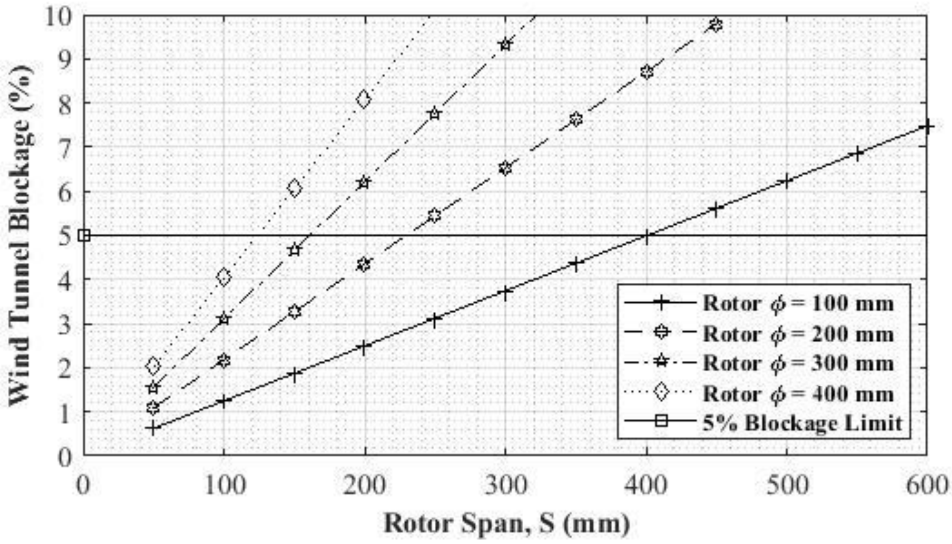

Figure 3.4 – Calculated wind tunnel blockage with changing rotor span and rotor diameter based on the University of Bath open jet wind tunnel 600 mm nozzle diameter

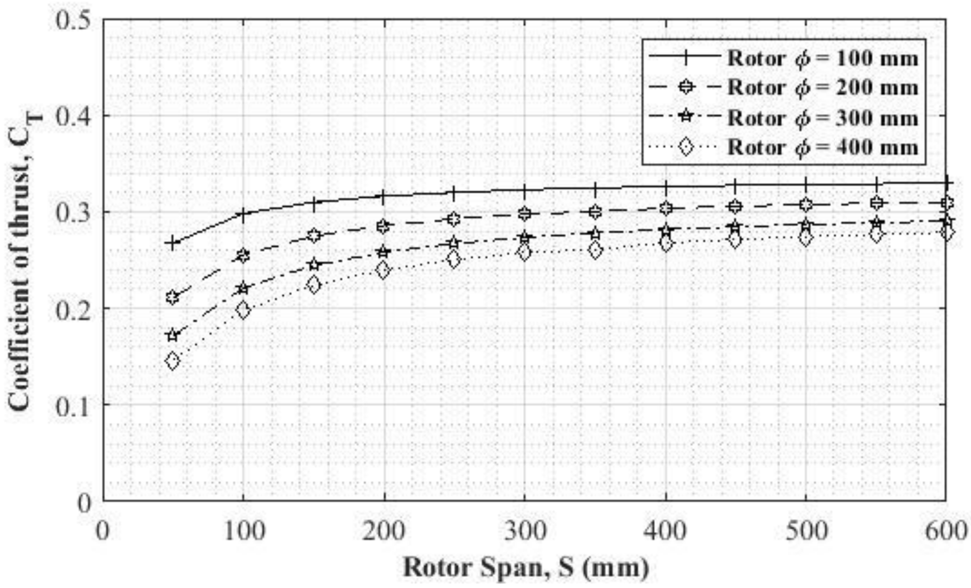

Figure 3.5 – Variation in test rig rotor Coefficient of Thrust with changing rotor diameter and span at a rotational speed of 2,000 RPM and 40° blade cyclic pitch angle. Data based on BET code results

3.3. Experimental Test Rig Design Requirements

Before conducting the preliminary design of the test rig, a set of clear and achievable functional requirements were defined to cover all likely aspects of the current research. Then, the experimental test rig was designed and analyzed to achieve the following criteria:

1. Operate over a full-speed range comparable to other independent cycloidal rotor experimental studies. A minimum rotor operating speed of 1,000 RPM is required, but 2,000 RPM is preferred.

2. The test rotor can operate at any speed between 0 RPM and 2,000 RPM with an independent drive system to maintain the rotational speed within 1% of the desired set point.

3. Rotor operates sub-critically to avoid the rotor's first critical speed, with a greater than 25% margin based on industry guidelines.

4. The system must be capable of being operated for extended periods by a single operator, including the use of any Data Acquisition (DAQ) requirements.

5. DAQ equipment must capture dynamic data at a sampling rate that allows for accurate results postprocessing in the frequency domain.

6. The blade pitching mechanism should be designed to operate at any cyclic pitch input angle from -45/+45°, anywhere within the rotor azimuth. This will allow for any combination of blade pitch and phase angle to be considered for hover and forward flight parameter sweeps.

7. To guarantee that the variation of blade geometric AOA is reduced in the span-wise direction, the blade design must accommodate a flexural (radial) deflection of less than 1 mm and a blade angle of twist along its length of up to 1° to ensure that aerodynamic performance is not degraded.

8. Test rig to be easily reconfigurable if required, following the findings of the initial experimental investigation.

3.4. Design Guidelines

3.4.1. General Design Safety Factors

The material strength constraints used in the design are based on the allowable material stress levels. All stresses in the blade and supporting structure must be less than the design allowable stress of the material for all load cases. The general safety factors used for the test rig design were as follows:

1. Material minimum properties = 85% of typical properties

2. Material minimum properties 0.2% Proof Stress Safety Factor = 1.5 Min.

3. Material minimum properties Ultimate Tensile Stress Safety Factor = 2.0 Min.

4. For metallic material fatigue conditions, component stress < material minimum properties High Cycle Fatigue (HCF) S/N Curve for 1×10^7 cycles.

5. A Tsai-Hill failure criterion is used based on the composite material stress limits.

6. Rotor drive motor torque margin Safety Factor = 2.0 Minimum.

3.4.2. Material Properties

The number of materials in the test rig design was limited to simplify the construction. Therefore, the materials were limited to the following:

1. Aluminium Alloy 6082 T6
   - 0.2% Proof Stress = 295 MPa
   - Ultimate Tensile Strength = 350 MPa

- Density = 2700 kg/m³
- Youngs Modulus = 70 GPa
- Fatigue Data = See Figure 3.6 [104]

2. Medium Carbon Steel EN24 T
   - 0.2% Proof Stress = 650 MPa
   - Ultimate Tensile Strength = 850 MPa
   - Density = 7850 kg/m³
   - Youngs Modulus = 70 GPa
   - Fatigue Data = See Figure 3.7 [105]

3. Composite +/-45° 210 g 2x2 Twill 3k Carbon Fiber Cloth
   - Tensile Strength = 4.1 GPa
   - Tensile Modulus = 234 GPa
   - Density = 1790 kg/m³

4. Composite 100 g Unidirectional Carbon Fiber Cloth
   - Tensile Strength = 4.9 GPa
   - Tensile Modulus = 240 GPa
   - Density = 1820 kg/m³

5. El2 High-performance General Purpose Epoxy Laminating Resin
   - Tensile Strength = 70 – 80 MPa
   - Flexural Modulus = 2.6 – 3.2 GPa
   - Density = 1050 kg/m³

6. Airex C70
   - Tensile Strength = 1.1 MPa
   - Flexural Modulus = 35 MPa
   - Density = 60 kg/m³

For blade design and blade mass estimation, it was estimated that a 200 gsm carbon fiber cloth in a single layer would be 0.25 mm thick when cured with the resin system specified above, with a density of 1750 kg/m³. This was based on a discussion with laboratory technicians based on their previous project experience.

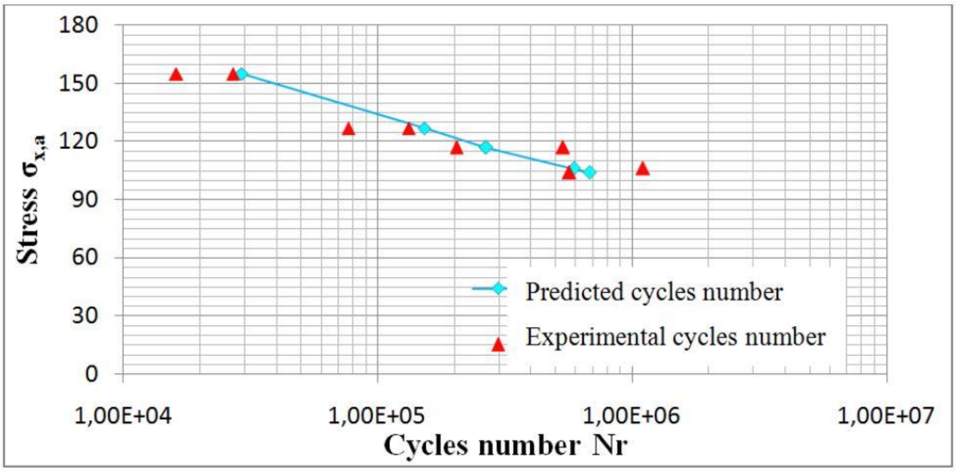

Figure 3.6 – Aluminium alloy 6082-T6 SN diagram [104]

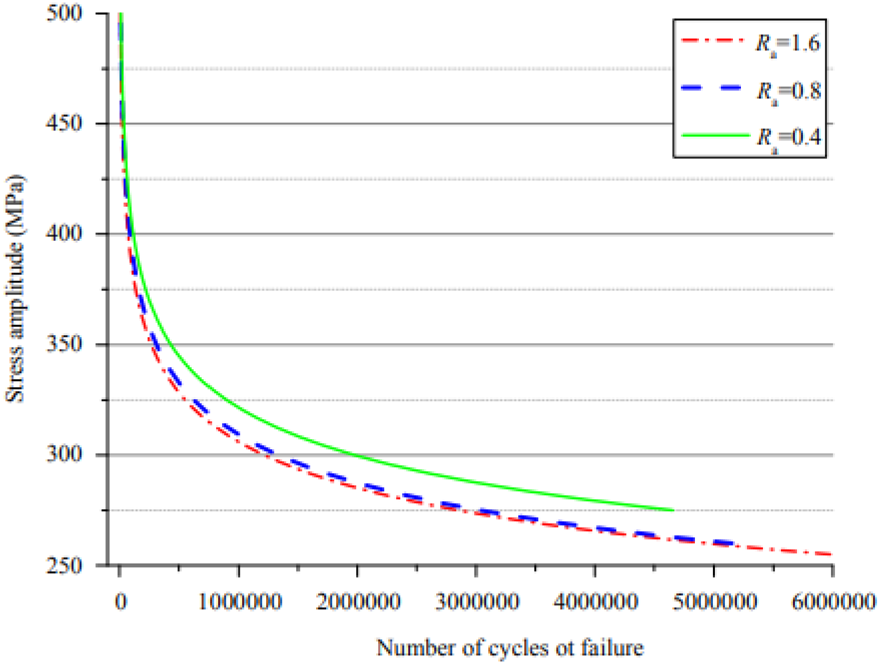

Figure 3.7 – Medium carbon steel SN diagram [105]

3.4.3. Bolted Connection Design

The test rig contains a number of bolted connections that connect the rotor end plates to the main rotor spindle and the rotor blades to the rotor endplates. A detailed description of the method behind the bolted joint design is outside the scope of the current work. However, the technique used was outlined by NASA [106]. The method covers general bolted joint design, analysis of pre-load, pre-load uncertainty, and pre-load loss. The bolted joint factor of safety against joint separation is based on the applied axial, shear, and bending loads. The bolted joints must meet the following requirements:

1. The fastener grade must be correct for the application. Grades 10.9 and 12.9 for the test rig design.

2. The joint separation factor under operation must be greater than 1. Hence the joint will not separate under operation.

3. The fastener grade will be pre-loaded to 75% of the 100% proof load to reduce the fastener alternating loads and improve fatigue life.

3.5. Rotor-Disc Burst Margin

The rotor end discs were designed for an over-speed condition, representing the discs being forced to operate beyond the 100% design speed. The over-speed condition was taken to be 120% of the design speed at 2,000 RPM, and the rotor disc burst speed was ≥ 125% of the design speed at 2,000 RPM.

The Robinson criteria [107] was used to calculate the burst speed and specified that bursting would occur when the mean hoop stress equals the material's ultimate tensile strength. The Robinson criteria is defined as:

$$\omega_b = \omega\sqrt{\frac{\sigma_{UTS}}{\sigma_H}} \tag{3.1}$$

where ω_b is the burst speed of the rotor, ω the rotor design speed and σ_H the mean hoop stress across the section of interest.

3.6. Design Load Analysis

3.6.1. Rotor Blade Loading

To design the respective rotor components, a baseline worst-case rotor operating condition of 2,000 RPM with a blade cyclic pitch amplitude θ_{BL} of 40° was assumed. The method of blade attachment to the upper and lower rotor end discs is via spherical bearings to reduce blade-induced bending loads, as shown in figure 3.8. As the basis of the structural design, blade loads were calculated as a function of blade azimuth to include blade unsteady aerodynamic loading generated by lift and drag forces on the blade aerofoil section, assumed to be constant in the span-wise rotor direction. Inertial blade loading due to rotor rotation and unsteady blade loading due to the blade pitching motion is also included. The coordinate system used at each support pin position is shown in figure 3.9. The method of calculating the load magnitudes and distributions for each load case is outlined in Appendix B for the baseline blade cyclic pitch input θ_{BL}. Only a summary of the results is given in the current chapter.

Support pin reaction forces were converted into blade flap-wise and edge-wise components, as shown in figures 3.10 (a) to 3.10 (e) for each load case, with resultant reaction forces also calculated. At the pitching pin and pin 1, the blade pitching motion dominates the edge-wise loading, as outlined in figures 3.10 (a) and 3.10 (b). As shown in figures 3.10 (c) to 3.10 (e), the rotor inertial loading dominated the remaining pin reaction forces. Overall resultant support pin loads are presented in figures 3.11 (a) and 3.11 (b) for pins 1 and 2. Pin 1 is positioned at the inboard rotor position at the blade pitching mechanism, where the increased reaction force unsteadiness is attributable to the contribution of the pitch pin at this position.

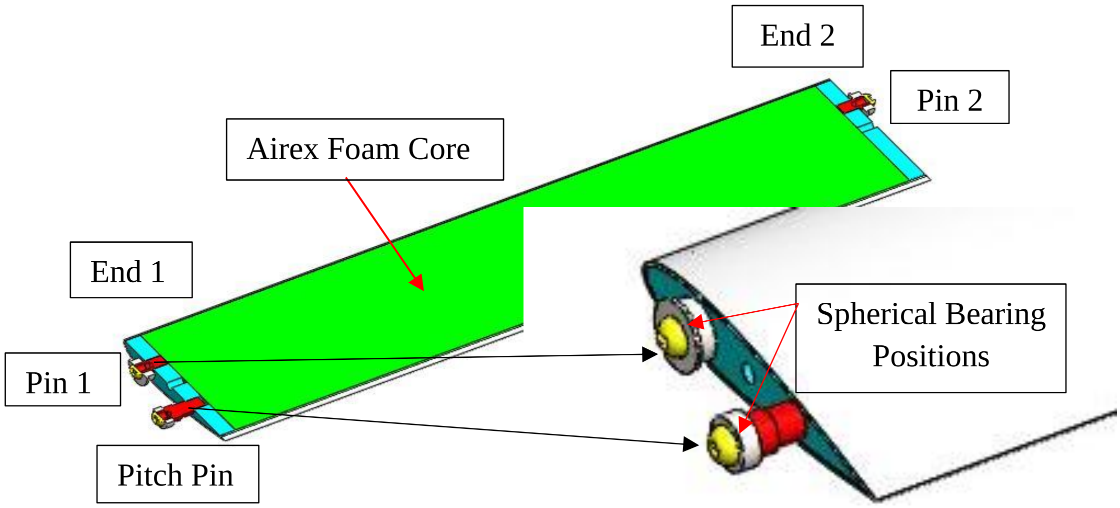

Figure 3.8 – Rotor blade constituent components and makeup, with the support pin geometry, defined

Based on the support pin reactions, blade shear force and bending moment diagrams were created to calculate the blade torsional, edge-wise, and flap-wise bending moments to be used in the blade design, as shown in figures 3.12 (a) to 3.12 (c). The edge-wise and torsional bending moments from a blade-loading perspective are not significant. The driver is the flap-wise bending moment in figure 3.12 (c), which is an order of magnitude higher, resulting from the overall resultant blade loading being dominated by the inertial loading due to rotor rotation.

3.6.2. Rotor End Disc Loading

Blade support pin reaction forces were calculated in the blade reference frame but converted to the rotor rotating frame for the rotor disc design. As a result, the rotor radial and tangential loads are calculated as per figures 3.13 (a) and 3.13 (b).

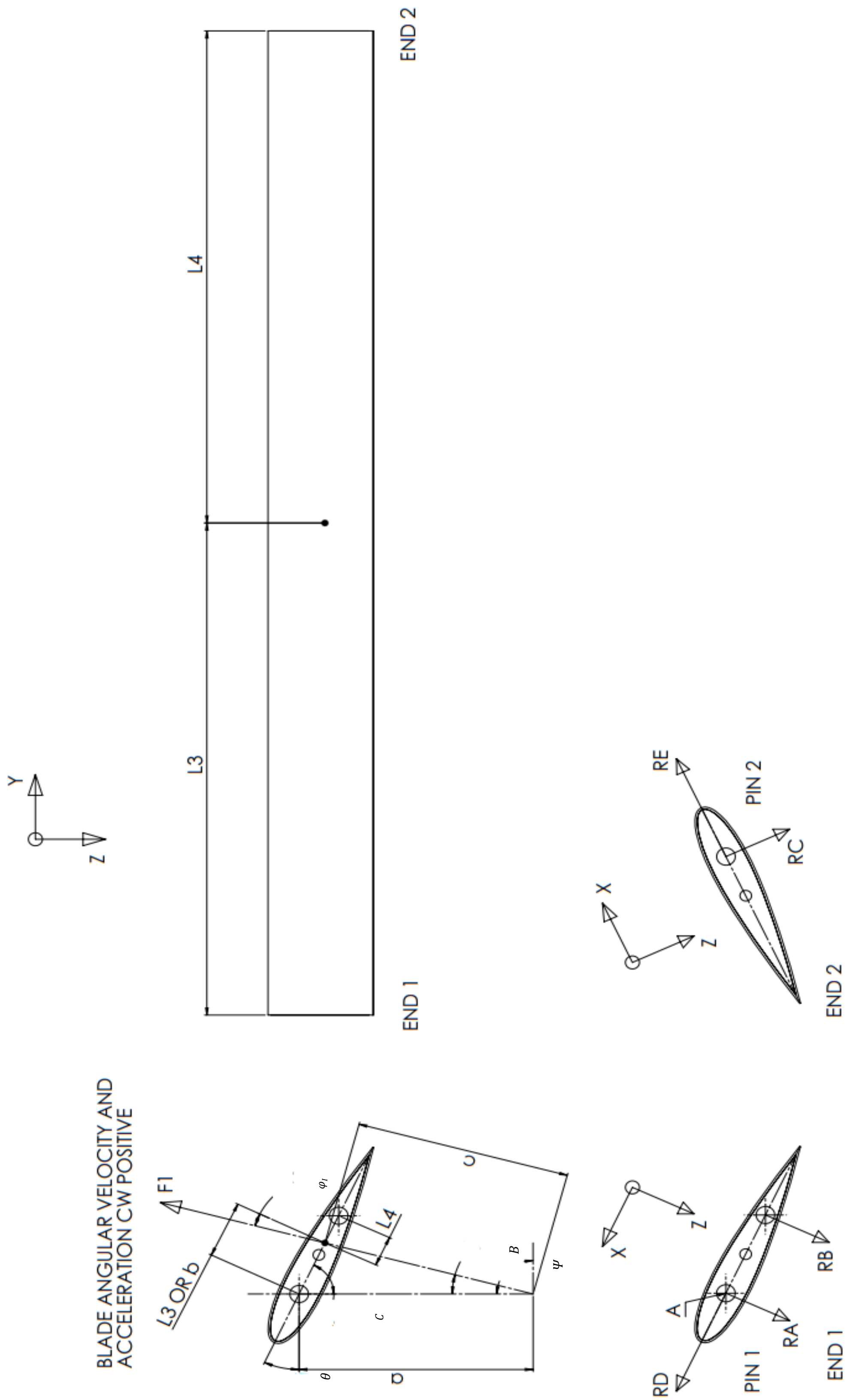

Figure 3.9 – Rotor blade-free body diagram

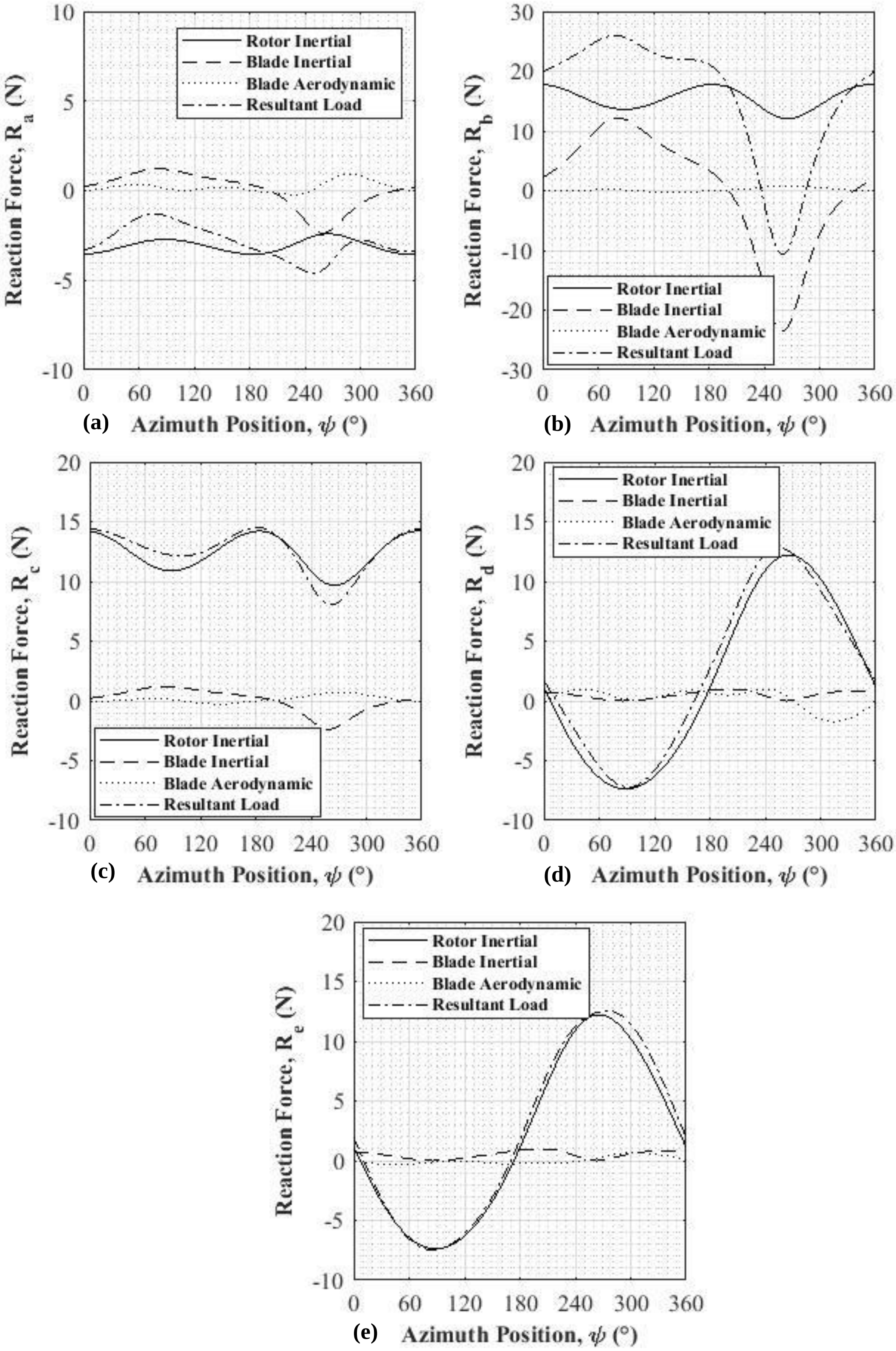

Figure 3.10 – Rotor blade support pins chordwise and edge-wise reaction forces at a rotor radius of 100 mm and span of 230 mm. Results were generated at a rotational speed of 2,000 RPM and a 40° blade cyclic pitch angle. Data based on BET code results

3.6.3. Bearing Loading

Using a four-bar blade pitching mechanism produces an unsymmetric blade pitching profile in the upper and lower half of the rotor. Coupled with the rotor inflow results in a residual rotor out of balance of approximately 7 N reacted at the bearing positions, which is trivial for the bearing diameters in question. However, more critical in designing an experimental rig is considering a 'blade-off' failure condition. In the event of a blade failure, an Out of Balance (OoB) force equal to the blade mass will be produced. Under this condition, the system must remain intact until the rotor is brought to rest to avoid further damage. The equations and methodology used are shown in Appendix B.

3.6.4. Drive Line Torque

The driveline power requirements were calculated by summing the mean torque over each rotor blade, considering only the blade aerodynamic tangential force components. The resulting torque curve was unsteady, but the peak torque magnitude was used to calculate the motor power requirements. An accurate estimate of driveline frictional losses was unknown, so the motor was over-dimensioned to ensure acceptable operation over the whole test envelope.

3.6.5. Component Fatigue Loads

As illustrated in figures 3.10 to 3.13, the loading conditions applied to the blade and associated structure are not static but dynamic. With the alternating stress amplitudes continually changing, fatigue analysis cannot be used in its basic form. The unsteady loads were considered as a series of spectral loads; Miner's rule was used to estimate the cumulative damage per rotor revolution.

Miner's rule uses bins to group each cycle's amplitudes and mean stresses, depending on the spectral content, and counts them via rain flow cycle counting. Once counted, the cumulative fatigue damage is calculated. If the stress levels are below the fatigue limit of the material from the SN diagram, it was assumed that no damage occurs, and the component can be deemed to have an infinite life, $1x10^6$ zero to maximum stress cycles in this instance.

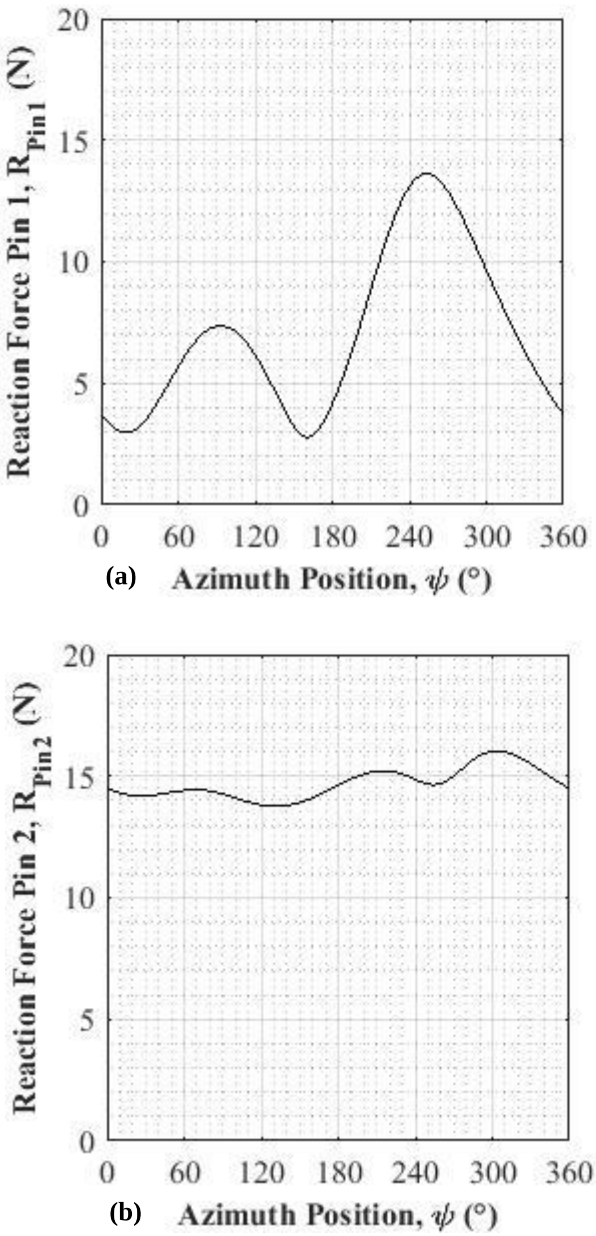

Figure 3.11 – Rotor blade Pin1 and Pin 2 resultant reaction forces at a rotor radius of 100 mm and span of 230 mm. Results were generated at a rotational speed of 2,000 RPM and a 40° blade cyclic pitch angle. Data based on BET code results

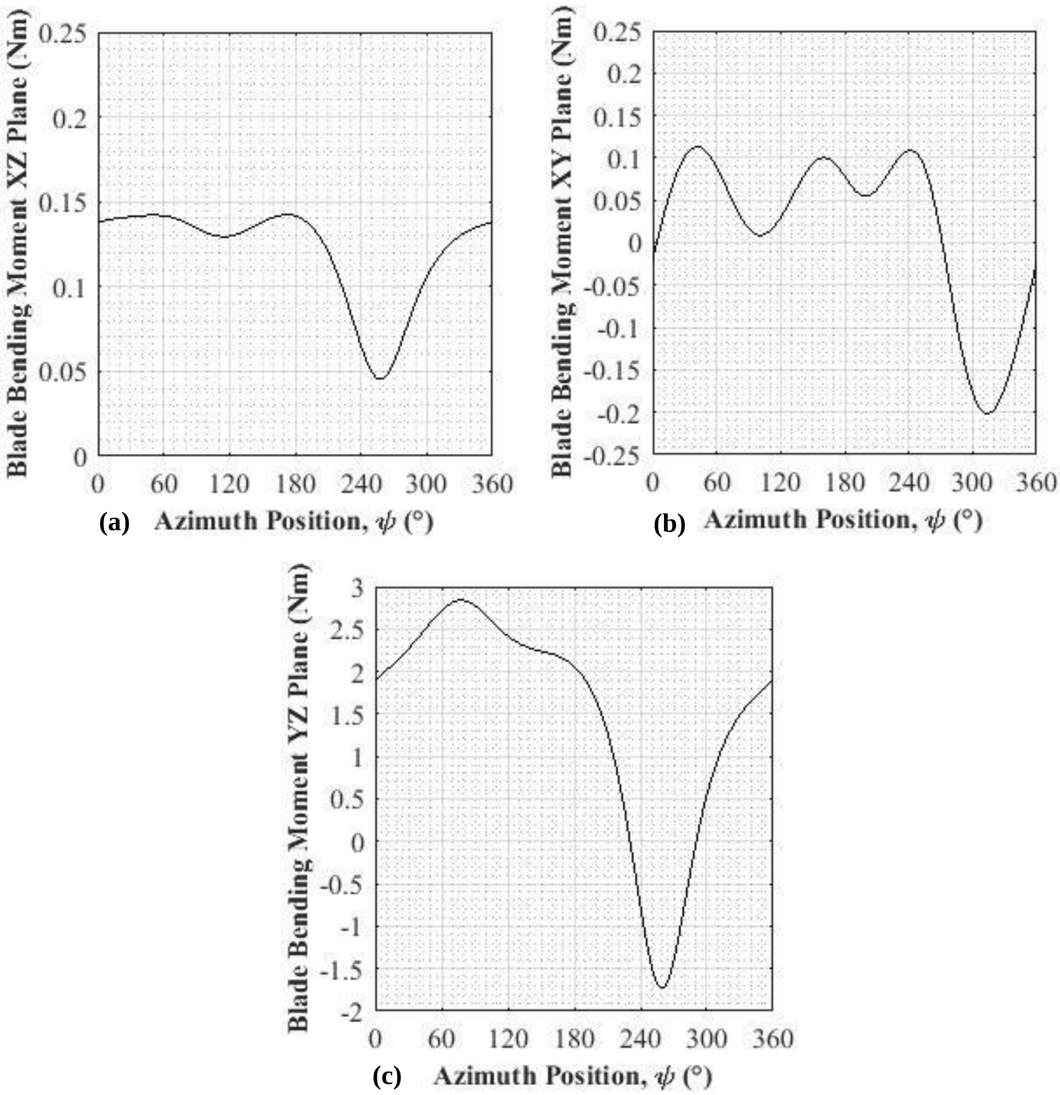

Figure 3.12 – Rotor blade orthogonal bending moments at a rotor radius of 100 mm and span of 230 mm. Results were generated at a rotational speed of 2,000 RPM and a 40° blade cyclic pitch angle. Data based on BET code results

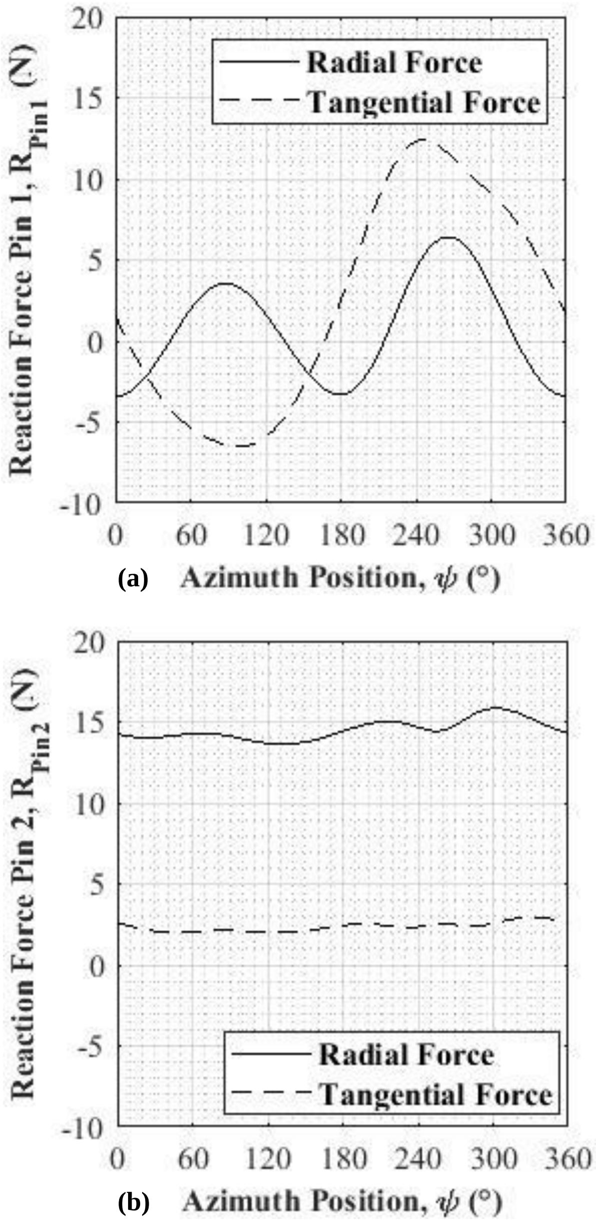

Figure 3.13 – Rotor upper and lower end disc blade support reaction forces at a rotor radius of 100 mm and span of 230 mm. Results were generated at a rotational speed of 2,000 RPM and a 40° blade cyclic pitch angle. Data based on BET code results

3.7. Component Analysis

3.7.1. Blade Design and Optimisation

As the blade mass increases, so does the potential mass of the rotor support structure to support the increased centrifugal blade loading. This drove the requirement of a minimum blade mass design with high flexural or transverse stiffness and ruled out using a metallic blade. A composite blade design was chosen to allow flexibility in design and to tailor the material properties of the blade to the design constraints. In composite blade construction, carbon fiber layers are bonded in a structural resin matrix. All calculations were based on a fiber volume fraction of 50%, in line with [108], to account for manufacturing process variability, assuming the material properties outlined in section 3.4.2 for readily available materials.

Crewed flight rotor blades are designed with a structural composite skin and D-Spar central core. The blockage and solidity requirements of the current design resulted in a blade chord of 50 mm being used with a NACA 0018 profile. The overall thickness of the blade is 9 mm, which made the use of a standard D-spar difficult, leaving areas of the blade skin unsupported at the leading and trailing edges. A structural foam core was adopted to support the outer skin, using a closed-cell polymer foam, Airex C70, to ensure the opposing skins are kept apart to maintain the blade bending stiffness.

Carbon fiber cloths are available with a unidirectional (UD) fiber or a 0° and 90° weave. The fibers are only strong in tension along their fiber axis; transverse to this, they have limited strength. A parametric study was undertaken based on the transverse and torsional deflection targets quoted in section 3.2 and bending moment diagrams in figures 3.12 (a) to 3.12 (c) to calculate the optimal blade layup. Varying symmetrical and nonsymmetric laminates were considered, using a combination of UD and weave layers at varying wrap angles.

Overall layup material properties were calculated using classical laminate plate theory to calculate blade deflections using standard beam theory equations. The optimal blade layup comprised a symmetrical laminate with a UD layer sandwiched between two weave layers at +/-45° to give adequate torsional and shear stiffness. In addition, the UD layer improved flexural stiffness with a limited mass penalty.

The blade design methodology required the use of two-blade structural models, one using classic theory and a finite element (FEA) model. The use of the classical laminate plate theory was extended after the parametric study to calculate the stress levels in the composite/epoxy laminate under the prescribed blade loads. This approach confirmed that the current design's laminate stress and strain levels were trivial compared to the allowable levels and did not need to be optimized further, with adequate strength factor of safety. A Tsai-Hill failure analysis was undertaken for completeness, confirming that failure should not occur.

It is usual to consider residual thermal stresses in large-scale blade design due to blade curing temperature during manufacture. However, the scale and simplicity of the current blade and the additional computational overhead to calculate the thermal stresses were deemed disproportionate.

While the laminate was acceptable, a more detailed computational study was required to include an analysis of the laminate and individual features, such as blade attachment points and component bond lines. An FEA model of the blade was developed in Ansys Mechanical using a combination of shell elements for the laminate skin and 3D structural tetrahedral elements for the attachment points and foam core. Bond lines were modeled as flexible elements. The blade attachment points were modeled to fit inside the blade skin to remove potential discontinuities from the blade's aerodynamic surface.

Meshing was completed for the total laminate thickness of three layers stacked correctly at 0° and +/-45° laminate orientation, considering both the resin and carbon fiber elements. Radial restraint boundary conditions were applied to each blade attachment point, and axial restraints were applied at the connections to the rotor end plates. The FEA model developed in ANSYS Mechanical was a linear static analysis, where a linear relationship holds between the applied forces and component displacements. A linear static analysis is applicable where the stress levels remain within the material's linear elastic range, which can be a significant assumption for composite material depending on the material layup and applied load cases. In this case, based on the stress levels calculated from classical laminate plate theory, a linear static stress analysis was deemed to be acceptable.

The quality of the mesh can have a significant effect on the predicted blade stress and deflection levels. Therefore, mesh dependency analyses were undertaken for five separate meshes to find an optimum mesh configuration. Each subsequent mesh contained an increased number of cell elements, achieved by increasing the number of mesh elements within the composite blade skin. The overall cell count of the five mesh configurations is outlined in table 3.2.

Table 3.2 – Finite element analysis mesh sensitivity analysis total mesh element count

Mesh Study	Number of Elements
Mesh 1	12,179
Mesh 2	28,654
Mesh 3	40,329
Mesh 4	60,184
Mesh 5	85,673

Peak blade deflection was used to gauge mesh efficacy, as shown in figure 3.14. A 3.1% deviation in peak deflection was calculated between mesh 3 and 5, but the run time increased by 93%. As a result, mesh 3 gives the best combination of solution accuracy and run time. The mesh was taken forward for subsequent FEA analyses. The final mesh used is outlined in figure 3.15.

The resultant blade deflection levels are shown in figure 3.16 (a), with von Mises stresses at the blade ends shown in figure 3.16 (b). In both cases, the target value for deflection and stress level factor of safety was achieved. Low and High cycle fatigue life was also checked for all metallic parts and calculated to be greater than 1×10^6 cycles in all cases.

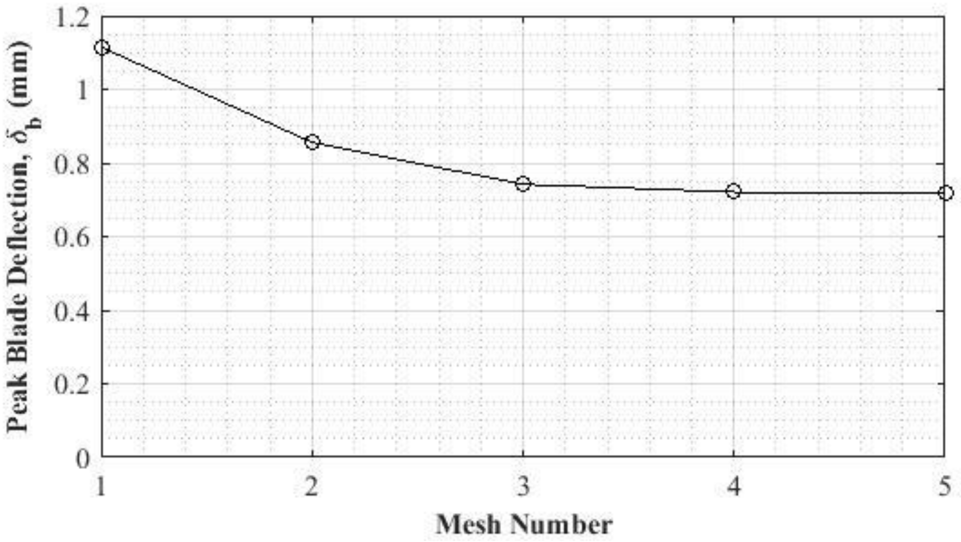

Figure 3.14 – Ansys Mechanical FEA rotor blade peak deflection mesh sensitivity analysis

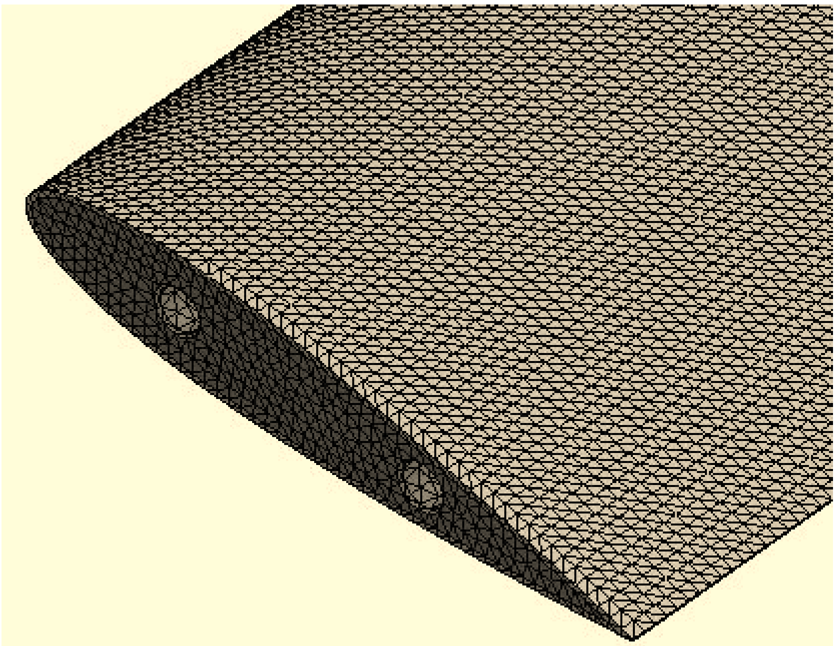

Figure 3.15 – Blade FEA mesh 3 generated for final linear static stress analyses in ANSYS Mechanical

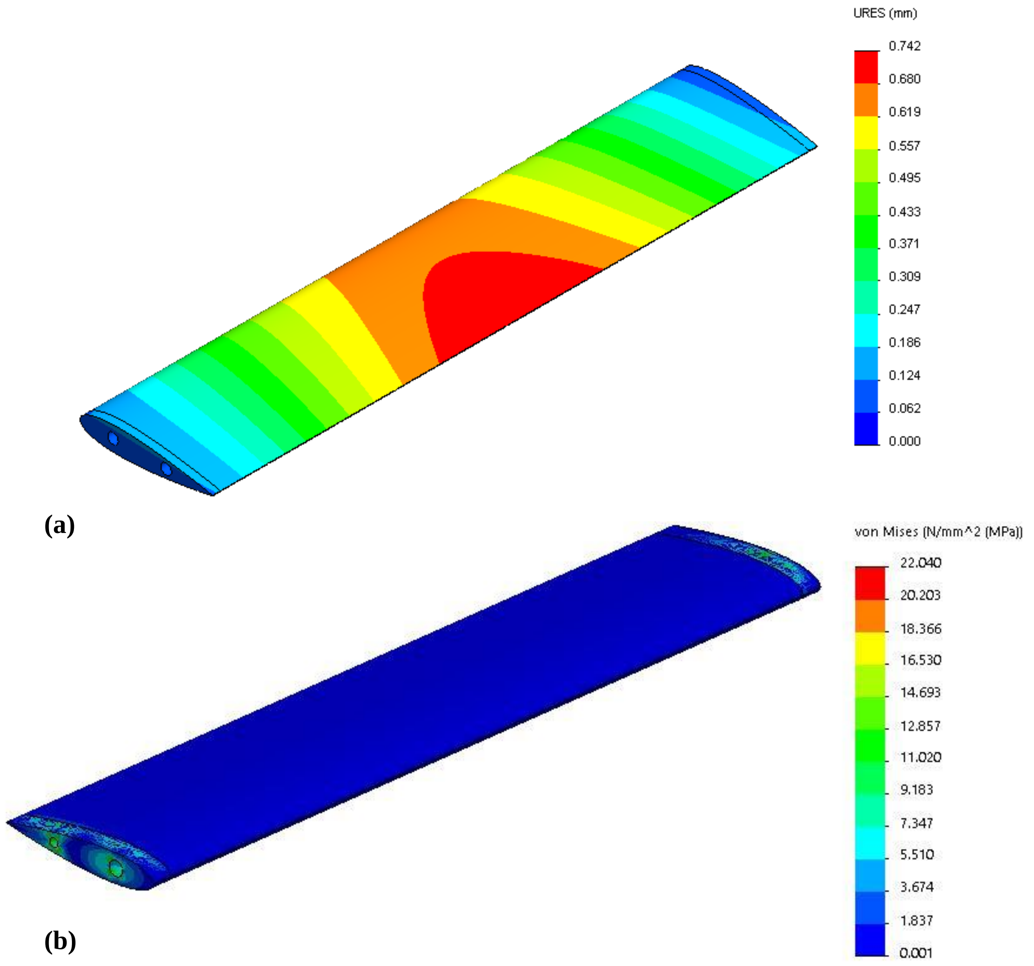

Figure 3.16 – Rotor blade (a) resultant deflection and (b) von Mises stress plot. Applied loads were generated at a rotational speed of 2,000 RPM and a 40° blade cyclic pitch angle and rotor radius of 100 mm. Applied loads based on BET code results

3.7.2. Blade Fabrication

For accurate blade manufacture and repeatability, a blade mold was CNC machined out of an aluminium alloy and assembled, as shown in figure 3.17, consisting of an upper and lower mold half. Each composite laminate layer was manufactured from a single cloth layer, with a bond line at the blade trailing edge to reduce the chance of a leading-edge laminate failure due to manufacturing error.

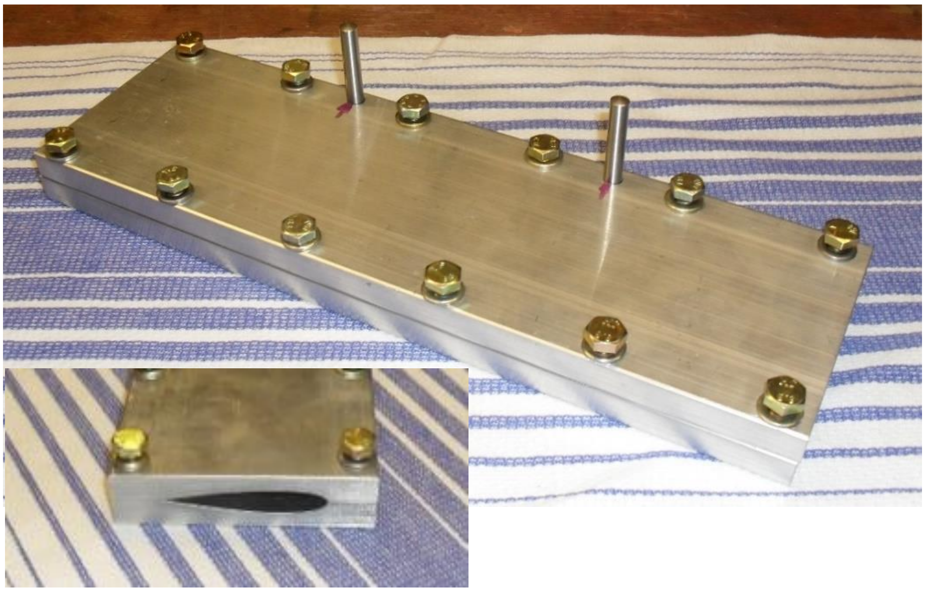

Figure 3.17 – Rotor blade mold design

The Airex C70, structural foam core, was profiled by hand to a NACA 0018 profile to suit the mold, taking into account the laminate thickness, as shown in figure 3.18. The overall layup was produced on a surface plate and impregnated with the resin before being wrapped around the core and transferred to the mold. The mold and blade assembly were then cured for 90 minutes at 120°C.

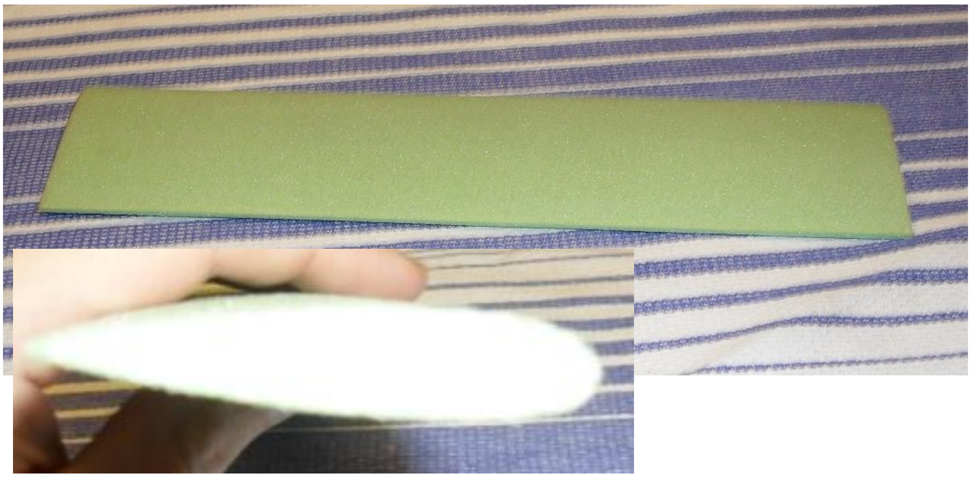

Figure 3.18 – Rotor blade structural Airex foam core geometry

The blade upper and lower attachment points were manufactured and designed to be the same to aid blade static balancing, as shown in figure 3.19. The attachment points were bonded into position inside the laminate skin as per figure 3.8, with a semi-flexible structural adhesive. The design ensured that the inserts were connected to the laminate skin and core material and gave the largest bond line surface area possible within the size constraints.

Figure 3.19 – Rotor blade end support insert design

3.7.3. Test Rotor Analysis

The following section outlines the structural analysis of the rotor top and bottom endplates and main central spindle. The rotor endplates were designed using the blade support pin reactions at 120% design speed, and the central spindle was analyzed at the rotor 'blade-off' condition.

The diameter of the rotor end blades was taken to be 270 mm for the top and bottom end plates, following a parametric analysis to meet the rotor's structural and vibratory requirements. Where larger diameter end plates typically reduced the rotor's first critical speed. A compromise was made between the mechanical and aerodynamic design to reduce any 3D flow effects. As the end plate diameter is increased, 3D flow effects reduce, and the closer the cycloidal rotor operates to 2D aerodynamic performance and efficiency. The planform of the test rig base is square to aid with the mounting of ancillary components. Test rig base corners will dampen some of the 3D flow effects and contaminate small flow regions at the test rig base corners. The bottom endplate diameter was also chosen to reduce these potential flow contamination effects.

A 3D finite element model of the upper and lower endplate was created due to concerns about the thin geometric sections required. The analysis considered the effect of geometric stress concentrations and the impact of unsteady blade reaction forces. The unsteady loads were applied as a transient load curve based on the radial and tangential forces presented in figures 3.13 (a) and 3.13 (b). Peak transient von Mises stress and deflection levels for the lower rotor disc are shown in figures 3.20 (a) and 3.20 (b), respectively. The peak von Mises stress levels occur around the support holes, giving a steady-state stress factor of safety on 0.2% proof stress of 13 and a burst margin of approximately 15, which is sufficiently higher than the 120% design criteria. A Miner's rule fatigue analysis showed that high cycle fatigue (HCF) was not a concern.

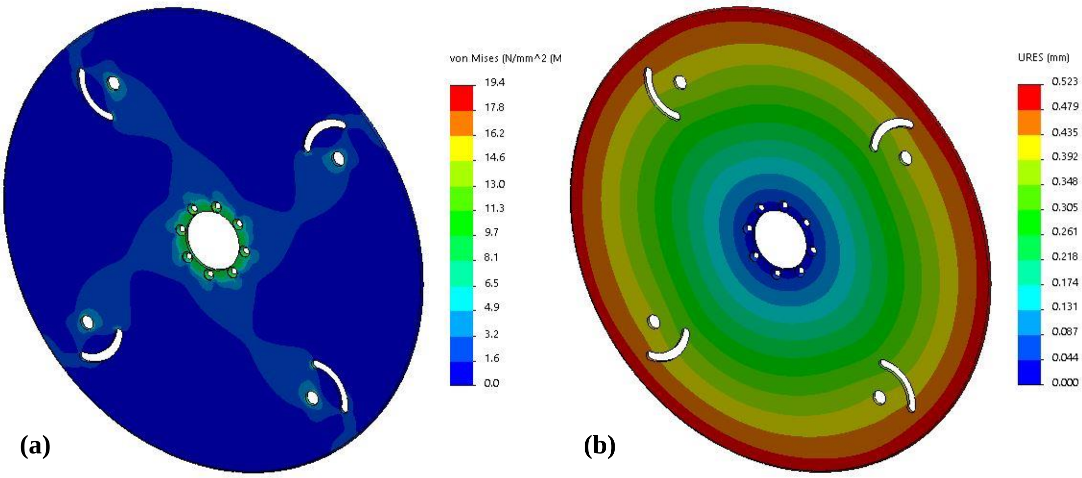

Figure 3.20 – Lower rotor-disc burst speed (a) von Mises stress and (b) resultant deflection plot. Applied loads were generated at a rotational speed of 2,000 RPM and a 40° blade cyclic pitch angle and rotor radius of 100 mm. Applied loads based on BET code results

The peak magnitude of the endplate vibratory stress was assessed using a Goodman diagram to calculate the allowable vibratory stress at the given mean stress level. A typical industry standard allows a 65 MPa margin on the peak vibratory stress to the maximum allowable, which was exceeded in the current design. The same approach was used for the upper rotor endplate, as shown in figure 3.21 (a) for von Mises stress level and 3.21 (b) for deflection. The safety margins calculated based on

0.2% proof stress were greater than the lower rotor endplate, so it will not be considered further, with both designs deemed acceptable.

The geometry of the central spindle was driven by the rotor critical speed requirements, discussed in section 3.8, as opposed to applied rotor loads. Under 'blade-off' and peak drive torque conditions, the peak bending moment was 22 Nm as per figure 3.22, resulting in a peak von Mises stress of approximately 9 MPa, as shown in figure 3.23, which is well within the allowable material limits.

3.7.4. Blade Pitching Mechanism Design

Cycloidal rotor experimental studies to date have assumed a cyclic blade pitch input that approximates pure sinusoidal motion using a passive four-bar mechanism [4]. The mechanism is made up of a central bearing and arms connected to each pin's pitch point to prescribe the required blade motion. The exact motion is described in Appendix B. A face cam of the required profile was designed to eliminate mechanism rotation in the current design. The pitch pin of each blade ran within the cam and pitched via a rolling element bearing to simplify the design and keep frictional losses to a minimum.

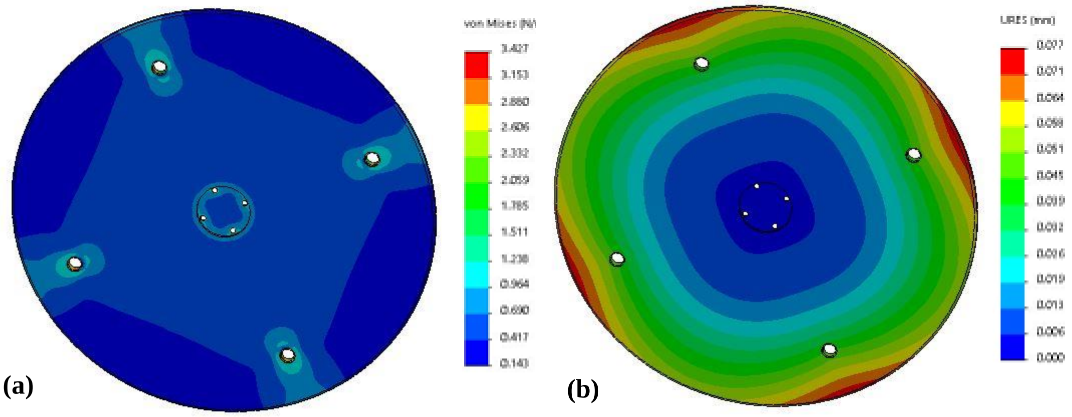

Figure 3.21 – Upper rotor-disc burst speed (a) von Mises stress and (b) resultant deflection plot. Applied loads were generated at a rotational speed of 2,000 RPM and a 40° blade cyclic pitch angle and rotor radius of 100 mm. Applied loads based on BET code results

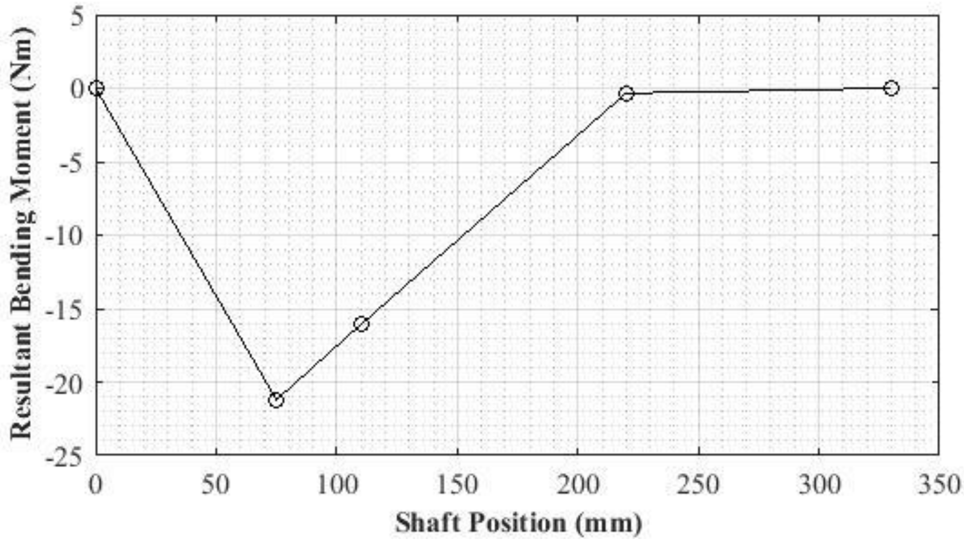

Figure 3.22 – Main rotor support shaft 'blade-off' bending moment diagram. Applied loads were generated at a rotational speed of 2,000 RPM and a 40° blade cyclic pitch angle and rotor radius of 100 mm. Applied loads based on BET code results

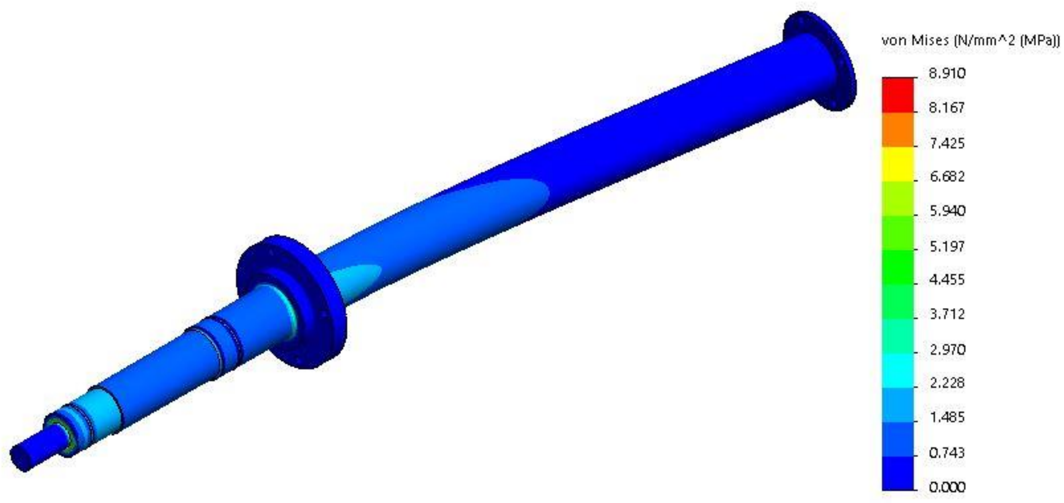

Figure 3.23 – Main rotor support shaft 'blade-off' von Mises stress plot

To enable thrust to be vectored in any direction and the blade cyclic pitch amplitude θ_{BL} to be varied from -45° to +45°, the cam was mounted onto four orthogonal linear slide stages, as shown in figure 3.24 (a). Each slide is driven by a separate 200 pulse per revolution (PPR) stepper motor to allow accurate cam placement through a 1:1 bevel gear drive. The pitch and helix angle of the slide drive screw was specified to ensure that back driving would not occur under operation, which would result in loss of blade motion. Figure 3.24 shows the baseline cam design, which encases the slide mechanisms. The cam was manufactured from ABS Nylon and designed to meet the pitch pin load case in figure 3.10 (b)

Test rig design and manufacture were undertaken in parallel with the literature review. The initial project scope included the study of forward flight for rotor vibration measurement and optimization. Project goal refinement due to wind tunnel time constraints led to the focus of the current research concentrating on a rotor under hovering conditions. The literature review also highlighted that the vibration characteristics of the cycloidal rotor at present have not even been researched for a rotor under hovering conditions. A decision was made to gain a fundamental understanding of the cycloidal rotor without the added freestream velocity for forward forward flight operation, which adds additional justification to not considering the Magnus effect of the rotor. The investigation of forward flight will form the focus of future work building on the work undertaken in the current research.

The final experimental studies, including the use of HHC, were analyzed at a set blade cyclic pitch amplitude and phase angle, eliminating the need for cam positioning. The test rig was modified as shown in figures 3.25 (a) and 3.25 (b), utilizing an indexing plate for repeatability and 3D printed cams through Selective Laser Sintering (SLS) for each test case considered. The cams were designed under the same loading condition as the baseline cam mechanism due to HHC input giving an estimated 15% increase in control loads.

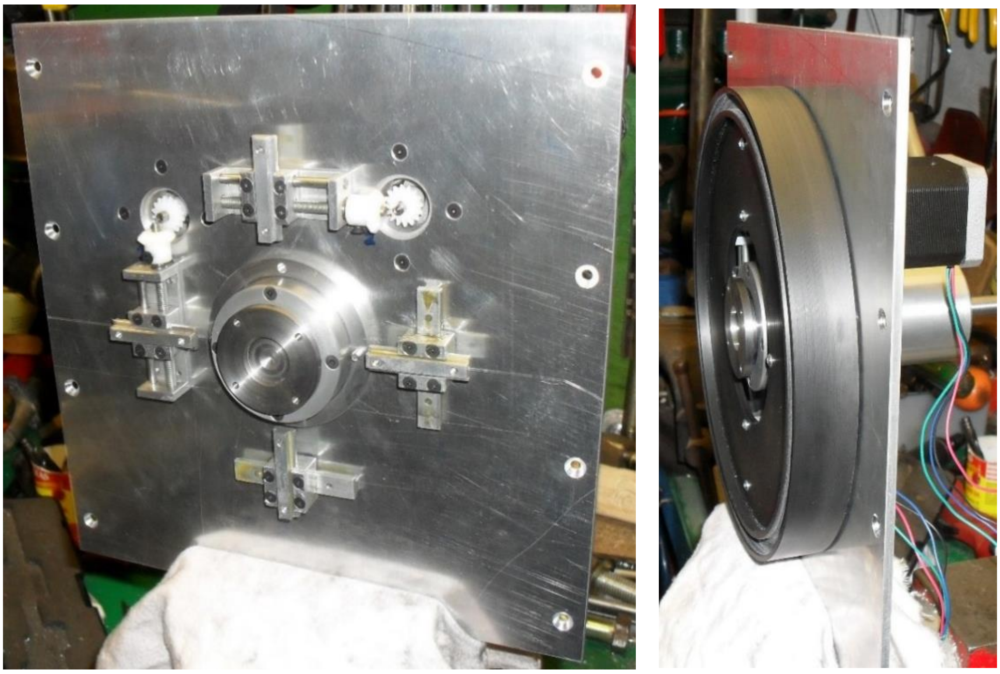

(a) (b)

Figure 3.24 – Baseline blade cyclic pitch input cam mechanism

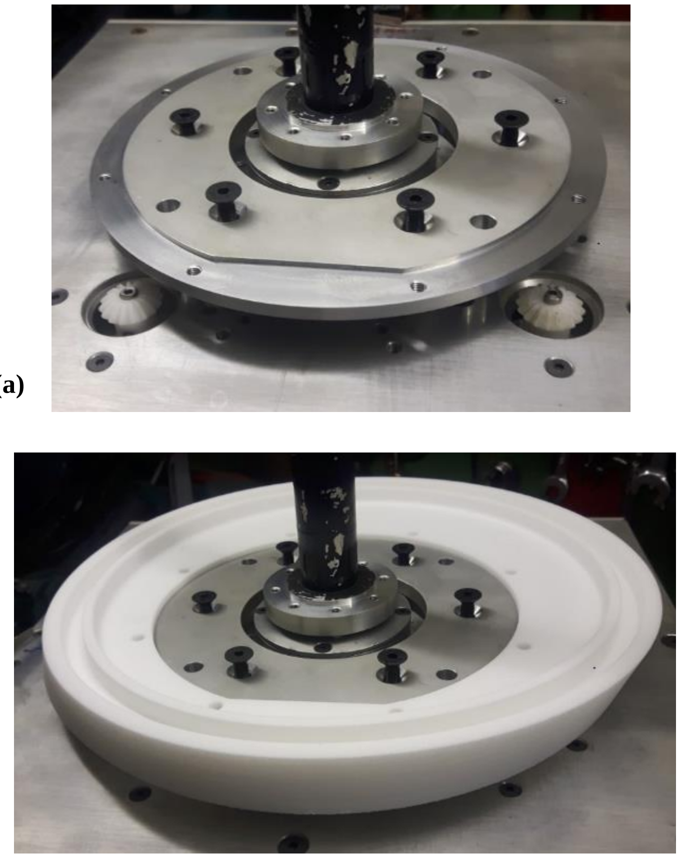

(a)

(b)

Figure 3.25 – Test rig modified cam mechanism to include HHC control input (a) index ring and (b) SLS cam design

3.7.5. Driveline Design

Current BET code analyses and comparisons over a wide range of blade numbers and profiles [4] provided an upper limit for the rotor mean Coefficient of Power of approximately 0.3. A maximum rotor rotational speed of 2,000 RPM gave a mean motor power requirement of 135 W, which was increased to 270 W to allow for unsteady effects and frictional losses. The final design used a 300 W 24V geared motor through a 1:3 bevel gear drive, controlled through a Pololu brushed DC motor controller.

3.7.6. Bearing Selection

The bearing arrangement used for the current cantilevered rotor design is shown in figure 3.26. It uses medium-speed grease-lubricated angular contact bearings at each position, arranged in a back-to-back formation for increased stiffness. With the allowable bearings speed reduced by 20% to account for the back-to-back arrangement, the permissible speed is still 10,000 RPM. The overriding bearing speed limit is 1.35 x 10^6 DmN, which represents the mean bearing diameter multiplied by the maximum rotor rotational speed. The current rotor design bearing DmN value is 0.1 x 10^6 at maximum conditions and is acceptable. Under 'blade-off' conditions, the resultant bearing loads are an order of magnitude lower than the maximum recommended bearing permissible value. The bearing bore was governed by the test rotor rotor-dynamics requirements rather than bearing loading.

A standard arrangement with a non-located and located bearing set was used to allow thermal expansion within the spindle during operation. The located bearing set was positioned closest to the rotor to provide optimal alignment. Standard bearings with standard C3 clearances were used as the loss of bearing fit under maximum rotational speed was significantly less than 1μm. Bearing pre-load was controlled using universally matchable bearings sets, and the manufacturer-recommended shaft tolerances were used where possible. The non-located bearing set is designed to slide axially during operation with thermal growth. The bearing housing tolerance was specified not to bind during sudden bearing temperature increases and maintain rotor run-out.

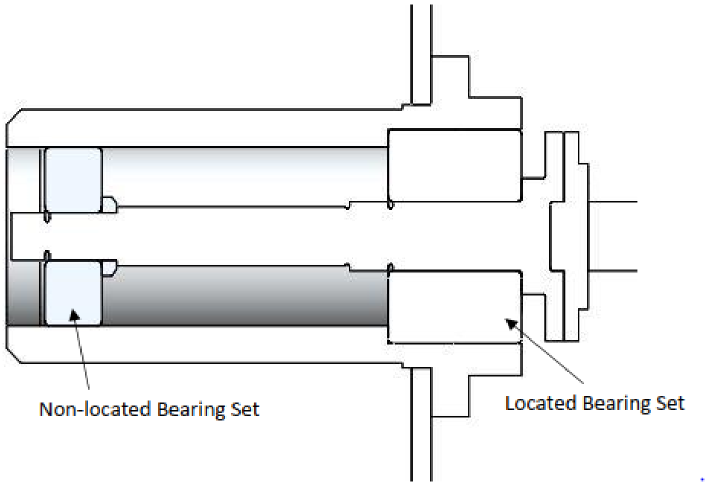

Figure 3.26 – Rotor spindle bearing arrangement

The L10 bearing life was calculated and is the standard method of specifying the number of rotations a bearing can undertake before reaching its fatigue life under the specified loading. For the current design, the L10 is greater than 1×10^7 cycles in all cases.

3.8. Rotor Vibration Analysis

Modal analysis of the individual blade and overall support rotor was also performed to determine whether or not resonance is likely to occur during the operation of the test rig. For a four-bladed test rig, the expected forcing functions and harmonics of interest are N_b-1, N_b, and N_b+1, where N_b is the blade number. The three fundamental blade frequency modes are shown in figures 3.27 (a) to 3.27 (c) for the first flexural, first torsional, and second flexural modes. A Campbell diagram was created to compare the resonant frequencies to the expected forcing functions, as shown in figure 3.28 for a rotor blade. For a safe design, interferences are typically removed where possible from the 60% to 100% design speed range. Therefore, from figure 3.28, the blade frequency alone will not be an issue.

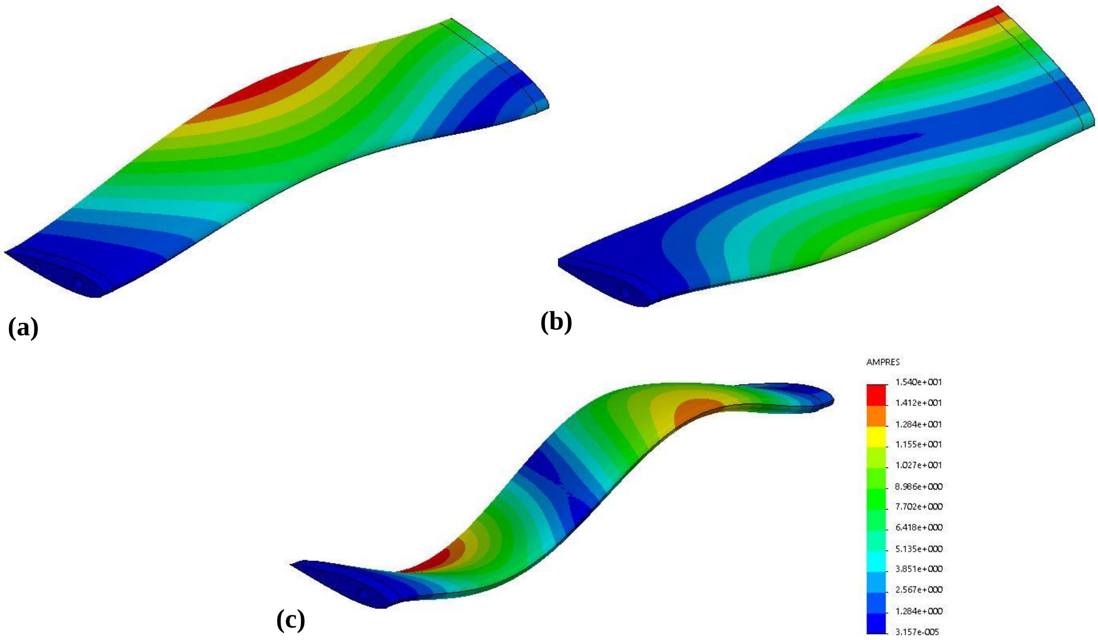

Figure 3.27 – Rotor blade normal vibration modes (a) First flexural mode 1F. (b) First torsional mode 1T and (c) Second flexural mode 2F

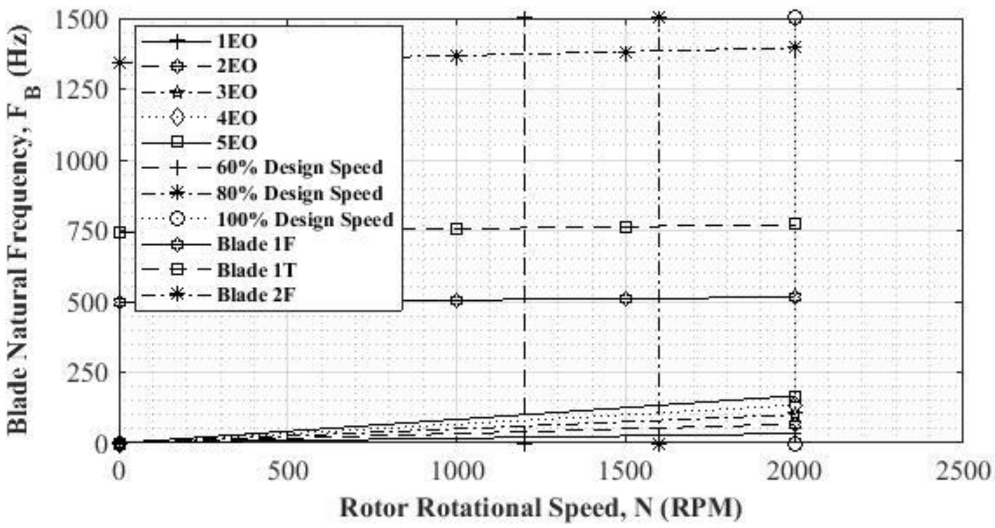

Figure 3.28 – Rotor blade Campbell diagram based on a NACA 0018 50 mm blade chord and a span of 230 mm

When the analysis was extended to the assembled rotor, an effective mass participation factor was calculated for each mode to establish the dominant resonant frequencies. The mass participation factor is a measure of the energy contained within the mode. Anything over 1% of the component mass is deemed significant in the system's dynamic response. For the rotor, the modes of interest were the first two flexural modes that occur in orthogonal directions and the first torsional mode, as shown in figures 3.29 (a) and 3.29 (b).

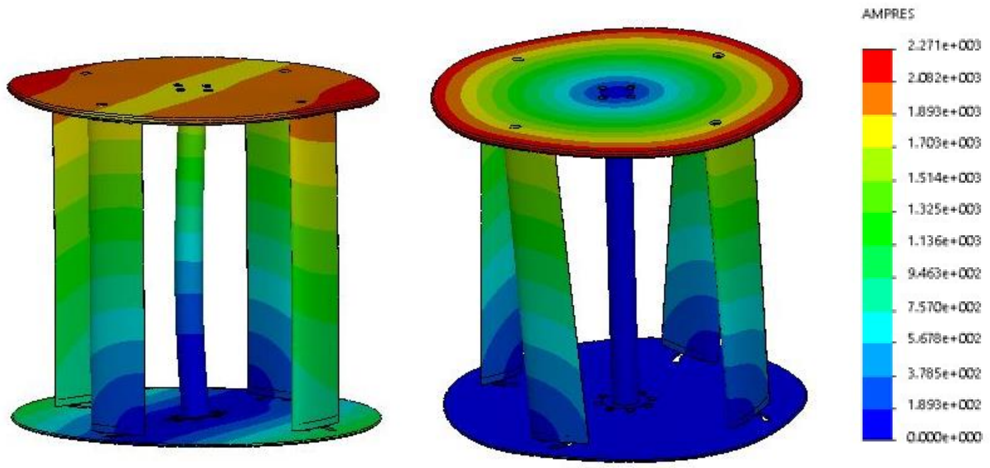

(a) **(b)**

Figure 3.29 – Assembled rotor normal vibration mode (a) First and second flexural modes 1F and 2F. (b) First torsional mode 1T

The Campbell diagram for the complete rotor is shown in figure 3.30 and shows that multiple interferences occur in the 60% to 100% design speed range of interest across the 3 to 5/Rev harmonics. Additional analyses showed that the dynamic response of the rotor was sensitive to rotor endplate geometry. But to eliminate all interferences would result in an unrealistic endplate geometry. The maximum operational speed was reduced to 1,000 RPM to eradicate all interferences while maintaining experimental rigor. The rotor's first flexural mode results in interference at 1,050 RPM with the 5/Rev harmonic. Based on the rotor being a development rotor only, the 1,050 RPM interference was deemed to be acceptable.

Torsional vibration analysis was undertaken on the rotor and driveline, including the contribution of the gear interface and drive motor, based on the Holzer tabular method. The first torsional mode was calculated to be approximately 4,000 RPM, double the maximum design intent rotational speed. A relative amplitude diagram showing the torsional motion amplitude is shown in figure 3.31, showing that if torsional vibration were an issue, most motion would be lost in the motor and gearbox, illustrated by nodes 4 to 6.

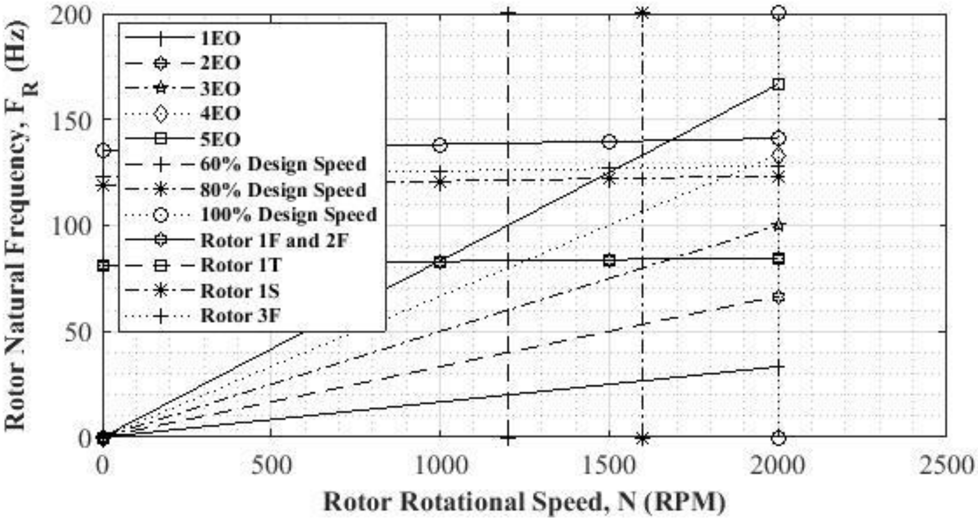

Figure 3.30 – Assembled rotor Campbell diagram based on a four-bladed rotor with NACA 0018 50 mm blade chord. A span of 230 mm and 270 mm diameter rotor end plates

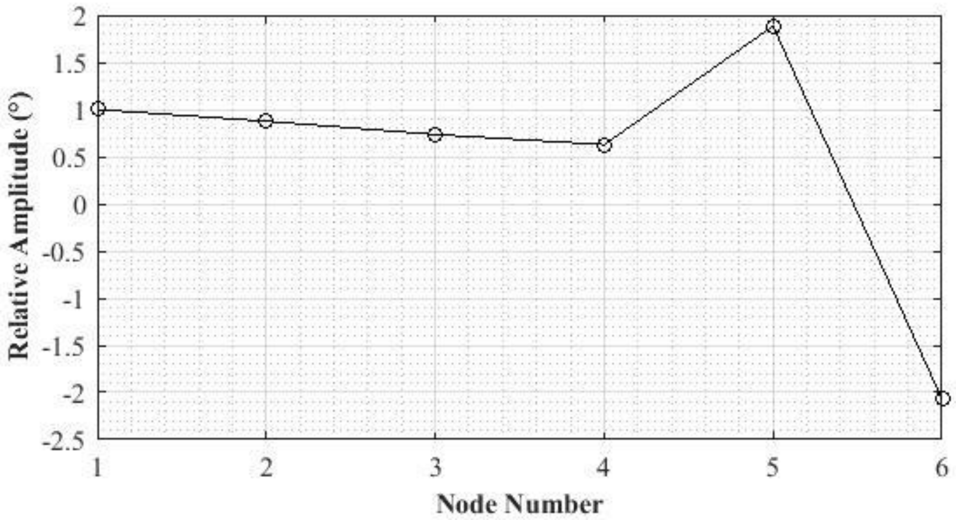

Figure 3.31 – Fundamental torsional vibration relative torsional motion diagram based on a four-bladed rotor with NACA 0018 50 mm blade chord. A span of 230 mm and 270 mm diameter rotor end plates. Rotor central spindle diameter 20 mm

3.9. Rotor-dynamic Analysis

A basic rotor-dynamics analysis was undertaken to calculate the rotor assembly's first critical speed. The test rig is mounted on a force sensor in operation that has its own dynamic response, considered in Chapter 4, which changes the overall test rig dynamic response. The sensor stiffness was estimated during test rig design by applying a known mass to a rigid beam of known length that was connected to the sensor interface. This enabled the beam deflection to be measured with a test indicator and an effective stiffness calculated in each measurement direction. The effective stiffness was then used in the subsequent rotor-dynamic analysis.

A critical speed map was created, shown in figure 3.32, considering a wide range of assumed bearing stiffness values. Based on manufacturer data and bearing housing stiffness, the estimated resultant bearing stiffness results in a first critical speed of approximately 2,000 RPM, effectively 100% of the original design speed. Typically the maximum running speed is limited to 70% of the first critical speed, 1,400 RPM, to run the rotor subcritical. The decision to reduce the design speed to 1,000 RPM alleviates this requirement.

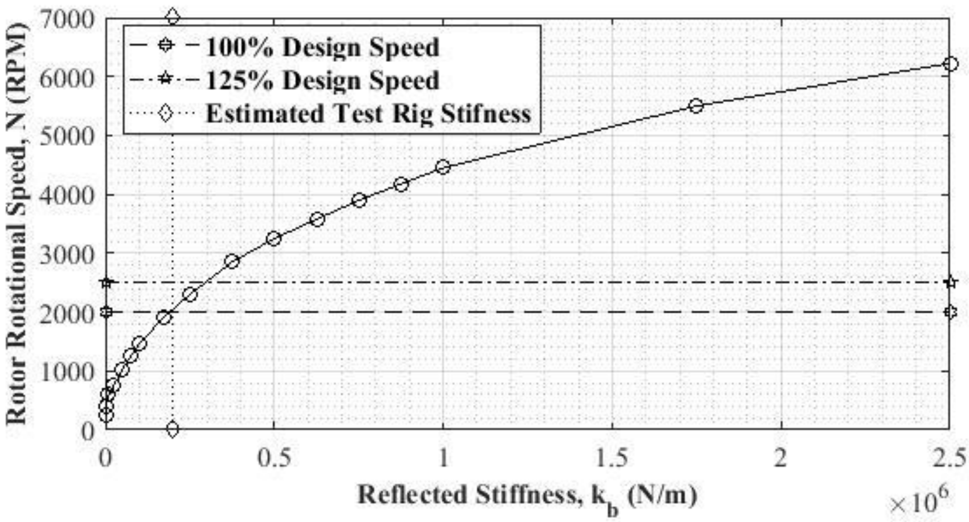

Figure 3.32 – Assembled rotor critical speed map based on a four-bladed rotor with NACA 0018 50 mm blade chord. A span of 230 mm and 270 mm diameter rotor end plates. Rotor central spindle diameter 20 mm with a bearing span of 80 mm

3.10. Rotor Assembly

Rotating assemblies are typically balanced to an ISO standard or at least checked balanced to calculate the residual out-of-balance (OoB). However, the design of the current test rig made dynamic balancing difficult, so a method of static balancing was developed based on total-indicator run-out (TIR) on each component. A TIR of 0.01mm was chosen to achieve an overall rotor balancing grade between G6.3 and G16. This was achieved through careful design and manufacture to reduce machine setup steps to a minimum. Design adjustment was also provided to allow for tuning during assembly. Blade masses were matched by including balancing holes in the blade end supports to add balancing masses, and blade span-wise center of gravity (CoG) was matched by simply supporting the blade on multiple measuring scales.

3.11. Electrical Cabinet Design and Control

The main test rig drive motor and pitching mechanism stepper motors require 24V DC for operation. An electronics control cabinet was designed and built to step down from domestic supply Voltage to 24V DC. The cabinet included the power supply modules, stepper motor drivers, and bespoke PCB board required for overall test rig operation, sized according to the motor power requirements. The final configuration is shown in figures 3.33 (a) and 3.33 (b) for the internal and external components.

Two key variables needed to be tightly controlled during testing: rotor rotational speed and blade cyclic pitch amplitude input θ_{BL}. Drive to the rotor was supplied via a 24V DC brushed motor that also drove a rotary encoder through a parallel gear drive. The encoder was a British Encoder Model 755RG, which provided a combined 360 pulse per revolution (PPR) and 1/Rev signal for rotational speed measurement. Test rig control was achieved through an Arduino Mega 2560 microcontroller interface. Rotor rotational speed was controlled using a PID control loop within the main Arduino control program. The rotor rotational speed was maintained within 1% at maximum speed.

(a)

(b)

Figure 3.33 – Rotor electrical control cabinet (a) internal components and (b) external control panel

3.12. Test Rig Instrumentation

Only one test setup for each measurement point of blade cyclic pitch amplitude and rotor speed was required to acquire the test data to calculate the rotor mean and vibratory hub loads. All in-plane forces and torques applied to the rotor were measured simultaneously with a six-degree-of-freedom (DOF) iCUB force-torque sensor. Voltage readings were output for each measurement axis based on the manufacturers' calibration matrix. After calibration, the iCUB force-torque sensor has a resolution of 0.25 N in the X and Y force measurement directions and a resolution of 0.004 Nm for torque measurements about the Z axis. A full sensor specification is given in Appendix C.

Data acquisition (DAQ) was undertaken with a National Instruments (NI) cRIO 9014 chassis used in conjunction with an NI 9853 High-Speed CAN module for connection to the iCUB sensor sampling at 1 kHz and an NI 9411 digital module interfacing with the 360 PPR rotary encoder previously mentioned. The encoder measurement was also sampled at 1 kHz to match the sampling frequency of the iCUB sensor. Rotor load data and the corresponding encoder reading were automatically saved in a test matrix within the NI control program with an associated timestamp at each measurement point for the full test duration.

3.13. Chapter Review

The test rig design outlined in this chapter is first dynamically calibrated in Chapter 4, then used to produce experimental validation results again in Chapter 4 for comparison with the computational model results in Chapters 5, 6, and 7. In Chapter 8 it is then used as a final validation of the numerical HHC studies.

Chapter 4 – Experimental Test Procedure, Results Processing, and Analysis

4.1. Introduction

A systematic experimental study was undertaken utilizing the four-blade cycloidal rotor developed in Chapter 3. Transient Force and torque measurements were conducted to calculate mean rotor performance and vibratory response over a range of blade cyclic pitch amplitude inputs from 0° to 40° and a range of rotor speeds, from 500 RPM to 1,000 RPM, as outlined in table 4.1. The blade cyclic pitch angles represent each blade's pitch profile during each rotor revolution. The force measurement test procedure was the same for measuring the mean and dynamic rotor loads. However, the measurement post-processing differed between the load types, and these are considered separately.

The present chapter describes the overall methodology used for each of the tests conducted to calculate the mean rotor performance. A force sensor dynamic calibration method is also outlined to identify the test rig dynamic response and enable inference of dynamic rotor hub loads. Test rig control, measurement methodologies, and data reduction techniques are presented. Test rig validation compared against independent experimental studies is also presented.

Table 4.1 – Experimental operational parameter and uncertainty summary

Parameter	Range Considered	Uncertainty
N	500 - 1000 RPM	+/- 1 %
θ_{BL}	0 - 40°	+/- 1 – 4 °

4.2. Experimental Setup – Hovering Rotor

The test rig was mounted onto a stiff bespoke base and support pillar, as shown in figure 4.1, which is effectively a mini rotor whirl tower. This facilitated the testing of the rotor freestanding in an open space to reduce any wall effects. A T-type thermocouple was used to measure ambient temperature, and a digital barometer was used to measure atmospheric pressure in all test cases. This was used in the calculation of the air density used in the calculation of rotor non-dimensional coefficients. Uncertainties associated with these two parameters are measured within 0.05 bar for pressure and 0.5°C for temperature, respectively. The range of rotor speed and blade cyclic pitch amplitudes tested is outlined in table 4.1.

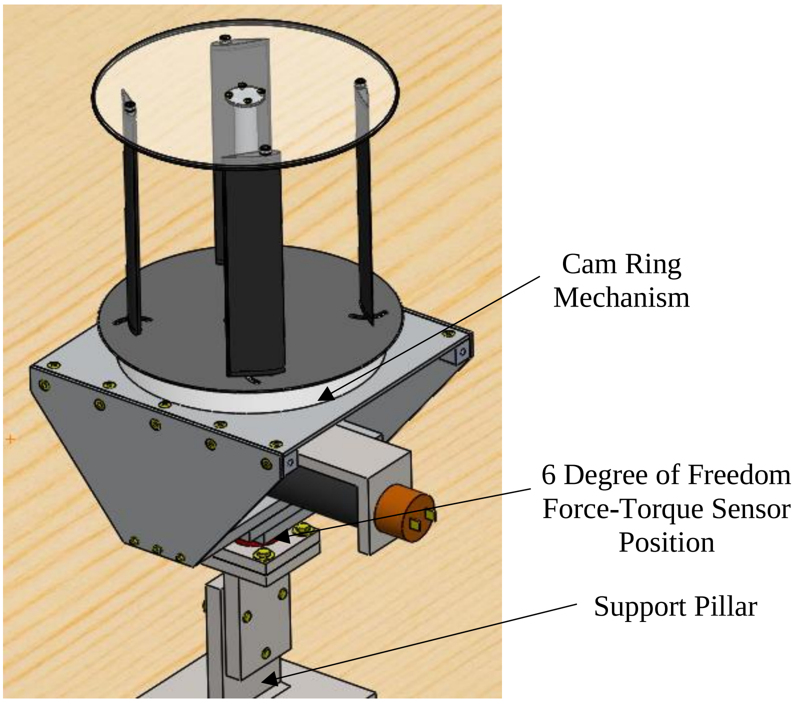

Figure 4.1 – Cycloidal rotor experimental setup

4.2.1. Test Rig Control

The blade cyclic pitch amplitude is controlled by changing the cam ring mechanism's eccentric point offset and phase angle. This is achieved through the movement of the cam ring mechanism in the X and Y measurement directions, as shown in figure 4.1. The relative amplitudes of the X and Y displacements govern the amplitude and phase of the blade cyclic pitch input. All test cases assume the maximum positive blade pitch amplitude occurs at an azimuth position of +90°, which coincides with the positive Y measurement direction. The design of the test rig facilitates an infinite variation of blade cyclic pitch amplitude and phase to be tested. This is achieved by using four 200-step stepper motors and four pairs of orthogonal linear slides driven through a low backlash bevel gear on each stepper motor to eliminate lost motion between moves.

The main control program contains a control loop to calculate the required X and Y movements based on the required pitch angle amplitude and phase input at the LCD control screen. The control program gives a linear movement resolution of 0.01 mm and facilitates a blade cyclic pitch angle input up to 45°. The movement of the cam ring mechanism to the desired test position was achieved through open-loop control of the stepper motors. To facilitate the use of open-loop control, 'datum position' limit switches were used in each measurement direction to calibrate the system daily before any tests were undertaken,

The blade cyclic pitch amplitude setpoint has an associated uncertainty due to errors in component manufacture and test rig setup. The overall error associated with each pitch angle setpoint was calculated using the methods defined by Moffat [109], where applicable, as summarized in table 4.1 and outlined in Appendix D.

The final series of tests performed to optimize the blade cyclic pitching schedule was tested on the same test rig setup, but the necessity to drive to a given pitch input was removed due to the use of individual cam mechanisms for each test point. The requirement to control the rotor rotational speed remained unchanged.

4.2.2. Rotor Test Procedure

Within the main Arduino control program, a cam mechanism datum cycle was defined for the X and Y measurement directions to set the pitching mechanism concentric with the rotor spindle to define the 0° blade cyclic pitch amplitude position. This was implemented at the start of each test session. The required blade cyclic pitch test point is then defined on the LCD control screen, and the cam mechanism is traversed to this point. The movement of the cam mechanism was not designed for 'on the fly' movements while the rotor was rotating to enable tare tests to be performed.

Tare tests were performed before and after each test for every test point, with the cam mechanism at the correct traversed position to eliminate the effect of sensor drift. Each test point was repeated three times and sampled for 45 seconds (45,000 samples), and tare tests were performed between runs. The rotor speed for each test is defined on the LCD control screen and implemented through a control loop. Data acquisition was started when the system's steady-state response was achieved.

A series of additional tests were performed with the rotor blades removed to calculate a set of aerodynamic tares at each rotational speed to determine the losses and profile power for the support structure only. The rotor power measured for the 'blade-on' case includes the rotor-induced power, profile power, and rotor structure flow losses. The aerodynamic tares compensate for this.

4.3. Hover Testing Data Reduction and Post-processing – Mean Rotor Performance

Before presenting the test data, data processing and reduction methodologies are presented to calculate the mean rotor performance. The experimental parameters investigated and presented in non-dimensional form are shown in table 4.2 with their associated uncertainty. A complete uncertainty methodology is provided in Appendix D.

Table 4.2 – Experimental non-dimensional coefficient summary

Parameter	Uncertainty
Coefficient of Thrust, C_T	+/- 15 %
Coefficient of Power, C_P	+/- 15 %

The raw measured force and torque data include both transient aerodynamic and inertial forces due to rotor rotation and blade pitching. Through time-averaging in MATLAB, all transient force components were eliminated. The mean rotor thrust, F_R, was calculated from the mean of the two orthogonal in-plane rotor force components F_x and F_y as shown in figure 4.2. The test data sets were averaged over the whole test duration, and the tare test data was subtracted for the relevant axes as required. The mean resultant rotor thrust F_R was calculated from

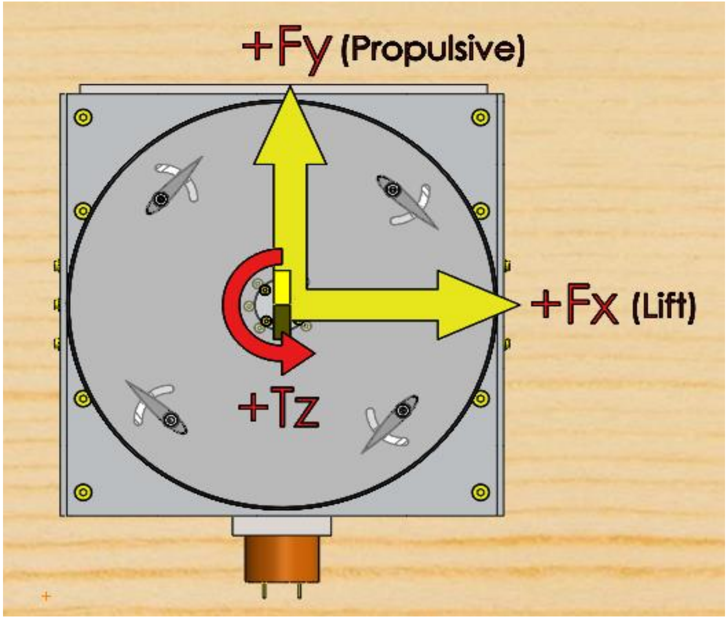

Figure 4.2 – Test rig measurement reference coordinate system

$$F_R = \sqrt{F_x^2 + F_y^2} \tag{4.1}$$

The rotor power was calculated from

$$P = Q\omega \tag{4.2}$$

where Q is the mean torque about the rotor spindle, and ω is the rotor angular velocity.

All results are presented as non-dimensional coefficients for comparison with independent studies, where C_T and C_P represent the Coefficient of Thrust and Power, respectively, defined by

$$C_T = \frac{T}{\rho_a A_R \omega^2 R^2} \tag{4.3}$$

and

$$C_P = \frac{P}{\rho_a A_R \omega^3 R^3} \tag{4.4}$$

where ρ_a is the air density, A_R is the rotor planform area, and R is the radius of the rotor.

4.4. Experimental Setup – Force Balance Dynamic Calibration

Strain gauge-based sensors like the iCUB sensor typically have a much lower stiffness than the test rig to which they are mounted. The sensor stiffness ensures that the required measurement resolution can be obtained. As a result, the system dynamic response can contain natural frequencies in the experimental measurement range of interest, making the characterization of the cycloidal rotor vibratory response difficult as the results at and close to these frequencies would be highly inaccurate.

To allow the measured dynamic forces to be corrected for the dynamics of the test rig, a dynamic sensor calibration needs to be completed. This requires that a transfer function or frequency response function (FRF) be developed relating hub loads to measurements at the iCUB force sensor.

The scale of the current test rotor ruled out the use of the available electromechanical shakers at the University of Bath, which were much too large to incorporate into a test setup. As a result, a bespoke shaker was designed and manufactured from a modified high-power speaker, as shown in figure 4.3 (a). The speaker is connected through a DC close-coupled amplifier connected to a PC and driven through the PC sound card. A bespoke MATLAB code was written to output the signal required to the amplifier. The shaker was connected at multiple rotor span positions via a piano wire stinger in series with a force sensor to the central rotor spindle to apply the known input force, as shown in figure 4.3 (b). The physical test setup is shown in figure 4.4.

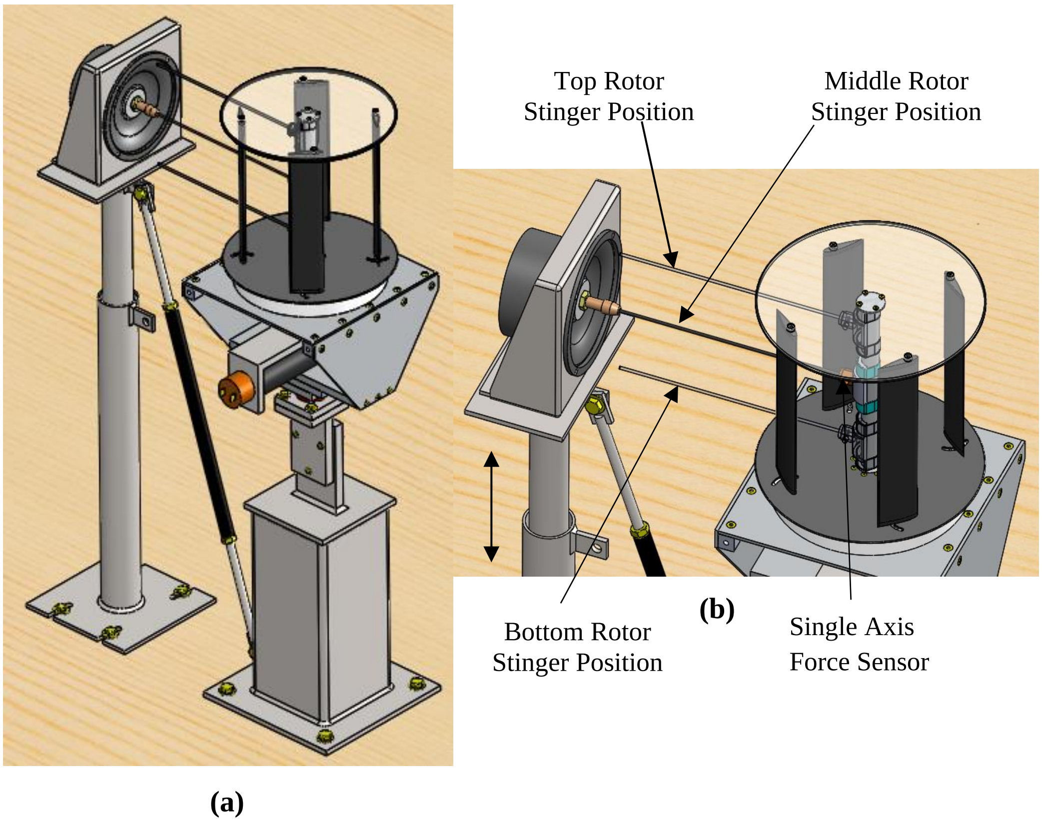

Figure 4.3 – Dynamic shaker testing experimental setup at varying rotor spanwise positions

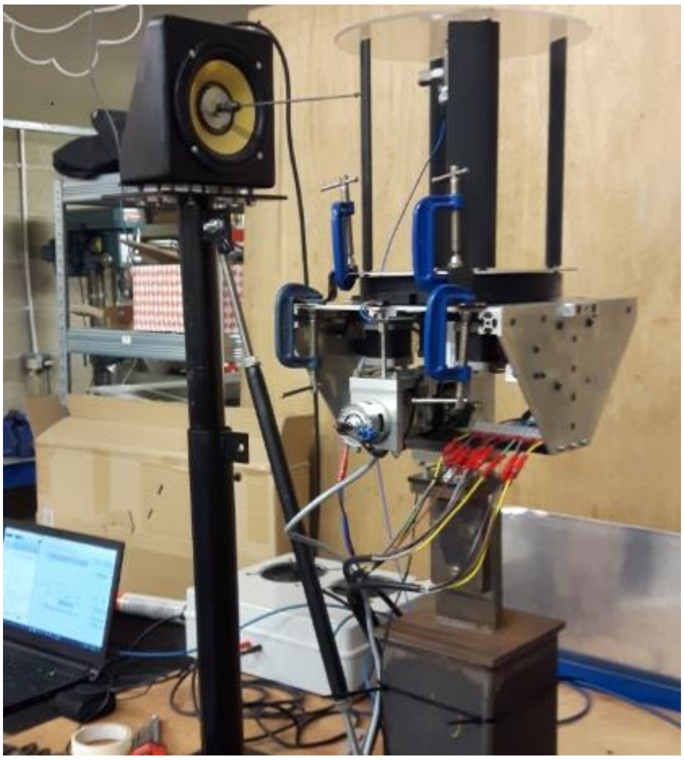

Figure 4.4 – Physical dynamic shaker testing experimental setup

The two in-plane rotor directions and rotor rotation axis were tested to consider the three principal rotor loading directions. Coupling between iCUB sensor axes was not considered, with each axis considered independent in line with independent studies by Russell [100,101]. For calibration of the rotor rotation axis, an additional torque arm was manufactured and attached to the central rotor spindle to apply the input force at a known offset position, as outlined in figure 4.5.

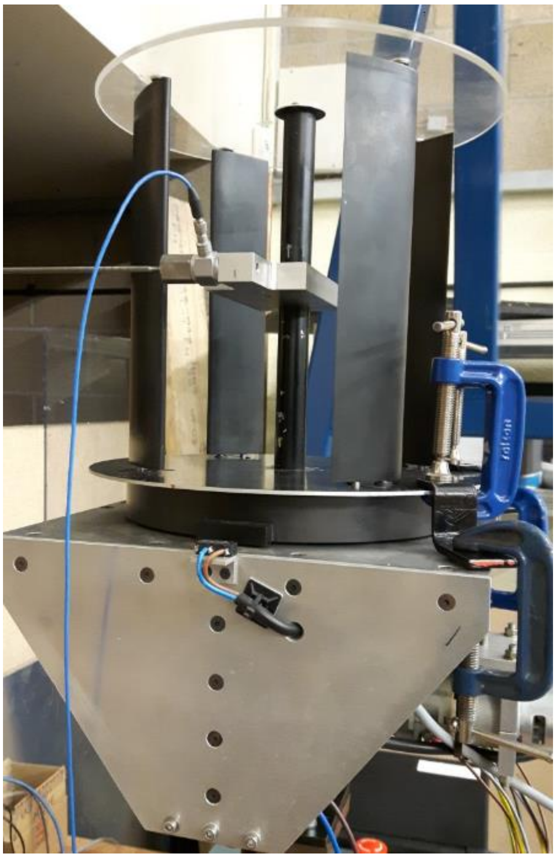

Figure 4.5 – Physical dynamic shaker testing experimental setup torque arm

4.4.1. Test Rig Instrumentation During Dynamic Calibration

The hardware used for the iCUB sensor dynamic calibration was as per the that used for the baseline rotor tests outlined in section 4.2.2, with two exceptions. Input force applied to the rotor via the stinger was measured with a PCB 208C02 force sensor, connected in series with the shaker and stinger system. The PCB sensor selected has an assembled resonant frequency of 36,000 Hz, so the sensor response should not be changed by its resonance frequency within the current test parameters. The PCB 208C02 was connected to a NI-9234 IEPE module within the cRIO chassis.

Input force data from the PCB 208C02 sensor and output sensor data from the iCUB sensor were measured simultaneously. Data acquisition of the two forces simultaneously enables accurate calculation of the amplitude and phase difference between the two signals. The PCB 208C02 single-axis force sensor has a resolution of 0.004 N. A full sensor specification is given in Appendix E.

4.4.2. Dynamic Calibration Test Procedure

All methods of dynamic calibration of this type require the same physical setup. The differences lie in the input force signal used and the associated results post-processing requirements. The input force can be periodic, random, pseudorandom, or transient. Selecting the most appropriate input force depends on the test equipment available and the testing requirements of the system. In all cases, the acquisition of force sensor signals of sufficient strength and clarity at low force level amplitudes can be difficult to measure accurately [110].

Discrete sine wave testing was adopted in line with [111] in conjunction with a stationary rotor to ensure that the input force applied via the stinger was constant throughout the frequency range of interest. During initial tests, the test frequency was stepped in 0.5 Hz increments from 0-134 Hz in separate tests to capture up to the 8/Rev harmonic response at the maximum rotor speed of 1,000 RPM. In follow-up tests, to investigate the rotor 12 and 16/Rev vibratory response for each rotor speed, shaker tests were conducted at the respective test point frequencies only. The two in-plane rotor directions and rotor rotation axis were tested similarly with the stinger connected to the central rotor shaft to consider all three principal rotor loading components.

The excitation's maximum peak-to-peak amplitude was kept to approximately ±5N, in line with the range of forces measured during normal rotor operation. Separate tests were also conducted in the same manner at varying excitation force amplitudes to establish the sensitivity of the system to input force variation, considered further in section 4.8.

Tare tests were performed before and after each 0.5 Hz test point increment to eliminate the effect of sensor drift and to allow for each discrete sine wave test to be post-processed separately. Each test point was sampled at a predetermined sample time to ensure that a minimum of 100 periods were captured for each test frequency, which for the lowest test frequency of 0.5 Hz was 200 seconds (200,000 samples). Data acquisition was started when the system's steady state was achieved to eliminate the effect of shaker start-up transience. Measurements were repeated three times to ensure repeatability and check that the test tig and measurement system was not changing during testing due to any loosening of components.

4.5. Dynamic Calibration Test Data Reduction and Post-processing

All results post-processing of the dynamic calibration test data was completed using bespoke MATLAB codes. The raw input and output force sensor signals were stored as discrete samples at each time step during the test. Each data set was then interpolated to ensure that the timestep between each data sample was equal. The data set for the input and output forces for each frequency were phase averaged over the whole data set initially to remove any noise in the signals and secondly to produce an input and output force signal that was exactly one period in length. Based on this, a Fast Fourier Transform (FFT) was undertaken on both the input and output force phase averaged data sets, and the phase and magnitude of each signal component were extracted.

A transfer function is used to describe the relationship between the output and input force components and is a complex-valued function that describes both magnitude and phase. The magnitude of the transfer function is defined as the ratio of the output and input signal magnitude given by

$$|H(\omega)| = \frac{|F|}{|G|} \tag{4.5}$$

Where the amplitude $|F|$ and $|G|$ represent the magnitude of the output and input force signal, respectively, from the FFT analysis. The shaker input force signal phase angle $\angle G$ is then subtracted from the output force signal phase angle $\angle F$ to give the phase difference between the input and output signals to correct for phase, $\angle H$ defined as

$$\angle H = \angle \mathrm{F} - \angle \mathrm{G} \tag{4.6}$$

Importantly equations 4.5 and 4.6 can only be used to determine the magnitude and phase at one single frequency at a time, in line with Heachcote [111]. The same analysis methodology was used for each discrete test point in each of the three rotor loading directions in turn to enable the magnitude of the transfer function and phase difference to be generated.

4.6. Hover Testing Data Reduction and Post-processing – Dynamically Corrected Rotor Loads

Each data set used for the calculation of the mean rotor performance was reanalyzed to calculate the rotor vibratory response. For each test undertaken to consider rotor speed and blade cyclic pitch input, the experimental data in the X and Y measurement directions and rotor rotation axis were phase averaged similarly to section 4.5 to produce the resulting rotor vibratory response over one rotation in the three axes. From this, a Fast Fourier Transform (FFT) was undertaken, and the magnitude and phase of each signal were extracted for the first 16 rotor harmonics from 1/Rev to 16/Rev.

The magnitude and phase are defined as $|\mathrm{F_n}|$ and $\angle \mathrm{F_n}$, respectively, where n represents the harmonic of interest in the loading direction required. Rearranging equations 4.5 and 4.6 to calculate the rotor input force magnitude $|\mathrm{G_n}|$ and phase $\angle \mathrm{G_n}$ to correct for the test rig dynamic response at the harmonic of interest yields

$$|\mathrm{G_n}| = |\mathrm{H_n}(\omega)|^{-1} \times |\mathrm{F_n}| \tag{4.7}$$

and

$$\angle \mathrm{G_n} = \angle \mathrm{F_n} - \angle \mathrm{H_n} \tag{4.8}$$

Where $|\mathrm{H_n}(\omega)|$ and $\angle \mathrm{H_n}$ are the transfer function amplitude and phase difference at the required dynamic calibration test point corresponding to the n/Rev harmonic.

The amplitudes of the corrected force measurements at each discrete harmonic from 1/Rev to 16/Rev, obtained from equation 4.7, were converted to non-dimensional coefficients using equation 4.3. The amplitude of the respective harmonic was substituted into equation 4.3 as the value of T. Non-dimensionalising the amplitude of each harmonic aided further results analysis across multiple test points at varying rotor rotational speeds.

4.7. Test Rig Mean Results Validation

4.7.1. Test Rig Problems and Their Solutions

Once built, the commissioning of the test rig was an iterative process. Early on, multiple cycles of hover testing were undertaken to validate the mean rotor force components. Testing provided insight into the test rig operation and highlighted areas of the test rig operation that required further investigation due to inconsistency in mean results. Following results processing at a cyclic blade pitch amplitude of 40° from 500 to 1,000 RPM, a dominant 15/Rev vibratory response was noted in all cases, as shown in figure 4.6 for a rotational speed of 500 RPM. The 15/Rev vibratory response was identified by undertaking an FFT on the measured force data. The results of the FFT performed on the data in figure 4.6 are shown in figure 4.7, which clearly shows a dominant system response at the 15/Rev harmonic.

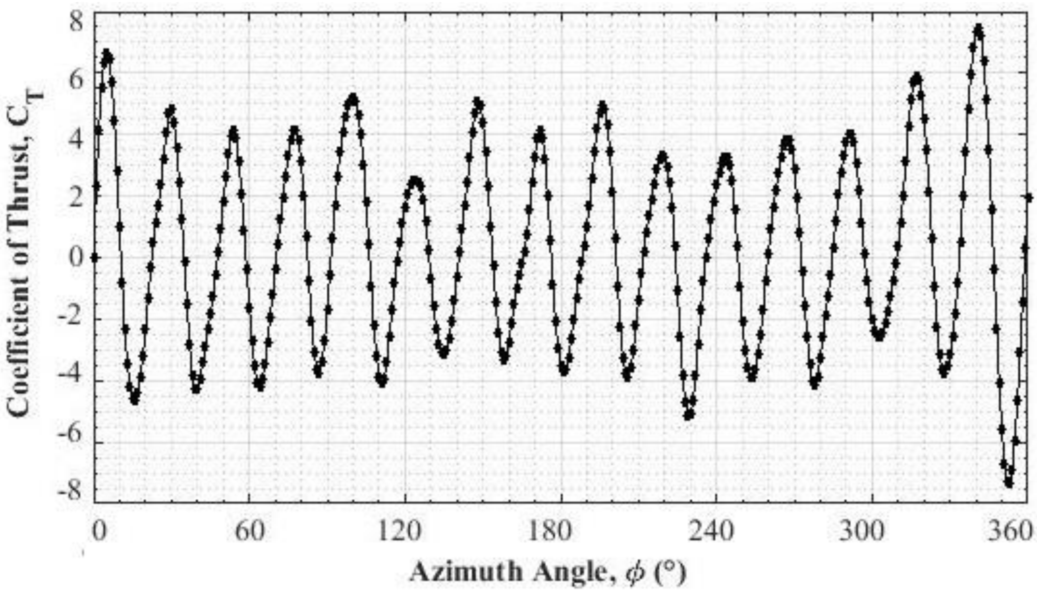

Figure 4.6 – Rotor resultant instantaneous Coefficient of Thrust at N = 500 RPM and a blade cyclic pitch angle of 40°

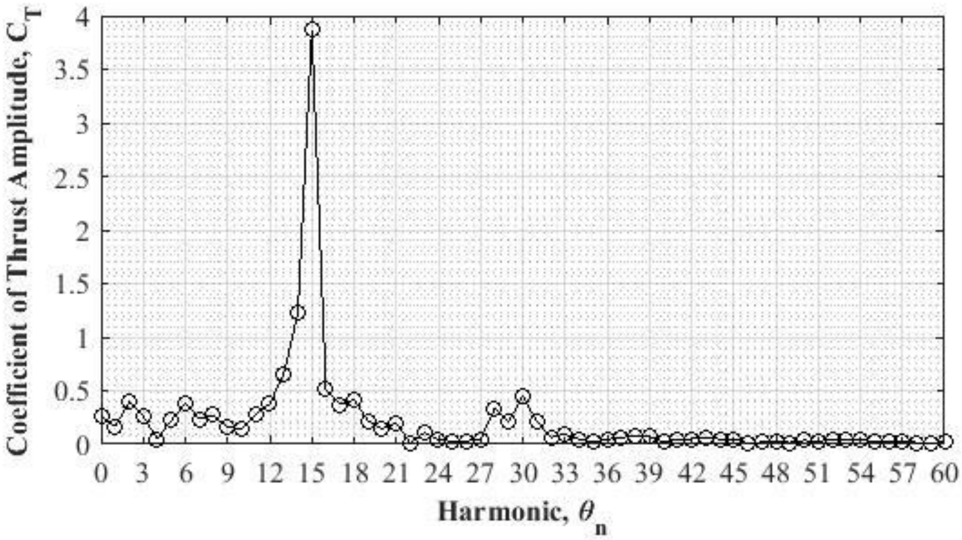

Figure 4.7 – Rotor resultant instantaneous Coefficient of Thrust amplitude at discrete rotor harmonics at N = 500 RPM and a blade cyclic pitch angle of 40°

A full analysis of the test rig driveline and rolling element frequencies, as shown in tables 4.3 and 4.4, confirmed that the 15/Rev response was due to the excessive backlash due to the drive gearing tooth mesh frequency. A bearing housing redesign allowed for accurate setting of gear backlash and reduced the 15/Rev vibratory response in the X and Y measurement directions by up to 90%.

Table 4.3 – Test rig driveline frequency harmonic summary

Parameter	Rotor Harmonic, N/rev
Rotor Gear Frequency	1
Rotor Pinion Frequency	1/3
Drive Gearing Tooth Mesh Frequency	15
Drive Gearing Assembly Phase Frequency	5
Drive Gearing Tooth Repeat Frequency	1/15
Main Drive Motor Frequency	7.05
Main Drive Motor Gearbox Frequency	10.22

Table 4.4 – Test rig rolling element bearing frequency harmonic summary

Parameter	Rotor Harmonic, N/rev
Rotor Spindle Bearing Fundamental Train Frequency	0.397
Rotor Spindle Bearing Ball Pass Frequency Inner Race	4.82
Rotor Spindle Bearing Ball Pass Frequency Outer Race	3.18
Rotor Spindle Bearing Ball Spin Frequency	2.022
Motor Spindle Bearing Fundamental Train Frequency	0.14
Motor Spindle Bearing Ball Pass Frequency Inner Race	1.931
Motor Spindle Bearing Ball Pass Frequency Outer Race	1.402
Motor Spindle Bearing Ball Spin Frequency	0.887

4.7.2. Initial Hover Testing Validation

Benedict [4] showed that rotor thrust is proportional to the square of rotor speed, and power is proportional to the cube of rotor speed for a hovering rotor. For a given blade cyclic pitch amplitude input, the thrust and power non-dimensional coefficients should thus be constant when plotted against changes in rotor rotational speed. Rotor thrust and power coefficients were plotted for two independent experimental studies [46,112] for a three and four-bladed rotor in hover, as shown in figure 4.8 and figure 4.9. Both studies confirm this trend and give confidence in using this as a basis for mean results validation. Figure 4.8 is recreated from the data supplied in [112] in non-dimensional form. No data was presented between a rotational speed of 900 RPM and 1,200 RPM, with no explanation as to why it was omitted given.

Non-dimensional coefficients for the current test rig are shown in figures 4.10 (a) to 4.10 (d), outlining the change in rotor thrust components and power, respectively, for increasing blade cyclic pitch amplitude input. The 'Measured Extent 'in figure 4.10 (a) to figure 4.10 (d) represents the change in results with changes in rotor rotational speed from 500 to 1,000 RPM at a set blade cyclic pitch angle input. It is important to note that 500 RPM does not necessarily represent the minimum, and 1,000 RPM is not necessarily the maximum data point presented. The uncertainty associated with the non-dimensional parameters is shown in table 4.2.

The small deviation in the coefficients at each value of blade cyclic pitch amplitude illustrates that the non-dimensional coefficients approximate a straight line when converted to non-dimensional coefficients, confirming the expected behavior in line with [46,112]. However, there are some discrepancies in the data presented in figure 4.10, and it is important to caveat that the straight-line linear assumption is only valid for attached flow and assumes that there is no major flow separation from the rotor blades. This means the system is assumed to operate within the linear force characteristics range for the aerofoils used.

The rotor rotational speeds considered between 500 RPM and 1,000 RPM represent a blade chordwise Reynolds number variation between 17,325 and 34,650 for the current test rig blade chord of 50mm, respectively, which is well below the typical NACA 4-digit transition Reynolds number of 1×10^5 [113]. Based on the range of Reynolds numbers considered, there is no significant change in the separation effect with increasing rotor rotational speed, as confirmed by the small results deviation presented in figure 4.10 at each blade cyclic pitch angle. The small deviation presented shows that there is very little Reynolds number effect across the range of results considered.

Further analysis of the non-dimensional coefficients for the current test rig in figures 4.10 (a) to 4.10 (d) shows that X direction (propulsive) thrust in figure 4.10 (a) increases linearly with changes in blade cyclic pitch angle up to a maximum of 0.1 at 40°. Conversely, at blade cyclic pitch angles between 0° and 10°, the rotor produces a negative thrust in the Y direction (lift). A reason for this is attributable to manufacturing tolerances and inaccuracies

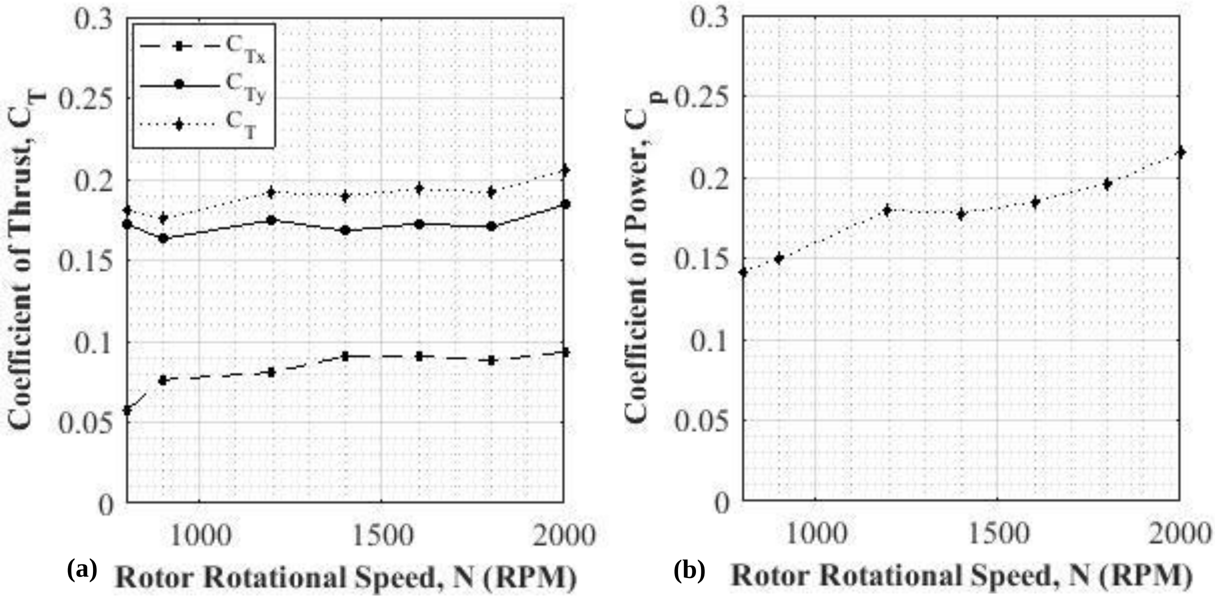

Figure 4.8 – Independent experimental mean performance parameters for a three-blade cycloidal rotor [112] with a blade cyclic pitch angle input of 40° and a blade chord of 25.4mm. The rotor diameter of 152mm, and the rotor span of 152mm

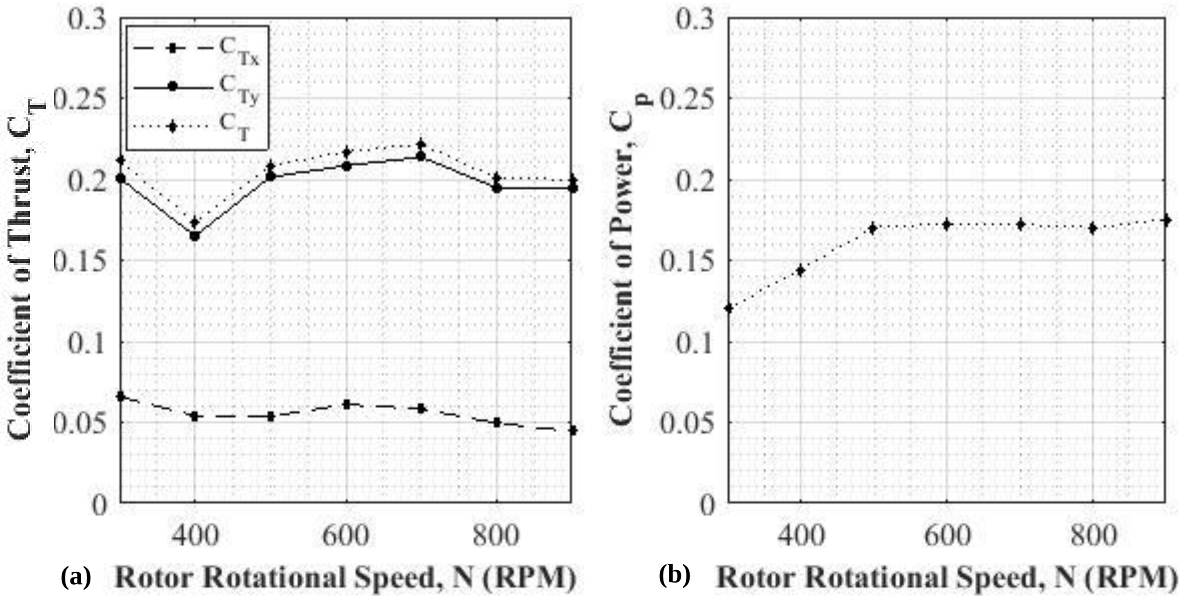

Figure 4.9 – Independent experimental mean performance parameters for a four-blade cycloidal rotor [46] with a blade cyclic pitch angle input of 45° and a blade chord of 70mm. The rotor diameter of 360mm, and the rotor span of 270mm

As expected, the resultant thrust increases with an increased blade cyclic pitch angle. At cyclic pitch angles greater than 35°, the rate of change of the coefficient of thrust reduces and appears to be approaching a maximum, as shown in figure 4.10 (c). The coefficient of power also increases with increasing blade cyclic pitch amplitude up to a maximum of 0.28 at 40° cyclic pitch input, as shown in figure 4.10 (d). The rate of change of the coefficient of power increases above a cyclic pitch angle of 25° when compared to lower values, attributable to blade profile drag increase with potential flow separation and dynamic stall

4.8. Analysis of Dynamic Calibration Results

The frequency response functions for the system in the X, Y, and Z-axis measurement directions with the excitation applied at the rotor center span are outlined in figures 4.11 to 4.13 for amplitude ratio and phase. Figure 4.11 (a) shows several narrowband un-damped resonance peaks in the system response, with the first X-direction natural frequency at around 11.66 Hz, followed by an anti-resonance at 12 Hz. A second natural frequency mode is predicted at 18 Hz with an amplitude ratio of approximately 40. The rapid change in phase angle at these positions again indicates resonance identified in figure 4.11 (b).

Two higher-order natural frequencies are calculated at 46.66 Hz and 53.33 Hz, corresponding to the 4/Rev vibratory response at 700 RPM and 800 RPM. However, the amplitude ratios are significantly reduced at these positions. In the X and Y measurement directions, the characteristics of the system are similar in terms of both fundamental natural frequencies and the presence of undamped resonance peaks, as shown in figures 4.12 (a) and 4.12 (b).

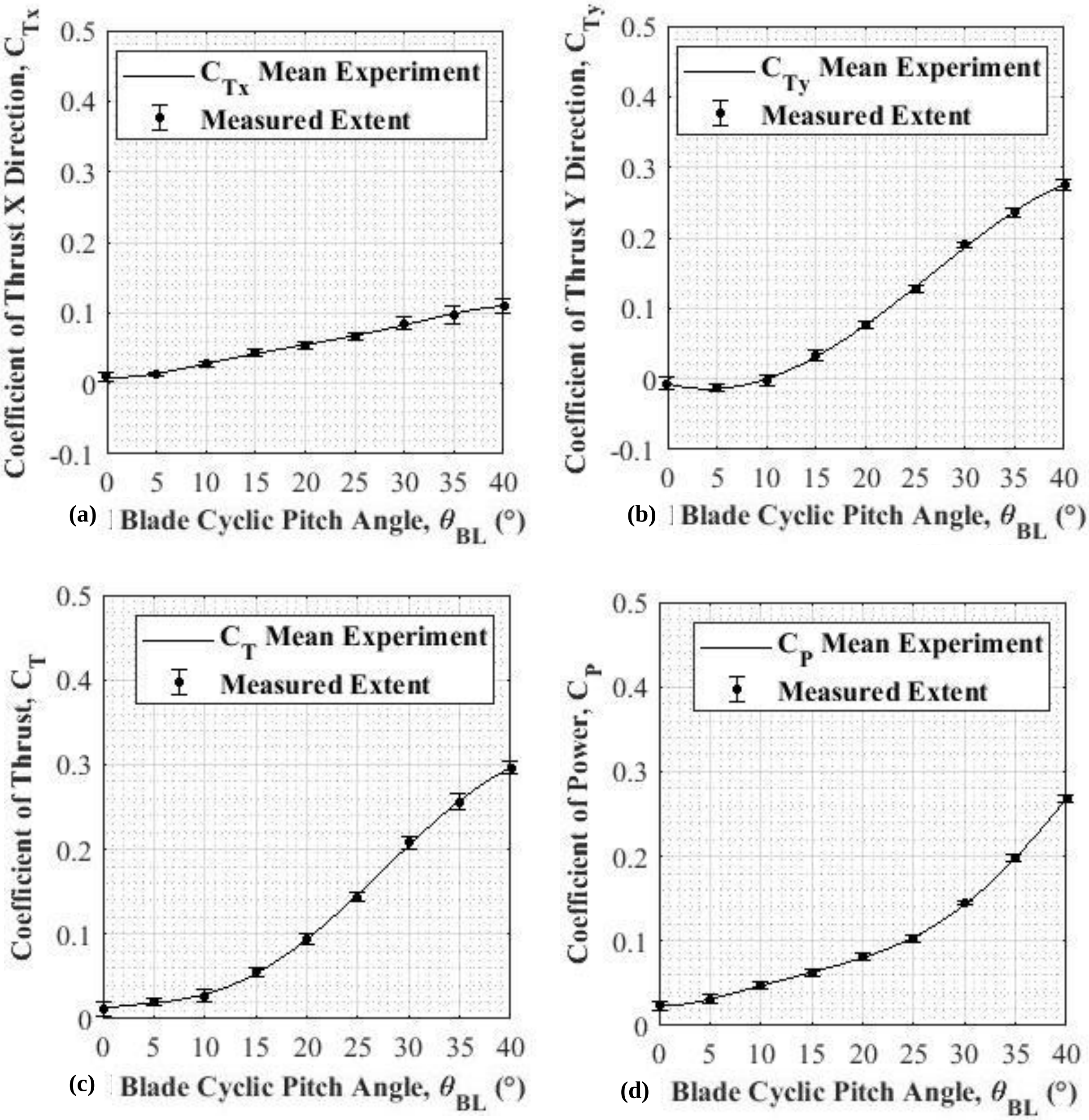

Figure 4.10 – Rotor mean rotor performance coefficients in hover with measured extents shown from 500 to 1,000 RPM

There is increased damping in the Z-axis measurement direction, with secondary peaks shown around 14 to 16 Hz, illustrated in figure 4.13 (a). The first torsional frequency mode is calculated at 53.33 Hz, corresponding to the 4/Rev vibratory response at 800 RPM with an amplitude ratio of approximately 3. The results close to 12 to 18 Hz presented in the X and Y-measurement directions typically fall within the rotor 0-1/Rev range, depending on rotational speed. However, they are outside the range required in the final rotor vibratory response analysis at harmonics of the blade pass frequency.

The application of the excitation force in similar test setups [100,101] is applied at a single point. In reality, the aerodynamic and inertial forces are spread across the full rotor span, which is a limitation of any shaker testing setup. Frequency response function variation in each direction to changes in rotor span excitation position is shown in figures 4.14 (a) to 4.14 (c). Variation is identified with spanwise location, but the central span position is a reasonable approximation of the mean of the two positional extremes. Variations in the magnitude of the excitation force were also investigated at the center span position. The calculated frequency response function changes at the frequencies of interest were typically ±2%.

The presence of a number of un-damped resonant modes in the system makes the determination of in-plane loads close to resonance difficult, if not impossible, due to the high level of measurement nonlinearity. Therefore, all results are slightly unreliable within this range. Close to these frequencies, measurements have a higher uncertainty than conditions away from resonance. This was corroborated by Heathcote [111], who analyzed the response of an oscillating aerofoil force balance. The amplitude ratio uncertainty was typically ±5%, increasing to ±18% at resonance. Similarly, for phase, the uncertainty was typically ±2° and ±45° at resonance.

In the presentation of the phase angle data for the iCUB sensor dynamic calibration, there are some rapid changes in phase angle between adjacent measurement points. An example is shown in figure 4.12 (b) around 12 Hz. While the results presented are specific to the current test rig, rapid changes in phase angle are associated with system resonance and anti-resonance. They correspond to the resonant and anti-resonant points shown in figure 4.12 (a) at the same frequency. This is not an uncommon occurrence for such as system. A similar analysis was undertaken by Peterson [99], as shown in figure 4.15, for a standard rotorcraft setup that shows phase angle variation of +/-180° at resonance.

A Total Harmonic Distortion (THD) analysis of the input and output force sensor signals was undertaken, as shown in figures 4.16 (a) to 4.16 (c), to ascertain the extent of nonlinearity in the system. Where system nonlinearity makes the transfer functions change at different excitation amplitudes. The THD analysis calculates the distortion in the measured signals relative to a pure sinewave. It is typically used in audio equipment where it should be kept as low as possible to improve accuracy, but a 10% threshold is generally used.

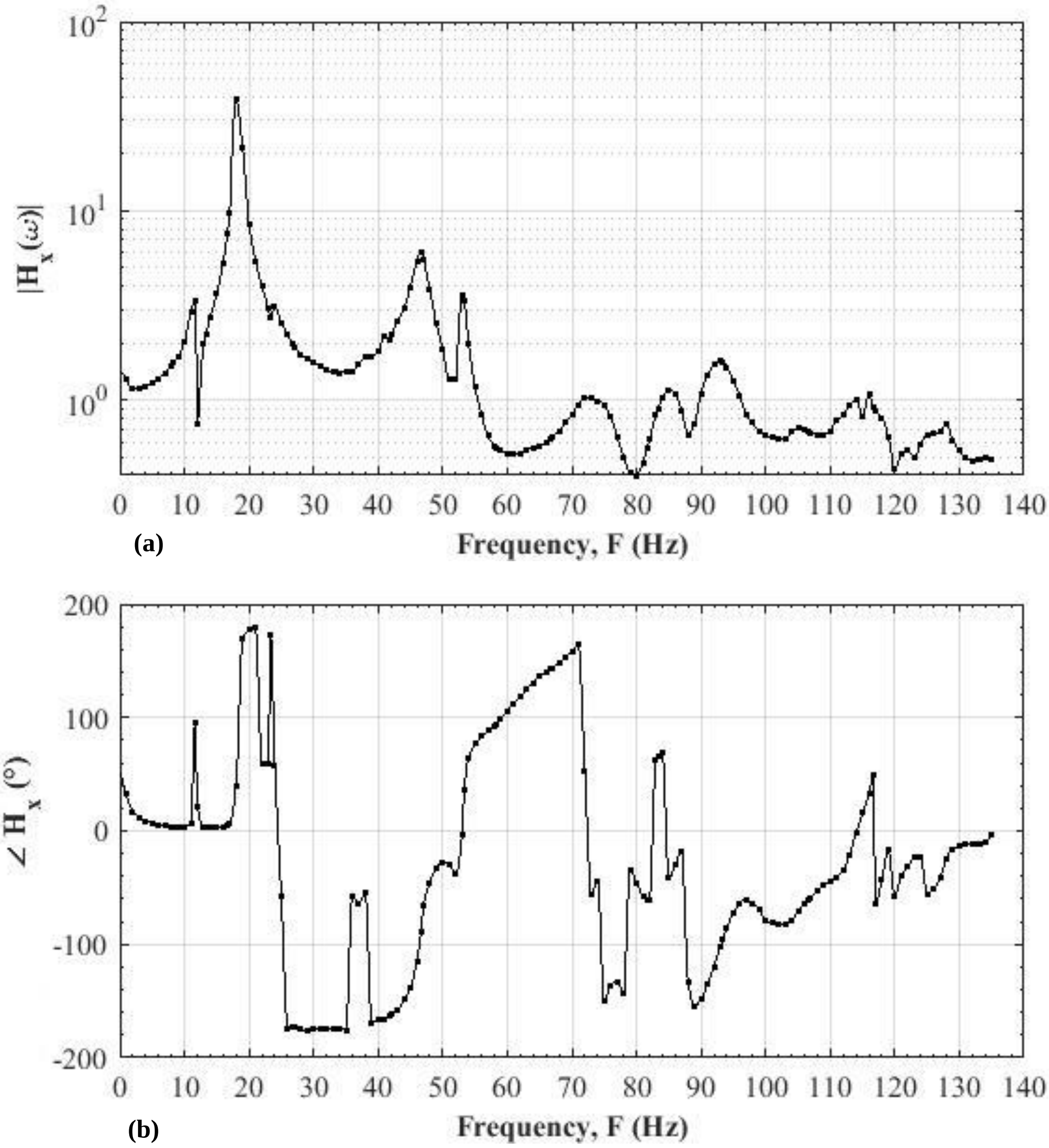

Figure 4.11 – Force sensor dynamic calibration frequency response function (a) Magnitude and (b) Phase in the force measurement X-direction

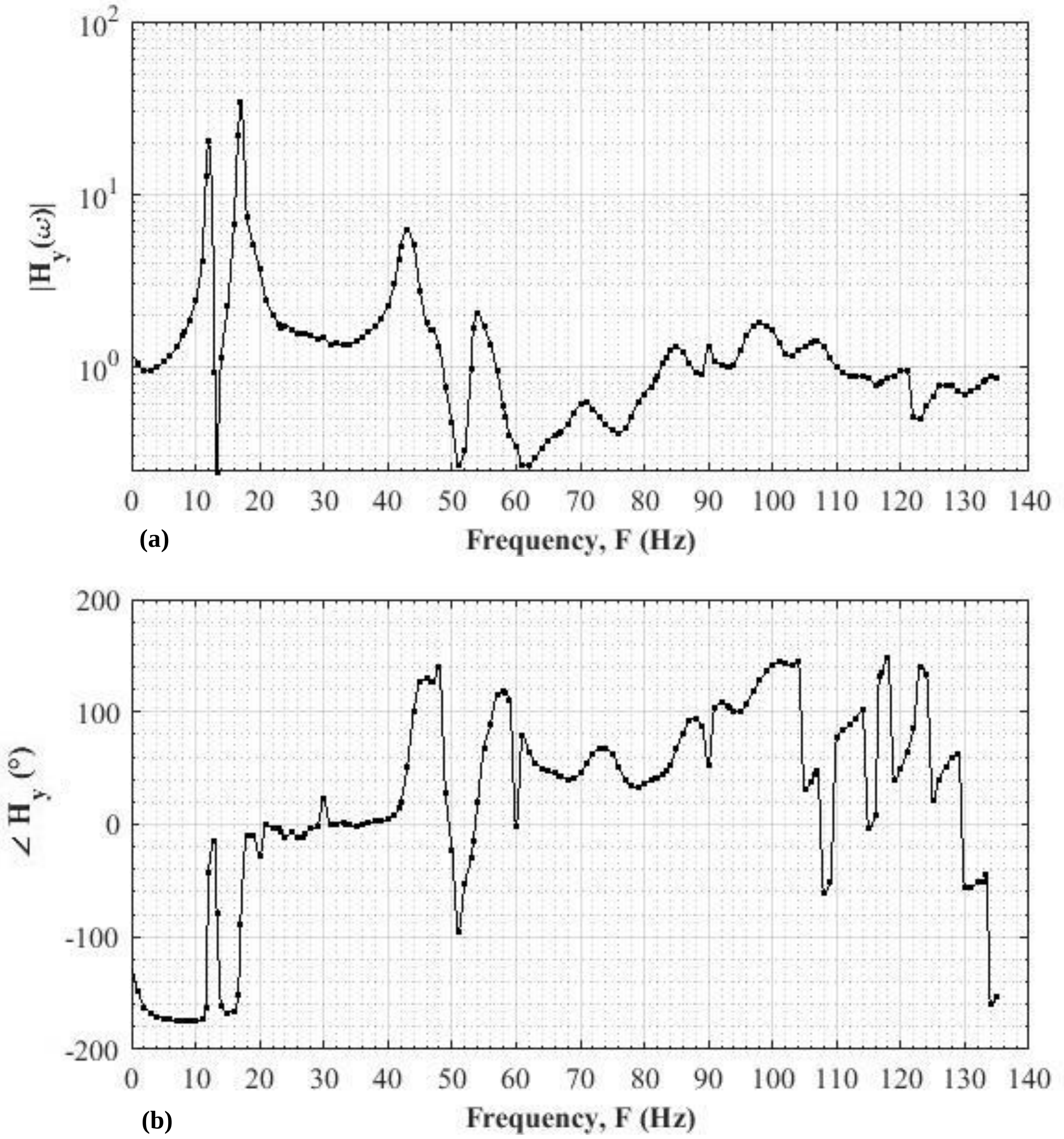

Figure 4.12 – Force sensor dynamic calibration frequency response function (a) Magnitude and (b) Phase in the force measurement Y-direction

The THD analysis aligned with the vibration tests, with significant THD up to 20% calculated in the output signal close to resonance peaks at 12-18 Hz in the X and Y measurement directions as per figures 4.16 (a) and 4.16 (b), which reduces to 11% in the Z-axis direction in figure 4.16 (c) at resonance. All cases confirm nonlinearity in the system in the regions at high response levels close to resonance. The THD value is between 0-2% for both the input and output signal outside of the resonance peaks, indicating that the system can be taken to be linear away from the resonance regions.

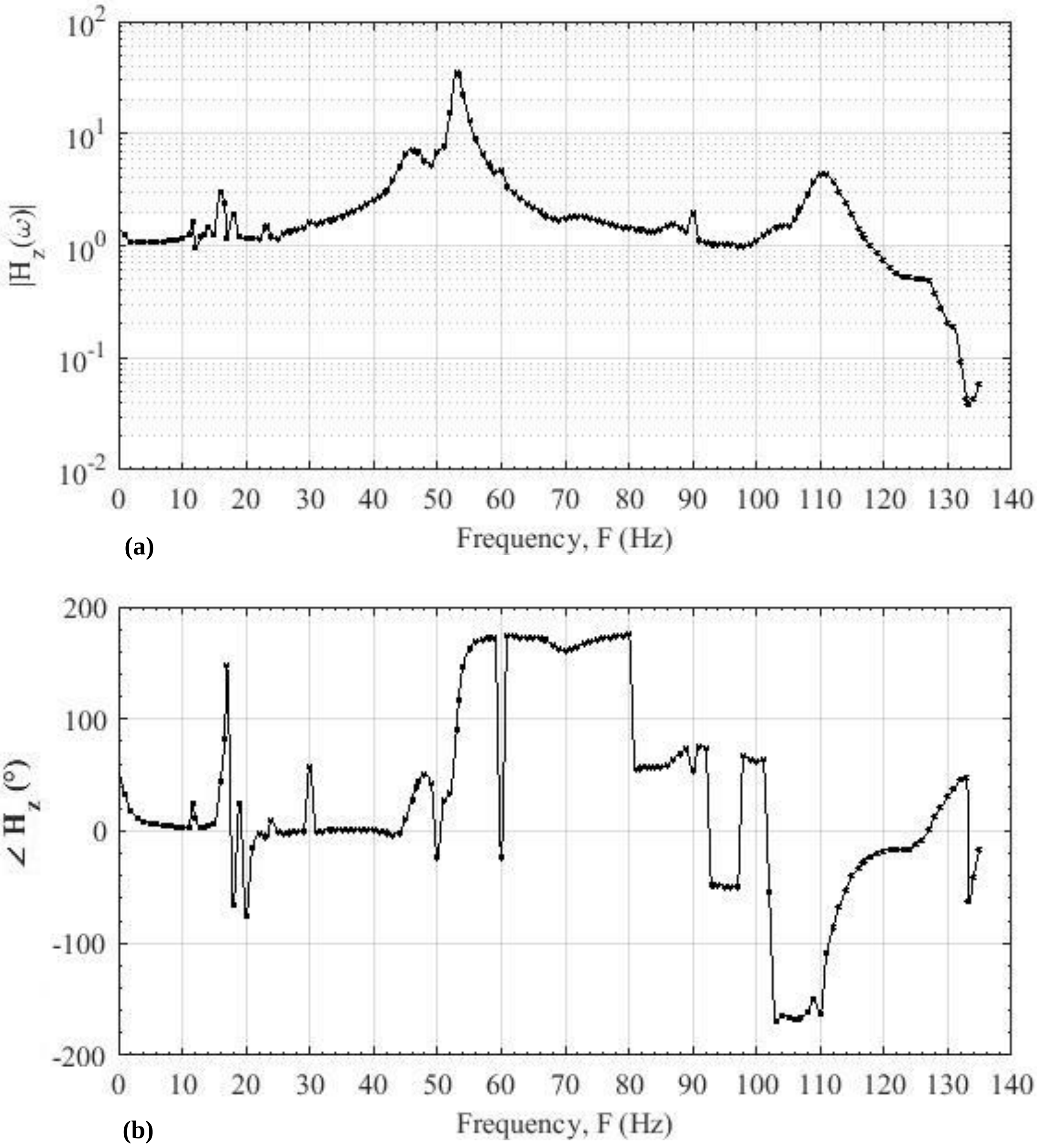

Figure 4.13 – Force sensor dynamic calibration frequency response function (a) Magnitude and (b) Phase in the torque measurement Z-axis direction

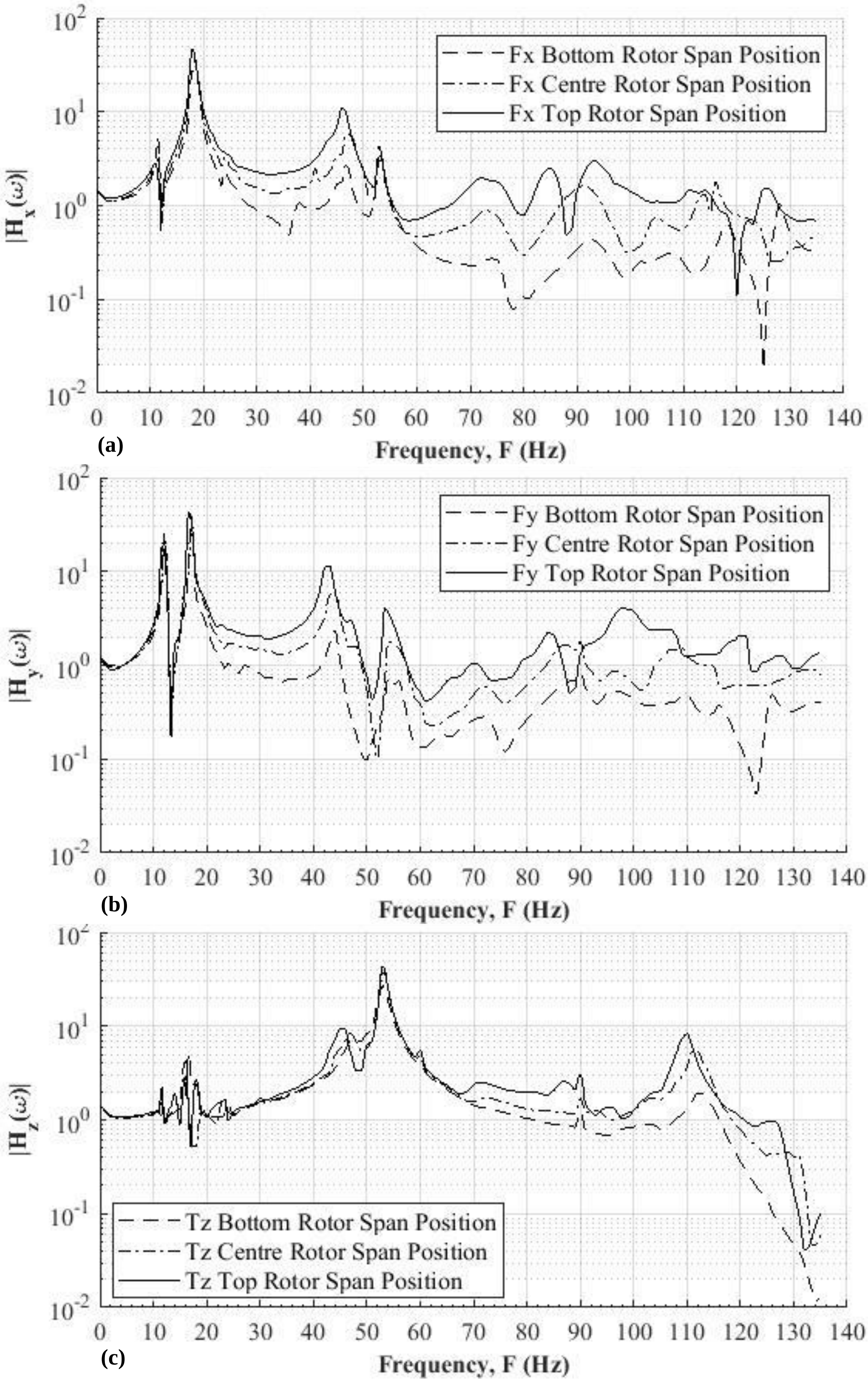

Figure 4.14 – Force sensor dynamic calibration frequency response function variation in spanwise stinger position (a) X-direction (b) Y-direction (c) Z-axis direction

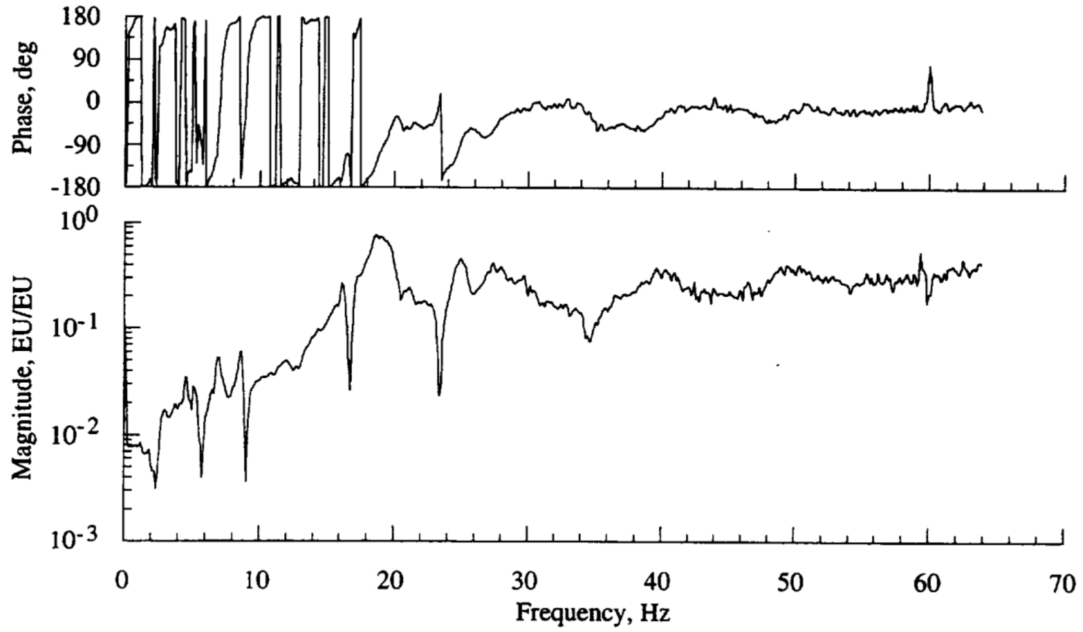

Figure 4.15 – An Example of dynamic calibration frequency response function for the NASA Ames Rotor Test Apparatus Rotor Balance [99]

4.9. Chapter Review

The current chapter has outlined the methods used to validate the design of the current test rig and measure the cycloidal rotor vibratory response. The need to perform a force sensor dynamic calibration is confirmed, and the 1D dynamic calibration transfer function approach is shown to be satisfactory for assessing vibratory loads. But the study has shown that there is no simple way of measuring and adjusting phase-averaged dynamic load data, particularly close to system resonances, in line with findings from standard rotorcraft studies [100]. Away from resonance, however, the results are found to be a reliable indicator of hub loading.

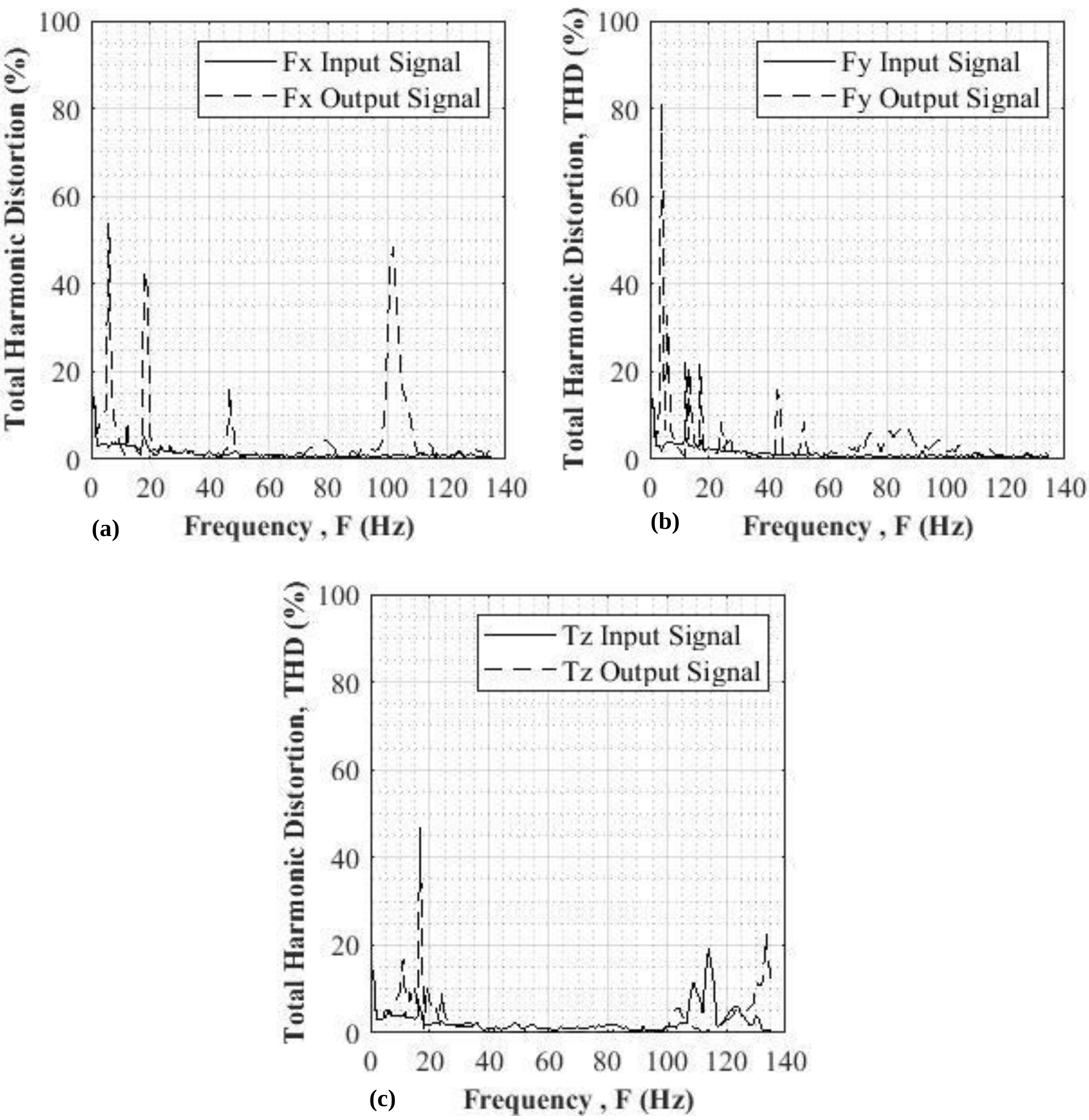

Figure 4.16 – Total harmonic distortion analysis of the input and output force sensor signals in the three measurement directions (a) X-direction (b) Y-direction (c) Z-axis direction

Chapter 5 – Blade Element Theory Code (BET code) Development and Validation

5.1. Introduction

The current chapter initially gives a brief overview of previous independent cycloidal rotor aerodynamic models that have been investigated. This is followed by a description of the aerodynamic code developed in the present study and any modeling assumptions. The current study aims to develop a reduced-order computational model to include the rotor unsteady aerodynamics that can calculate rotor mean performance, blade loads, and rotor vibratory response with sufficient accuracy over a range of blade cyclic pitch amplitudes and rotational speeds so that it can be used as a means of performing preliminary calculations in the early stages of craft design.

Higher fidelity modeling approaches such as comprehensive analysis and CFD in both 2D and 3D can be used to capture rotor flow features such as blade wake interactions and dynamic stall with increased accuracy. But both have the disadvantage of increased setup and run times that can be prohibitive in the early design stages. A CFD study will be undertaken here as well, described in the next chapter.

5.2. Independent Cycloidal Rotor Aerodynamic Model Development

In recent years there have been a number of attempts to model the mean performance of the cycloidal rotor at changing blade cyclic pitch amplitude and rotational speeds, with no clear recommended method of analysis. Most [4, 32, 34] have used helicopter momentum theory, where the blade-induced velocity at each blade is dependent on the resultant rotor thrust. An iterative process is used to calculate the individual blade lift and drag loads based on stream tube theory. The lift and drag forces with changes in azimuth position are then summed over each blade to determine rotor performance.

Benedict [4] used single and multiple stream tube models to model rotor mean performance. The upper and lower halves of the rotor were initially considered as one continuous stream tube and, secondly, as two separate actuator discs to represent the upper and lower halves of the rotor separately in an attempt to model the wake. It was found that both approaches modeled the mean rotor performance with reasonable accuracy when compared to CFD and experimental studies undertaken [4]. However, the single-stream tube model overpredicted the propulsive (side) force component for the hovering rotor in the lower half of the rotor. This was thought to be due to the inflow remaining constant with changing azimuth position in the single-stream tube model, but this was not confirmed.

Wheatley [8] was one of the first to assess cycloidal rotor performance based on static aerofoil theory at each azimuth position, ignoring the physical oscillation of the blades. Using this basic approach from [8], McNabb [34] incorporated unsteady aerodynamic effects to take account of the blade oscillation, angular rotation, and acceleration. 2D unsteady lift and moment equations from Garrick [114] were assumed to model a blade moving in a sinusoidal motion, ignoring any 3D flow effects. The equations in [114] are based on the reduced frequency of the oscillation. It was concluded that the inclusion of unsteady effects showed a marked improvement in the correlation with experimental data over the range of blade cyclic pitch angles considered.

Utilizing the methods developed by McNabb [34], Xisto et al. [32] analyzed a six-blade NACA 0012 rotor with an aspect ratio of one and a diameter of 1.2m. It was noted that the inclusion of rotor inflow significantly reduces the calculated thrust values due to the inflow reducing the blade effective AOA.

All of the methods described are 2D modeling techniques that are very similar in approach and benefit from increased computational efficiency. With 3D flow effects ignored in the main, their ability to model rotor blade instantaneous force and vibratory response is unknown, despite modeling mean rotor performance with reasonable accuracy. In an attempt to improve model accuracy and model 3D effects, Tang et al. [115] are the first to implement an unsteady free wake model, representing the wake as a number of shed and trailing vortex filaments. The model makes use of momentum theory in conjunction with the Leishman–Beddoes semi-empirical dynamic stall model, coupled with the free-wake model. The calculation process has two parts where the uniform rotor inflow model is used initially to calculate the induced velocity for the free wake model for the initial time step. Compared to CFD and experimental data, the mean rotor performance is in very good agreement, but the thrust is over-predicted in some instances. Instantaneous blade forces between the CFD and free wake model show qualitative agreement, but the improvement in rotor vibratory response calculation compared to the 2D modeling methods is difficult to assess due to insufficient data.

Studies to date have utilized momentum theory to model the ideal cycloidal rotor performance predictions similarly to standard helicopter analyses. Using a uniform-induced velocity assumption has typically been used to reduce computational overhead and allow a first-order prediction of the rotor thrust that can be used to form the foundations of higher-order aerodynamic analyses.

An axial inflow model is not fully appropriate for a cycloidal rotor as the flow is substantially different from a standard rotorcraft, particularly when the rotor is analyzed under forward flight operation. The cycloidal rotor induces a rotational circulation like a helicopter inflow, but the inflow axis is rotated. The Magnus-induced circulation is ignored in the axial inflow model, which is also an assumption in forward flight, where the circulatory AOA component is not considered. This emphasizes the need to develop specific inflow models for cycloidal rotors, particularly in forward flight.

The inflow models are usually formulated based on experimental results or more advanced vortex theories, taking into account the effects of the individual tip vortices and rotor wake that tend to produce a highly nonuniform inflow over the rotor. The development of cycloidal rotor-specific inflow models will enable the performance of the rotor to be analyzed with the aid of simpler inflow models that will represent the basic effects of the cycloidal rotor inflow resulting from the tip vortices and rotor wake.

5.3. Current Aerodynamic Code Development

A flow diagram has been developed, as shown in figure 5.1, to outline how the cycloidal rotor aerodynamic performance is calculated and to define the architecture of the aerodynamic model developed in the present chapter.

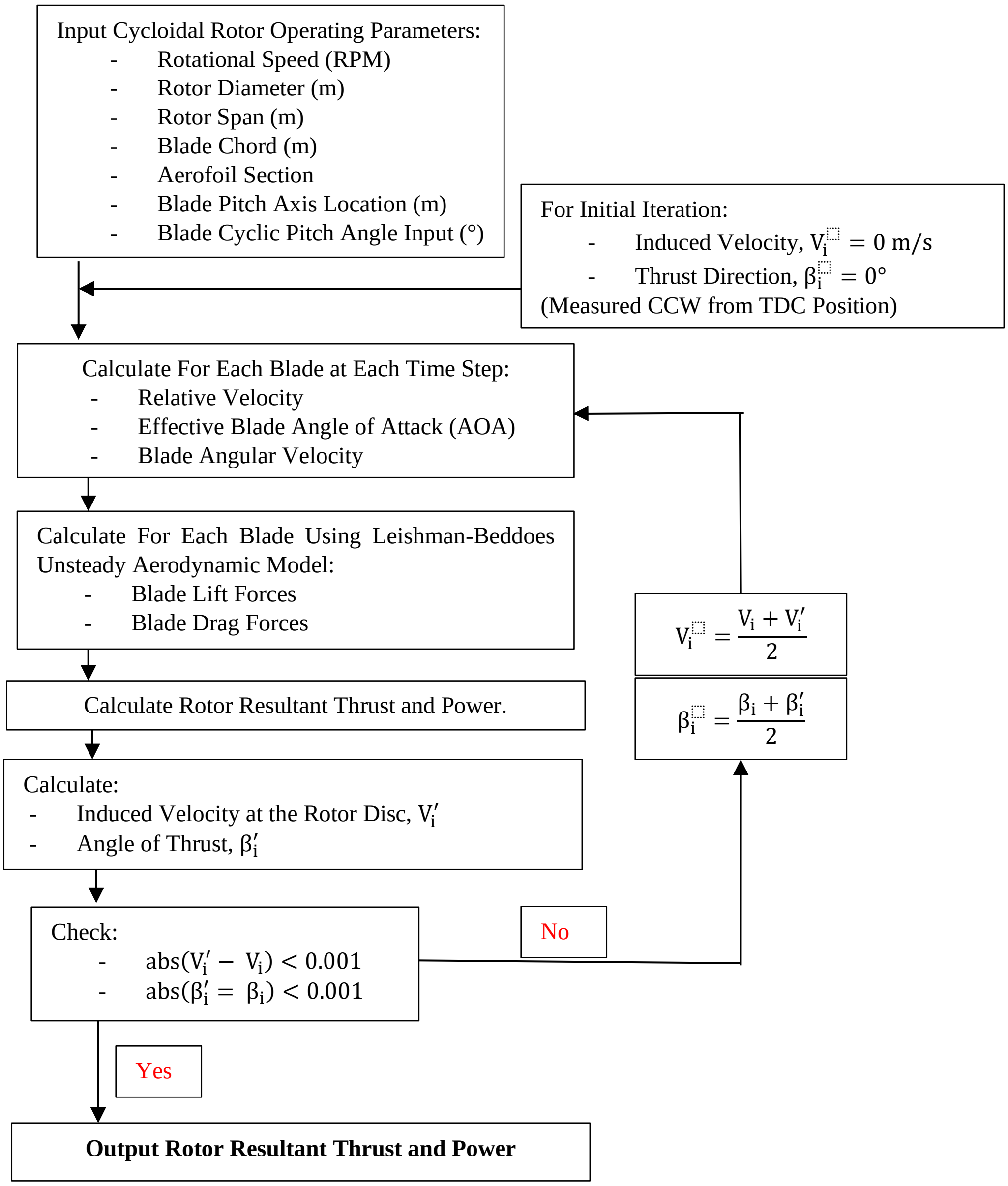

Figure 5.1 – Aerodynamic model flow diagram outlining the system architecture

5.3.1. Baseline Blade Cyclic Pitch Angle Definition

Conventional rotorcraft assume a sinusoidal cyclic pitch profile provided by a swashplate. Previous cycloidal rotor studies have utilized a passive four-bar mechanism [116]. The motion produced by the mechanism is shown in figure 5.2, which approximates pure sinusoidal motion. The exact baseline blade cyclic pitch input amplitude, θ_{BL} used for the development of the current model is given by

$$\theta_{BL} = \frac{\pi}{2} - \cos^{-1}\left(\frac{a^2 - L^2 + t^2}{2at}\right) - \sin^{-1}\left(\frac{e}{a}\cos(\Psi + \varepsilon)\right) \tag{5.1}$$

where

$$a = \sqrt{e^2 + R^2 + 2eR\sin(\Psi + \varepsilon)} \tag{5.2}$$

e is the offset position of the eccentric point that controls the amplitude of the blade cyclic pitch input, and length L is the theoretical distance between the eccentric offset position and the blade pitch pin, defined by

$$L = \sqrt{(0.5D)^2 + t^2} \tag{5.3}$$

where D represents the rotor diameter and t, the pitch link offset distance is shown in figure 5.2 between the blade pitching axis and blade pitch pin for connection to the four-bar mechanism. The blade cyclic pitch amplitude input phase can be changed by modification of ε anywhere in the rotor azimuth. It is typically fixed for a hovering rotor study, where

$$\varepsilon = \tan^{-1}\left(\frac{t}{0.5D}\right) \tag{5.4}$$

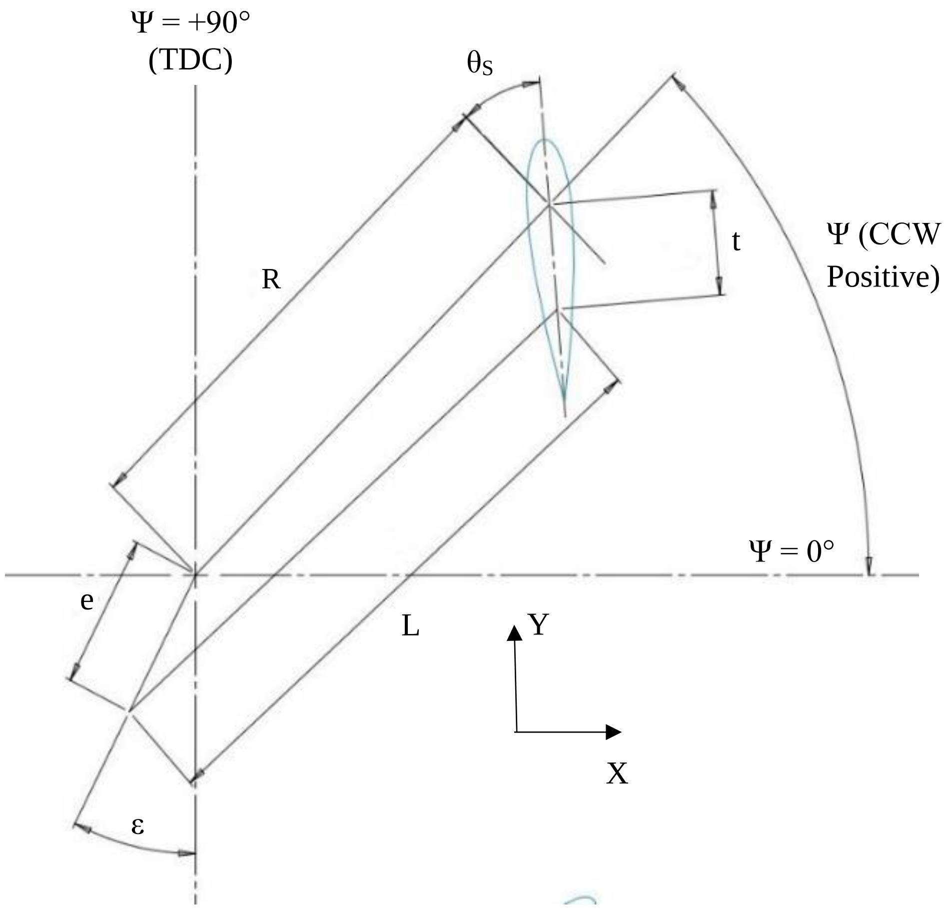

Figure 5.2 – Cycloidal rotor BET code reference coordinate system

5.3.2. Blade Cyclic Pitch Angle Definition With HHC Input

During the final optimization stage of the current research, the aerodynamic model was modified to include HHC. To implement HHC within the computational model, an additional higher harmonic blade cyclic pitch input θ_n was superimposed onto the baseline cyclic pitch amplitude θ_{BL} where n represents the higher harmonic of interest. During HHC, the blade total pitch angle in the rotating frame is

$$\theta_s = \theta_{BL} + \theta_n \tag{5.5}$$

and

$$\theta_n = \theta_{ns}\sin(n\Psi) + \theta_{nc}\cos(n\Psi) \tag{5.6}$$

θ_n is made up of HHC control input sine and cosine components θ_{ns} and θ_{nc}, defined as

$$\theta_{ns} = A_n \cos(n\phi_n) \tag{5.7}$$

and

$$\theta_{nc} = A_n \sin(n\phi_n) \tag{5.8}$$

ϕ_n and A_n represent the phase angle and amplitude of the HHC control input, respectively, and Ψ the rotor azimuth angle. The respective blade azimuth angle of the qth blade, Ψ_q is

$$\Psi_q = \Psi + \frac{2\pi}{N_b}(q-1) \qquad q = 1,2,\ldots.N_b \tag{5.9}$$

The 0° azimuth position is defined in figure 5.2.

5.3.3. Rotor Inflow Model

The use of an accurate aerodynamic inflow model is important to the calculation of blade aerodynamic loads on standard rotorcraft, and the cycloidal rotor is no exception. Independent studies to date, as eluded in section 5.2, have not considered the aerodynamic inflow models' ability to predict the rotor's vibratory response with changing blade cyclic pitch amplitude. With the flow physics of the cycloidal rotor being so complex, all known rotor inflow models may not accurately model the true flowfield.

In its simplest form, a uniform rotor inflow model has been shown to predict the mean performance of the cycloidal rotor with good accuracy [4], and the current work aims to build on this. Increasing the complexity of the model in stages will enable limitations in the modeling to be identified and computational overhead to be reduced when running large numbers of analyses during the optimization parametric studies.

The uniform rotor inflow model used in the current analysis is implemented based on a number of assumptions. The uniform rotor inflow model assumes that the cycloidal rotor can be analyzed as a disc, as per conventional rotorcraft, which is a big approximation. The air velocity through the rotor disc is constant, and there is no swirl imparted into the wake. Hence the air passing through the rotor disc is axial, and the pressure across the rotor disc is constant. The rotor airflow is considered as a single stream tube where the flow is considered as two separate regions. In region one, the airflow passes through the rotor disc, and region two is made up of the areas where the airflow is external to the rotor disc. In using a single stream tube model, the system is assumed to have an infinite number of blades. Thrust is obtained by transferring momentum to the airflow passing through the rotor based on an induced velocity through the rotor disc, as shown in figure 5.3, defined by equation 5.10. The rotor disc is a plane perpendicular to the induced velocity through the centre of the rotor.

$$V_i = \sqrt{\frac{T}{2\rho_a A_R}} \tag{5.10}$$

Where T represents the resultant rotor thrust, ρ_a the air density and A_R the rotor planform areas calculated from

$$A_R = SD \tag{5.11}$$

S is the rotor or blade span. The model iteratively converges on an induced velocity and inflow angle ϕ. For both parameters, a convergence error of 0.001 was utilized.

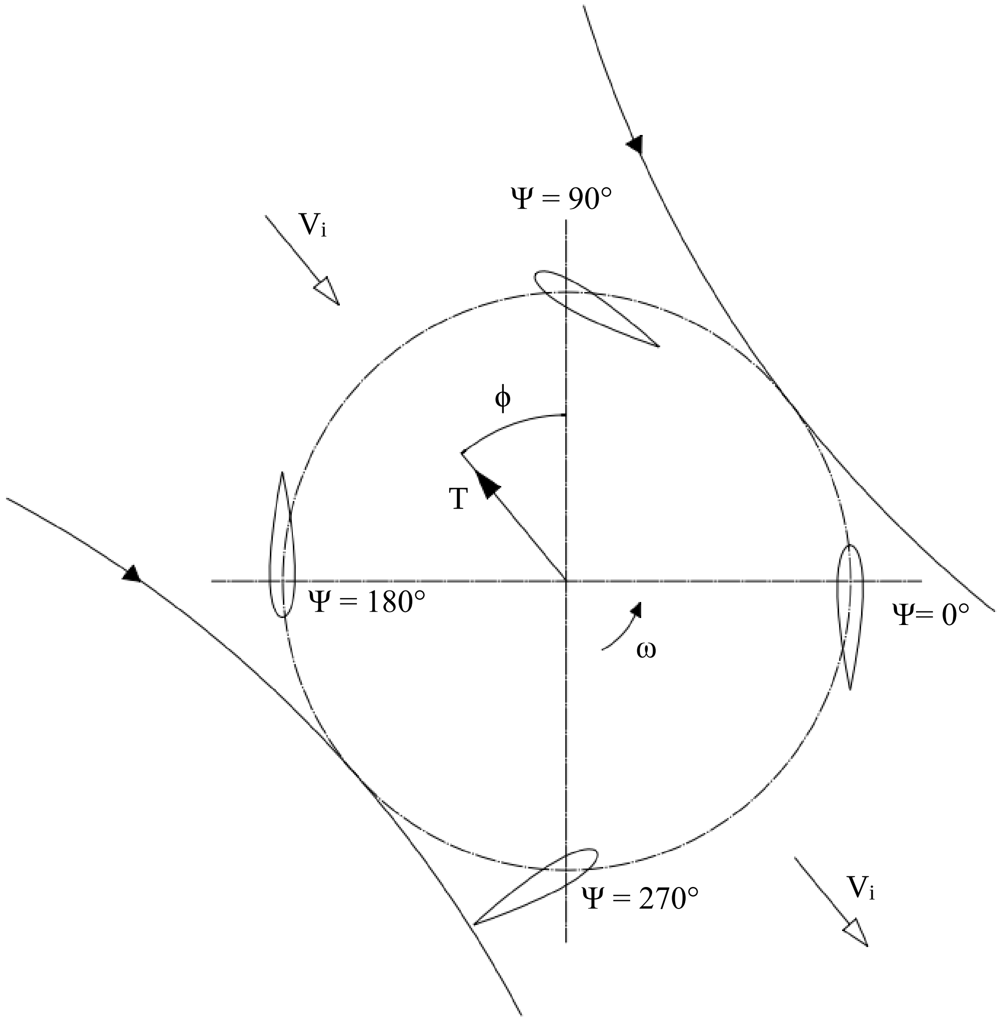

Figure 5.3 – BET code uniform rotor inflow model single stream tube approximation

5.3.4. Potential Forward Flight Rotor Inflow Model Development

With further development of cycloidal rotor-specific inflow models to account for forward flight operation, a significant amount of information on the rotor performance can be obtained across a wide range of rotor advance ratios. Including the Magnus-induced circulation field around the rotor would enable the contribution of the circulatory flow to the rotor flow field to be included in both the advancing and retreating sides of the rotor.

A tip loss factor similar to the Prandtl tip loss factor in standard rotorcraft analysis [117] can be used to account for the effects of the high-induced velocities produced locally at the blade tips and trailing edges due to the shedding of blade tip vortices.

During hover and forward flight operation, there is potential for blade vortex interaction (BVI). These interactions can occur at any position within the rotor diameter or in the shed wake downstream of the rotor. A number of vortex models can be used to consider the effects of BVI more accurately by utilizing the Biot-Savart law, where the induced velocity contributed by a vortex filament in the rotor wake is calculated at discrete points along the vortex filament. The total velocity is then obtained by integration along the lengths of each vortex filament.

Vortex methods fall into two main categories: prescribed wake and free-wake models. Prescribed wake models require a semi-empirical representation of the blade tip vortices and shed wake before a computational model can be developed. A number of models have been developed for standard rotorcraft [117] where the age of the shed wake defines the locations of the rotor tip and shed vortices based on experimental data. On the other hand, free-wake models do not require prior experimental data and solve the rotor wake starting from initial conditions, which are used to define the initial positions of the vortex filaments and are not predefined. The final vortex positions are calculated based on repeated application of the Biot-Savart law.

5.3.5. Blade Element Velocity

The blade angle of attack (AOA) must be calculated as an initial step to calculate the blade aerodynamic loads. The blade relative velocity comprises two velocity components in the tangential and normal directions, as shown in figure 5.4 in the rotor rotating frame. The tangential and normal velocity components have been calculated using the equations defined by Benedict [4]. The velocity components contain contributions from rotor angular velocity, velocity perturbations normal to the blade chord due to blade pitching motion, and induced velocity contributions; spanwise flow variation is not considered. The blade velocities are calculated at the effective three-quarter chord position due to the imposed blade pitch rate [4,117].

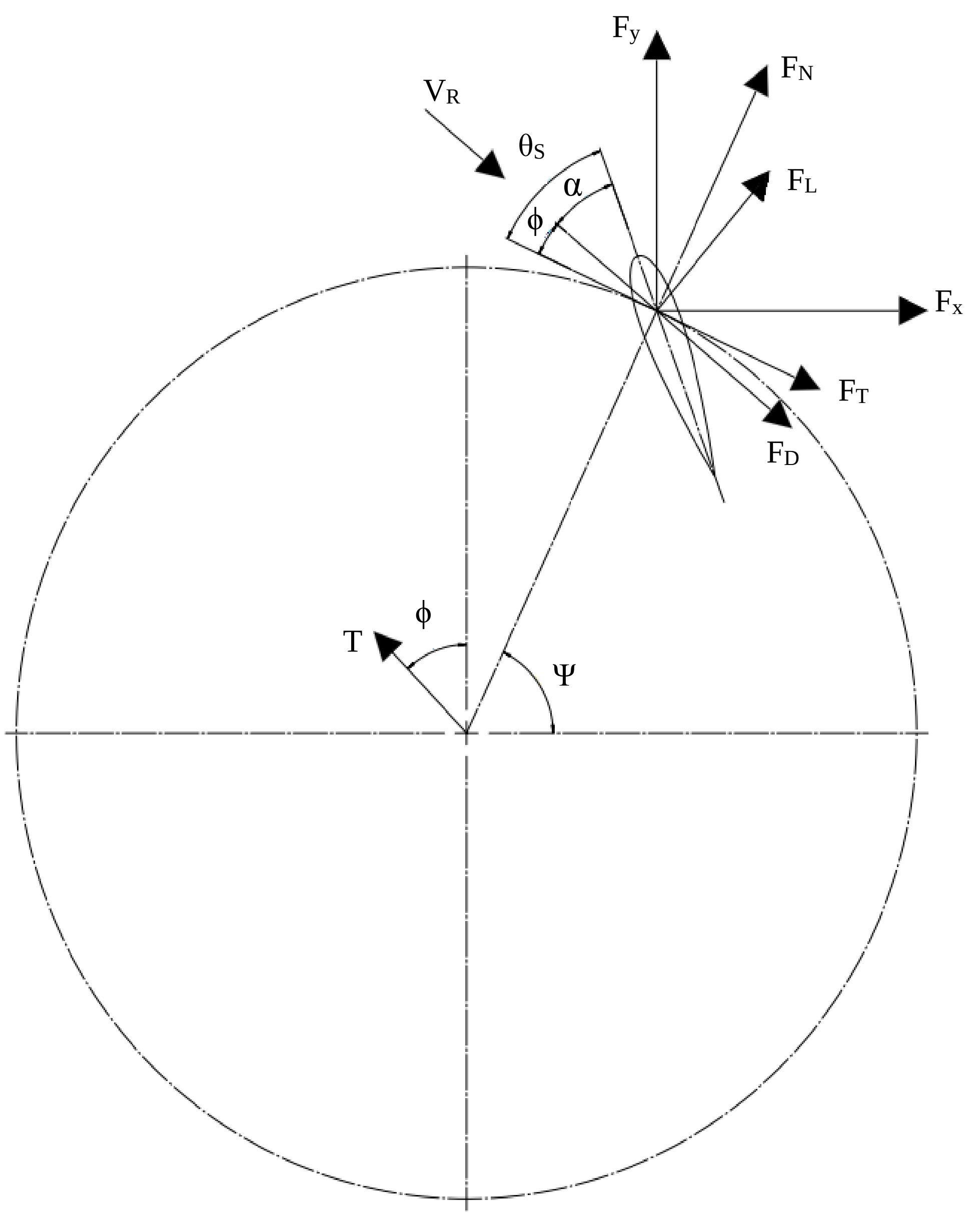

Figure 5.4 – Single rotor blade velocity and force components direction definition

The blade tangential velocity due to rotor rotation and blade pitching [4] is given by

$$V_{T_B} = -\left(0.75 - P_p\right)C\dot{\theta}_S\sin(\theta_S) + \omega\left(0.5D - \left(0.75 - P_p\right)C\sin(\theta_S)\right) \tag{5.12}$$

P_p defines the distance from the LE of the blade to the actual blade pitch axis location to take account of the chordwise distance between the actual pitch axis and the three-quarter chord position assumed in the analysis. C is the blade chord, $\dot{\theta}_S$ the blade angular velocity, and ω is the rotor angular velocity defined as

$$\omega = \frac{2\pi N}{60} \tag{5.13}$$

where N is the rotor rotational speed.

The blade tangential velocity component due to the rotor induced velocity is

$$V_{T_i} = V_i \sin(\phi)\cos(0.5\pi - \Psi) + V_i \cos(\phi)\cos(\Psi) \tag{5.14}$$

The blade tangential velocity components are then added to define the resultant tangential velocity component:

$$V_T = V_{T_B} + V_{T_i} \tag{5.15}$$

Similarly, the blade's normal velocity due to rotor rotation and blade pitching [4] is given by

$$V_{N_B} = -\left(0.75 - P_p\right)C\dot{\theta}_S\cos(\theta_S) - \omega\left(\left(0.75 - P_p\right)C\cos(\theta_S)\right) \tag{5.16}$$

The blade normal velocity component due to the rotor induced velocity is

$$V_{N_i} = V_i \sin(\phi)\sin(0.5\pi - \Psi) + V_i \cos(\phi)\sin(\Psi) \tag{5.17}$$

The blade normal velocity components are then added to define the resultant tangential velocity component:

$$V_N = V_{N_B} + V_{N_i} \tag{5.18}$$

The blade resultant velocity V_R as shown in figure 5.4, is then

$$V_R = \sqrt{V_{Tan}^2 + V_{Nor}^2} \tag{5.19}$$

Based on the blade normal and tangential velocity components, the induced velocity inflow phase angle is

$$\phi = \tan^{-1}\left(\frac{V_N}{V_T}\right) \tag{5.20}$$

5.3.6. Blade Aerodynamic Loads

The blade aerodynamic loads were calculated in the same manner as a fixed-wing system, using the blade sectional lift and drag coefficients. The lift and drag force direction is defined in figure 5.4, where

$$F_L = 0.5\rho_a A_B V_R^2 C_L \tag{5.21}$$

and

$$F_D = 0.5\rho_a A_B V_R^2 C_D \tag{5.22}$$

C_L and C_D represent the blade lift and drag coefficients at the required angle of attack, and A_B the blade planform area. Limited data is available to predict the nonlinear aerodynamic behavior of aerofoil at high angles of attack, at or beyond stall. In standard rotorcraft models, lookup tables are sometimes used to store experimentally derived sectional coefficients over the range of angles of attack required at a given Mach number. Alternatively, higher-order curve-fitting polynomials are used [117]. The extraction of accurate geometric angles of attack from experimental and higher-fidelity computational modeling is a significant challenge for cycloidal rotors. CFD models generated in the current study (described in the next chapter) show stall and dynamic stall were only significant at a blade cyclic pitch input of 40°, which was corroborated by Benedict [4], who found that stall only occurred above a blade cyclic pitch amplitude of 35°.

The resulting blade lift and drag coefficients are based on thin aerofoil theory with confirmation studies undertaken with single blade 2D CFD analyses at similar Reynold's number and reduced frequencies to represent the rotor operation from 500 to 1,000 RPM. A linear aerodynamic model was used throughout, in line with the work undertaken by [4, 34].

Standard thin aerofoil theory uses a lift curve slope C_{L_α} of 2π, but based on the 2D static CFD cases analyzed in the current study, a 2D lift curve slope of 5.20 has been assumed. The lift curve slope has been modified to account for the length of the blades and 3D effects, such as blade tip losses, to give

$$C_{L_{3D}} = \frac{C_{L_\alpha}}{1+\frac{C_{L_\alpha}}{AR\pi}} \tag{5.23}$$

Where AR is the blade aspect ratio:

$$AR = \frac{S^2}{A_B} \tag{5.24}$$

It is worth noting that the current analysis calculates the worst-case aerodynamic efficiency without end plates to compare with published data directly. Including end plates would improve the aerodynamic efficiency of the cycloidal rotor by reducing the blade tip vortices effects. But a trade-off would need to be made with the increased power requirements of end plates and the additional mass penalty.

The blade lift coefficient is made of two components, C_L^c and C_L^{nc}. These represent the circulatory and non-circulatory components of lift, respectively. The circulatory terms are related to bound and shed vorticity in the flow around the aerofoil. Non-circulatory terms are generated due to the forces required to accelerate the flow near the blade. The overall lift coefficient is then defined as

$$C_L = C_L^c + C_L^{nc} \tag{5.25}$$

The calculation of $C_L^c$and C_L^{nc} will be considered further in section 5.3.7. The overall drag coefficient is made up of two components, C_{D_p} which represents the blade profile drag coefficient defined by [117], where

$$C_{D_p} = d_0 + d_1\alpha + d_2\alpha^2 \qquad (5.26)$$

d_0, d_1, and d_2 are coefficients derived by curve fitting of experimentally or computationally derived data. They were calculated to be 0.031, 0.0, and 2.40, respectively, for the NACA0018 used, estimated from static 2D CFD calculations, and are comparable to findings in [4] for a NACA 0015 aerofoil. And the induced drag coefficient C_{D_i}, which is the drag generated during lift generation, where

$$C_{D_i} = C_N \sin(\alpha) - C_C \cos(\alpha) \qquad (5.27)$$

where α is the blade's effective angle of attack and C_N and C_C the normal and chordwise blade force coefficients. The overall drag coefficient is calculated by adding the two contributions, resulting in

$$C_D = C_{D_p} + C_{D_i} \qquad (5.28)$$

From calculating the lift and drag forces, the individual blade forces are converted into X and Y force components to aid with results post-processing. The force in the X-direction F_x is

$$F_x = F_L \cos(\Psi - \phi) + F_D \cos(0.5\pi - \Psi + \phi) \qquad (5.29)$$

and in the Y-direction, F_y:

$$F_y = F_L \sin(\Psi - \phi) - F_D \sin(0.5\pi - \Psi + \phi) \qquad (5.30)$$

Individual blade forces are then summed over the total number of blades to calculate the instantaneous rotor forces in the two measurement directions,

$$F_{x_R} = \sum_{q=1}^{N_b} F_x \qquad (5.31)$$

and

$$F_{y_R} = \sum_{q=1}^{N_b} F_y \tag{5.32}$$

The resultant rotor instantaneous force profile is then given by

$$F_{R_R} = \sqrt{{F_{x_R}}^2 + {F_{y_R}}^2} \tag{5.33}$$

The individual and resultant instantaneous force components are converted to non-dimensional coefficients to represent the Coefficient of Thrust components to aid with results post-processing in the X-direction.

$$C_{T_x} = \frac{F_{x_R}}{\rho_a A_B \omega^2 R^2} \tag{5.34}$$

In the Y-direction

$$C_{T_y} = \frac{F_{y_R}}{\rho_a A_B \omega^2 R^2} \tag{5.35}$$

and finally, for the resultant rotor thrust force

$$C_T = \frac{F_{R_R}}{\rho_a A_B \omega^2 R^2} \tag{5.36}$$

The non-dimensional coefficients are then averaged to calculate the mean rotor thrust performance. In addition to the rotor forces, calculation of rotor power is calculated from individual blade instantaneous torque from F_T for each blade where the individual blade torque is

$$F_T = F_L \sin(\phi) + F_D \cos(\phi) \tag{5.37}$$

Therefore the individual blade torque is

$$T_B = 0.5DF_T \tag{5.38}$$

and individual blade power

$$P_B = T_B\omega \tag{5.39}$$

Individual blade powers are then summed over the total number of blades to calculate the instantaneous rotor power given by

$$P_R = \sum_{q=1}^{N_b} P_B \tag{5.40}$$

Instantaneous rotor power is then converted to non-dimensional form to represent the Coefficient of power, where

$$C_P = \frac{P_R}{\rho_a A_B \omega^3 R^3} \tag{5.41}$$

5.3.7. Calculation of Blade Angle of Attack – Attached Flow

Unsteady aerodynamic flow effects are known to delay blade stall to higher angles of attack when compared to a static aerofoil. An attached flow model was developed initially for model validation. Unsteady aerodynamic effects were included in the computational model by utilizing indicial aerodynamics in the form of a Wagner function, using the method developed by Leishman and Beddoes [118,119] to account for the shed wake of the blade.

A Wagner function accounts for the effects of the shed wake to arbitrary changes in blade angle of attack and pitch rate, analyzed in the time domain by calculating the indicial lift at each time step based on semi-empirical indicial response functions. The circulatory lift change to a step-change in the angle of attack can be defined in the form of a Wagner function as

$$C_L^c(t) = C_{l\alpha}\left(\alpha(0)\phi(s) + \int_0^s \frac{d\alpha(\sigma)}{ds}\phi(s-\sigma)d\sigma\right) = C_{l\alpha}\alpha(t) \tag{5.42}$$

where s is the distance traveled by the shed wake in semi-chords [117]

The Wagner function is usually replaced by an algebraic approximation [117], defined by

$$\phi(s) \approx 1 - A_1 e^{-b_1 s} - A_2 e^{-b_2 s} \qquad (5.43)$$

The coefficients A1, A2, b1, and b2 define the indicial lift approximations from experimental data [118] and are taken to be 0.165, 0.335, 0.0455, and 0.3 in the current analysis in line with data presented in [117]. The circulatory lift contains contributions from the step change in blade effective unsteady angle of attack, α, and effective pitch rate, q, which contains the time histories of the angle of attack and pitch rate changes [4], where

$$C_L^c = C_{L_\alpha}\alpha + \frac{1}{2}C_{L_\alpha}q \qquad (5.44)$$

With the time histories included in the calculation of the effective unsteady angle of attack and pitch rate to account for the shed wake, α and q are then calculated from

$$\alpha = \alpha_e - X_{\alpha_n} - Y_{\alpha_n} \qquad (5.45)$$

and

$$q = q_e - X_{q_n} - Y_{q_n} \qquad (5.46)$$

The blade angle of attack without time histories included representing the quasi-steady angle of attack is given by

$$\alpha_e = \theta_S - \phi \qquad (5.47)$$

and the blade's quasi-steady pitch rate

$$q_e = \frac{\dot{\theta}_S c}{V_R} \qquad (5.48)$$

$\dot{\theta}_S$ represents the blade pitching angular velocity. The parameters X_{α_n} and Y_{α_n} define the blade angle of attack deficiency functions, and X_{q_n} and Y_{q_n} the pitch rate deficiency functions. The deficiency functions are analyzed in a single step recursive manner and contain the previously shed wake effect of the effective angle of attack and pitch rate [119], where

$$X_{\alpha_n} = X_{\alpha_{n-1}} e^{(-b_1 \delta s)} + A_1\left(\alpha_{e_n} - \alpha_{e_{n-1}}\right) e^{(-0.5 b_1 \delta s)} \tag{5.49}$$

$$Y_{\alpha_n} = Y_{\alpha_{n-1}} e^{(-b_2 \delta s)} + A_2\left(\alpha_{e_n} - \alpha_{e_{n-1}}\right) e^{(-0.5 b_2 \delta s)} \tag{5.50}$$

$$X_{q_n} = X_{q_{n-1}} e^{(-b_1 \delta s)} + A_1\left(q_{e_n} - q_{e_{n-1}}\right) e^{(-0.5 b_1 \delta s)} \tag{5.51}$$

and

$$Y_{q_n} = Y_{q_{n-1}} e^{(-b_2 \delta s)} + A_2\left(q_{e_n} - q_{e_{n-1}}\right) e^{(-0.5 b_2 \delta s)} \tag{5.52}$$

When changing the angle of attack and pitch rate, the blade is subject to non-circulatory loading due to localized pressure variation. The magnitude of the non-circulatory impulse [119] can be calculated from

$$C_L^{nc} = C_{Li_\alpha} + C_{Li_q} \tag{5.53}$$

where the non-circulatory lift impulse component due to the angle of attack C_{Li_α} [118, 119] is

$$C_{Li_\alpha} = \frac{(4 k_i T_i)}{M_n}\left(d\alpha_n - D_{\alpha_n}\right) \tag{5.54}$$

and the non-circulatory lift impulse component due to the pitch rate C_{Ni_q}, is

$$C_{Li_q} = \frac{(-k_i T_i)}{M_n}\left(dq_n - D_{q_n}\right) \tag{5.55}$$

k_i is a function of Mach number, M_n and is typically taken to be 0.75 [119] for all values of M_n. T_i represents the non-circulatory time constant [119]:

$$T_i = \frac{C}{\sqrt{\gamma Rt}} \tag{5.56}$$

and Mach number

$$M_n = \frac{V_{Res}}{\sqrt{\gamma Rt}} \tag{5.57}$$

The change in blade angle of attack during a single time step is given by

$$d\alpha_n = \frac{(\alpha_{e_n} - \alpha_{e_{n-1}})}{dt} \tag{5.58}$$

and for pitch rate

$$dq_n = \frac{(q_{e_n} - q_{e_{n-1}})}{dt} \tag{5.59}$$

The deficiency functions for the non-circulatory lift impulse components in the angle of attack and pitch rate [118, 119] are defined as

$$D_{\alpha_n} = D_{\alpha_{n-1}}\left(e^{\left(\frac{-dt}{k_i T_i}\right)}\right) + (d\alpha_n - d\alpha_{n-1})\left(e^{\left(\frac{-dt}{k_i T_i}\right)}\right)^{0.5} \tag{5.60}$$

and

$$D_{q_n} = D_{q_{n-1}}\left(e^{\left(\frac{-dt}{k_i T_i}\right)}\right) + (dq_n - dq_{n-1})\left(e^{\left(\frac{-t}{k_i T_i}\right)}\right)^{0.5} \tag{5.61}$$

Where dt represents the Wagner indicial response time increment, given by

$$dt = \left(\frac{1}{(N_R/60)}\right)/360 \tag{5.62}$$

Finally, the distance traveled by the wake over the time increment dt is given by

$$\delta s = \frac{(V_{Res_n} - V_{Res_{n-1}})}{c} dt \quad (5.63)$$

5.3.8. End Plate Effects

The method outlined by Childs [120] has been considered to estimate the effects of the rotor end plates. The end plates have been analyzed as the summation of the effects of a rotating cylinder for the outer diameter surface and a free disc rotating in an initially static flow for the end plate side faces. The outer surface of the disc will be considered first, based on an empirical correlation for turbulent flow for smooth cylinders [120], defined as

$$C_{mc} = \left(\frac{1}{-0.5872 + 1.25 \ln (Re_{\phi} \sqrt{C_{mc}})}\right)^2 \quad (5.64)$$

C_{mc} defines the moment coefficient for a rotating cylinder, and Re_{ϕ} is the rotational Reynolds number given by

$$Re_{\phi} = \frac{\rho \omega d^2}{\mu} \quad (5.65)$$

The moment coefficients in equation 5.60 must be solved iteratively. The power required to overcome the frictional drag at the end plate's outer diameter can be determined from

$$P = T_E \omega \quad (5.66)$$

where

$$T_E = 0.5 \pi \rho \omega^2 r^4 L C_{mc} \quad (5.67)$$

and L is the end plate thickness

In a similar manner to the end plate's outer diameter, the moment coefficient C_m for one side of the end plate can be calculated from

$$C_m = 1.935 Re_{\phi}^{-0.5} \tag{5.68}$$

The power required to overcome the frictional drag at the end plate side faces can be determined for one face from

$$P = T_F \omega \tag{5.69}$$

where

$$T_q = 0.5 \rho \omega^2 d^5 C_m \tag{5.70}$$

As there are two sides and one outer diameter to each end plate, the total power is calculated from the summation of equation 5.63 and double equation 5.66. For the current test rig geometry, the frictional drag torque of both ends plates is estimated to be a maximum of 3.7% of the total rotor aerodynamic power at a rotor rotational speed of 1,000 RPM and a blade cyclic pitch amplitude of 40°.

5.4. Aerodynamic Model Validation – Mean Rotor Performance

The current BET code was validated against independent studies [30, 46, 112]. The three studies covered a combination of experimental and computational modeling at a single-blade cyclic pitch amplitude with increasing rotor speed for a three and four-blade cycloidal rotor, as shown in figures 5.5 and 5.6. For the three-bladed configuration [30,112] in figures 5.5 (a) and 5.5 (b), the thrust and power calculated in the current BET code are in very good agreement across the speed range considered when compared to the independent experimental results. The current BET code results for the four-bladed configuration [46] are shown in figure 5.6 (a) for thrust and 5.6 (b) for power. Good agreement is seen at lower rotational speeds below 600 RPM when compared to experimental data, but the increased deviation is seen at rotor speeds above this, with thrust and power overpredicted by the current BET code.

Comparison with the independent computational model in figure 5.6 (a) shows the BET code is in good agreement across the full rotor speed range considered. Based on this, the ability of the current aerodynamic to model cycloidal rotor performance over a single blade cyclic pitch angle has been validated for low-order, low-rotor speed dynamics.

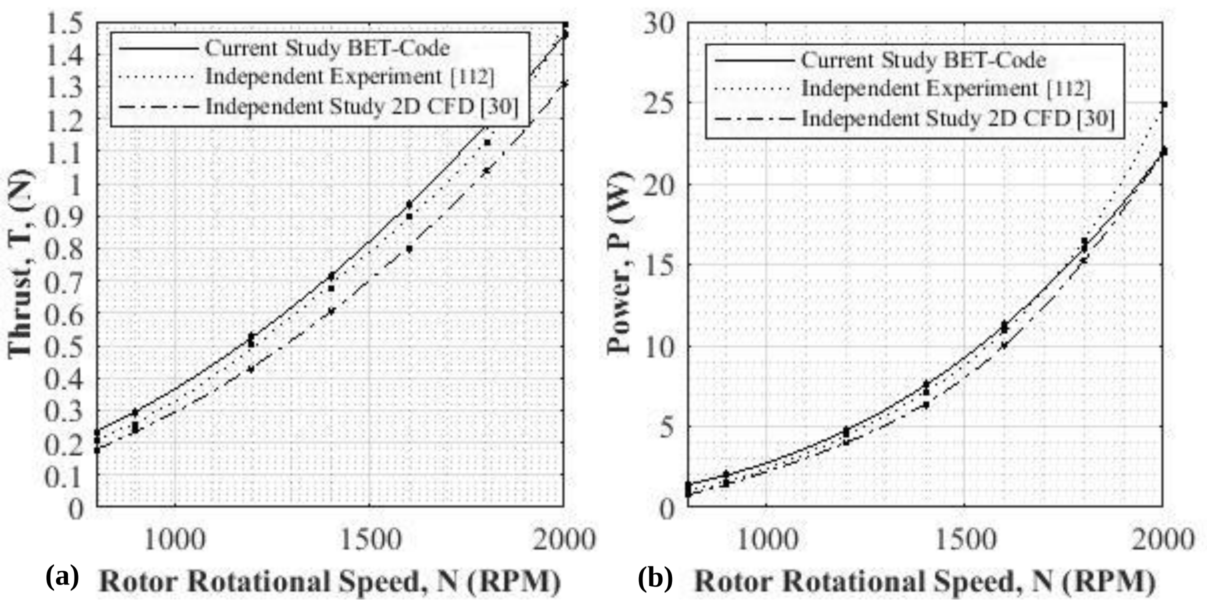

Figure 5.5 – Current study BET code mean performance parameter comparison to independent mean performance parameters for a three-blade cycloidal rotor [30, 112]. (a) Thrust and (b) Power

Additional validation of the BET code across a broad range of blade cyclic pitch amplitudes and rotor speeds was achieved by comparison to the baseline experimental measurements taken with the current test rig, as shown in figures 5.7 (a) to 5.7 (d) for thrust and power, respectively. Reasonable agreement is identified across the entire blade cyclic pitch angle range considered, with a number of areas requiring further discussion. Figure 5.7 (a) shows the X-direction force component (propulsive direction) and shows very good agreement with the experimental data. The X-direction force component varies linearly with increasing blade cyclic pitch angle in both cases. The Y-direction force components (lift direction) are shown in figure 5.7 (b). The overall trend between the experimental and computational model is identified, where thrust increases with increases in blade cyclic pitch angle.

Above 10° to 30°, the Y-direction thrust is overpredicted by the BET code. The experimental and BET code results cross over, and the BET code model then underpredicts the Y-direction force component. This suggests that as blade cyclic blade pitch amplitude is increased, there are quantitative changes in the flow physics of the cycloidal rotor that the BET code cannot fully capture. Confirming the findings of McNabb [34], where the induced drag was modified to improve the correlation between experimental and computational models by an induced drag correction factor, but that was only at a single cyclic pitch angle. The scope of the current model development was to determine whether the same model could be used across a full range of blade cyclic pitch amplitudes, so additional factors have not been included. Although some deviation is seen between the experimental and computational models, they are within 15% of one another.

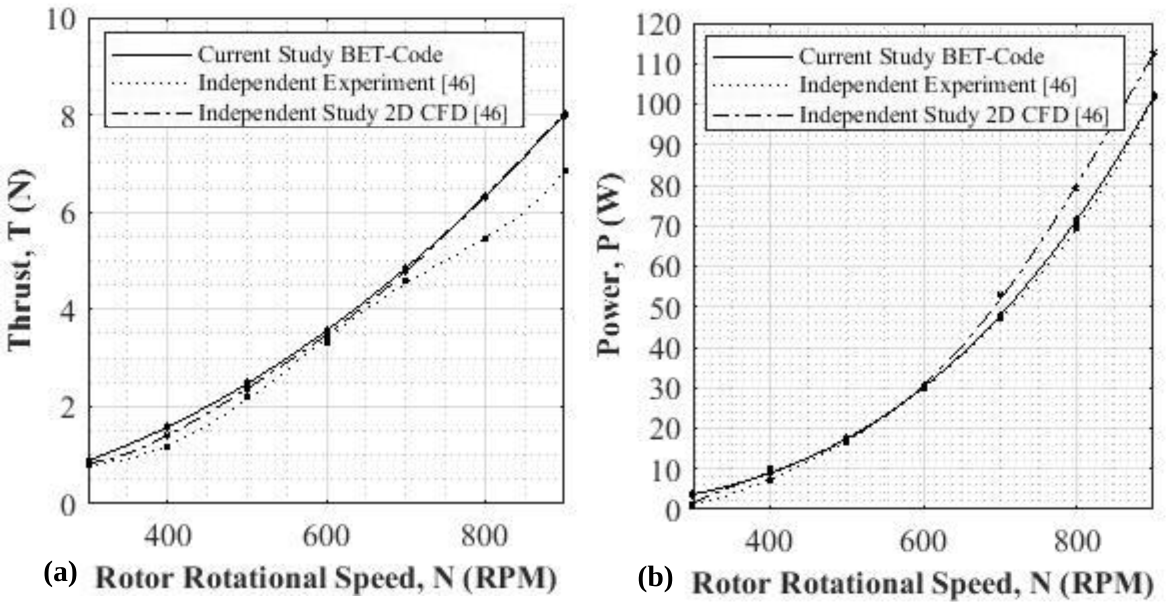

Figure 5.6 – Current study BET code mean performance parameter comparison to independent mean performance parameters for a four-blade cycloidal rotor [46]. (a) Thrust and (b) Power

Figure 5.7 (c) shows the resultant thrust level, where many of the same features of figure 5.7 (b) are identified. At 0° blade cyclic pitch angle, the resultant experimental thrust is considerably higher than the computational model prediction (zero), suggesting that flow swirl and rotor inflow associated with the rotor rotation are higher during the experiment than that considered in the 2D reduced-order model.

However, above 10°, the correlation with the experimental data shows considerable improvement in both thrust and power levels, as shown in figure 5.7 (d).

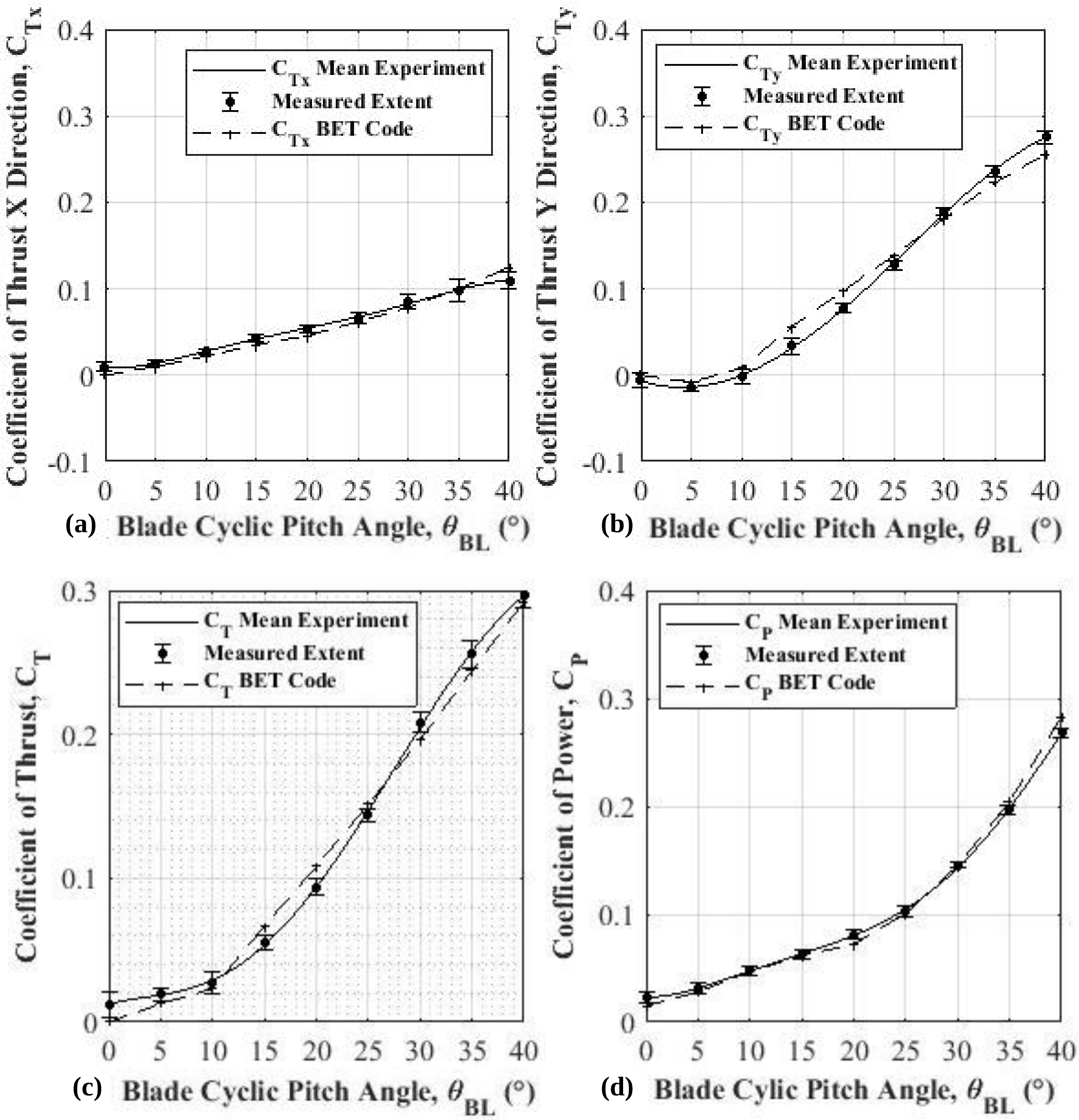

Figure 5.7 – BET code data comparison to current study baseline experimental mean performance parameters with changing blade cyclic pitch angle and rotor rotational speed. Measured extents are shown from 500 to 1000 RPM

5.5. Chapter Review

The BET code developed and validated with independent experimental and computational models in the current chapter is used to calculate the cycloidal mean and rotor vibratory response with changing blade cycle angle and rotor rotational speed. In Chapter 7, the BET code is used to determine the efficacy of the reduced-order model in cycloidal rotor analysis when compared to CFD and experimental data from the current research. Finally, utilization of the BET code in relation to cycloidal rotor vibration optimization is outlined in Chapter 8, covering both linear and nonlinear optimization strategies.

The aerodynamic model developed in the current chapter combines the original unsteady aerodynamic model developed by Leishman-Beddoes [118,119] for unsteady attached oscillating aerofoil flow and an extension of the analysis undertaken by Benedict [4] for a cycloidal rotor. The main novelty in the current aerodynamic model is that it has been extended to consider the dynamic vibratory response of the cycloidal rotor from 1/Rev to 16/Rev. The model enables multiple HHC control inputs to be superimposed onto the baseline blade cyclic pitch angle input and includes a sub-function to enable an optimal HHC input to be determined for maximum vibratory load suppression for each cycloidal rotor operating condition required.

Chapter 6 – Cycloidal Rotor CFD Modelling

6.1. Introduction

Physical experimentation is resource hungry in terms of both time and manufacturing costs. Therefore, additional computational modeling capability is justified to provide insight into cycloidal rotor operation and to inform and reduce the number of physical tests required to concentrate experimentation on key areas. Furthermore, CFD modeling has the advantage that design and optimization studies can be undertaken with reduced overhead.

The current chapter provides a brief overview of some of the latest cycloidal rotor CFD studies, detailing the model setup, solver used, and mesh generation approach, where possible, to inform the current model design. This is followed by a description of the CFD model used as the basis for all CFD models used in the current research, both for the standard and optimized cycloidal rotor. This includes an explanation of the 2D CFD solver, mesh and model development, and relevant post-processing techniques. Methods used for results and model validation are also presented.

The CFD models aim to calculate rotor mean performance and rotor vibratory response with sufficient accuracy to verify the data predicted in the BET code in Chapter 5 and for comparison to experimental data from the current research to determine the efficacy of the CFD modeling approach. CFD modeling allows for improved calculation of the instantaneous blade forces and the generation of flow field plots with changing blade cyclic pitch amplitude to gain further insight into the overall flow physics of the cycloidal rotor and identify limitations of the reduced-order models.

6.2. Independent Cycloidal Rotor CFD Model Development

Various CFD models have been developed to investigate cycloidal rotor mean performance in both 2D and 3D. Some investigate rotor performance for a general configuration, and others use CFD modeling to study a specific effect. Hu et al. [46] used 2D CFD models to determine the effect of aerofoil thickness on a micro air vehicle (MAV) scale rotor, utilizing a Reynolds Averaged Navier Stokes (RANS) solver, OVERTURNS.

An unstructured mesh was used throughout the computational domain, with prism mesh elements used at the blade surface to accurately capture the boundary layer flow effects. The model assumed a four-blade cycloidal rotor and a moving mesh interface was defined at each blade to the rotor connection point, allowing each blade to pitch and rotate as required. The rotor diameter and rotational speeds considered produced a Reynolds number between 20,000 and 80,000. A shear stress transport (SST) k-ω model was used, with low Reynolds correction, to model blade flow separation more accurately compared with the k-ε and conventional k-ω model [46]. A computational domain of 30D was chosen to eliminate far-field boundary effects. Following a mesh sensitivity and time step sensitivity analysis, a mesh with 933 elements on a 70mm chord blade was optimal in conjunction with 1,200 steps per rotor rotation.

The CFD model's mean performance results were validated against experimental data and showed that the 2D analyses produced results comparable to experimental data for all cases. The 2D CFD analysis predicted the instantaneous velocity field at the rotor center span with reasonable accuracy, showing qualitative agreement with experimental particle image velocimetry (PIV) studies. The 2D models capture the LE and shed vortices at the blades highlighted in the PIV studies but confirmed that the 2D simulations could not capture blade tip effects. Hu [121] concluded that for low aspect ratio rotors, blade tip vortices could significantly affect the flow distribution at the edges of the rotor.

Tang et al. [115] developed a 3D model using Ansys FLUENT 14.0 with a RANS solver for multiple geometries. A structured mesh was developed for each model subdomain. In the same way as [46], the sliding mesh interface allowed blade pitching. The 3D analysis assumes that the blades were rigid in the spanwise direction and blade twist did not occur.

The computational domain extended 20D compared to the 30D analyzed by [46] to reduce computational overhead. A k-ω SST turbulence model with low Reynolds correction was again used for all analyses. A mesh sensitivity analysis was undertaken, but limited details on the mesh at the blade were given; only overall mesh cell numbers were quoted. In the final analysis, 400 steps per rotor revolution were used as a time step for twelve rotor rotations, somewhat coarser than that used by Hu et al. [46]. Still, validation with independent experimental and computational studies showed good agreement.

Hu et al. [121] developed studies for a four-blade hovering cycloidal rotor at MAV scale, again with a 70mm chord, based on an unsteady Reynolds Averaged Navier Stokes (URANS) solver with 2D, 2.5D, and 3D models. The 2.5D model was created from the 2D model mesh, where the 2D mesh was extruded in the spanwise rotor direction, creating a pseudo-3D analysis. The study confirmed the existence of a three-dimensional flow field, but that 2D modeling can still predict the mean cycloidal rotor performance when compared to experimental data.

A structured mesh was used throughout for each model type [121], with a mesh sensitivity analysis undertaken for the 2D geometries validated against experimental data. The final mesh of 240 elements in the chordwise direction was used to give satisfactory results when compared to experimental data. In all cases, the computational domain stretched 20D in all directions. The Pressure Implicit with Splitting of Operators (PISO) scheme was used to model transience, with the second-order implicit time step method used to increase solution accuracy.

6.3. 2D CFD Modelling Assumptions

The use of CFD to inform future experimentation to reduce both time and cost burden validates the use of CFD as a modeling technique in the current study. The optimization studies rendered 3D CFD models unrealistic due to the large number of analyses to be undertaken, as the model run time was prohibitive. A decision was made to use a 2D CFD modeling approach to represent a plane through the motor midplane to reduce model run time while still being able to predict the mean cycloidal rotor performance compared to experimental data Hu [121].

The use of a 2D analysis is subject to a number of assumptions, as the flow within the rotor is never truly 2D. Firstly the blades are rigid, and blade deflection and or vibration does not affect the flow. Secondly, blade tip vortices, spanwise flow variation, and spanwise flow separation are not accounted for within the 2D model. As a result, separation flow eddies that are 3D in nature are not captured in the current analysis. For low aspect ratio rotors, blade tip vortices have the potential to significantly affect the flow distribution at the edges of the rotor.

Despite this, the work undertaken by Ferrier [122] suggested the use of 2D modeling could be used based on the assumption that the cycloidal rotor being analyzed uses end plates in the rotor design. The current experimental test rig uses end plates at each end of the rotor to reduce 3D flow effects in the spanwise rotor direction to justify the use of 2D CFD modeling.

6.4. Current Study Turbulence Model

From the recent cycloidal rotor studies outlined in section 6.2., all studies use Reynolds Averaged Navier-Stokes (RANS) turbulence modeling methods. Alternative turbulence methods such as Detached Eddy Simulation (DES) and Large Eddy Simulation (LES) are available to improve solution accuracy, although simulation complexity and computational solve time are much higher. Ferrier [122] concluded that when used in conjunction with a 2D geometry, a RANS turbulence model is the best suited for parametric studies due to the reduced solution time compared to DES and LES simulation while maintaining reasonable solution accuracy.

Typically, a k-ω model is chosen to model the boundary layer and near-wall interactions more accurately than the k-ε model, which contains high levels of swirl and vorticity [123]. Wilcox [124] confirmed that the k-ω and k-ε models are well suited to modeling complex flows with high levels of recirculation. But in some instances, they tend to overpredict flow separation and boundary layer shear stress [123]. For this reason, a k-ω SST model has been implemented to predict flow separation and reattachment with increased accuracy compared to the standard k-ω model. Ferrier [122] noted that the k-ω SST is commonly used for modeling dynamic stall on an oscillating aerofoil in an axial free stream and cycloidal motion. Computational model results [122] showed qualitative agreement with experimental data for a single pitching aerofoil with LE and TE vorticial shedding behavior captured when the k-ω SST was used.

Singh and Pascoa [125] analyzed seven turbulence models on a 2D single oscillating aerofoil pitching in a sinusoidal motion to validate the model selection when operating under dynamic stall conditions. The models included a k-ω and a k-ω SST model, including low Reynolds number correction, using the SIMPLE algorithm for pressure velocity coupling developed in [126]. It was concluded that the k-ω solvers modeled the pre-stall characteristics of the flow well and showed good agreement with experimental results [127]. However, at post-stall angles of attack, some deviation in the blade aerodynamic coefficients was noted compared to experimental data, which was expected because 3D effects are not considered.

Based on the number of CFD analyses to be run in the current research and validation of independent CFD studies to experimental data outlined in section 6.2, a RANS turbulence model was used in line with [122]. This gave the best comprise between solution accuracy and computational cost. Based on the work of Singh and Pascoa [125], the k-ω SST turbulence model was used for accuracy in the prediction of aerodynamic blade loads, including the effects of dynamic stall and flow separation. Low Reynolds number correction was also used due to the current study's chordwise Reynolds number varying between 17,500 and 35,000.

6.5. Model Geometry

With each blade of the cycloidal rotor required to pitch cyclically, the inclusion of blade pitching motion can be included through the use of dynamic mesh zones or sliding mesh interfaces [46]. The use of dynamic mesh zones surrounding the blades requires the mesh to be deformed at each time step, which can lead to reduced mesh quality due to increased cell skew and aspect ratio, which may require areas to be re-meshed if the quality is too low. Sliding mesh interfaces are used to control mesh quality and simplify the overall geometry, where the mesh is not required to be updated, and the mesh at the interfaces does not overlap. Hence the sliding mesh approach gives the best solution accuracy [46].

Three levels of mesh hierarchy are used for the current cycloidal rotor configuration to implement the sliding mesh interfaces, as shown in figure 6.1. The far-field is modeled as the stationary domain that interfaces with the outer rotor rotating region that encases the blades. Within the rotor, separate subdomains are specified to allow each blade to pitch independently of the rotor. The stationary and rotating domains communicate with one another through sliding mesh interfaces. Split geometry lines were used on either side of the interfaces to control the mesh element sizes so that their size ratio on opposing sides is less than 2.0, eliminating the influence of mesh quality at the boundary [128]. The overall computational domain is modeled to be 30D in all directions from the rotor center, in line with [46]

6.6. Mesh Generation

In setting up a CFD analysis, the type of mesh and mesh resolution can significantly impact the reliability and accuracy of the results, as the flow field physics is solved for each mesh cell. CFD meshes commonly fall into two broad categories, structured and unstructured meshes. Typically in 2D analyses, structured meshes use quadrilateral elements, and unstructured mesh use predominantly triangles but can use a combination of the two-element types [129]. Structured meshes are characterized by their regular connectivity and formation to conform to the geometry being solved, resulting in improved convergence, run times, and computational overhead. Structured meshes are typically better suited to geometries where the flow is predominantly axial [122]. But these meshes have the disadvantage that model and mesh complexity can increase with complex model geometries and lead to small geometric features being removed. This can be overcome in many cases by splitting the geometry up into multiple areas, known as structured multi-block meshing. A structured mesh is then applied to each sub-domain with common mesh sizes used at the interfaces so that the element vertices match in each domain to maintain connectivity.

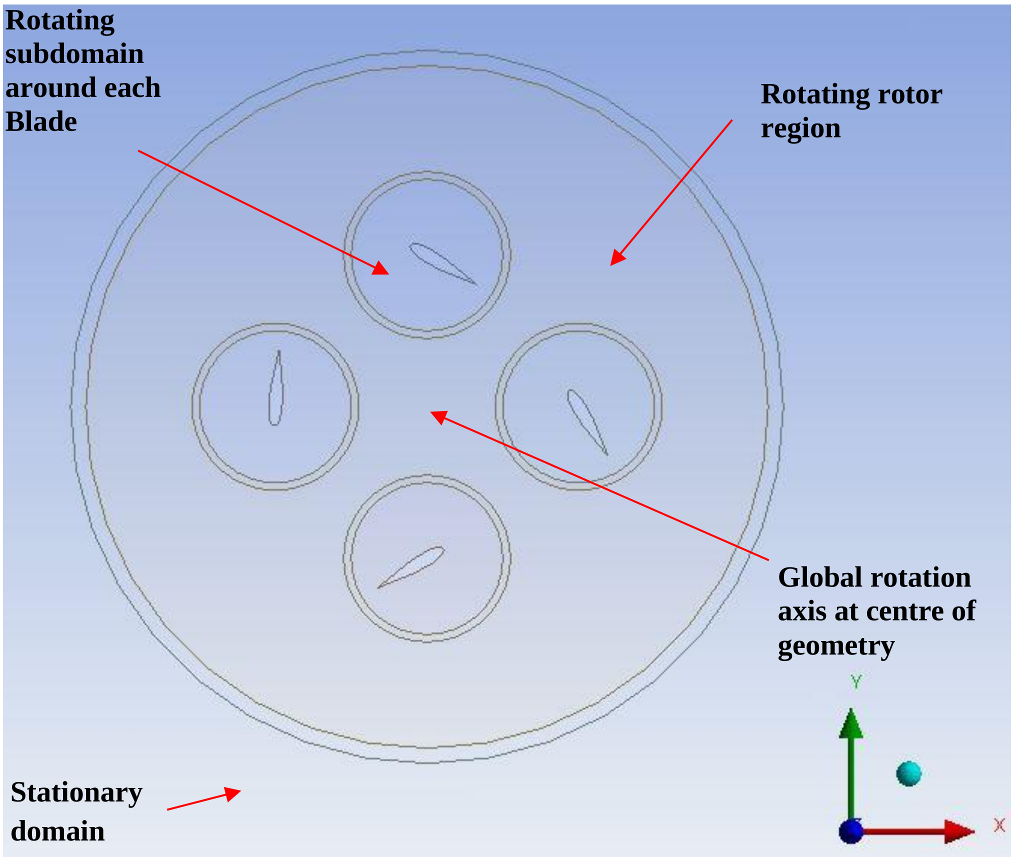

Figure 6.1 – Cycloidal rotor 2D CFD model geometry and coordinate system

By contrast, unstructured meshes are characterized by their irregular connectivity but can still be distributed efficiently within the model domain. They are not as easily stored in a 2D computational array as a structured mesh, which results in increased computational storage requirements on mesh connectivity data and run times. Although unstructured meshes have the advantage that they can incorporate a wider range of geometry types without the need for model modification and defeaturing. Higher mesh resolution can also be applied in critical areas of the geometry, such as near walls and boundaries. In standard aerofoil CFD modeling, many studies adopt an unstructured grid in most of the computational domain, with a structured prism layer used only at the aerofoil wall [130, 131].

Both unstructured [46] and structured meshes [121] have been used in the analysis of the cycloidal rotor in 2D and 3D with success. The current geometry uses a 50mm chord, and to incorporate the small LE and TE of the blade geometry, a hybrid mesh of quadrilateral and tri-mesh elements, using a combination of structured and unstructured mesh regions, has been used, as shown in figure 6.2. A structured mesh using multiple layers of prism elements was specified at the blade wall, as shown in figure 6.3. Prism elements allow near-wall mesh refinement via high aspect ratio elements, reducing numerical diffusion at the wall and improving solution accuracy [129]. For the current study, the number of prism layers was set to 30, but the minimum requirement is usually between 10-20 [122]

The y+ value was set to less than or equal to 1.0 for the first row of mesh elements closest to the blade to accurately capture the boundary and viscous sub-layer region [132], as outlined in figure 6.4 for the current turbulent model solver. y+ is a non-dimensional distance that defines the ratio between the laminar and turbulent flow within the cell. A low value of y+ represents a flow that is assumed to be laminar, and as y+ increases, a transition to turbulent flow is assumed [129]. Previous cycloidal rotor CFD studies have assumed a constant height for the first row of mesh elements to achieve the y+ value required [20].

To improve solution convergence, meshing metrics, as defined by ANSYS [129], were used to ensure mesh quality, covering mesh orthogonality, skewness, and aspect ratio. Othrogonaility values were kept above the minimum recommended of 0.1 and skewness less than the recommended maximum of 0.85 for a quadrilateral and triangular mesh in all cases.

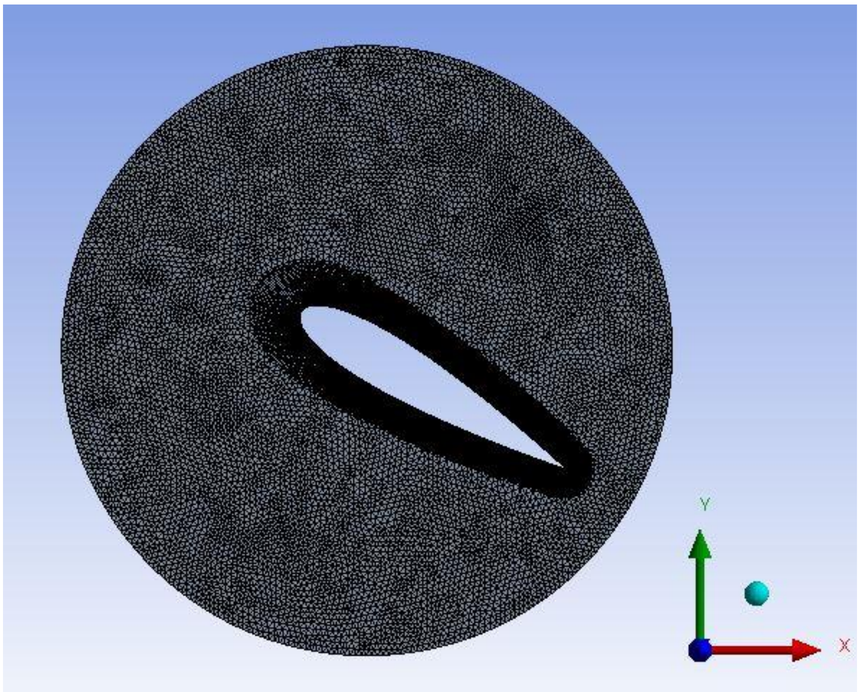

Figure 6.2 – Blade rotating subdomain mesh definition

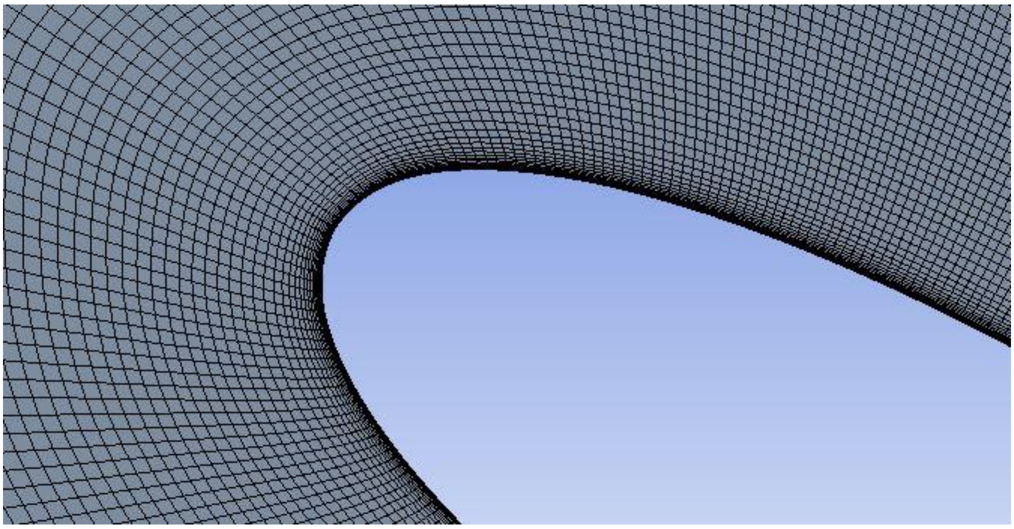

Figure 6.3 – Blade wall structured mesh definition

6.7. Boundary Conditions

At each blade-to-rotor domain interface, a non-conformal boundary was specified to define the zones on either side of each interface. This enables a sliding mesh approach to be implemented, allows flow information to be shared across interface regions, and allows relative motion between domains. A non-conformal contact was also used to remove the need for the mesh element vertices to be identical on either side of the interface. The non-slip boundary applied at each blade wall modeled the assumption that the flow moves at the same velocity when in contact with the blade.

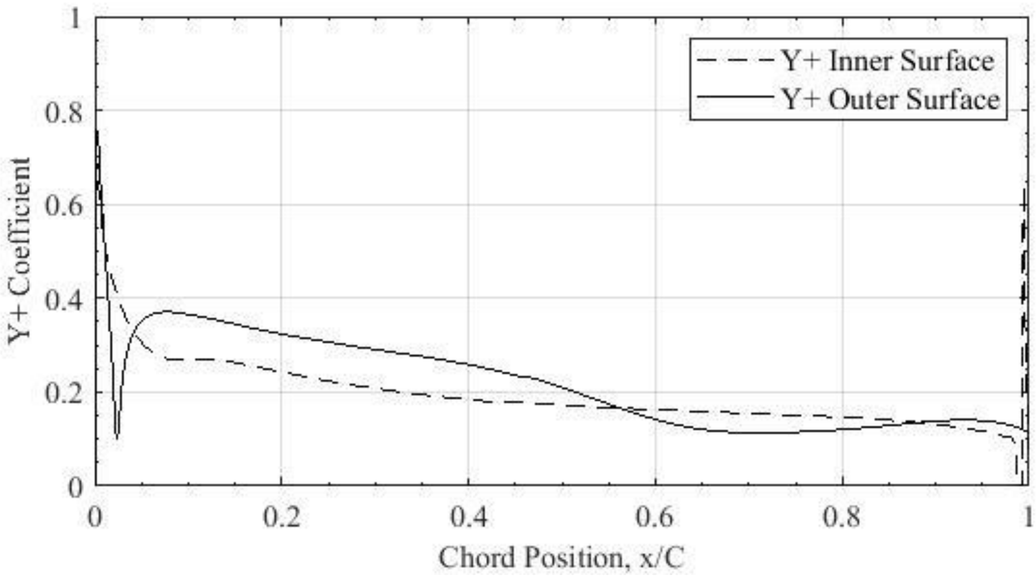

Figure 6.4 – Single blade Y+ contour plot with a 40° blade cyclic pitch input

At the extreme edges of the computational domain, a pressure far-field condition was used to model the free-stream conditions at infinity, or 30D, in the current setup. A turbulence intensity of 0.1% was assumed at each of the far-field boundaries, in line with [127].

The air was modeled as an incompressible gas, assuming that the density is constant with time. Air is considered close to incompressible below M_n of 0.3. The maximum flow velocity in the current research is up to M_n of approximately 0.1.

6.8. Problem Set up in Fluent

The angular velocity of the cycloidal rotor blade when undergoing pitching motion is not constant with time. This cannot be achieved within the Fluent user interface, and a user-defined function (UDF) needs to be created. A UDF is an additional C program that is dynamically loaded into Fluent to update the rotor and blade positions at each time step.

Lift, drag, and pitching moment monitors were created for each blade to enable post-processing of instantaneous data for comparison across models and calculation of rotor to mean performance and vibratory response. This also enabled the convergence criteria to be checked at the end of each run. As a result, the number of rotations to convergence sometimes varied between analyses. A coupled pressure-based solver with a second-order linear upwind differencing scheme was used to improve convergence and model stability. A second-order implicit time discretization was used throughout to account for the model's transient nature and improve accuracy.

6.8.1. High-Performance Computing Setup

A high number of CFD runs were required to undertake the baseline cycloidal rotor configuration and optimization analyses. Running each analysis on a desktop PC was impractical due to only one model running at any time. The High-Performance Computing (HPC) facility was used at the University of Bath, Balena, to overcome this. A Fluent journal file was created for each model to automate the model setup process and export results for post-processing.

6.9. Convergence Criteria

For the current setup, two criteria were used to monitor solution convergence. First, for each time step, a convergence criterion of $1x10^{-5}$ was used for all governing equations to ensure that the solution was well converged in each time step. A second check was also undertaken to monitor the instantaneous blade loads in the X and Y measurement directions during each rotor rotation, as shown in figure 6.5, where instantaneous rotor resultant thrust is shown over multiple rotations. An RMS error analysis was undertaken between each azimuthal position for subsequent rotations, and an overall error was calculated. The model was assumed to be converged when the overall RMS error between rotations was less than 0.1%. The example shown in figure 6.5 has an overall RMS of 0.065%.

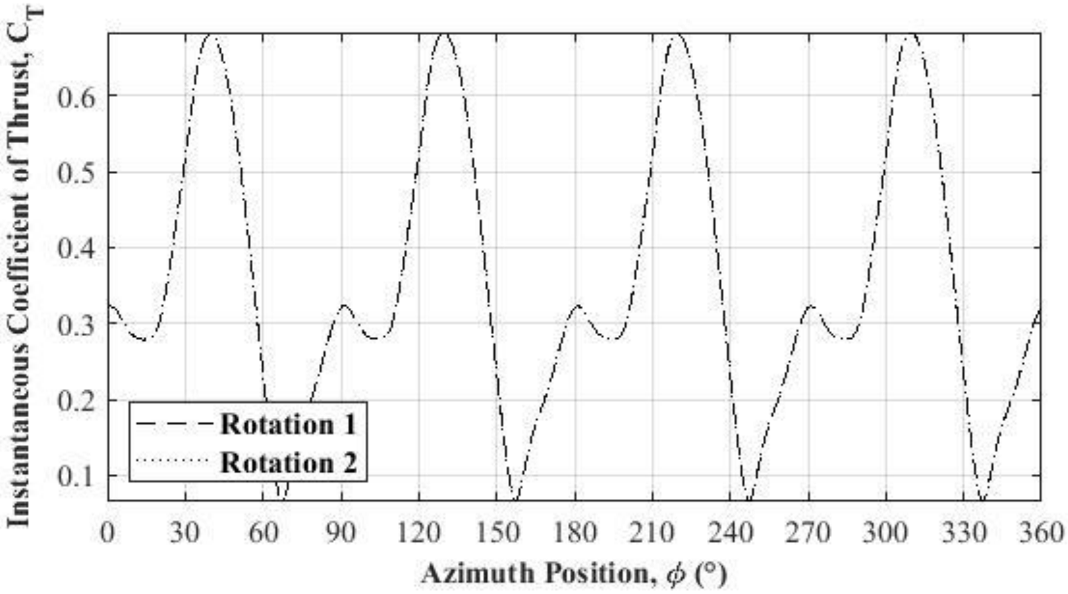

Figure 6.5 – Instantaneous rotor resultant thrust analysis over multiple rotor rotations

6.10. Grid Sensitivity Studies

The quality of the mesh can have a large effect on the predicted rotor mean and vibratory loads. Therefore, mesh dependency analyses were undertaken similarly to [30,121] for three separate meshes to find an optimum mesh configuration. Each subsequent mesh contained an increased number of cell elements, achieved by increasing the number of chordwise mesh elements on the blade chord for a single configuration, assuming a blade cyclic pitch amplitude of 40°. The overall cell count of the three mesh configurations was 175,486, 451,283, and 625,842, associated with 150, 300, and 450 elements on the pressure and suction sides of the blade, respectively. This gives a chordwise mesh element length of between 0.33mm and 0.11mm.

Mean rotor performance coefficients were used to gauge mesh efficacy. A 0.34% deviation in the resultant coefficient of thrust was calculated between the 300 and 450 chordwise element mesh, but run time increased by 48%. As a result, the mesh configuration with 300 chordwise mesh elements gives the best combination of solution accuracy and run time. The mesh was taken forward for subsequent analyses, giving a chordwise element size in line with [125].

6.11. Time Step Sensitivity Study

For transient analysis, mesh density is not the only optimization required. A time-step optimation must also be undertaken to ensure the solution is time-step independent. A total of six-time steps were considered corresponding to an azimuth increment between 0.1° and 5°, as shown in figure 6.6, where the resultant coefficient of thrust is calculated for the chosen mesh configuration. The calculated delta between the coefficient of thrust at a time-step increment of 0.1° and 0.5° reduces by 1.02%, but the solution time increases by a factor of 5, making each run computationally expensive. As a compromise, an azimuth increment of 0.25° was adopted for all studies, giving 1,440 increments per rotor revolution compared to 1,200 utilized by [46].

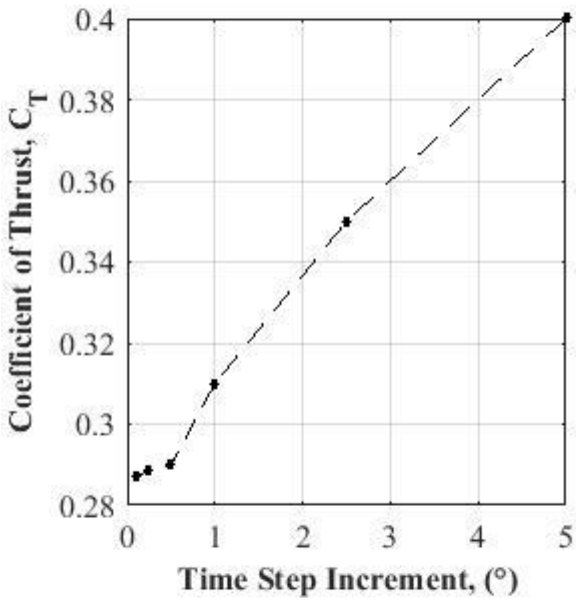

Figure 6.6 – Transient CFD mean rotor performance time step sensitivity analysis

6.12. Data Reduction

Before presenting the CFD model data, data processing and reduction methodologies are presented to calculate the mean rotor performance and dynamic vibratory response. Finally, the performance parameters are presented in non-dimensional form.

6.12.1. Mean Rotor Performance

The individual CFD instantaneous force data from the X and Y direction force monitors F_x and F_y are summed over the total number of blades to calculate the instantaneous rotor forces in the two measurement directions. The data sets were phase averaged over the last five analysis rotations once the convergence criteria had been met, as outlined in section 6.8. The resultant instantaneous forces in the X and Y directions are given by;

$$F_{x_R} = \sum_{q=1}^{N_b} F_x \tag{6.1}$$

and

$$F_{y_R} = \sum_{q=1}^{N_b} F_y \tag{6.2}$$

The resultant rotor instantaneous force profile is then given by

$$F_{R_R} = \sqrt{{F_{x_R}}^2 + {F_{y_R}}^2} \tag{6.3}$$

F_{R_R} is then used to calculate the mean rotor thrust, F_R.

The instantaneous blade forces in the X and Y directions were resolved into tangential and normal force components relative to the rotor base diameter to calculate the instantaneous blade torques, Q_B. The blade torque was calculated from the blade tangential force. Individual blade torques are then summed over the total number of blades to calculate the instantaneous rotor torque profile

$$Q_R = \sum_{q=1}^{N_b} Q_B \tag{6.4}$$

Q_R is then used to calculate the mean rotor torque, Q. The mean rotor power was calculated from

$$P = Q\omega \tag{6.5}$$

where ω is the rotor angular velocity.

All results are presented as non-dimensional coefficients for comparison with independent studies, where C_T and C_P represent the coefficient of thrust and power, respectively, defined by

$$C_T = \frac{T}{\rho_a A_R \omega^2 R^2} \tag{6.6}$$

and

$$C_P = \frac{P}{\rho_a A_R \omega^3 R^3} \tag{6.7}$$

where ρ_a is the air density, A_R is the rotor planform area, and R is the radius of the rotor.

6.12.2. Rotor Vibratory Response

Each CFD model data set, corresponding to a specific rotor speed and blade cyclic pitch angle, was analyzed to calculate the rotor vibratory response. Data in the X and Y directions were phase averaged in a similar manner to section 4.6 to produce the resulting rotor vibratory response over one rotation in two orthogonal measurement directions. A Fast Fourier Transform (FFT) was undertaken, and the magnitude and phase of each signal in the X and Y directions were extracted for the first 16 rotor harmonics from 1/Rev to 16/Rev for comparison with experimental and BET code data. The magnitude and phase of each harmonic were converted into equivalent sine and cosine components to aid later optimization studies.

6.12.3. Vortex Shedding Characteristics

The Q-criterion was calculated to enable comparison between cases with different blade cyclic pitch amplitude inputs. The Q-criterion defines vortices as areas where the vorticity magnitude is greater than the magnitude of the rate of strain, where

$$\mathrm{Q} = 0.5(||\Omega||^2 - ||\mathrm{S}||^2) \tag{6.8}$$

and Ω is the vorticity tensor and S the strain rate tensor. Using the Q-criterion, a region with $Q > 0$ represents the existence of a vortex and flow rotation.

6.13. Flow Periodicity

It was important to understand how the rotor flow and vortex shedding varies with time to enable a method to be developed for rotor vibration suppression. A system where the flow is random or periodically unsteady is difficult to optimize because the system response varies in every subsequent rotation. The induced rotor inflow and wake were overlaid for multiple rotor rotations as outlined in figure 6.7, with a 40° blade cyclic pitch input to assess the periodicity of the flow. Figure 6.7 illustrates that the resultant flow vectors overlapped on each rotation when the solution was converged, meaning the flow was a steady periodic flow. As a result, it becomes easier to predict rotor performance. In addition, it enables a control optimization methodology to be developed that does not change with time when the rotor is hovering.

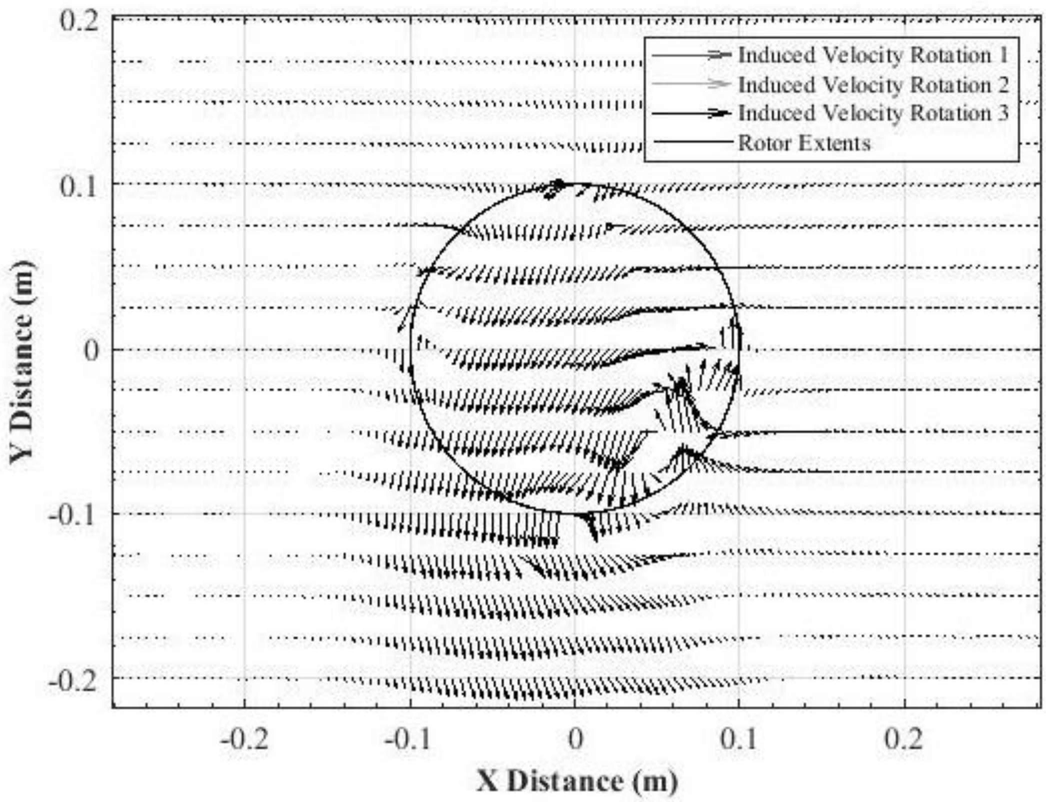

Figure 6.7 – Rotor wake periodicity check over three-rotor rotations, with a 40° blade cyclic pitch input

6.14. CFD Model Validation

The current section summarises the validation of the current CFD modeling approach against three independent studies [30, 46, 112] at a single blade cyclic pitch angle with increasing rotor speed for a three and four-blade cycloidal rotor by recreating the geometries defined in the respective papers. The studies include both computational and experimental data sets.

6.14.1. Independent Study Flow Field Comparison

A qualitative agreement was sought for the current CFD modeling approach before an in-depth analysis of mean rotor and instantaneous blade loads outlined in [98] was undertaken. This was achieved through a comparison of the velocity contours and streamline data published in [121], as shown in figures 6.8 and 6.9, respectively, to those developed in the current research for the same geometry. Figure 6.8 shows that at blade position B1, the blade is undergoing dynamic stall will LE vortices being shed. At the same time, blade B2 is beginning to separate at the LE. A vortex structure shed from the TE of blade B3 is also being convected into the blade wake in the northwest quadrant. The streamlines confirm the convection of vortices from blades B1 and B3 in figure 6.9. Vortices can be identified in the northwest and southeast quadrants and below the rotor in the far-field wake.

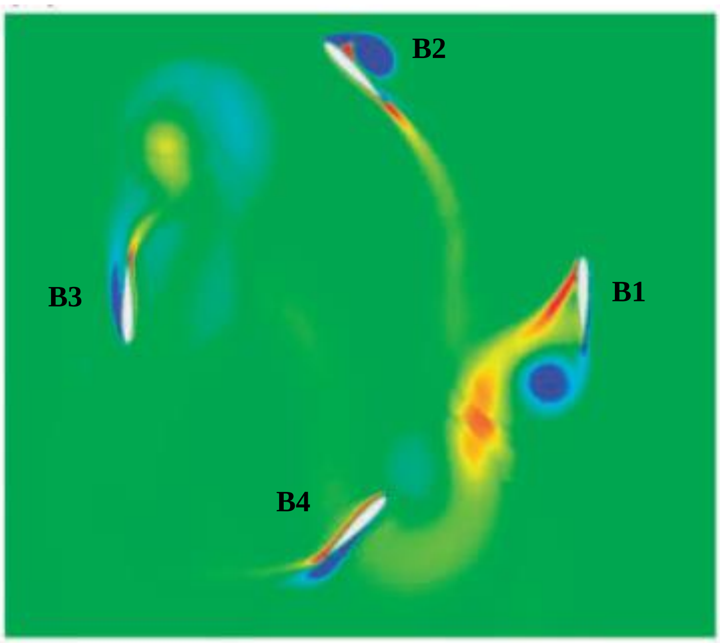

Figure 6.8 – Resultant velocity contour plot of a four-blade hovering cycloidal rotor with a 45° blade cyclic pitch input [121]

Reproduction of the model in [121] with the current methodology is shown in figure 6.10 for velocity contours. Concentrating on the flow artifacts highlighted above, it can be seen that the overall flow structure is in very good qualitative agreement between the two approaches, with the vortices being shed from blades B1 and B3 being almost identical visually. The vortices in the northwest and southeast quadrants are also identified. Blade instantaneous forces were also compared for one rotor revolution in the X and Y measurement directions. The peak RMS error was calculated to be 2.4% between the published and calculated data, providing initial validation of the proposed modeling approach.

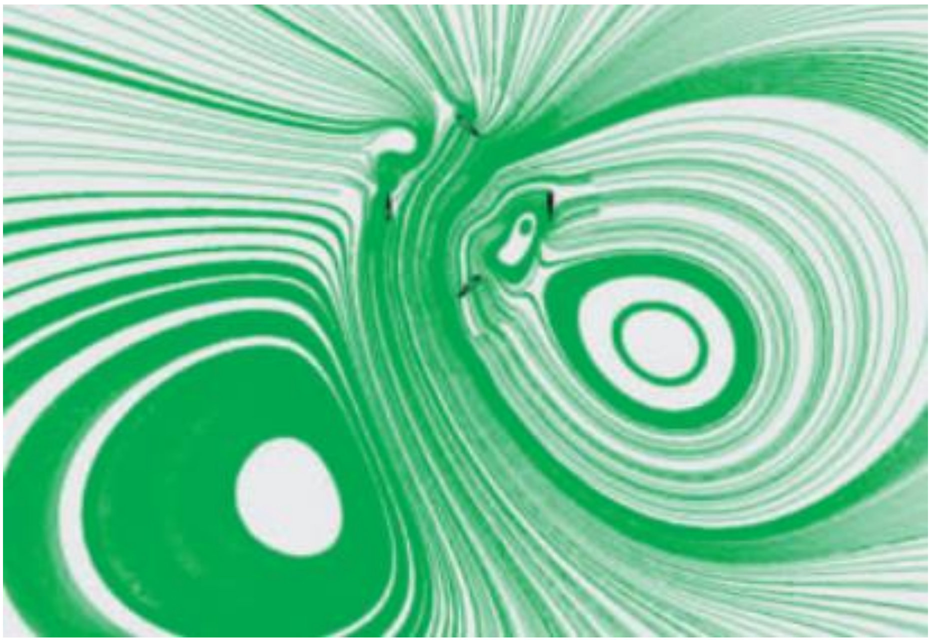

Figure 6.9 – Plot of velocity streamlines of a plot of a four-blade hovering cycloidal rotor with a 45° blade cyclic pitch input [121]

6.14.2. Independent Study - Mean Rotor Performance Comparison

A comparison of the current CFD modeling approach to the three-bladed configuration defined in [112] is shown in figures 6.11 (a) and (b) for mean rotor thrust and power. The thrust results from the current CFD model in figure 6.11 (a) are in very good agreement across the speed range 900 to 1,800 RPM compared to the independent experimental and CFD results. Above 1,800 RPM, the rate of change of thrust with rotational speed increases experimentally but is not replicated in the independent CFD analysis; the thrust is also underpredicted. Compared to the CFD results in [30], the current CFD study over-predicts the mean thrust but shows closer agreement with the experimental data. Between 1,800 and 2,000 RPM, the thrust is again underpredicted, which could be due to an experimental anomaly instead of a modeling inaccuracy. A similar trend is identified in figure 6.11 (b) for rotor power, with good agreement between results across the rotational speed range considered.

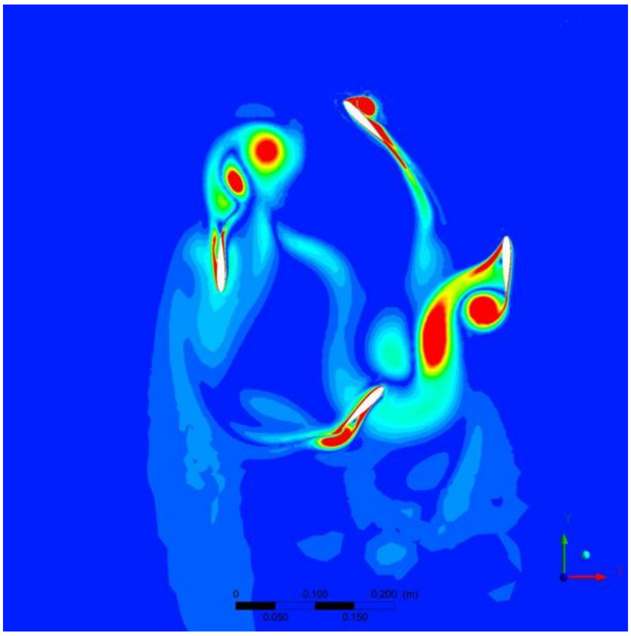

Figure 6.10 – Resultant velocity contour plot of the four-blade hovering cycloidal rotor from the current CFD analysis model, with a 45° blade cyclic pitch input

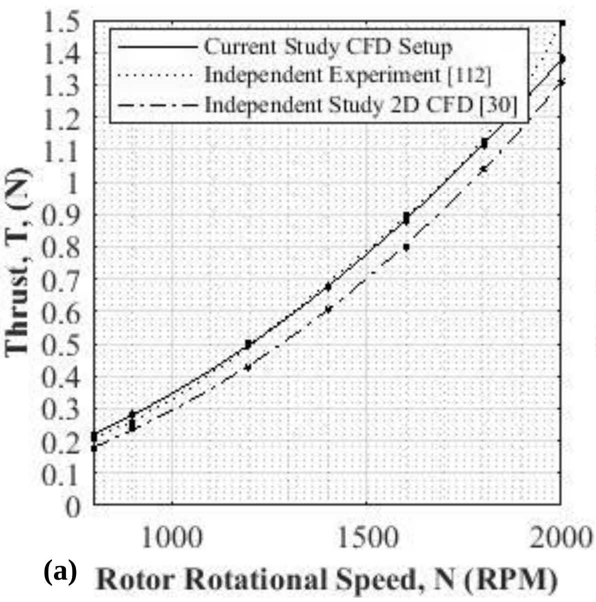

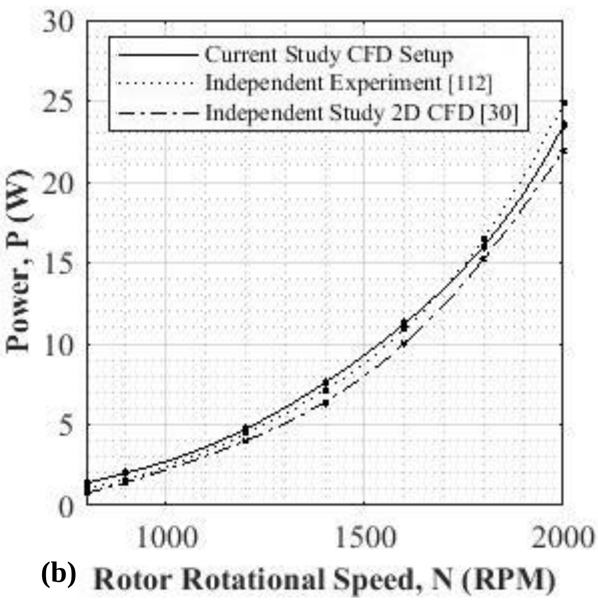

Figure 6.11 – Current CFD study methodology mean performance parameter comparison to independent mean performance parameters for a three-blade cycloidal rotor [30,112]. (a) Thrust and (b) Power

The current CFD model results for the four-bladed configuration [46] are shown in figure 6.12 (a) for thrust and 6.12 (b) for power. Good agreement is seen at lower rotational speeds below 700 RPM in both cases. Above this, an increased deviation between published experimental and CFD thrust results is seen, with the current CFD model results lying between the two published datasets. The calculated power at each analyzed rotational speed for the current CFD model, as shown in figure 6.12 (b), is in very good agreement with the experimental data presented in [46] up to 700 RPM and between the two data sets thereafter. Based on this, the ability of the current CFD modeling methodology to model cycloidal rotor mean performance comparable to independent studies is validated.

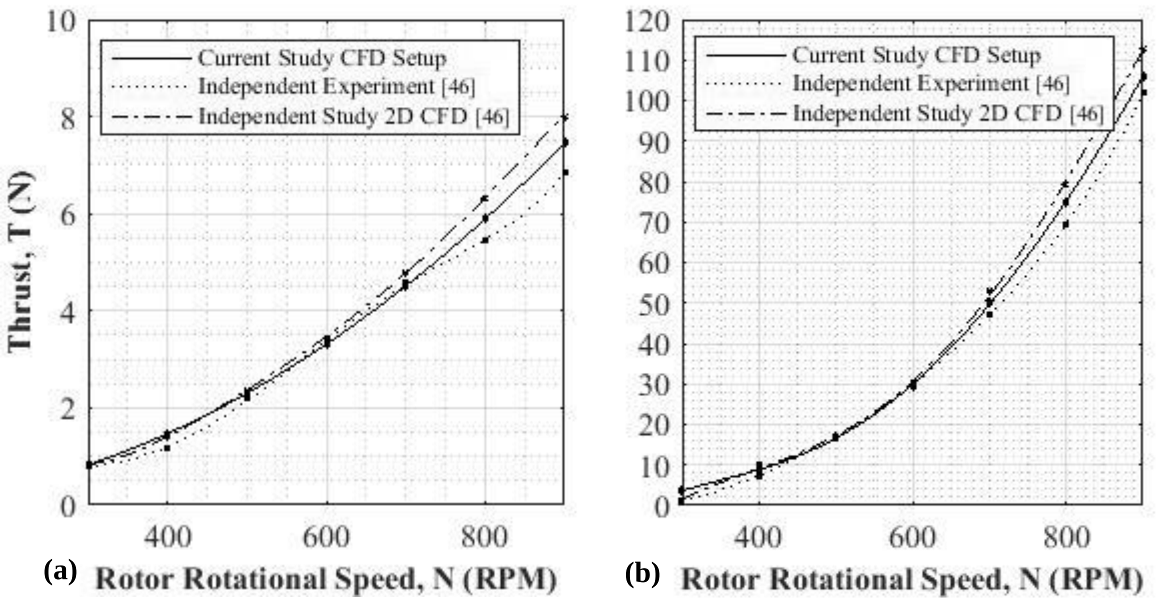

Figure 6.12 – Current CFD study methodology mean performance parameter comparison to independent mean performance parameters for a four-blade cycloidal rotor [46]. (a) Thrust and (b) Power

6.14.3. Current Research Model - Mean Rotor Performance Validation

Additional validation of the 2D CFD modeling approach was also undertaken by comparison to the baseline experimental measurements taken with the test rig and BET code developed in the present work. This is shown in figures 6.13 (a) and 6.13

(b) for thrust and power, respectively. Again, good agreement is identified across the entire blade cyclic pitch angle range considered. CFD calculated thrust values fall within the experimental measurement range in all cases, with one area requiring further discussion. At low blade cyclic pitch angles between 0° and 5°, the resultant experimental thrust is over the measured experimental range is considerably higher than those predicted by the computational models. The CFD model replicates the findings of the BET code results at the extreme low end of the blade cyclic pitch angle inputs, which is possibly attributable to the effect of the rotor end plates on force generation at low pitch amplitudes.

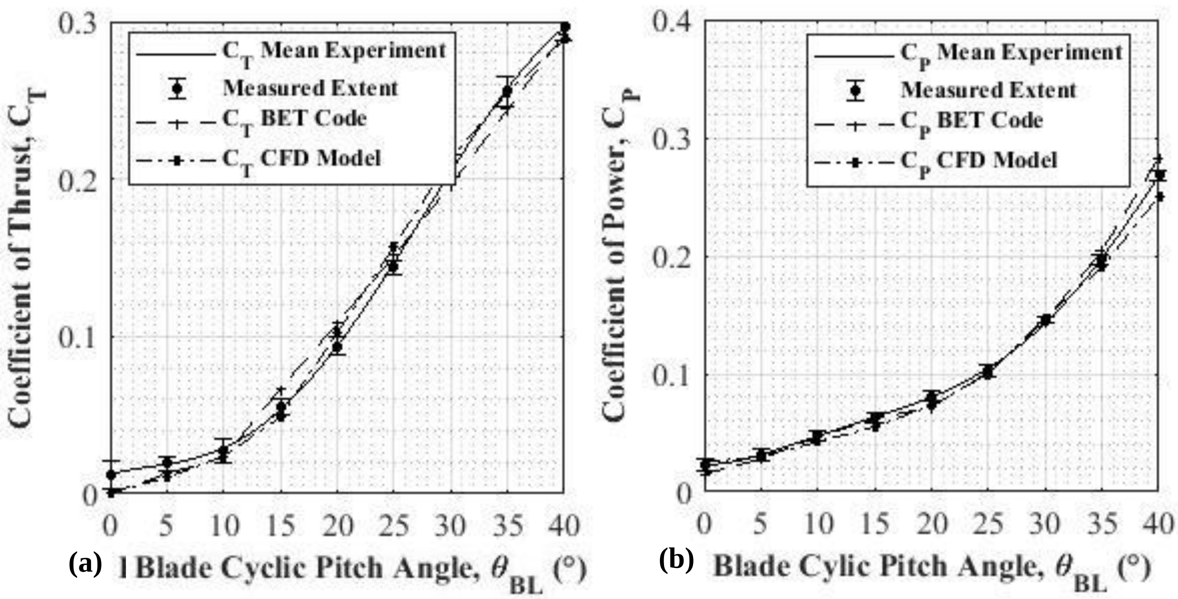

Figure 6.13 – Current CFD study data comparison to current study baseline experimental mean performance and BET-code parameters with changing blade cyclic pitch angle and rotor rotational speed. Measured extents are shown from 500 to 1,000 RPM

Figure 6.13 (b) shows the rotor power coefficient. Above a blade cyclic pitch angle of 30°, the computational model power is underpredicted by up to 10% at a blade cyclic pitch amplitude of 40° related to 3D flow losses due to spanwise flow variation and flow swirl. This is not accounted for fully in the 2D model that approximates the flow at the rotor center span. However, below 30°, the correlation with the experimental data shows considerable improvement. Based on this, the current CFD modeling methodology has been validated for cycloidal rotor performance over multiple rotational speeds and blade cyclic pitch amplitude between 5° and 40° when the maximum underprediction compared to experimental data is up to 10% at a blade cyclic pitch amplitude of 40° is considered.

6.15. Further Computational CFD Model Development

By nature, the flow with the cycloidal rotor is not 2D, with 3D effects becoming more significant in low aspect ratio (AR) configurations due to the contribution of blade tip vortices and blade vortex interaction (BVI). Both blade tip vortices and BVI are a large source of unsteady rotor air loads that can limit the cycloidal rotor's hover and forward flight performance. Many challenges still exist to capture these effects faithfully. To account for the 3D flow effects, the 2D CFD models can be extended to 3D to add more accuracy and consider 3D flow effects.

The analysis of a 3D CFD model will enable the influence of certain rotor design features on the performance of the cycloidal rotor to be considered. Two examples are; end plate diameter and blade twist. The effect of the end plate on the rotor flow cannot be captured with a 2D CFD analysis, but varying diameters can be analyzed in a 3D model to establish the sensitivity of the rotor aerodynamic performance to changes in end plate geometry. A 3D CFD analysis assumes the rotor blades are rigid without deflection or twist. Implementing a 3D fluid-structure interaction (FSI) model would enable a higher fidelity model to be developed accounting for blade deformation, which would be useful during aeroelastic and vibration analyses. However, it is worth noting that the transition to a 3D CFD model comes at the expense of computational setup and run time.

3D analyses will enable the modeling of several key features of the cycloidal rotor, including the modeling of dynamic stall and blade tip vortex formation. Both dynamic stall and blade tip vortices include large recirculating turbulent separated flow regions that require a large number of mesh points in the regions of interest to capture the phenomena accurately. The accuracy of nearly all CFD models is grid-dependent. Meshing techniques will need to be developed in a similar manner to conventional rotorcraft, where mesh grid adaptive techniques have been used to allow meshes to be refined only where required with good success [117] while reducing computational overhead. This will enable the 3D flow effects pertinent to the cycloidal rotor to be captured more accurately.

As a follow-on from modeling the 3D flow features on a micro level, a suitable meshing strategy must also be developed on a macro level to enable the rotor wake to be modeled and predict the subsequent convection of vorticity through the flow field. This will allow more information on the overall performance of the rotor to be obtained and an understanding of the overall flow field to be developed while reducing numerical error and artificial diffusion, which has posed a considerable challenge in conventional rotorcraft studies [117].

The majority of industrial CFD analyses assume a Reynolds Averaged Navier-Stokes (RANS) turbulence model to give a compromise between model run time and solution accuracy. An alternative method to model the larger vorticial structures is the use of Large Eddy Simulation (LES). LES is able to predict vortex shedding and flow recirculation accurately and model turbulence with much higher accuracy than RANS models, although run time can be significantly higher. There is much scope to model the 3D cycloidal rotor flow features accurately, but the scope and targets of each study need to be considered individually. The use of LES in the current research would have been time prohibitive.

6.16. Chapter Review

The current chapter has outlined the methods used to validate the development of the current CFD modeling approach with experimental results from the current research and independent experimental and computational models. The CFD study has shown that the 2D CFD modeling approach developed can predict the mean rotor performance with reasonable accuracy compared to the current experimental data and independent data sets.

In Chapter 7, the CFD model developed is compared with the BET code and experimental results generated in the current research to determine the efficacy of the 2D model in the calculation of cycloidal rotor vibratory response for the baseline cycloidal rotor configuration. Finally, the 2D CFD model is used in the cycloidal rotor vibratory response optimization study outlined in Chapter 8.

Chapter 7 – Dynamic Hub Loading of a Cycloidal Rotor

7.1. Introduction

The accurate calculation of rotor vibratory loads is important in designing for reduced component fatigue and increased rotorcraft reliability. However, compared to conventional rotorcraft, the vibratory response of the cycloidal rotor is little researched. The present chapter describes the first known experimental and computational modeling investigation to characterize the vibratory response of a cycloidal rotor in hover with varying blade cyclic pitch amplitude and rotor speed.

Following the successful validation of the reduced-order computational and CFD models with respect to the mean rotor performance, as developed in Chapters 5 and 6, this chapter aims to determine the extent to which numerical models of varying fidelity can be used to determine rotor vibratory hub loads.

The rotor vibratory response is analyzed, and differences between the computational models and the dynamic experimental test results are identified. The dynamic experimental test results are determined using the experimental techniques developed in Chapter 4 to dynamically calibrate the force-torque sensor instantaneous experimental results to account for the dynamic response of the test rig developed in Chapter 3. Further post-processing of the computational model flow fields is then used to gain further insight into the physical mechanisms behind the rotor vibratory response.

7.2. Background to Rotorcraft Rotor Vibration

Rotorcraft vibration emanates from several sources, including unsteady aerodynamic loads acting on the rotor blades, engine and gearbox vibration, and rotor-fuselage interaction. The current research focuses on the evaluation of rotor unsteady aerodynamic loads only.

Alternating aerodynamic loads are entirely periodic [133]. This means they repeat during each rotor revolution and must be multiples of the rotor rotational speed. The aerodynamic loads acting on the rotor blade occur due to the variation in blade effective angle of attack (AOA) with changes in rotor azimuth angle due to the changing blade relative velocity and overall blade geometric pitch angle, θ_S. In the calculation of the blade lift and drag forces, the calculated forces vary with the square of the blade's relative velocity using standard equations, resulting in $\sin^2(\Psi)$ terms from the definition of the blades' relative velocity in Chapter 5. Where $\sin^2(\Psi)$ can be written as

$$\sin^2(\Psi) = \frac{1}{2} - \frac{1}{2}\cos(2\Psi) \tag{7.1}$$

Equation 7.1 shows that blade velocity variation with azimuth contains multiple harmonics. When the interaction of all the rotor blades is considered, the individual blade aerodynamic loads sum at the rotor hub to generate higher harmonics of periodic force [133].

To validate the vibratory loads measured at the rotor hub in the nonrotating frame and to develop an optimization methodology to reduce rotor vibratory loads, it is vital to determine how the periodic blade forces combine to generate a resultant rotor hub load. In order to provide a check for the results presented in the current chapter and the higher harmonic control (HHC) optimization analysis undertaken in Chapter 8, an example to show how the individual blade forces change between the rotating and nonrotating frame will be provided based on a conventional helicopter blade lag hinge in-plane load provided in Gessow [133]. A typical two-bladed helicopter rotor is shown in figure 7.1, where the lag hinge tangential force F_{tan} is given by

$$F_{tan} = F_o \sin(n\Psi) \tag{7.2}$$

where F_o is the aerodynamic force amplitude. At any instant with changes in blade azimuth position, the component of F_{tan} acting is

$$\mathrm{F_{in}} = \mathrm{F_{tan}} \sin(\Psi) \tag{7.3}$$

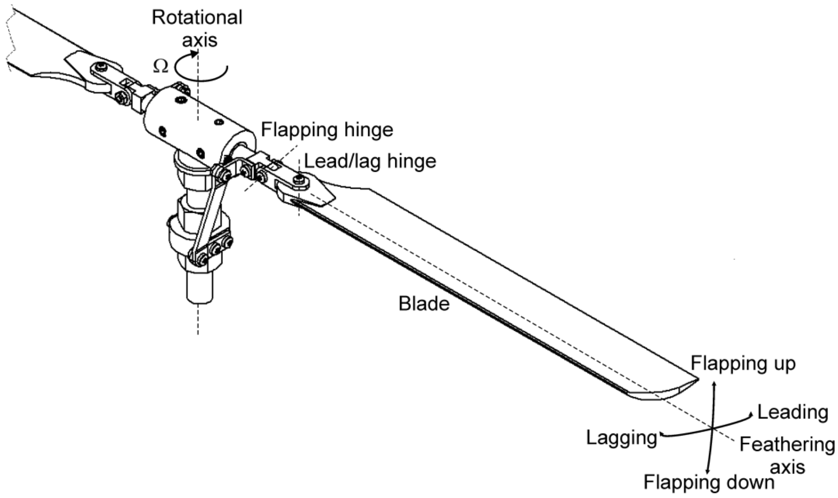

Figure 7.1 – Conventional helicopter two-blade rotor geometry [134]

Equation 7.3 contains the product of two sine terms, and, using standard trigonometric identities, the product of the sine terms can be written as

$$\sin(\mathrm{n}\Psi)\sin(\Psi) = \frac{1}{2}\big(\cos(\mathrm{n}\Psi - \Psi) - \cos(\mathrm{n}\Psi + \Psi)\big) \tag{7.4}$$

Factoring equation 7.4 then gives

$$\sin(\mathrm{n}\Psi)\sin(\Psi) = \frac{1}{2}\big(\cos(\Psi(\mathrm{n}-1)) - \cos(\Psi(\mathrm{n}+1))\big) \tag{7.5}$$

Equation 7.5 shows that the product of two sine terms (or cosine terms) can be written as the sum of terms at a frequency n + 1 and n – 1, where n represents the frequency per revolution. All analyses assume that the rotor is tracked, meaning that the design and manufacture of all rotor blades are identical [85], along with the applied individual blade aerodynamic loads. These assumptions mean that only forces that are integer multiples of the blade number will be transmitted to the rotor hub and the nonrotating frame [86]. Therefore a four-bladed rotor can experience rotor hub loads at only 4/Rev, 8/Rev, and 12/Rev, etc. All other frequencies cancel at the rotor hub [86].

The assumption that only integer multiples of the blade number are transmitted to the rotor hub is proven by the summation of sine terms at n + 1 and n – 1 in equation 7.5. For example, if a blade aerodynamic force acts at 3/Rev, assuming a four-blade rotor, the 3/Rev blade force can be broken down into a 2/Rev and 4/Rev component. The 2/Rev components will cancel due to the phase difference between individual blade loads [133], and only the 4/Rev force component force will be transmitted to the rotor hub in the nonrotating frame. Therefore, a 3/Rev force input in the rotating frame produces a 4/Rev force at the rotor hub in the nonrotating frame.

7.3. Analysis of Uncorrected and Corrected Experimental Rotor Vibratory Hub Loads

During the experiments, the rotor hub forces and torques measured at the iCUB sensor include the dynamic response of the cycloidal test rotor and the sensor system. For each test performed, at varying rotor rotational speed and blade cyclic pitch angle input, the dynamic response of the overall system was calculated using the methods developed in Chapter 4 to determine the overall system vibratory response at integer multiples of the rotor rotational speed.

To allow the calculated dynamic forces to be corrected for the dynamics of the test rig sensor system, the calculated system vibratory response is corrected using the transfer functions presented in Chapter 4 for each rotor force measurement axis. This process produces two sets of data, an uncorrected dataset based on the calculated experimental overall system vibratory response and a corrected dataset considering the sensor dynamic calibration process.

The uncorrected and corrected results were plotted for each test point. A representative example is shown in figure 7.2 and figure 7.3 for the X and Y measurement directions, respectively, for the first 16 rotor harmonics at a rotor speed of 600 RPM and 40° blade cyclic pitch amplitude. The effect of the dynamic calibration can be seen in figure 7.3, where the 4/Rev vibratory response is reduced by approximately 40% following results correction.

In standard rotorcraft theory, the rotor hub acts as a band-pass filter. Only kN_b/Rev harmonic loads are transmitted to the nonrotating frame [85], as previously mentioned, where N_b represents the blade number, and k is a positive integer. Figures 7.2 and 7.3 show that there is significant vibration at harmonics other than kN_b/Rev transmitted to the nonrotating frame for the current four-blade rotor.

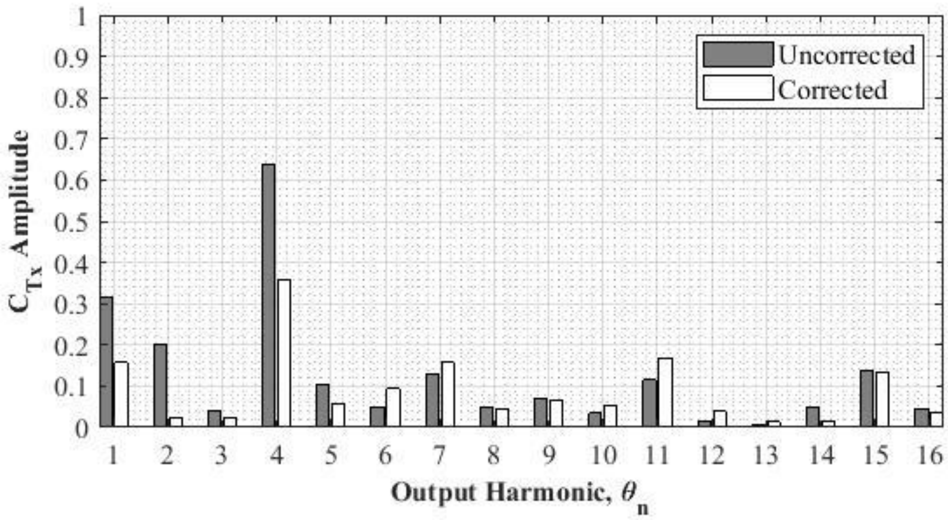

Figure 7.2 – Rotor X-direction uncorrected and corrected rotor Coefficient of Thrust amplitude vibratory response at a rotational speed N = 600RPM and blade cyclic pitch angle of 40°

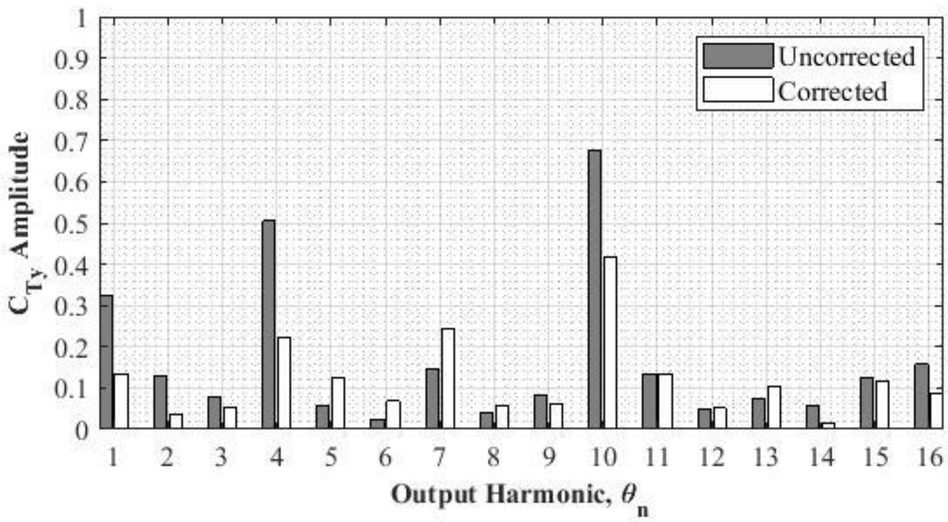

Figure 7.3 – Rotor Y-direction uncorrected and corrected rotor Coefficient of Thrust amplitude vibratory response at a rotational speed N = 600RPM and blade cyclic pitch angle of 40°

Based on the test rig driveline frequencies defined in tables 7.1 and 7.2, the main non-integer harmonic seen in the vibratory response, where possible, can be rationalized as follows. Manufacturing and setup discrepancies, such as variations in blade manufacture, produce the 1/Rev response, in addition to the 1/Rev force generated due to rotor asymmetric blade pitching. The 2/Rev is attributable to the spindle and motor bearing ball pass frequency, and the 5/Rev harmonic represents the drive gearing assembly phase frequency.

A 7/Rev harmonic is attributable to the main drive motor frequency, and the 10/11/Rev component is associated with the drive motor and corresponds to the estimated main drive motor gearbox frequency. Finally, the 15/Rev harmonic represents the main drive gearing tooth mesh frequency.

Table 7.1 – Test rig driveline frequency harmonic summary

Parameter	Rotor Harmonic, N/rev
Rotor Gear Frequency	1
Rotor Pinion Frequency	1/3
Drive Gearing Tooth Mesh Frequency	15
Drive Gearing Assembly Phase Frequency	5
Drive Gearing Tooth Repeat Frequency	1/15
Main Drive Motor Frequency	7.05
Main Drive Motor Gearbox Frequency	10.22

Table 7.2 – Test rig rolling element bearing frequency harmonic summary

Parameter	Rotor Harmonic, N/rev
Rotor Spindle Bearing Fundamental Train Frequency	0.397
Rotor Spindle Bearing Ball Pass Frequency Inner Race	4.82
Rotor Spindle Bearing Ball Pass Frequency Outer Race	3.18
Rotor Spindle Bearing Ball Spin Frequency	2.022
Motor Spindle Bearing Fundamental Train Frequency	0.14
Motor Spindle Bearing Ball Pass Frequency Inner Race	1.931
Motor Spindle Bearing Ball Pass Frequency Outer Race	1.402
Motor Spindle Bearing Ball Spin Frequency	0.887

To understand how the amplitude of the rotor harmonics change in the X and Y measurement directions with blade cyclic pitch angle variation from 0° to 40°, harmonics from 1/Rev up to 16/Rev at a rotational speed of 600 RPM were analyzed, as shown in figure 7.4. The error bars represent the measured variation in harmonic amplitude range when considering the full range of blade cyclic pitch amplitude tested from 0° to 40° in 5° increments. The bars are the mean values of the measured harmonic amplitudes in the X and Y measurement directions.

Figure 7.4 confirms that the non-blade pass frequency harmonics are relatively constant with increasing blade cyclic pitch amplitude and are not related to aerodynamic loading and thrust generation, as thrust increases with increasing blade cyclic pitch amplitude. While these non-blade pass frequency harmonics are pertinent to understanding the operation of the current test rig, these harmonics are not intrinsic in general cycloidal rotor operation and will not be considered further in the current research.

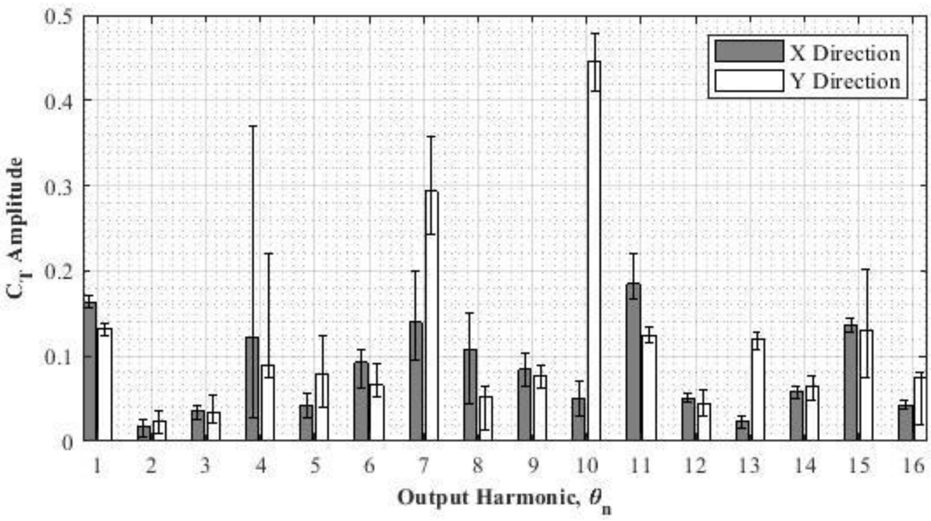

Figure 7.4 – Mean rotor vibratory hub load Coefficient of Thrust amplitude from a blade cyclic pitch angle θ_{BL} of 0° to 40° in the X and Y measurement directions, including the calculated measured range of the Coefficient of Thrust amplitude variation with changes in blade cyclic pitch angle at rotor rotational speed, N = 600 RPM

The 4, 8, 12, and 16/Rev harmonics in the X and Y measurement directions were considered to understand how the kN_b/Rev rotor harmonics vary with blade cyclic pitch angle and thrust generation, representing the first four harmonics of the blade pass frequency, N_b, $2N_b$, $3N_b$, and $4N_b$/Rev. The 4/Rev vibratory response is shown in figures 7.5 (a) and 7.5 (b) for the X and Y directions, where increased 4/Rev modulation is shown as the blade cyclic pitch angle increases past 15°. At low blade cyclic pitch inputs up to 20°, the X and Y mean 4/Rev components are comparable with an amplitude between 0.03 and 0.04. At 20° blade cyclic pitch angle and above, there is an increase in the rate of change in the X-direction 4/Rev response compared to the Y-direction, up to a maximum X-direction amplitude of 0.38 compared to 0.28 in the Y-direction. The reasons for this change will be analyzed further in subsequent sections.

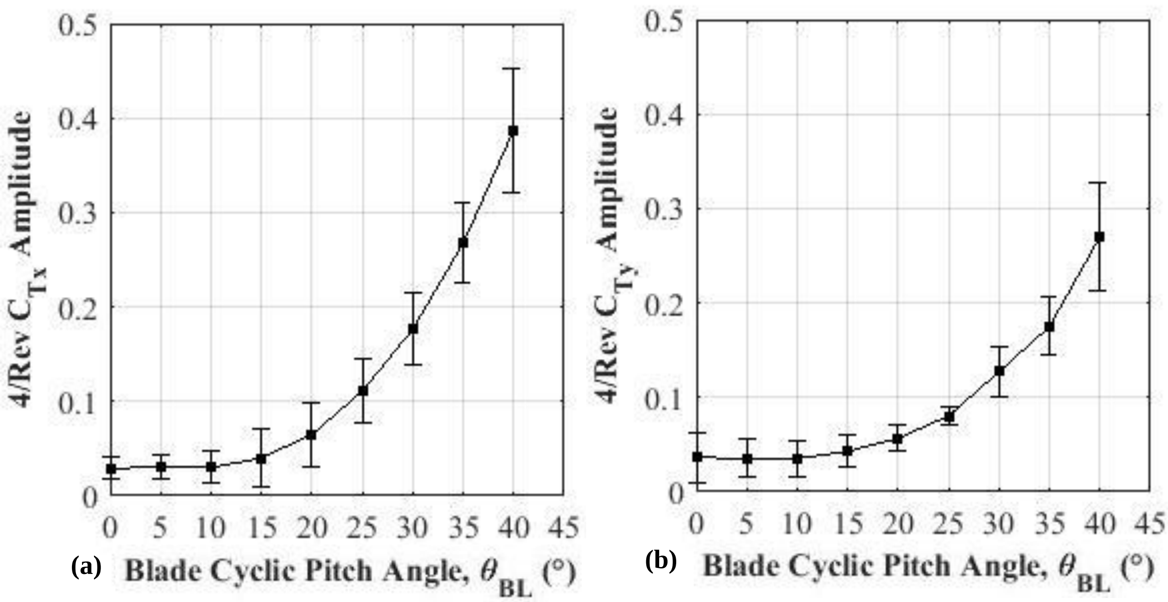

Figure 7.5 – Rotor 4/Rev Coefficient of Thrust amplitude variation with blade cyclic pitch angle. With the measured range shown from 500 to 1000 RPM (a) X measurement direction (b) Y measurement direction

Despite the mean rotor performance non-dimensional coefficients remaining constant with changing rotor rotational speed at a given pitch angle in Chapter 4, this was not found to be the same when analyzing the harmonic components identified by the measured range bars in figures 7.5 (a) and 7.5 (b) for the 4/Rev response. Above a blade cyclic pitch input of 15°, the X-direction variation with rotational speed is greater than the corresponding Y-direction test point. The X-direction amplitudes are skewed by the resonance peaks shown in figure 4.11 (a) at 46.66 Hz and 53.33 Hz, which coincide with the rotor 4/Rev response at 700 and 800 RPM, highlighting the sensitivity of the vibratory response to changes in rotor speed. This sensitivity is driven by the assumptions made in the dynamic calibration test setup, such as the excitation force application point and shaker test stand design effective stiffness and the nonlinearity identified in the THD study. The relative delta at each cyclic pitch angle increases with pitch angle increase due to modulation of the 4/Rev response, amplifying differences in results with changes in rotor speed.

The mean amplitudes of the higher harmonics of the blade pass frequency at 8, 12, and 16/Rev are shown in figures 7.6 (a-b), 7.7 (a-b), and 7.8 (a-b) for the X and Y-directions, respectively. A key finding from figures 7.6 to 7.8 is that the higher blade pass frequency harmonics do not change notably with increasing blade cyclic pitch amplitude and thrust generation. The higher blade pass frequencies can be assumed to be constant with changes in blade cyclic pitch input within the constraints of the current experimental setup. The 8/Rev response shows increased variation in the X and Y-directions when compared to the 12 and 16/Rev responses.

At low pitch angles below 15°, the amplitude of the higher blade pass harmonics is comparable to the 4/Rev response, but as the blade cyclic pitch amplitude increases, this finding breaks down. From this, the hub loads associated with higher harmonics of blade pass frequency at $2N_b$ (8/Rev), $3N_b$, and $4N_b$/Rev are much smaller than the N_b/Rev component with increasing cyclic pitch amplitude, which is not unexpected when compared to standard helicopter vibration [85].

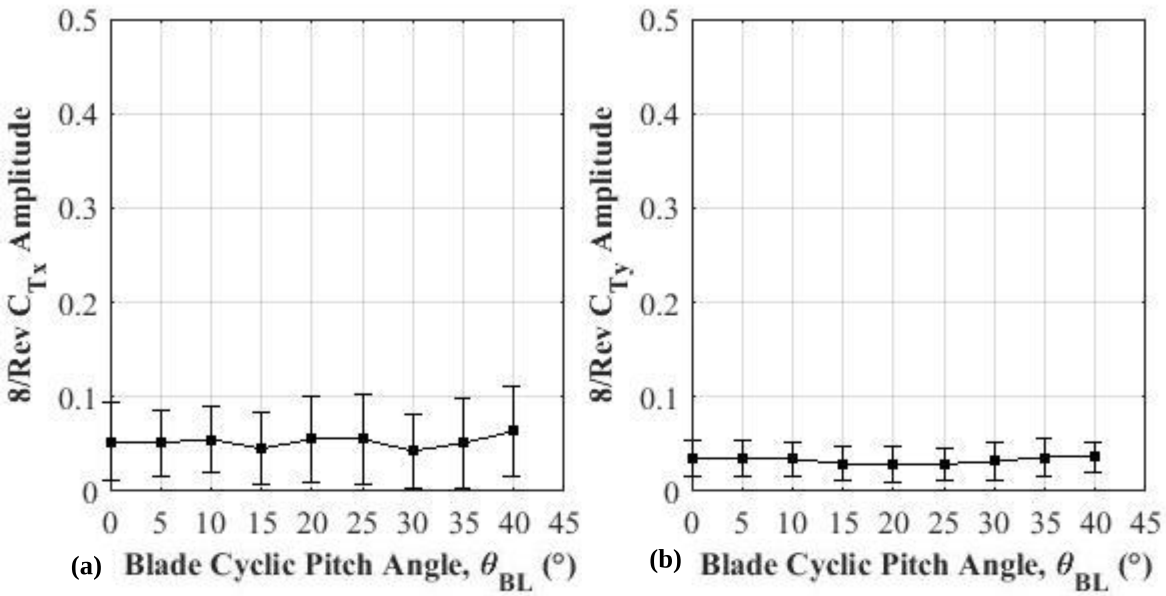

Figure 7.6 – Rotor 8/Rev Coefficient of Thrust amplitude variation with blade cyclic pitch angle. With the measured range shown from 500 to 1000 RPM (a) X measurement direction (b) Y measurement direction

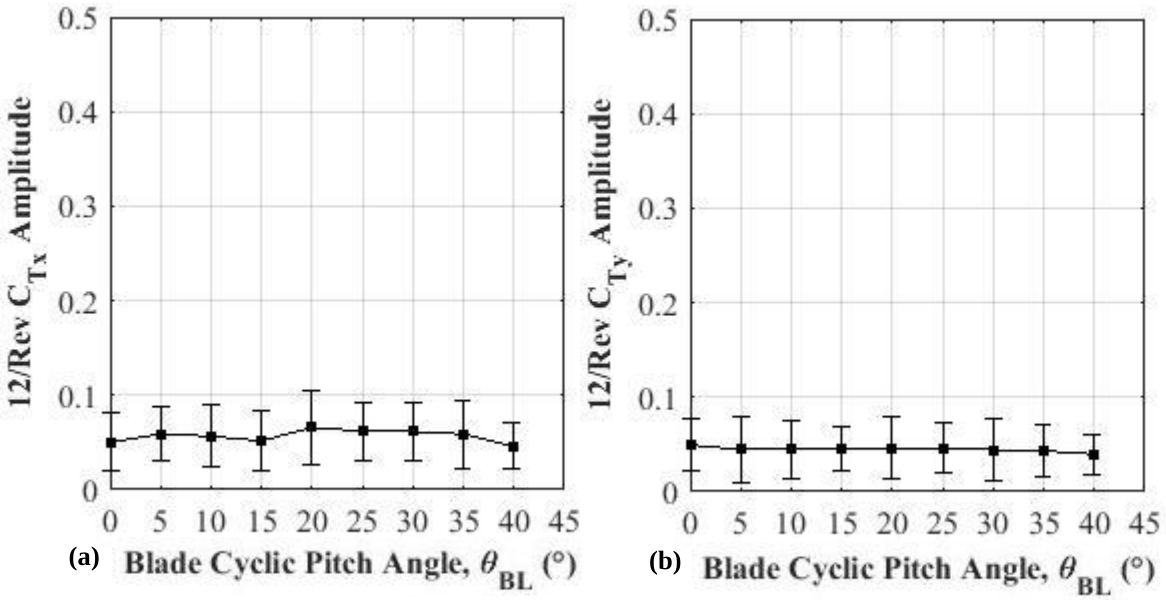

Figure 7.7 – Rotor 12/Rev Coefficient of Thrust amplitude variation with blade cyclic pitch angle. With the measured extents shown from 500 to 1000 RPM (a) X measurement direction (b) Y measurement direction

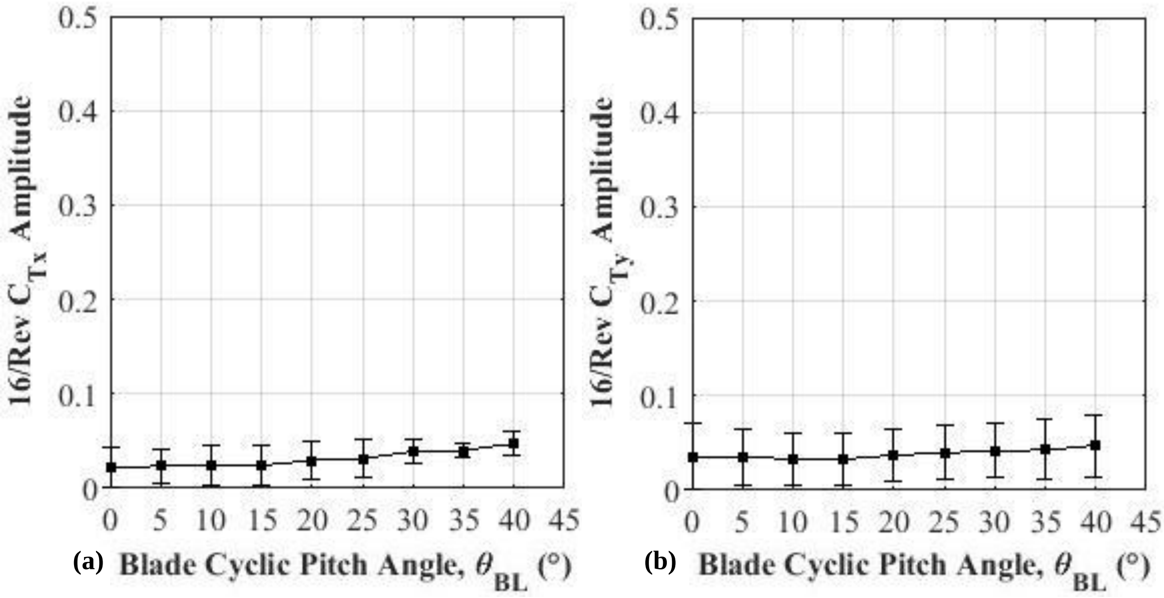

Figure 7.8 – Rotor 16/Rev Coefficient of Thrust amplitude variation with blade cyclic pitch angle. With the measured extents shown from 500 to 1000 RPM (a) X measurement direction (b) Y measurement direction

7.4. Computational Modelling Rotor Vibratory Hub Loads

The present section presents the 2D CFD and BET code computational model cycloidal rotor vibratory response over a range of rotor speeds and blade cyclic pitch amplitudes at the fundamental blade pass frequency of 4/Rev in line with standard rotorcraft studies as the main harmonic associated with rotor vibration [85] and based on the findings of section 7.3. Both computational models assume that the rotor is tracked; as such only harmonics of the blade pass frequency are transmitted to the nonrotating frame [85].

The rotor 4/Rev vibratory response, as predicted by the CFD and BET code model in the X and Y directions, is shown in figure 7.9 (a) and figure 7.9 (b). The BET code predicts a similar 4/Rev vibratory response in the X and Y directions due to the assumed uniform rotor inflow. Below a blade cyclic pitch amplitude of 15° minimal vibration is identified in the X and Y directions. The vibration level then begins to increase in both directions with increasing blade cyclic pitch amplitude up to a maximum of approximately 0.12 at a blade cyclic pitch amplitude of 40°.

Between a blade cyclic pitch amplitude of 0° and 15°, only a small deviation exists between the CFD and BET code results in the X and Y directions. However, above a blade cyclic pitch amplitude of 25° in the X direction and 20° in the Y direction, the deviation between the CFD and BET code model increases, with the CFD predicting a higher 4/Rev vibratory response in both measurement directions. At a blade cyclic pitch amplitude greater than 35°, the CFD model predicts a shift in the rate of change of 4/Rev amplitude with blade cyclic pitch amplitude increase, which is more pronounced in the X-direction.

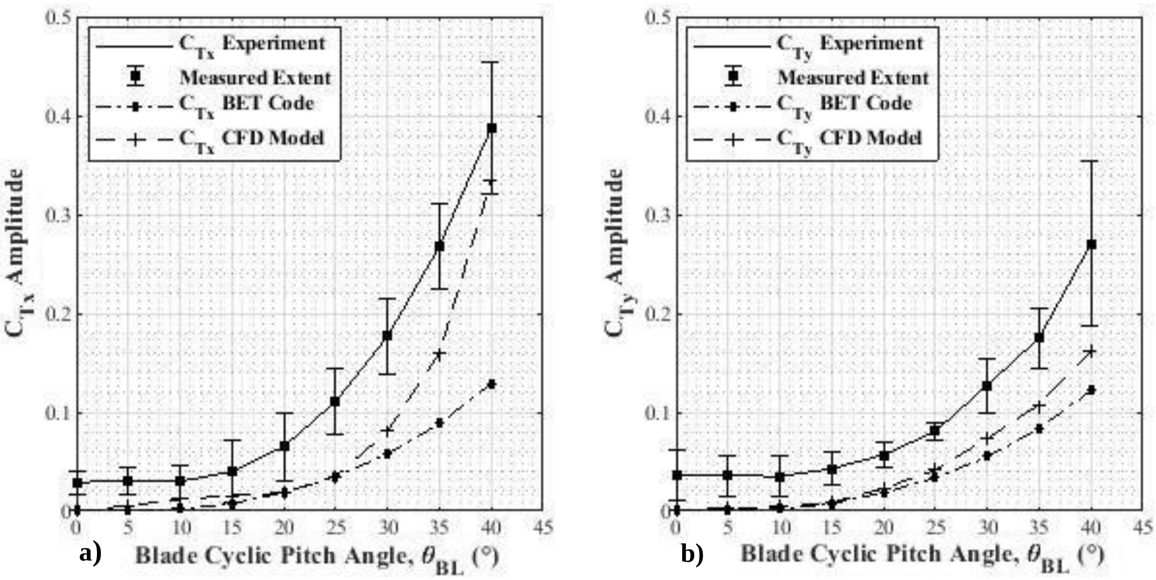

Figure 7.9 – Rotor $1N_b$/Rev Dynamic Thrust Coefficient amplitude (a) Rotor X Direction and (b) Rotor Y Direction

7.5. Experimental and Computational Model Vibratory Hub Load Comparison

It was hypothesized that the vibratory response of any blade pass frequency harmonics, when non-dimensionalized, would be constant with changes in rotor speed for a given blade cyclic pitch amplitude. Based on both computational models calculating the mean non-dimensional thrust and power coefficients to be almost constant with changing rotor speed for a given blade cyclic pitch amplitude. Both computational models calculate the rotor vibratory response to be constant with changing rotational speed, as shown in figure 7.9.

However, experimentally, significant variation with changes in rotational speed exists for the 4/Rev response in the X and Y directions, as shown in figure 7.9 by the error bars, which represent the measured range of 4/Rev amplitudes from 500 to 1,000 RPM. The variation in experimental results at a given blade cyclic pitch amplitude is down to a number of factors. Firstly test rig calibration setup, the dynamic shaker applies a point load at one rotor spanwise position, which is a typical approach (e.g., see [100]). In reality, the rotor aerodynamic and inertial loads are distributed across the rotor span and applied to the shaft at either end. Secondly, with rotor speed change, there will inevitably be some physical rotor inflow and flow distribution variation that will affect aerodynamic load generation and vibratory response. The computational models do not take the variation of rotor inflow into account.

An overarching trend can be identified in the 4/Rev vibratory response with changing blade cyclic pitch amplitude in both measurement directions, as shown in figure 7.9 (a) and figure 7.9 (b) when comparing both computational models to the experimental data. As the blade cyclic pitch amplitude increases, the amplitude of the 4/Rev thrust coefficient vibratory response sees increased modulation in both measurement directions. The 4/Rev response in the X and Y directions in all three approaches is reasonably constant up to a blade cyclic pitch amplitude of 15°, with the largest variation in vibratory response in all cases seen between a blade cyclic pitch amplitude of 20° and 40°.

The CFD model captures the flow features relevant to higher-order dynamics that cannot be captured by the BET model, including qualitative changes in flow regimes at different cyclic pitch amplitudes. As such, the correlation between the CFD model and experimental data is in closer agreement qualitatively than the BET code. In both measurement directions, the 4/Rev response predicted by the CFD model is in reasonable quantitative agreement with the experimental data but is offset, and the magnitude under all conditions is underpredicted. This suggests that the blade wake interactions and interaction of adjacent blades are stronger in reality than predicted computationally. Physical flow nonuniformity also affects the variation of the vibratory response between the CFD and experimental data.

7.6. Computational Model Blade Instantaneous Force Analysis

From the comparison of results in section 7.5, it is thought that the blade vortex interaction is responsible for the differences between CFD, BET code, and experimental vibratory response. The modeling of this behavior is critical in predicting the response of the rotor. Of particular interest is the more significant qualitative change seen in the behavior of the CFD and experimental results between blade cyclic pitch amplitude of 20° and 40°. This section further examines the computational results from these two cases to establish how qualitative changes in the rotor flow field affect rotor vibratory response to understand the differences between the computational model results.

Instantaneous blade loads from the CFD study are plotted in figure 7.10 (a-b) for a blade cyclic pitch amplitude of 20° to check the validity of the uniform rotor inflow assumption used in the BET code at lower blade cyclic pitch amplitudes. Correlation between the four-bladed rotor CFD and BET code at a cyclic pitch amplitude of 20° is reasonable, with deviation noted in a few areas in both the X and Y directions.

Figure 7.10 (a) shows that the BET code underpredicts the X-direction force at Ψ = 180°, representing the rotor's left-side position. Figure 7.11 shows a plot of rotor inflow velocity, non-dimensionalized by rotor speed. At Ψ = 180 (position -0.1,0), there is little downwash on either side of the blade. At this position, the direction of the inflow within the rotor would reduce the relative blade velocity predominantly in the tangential direction. Whereas the BET code, with its uniform rotor inflow assumption, considers the influence of the inflow at this position, a key difference between the modeling approaches. The reduction in the blade tangential velocity component at this position is a factor in the BET code X-direction force underprediction. The phase averaged velocity plot, shown in figure 7.11, assumes static air external to the rotor in the rotor far-field. This is not strictly true for physical rotor use, as there will be air flow variation due to weather conditions and rotor operation. The analysis would need to include an induced velocity inflow model to overcome this assumption, which has typically been used in previous analyses [4].

Figure 7.10 (b) outlines the change in Y-direction force for a blade cyclic pitch amplitude of 20°. The CFD and BET code deviate significantly in the lower half of the rotor between Ψ = 210° and Ψ = 330°, where the CFD predicted forces plateau, a feature not experienced by the BET code. In order to understand the effect of the wake from preceding blades on force generation, a single-blade CFD model undergoing cycloidal motion was analyzed at a blade cyclic pitch amplitude of 20°. While a single blade undergoing cycloidal motion will pass through its own wake generated in the previous rotation, the effects of blade wake interaction will be less pronounced for one blade, with weaker blade-vortex interactions, due to not operating close to a preceding blade or blades at any azimuth position.

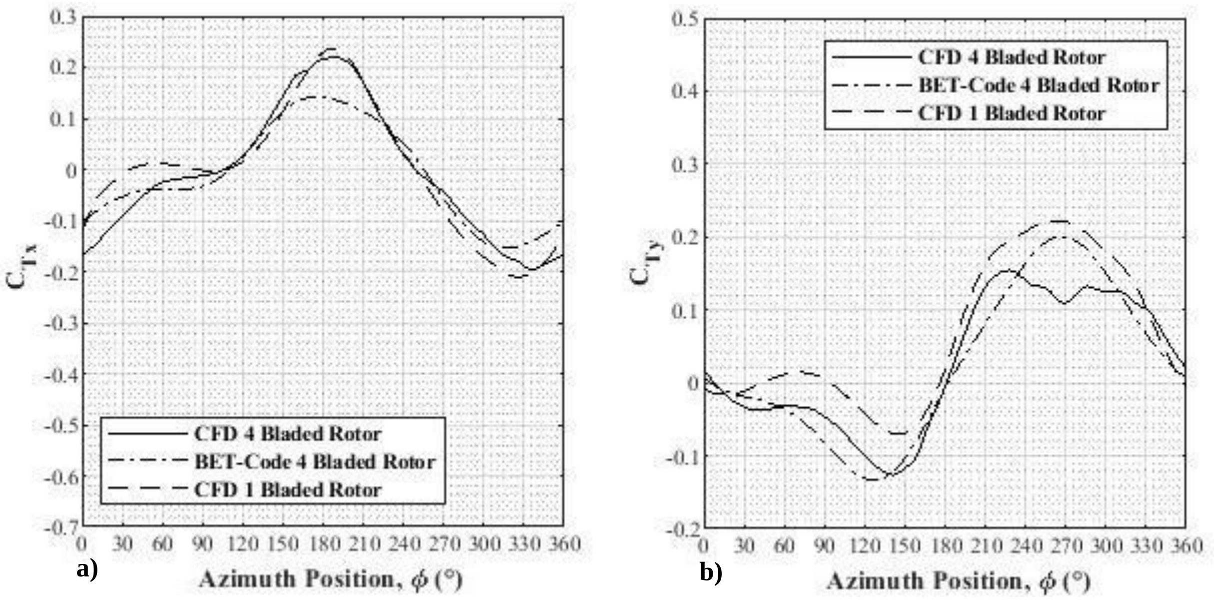

Figure 7.10 – Blade instantaneous Coefficient of Thrust at a blade cyclic pitch angle θ_{BL} of 20° (a) Rotor X Direction and (b) Rotor Y Direction

The Y-direction force plateau in figure 7.10 (b) for the four-bladed CFD model is not replicated in the one-bladed rotor case. Between Ψ = 210° and Ψ = 330° in figure 7.10 (b), the one-blade rotor with weaker blade-vortex interactions shows better qualitative agreement with the BET code results than the four-blade rotor. This suggests that the strength of the blade wake interactions increases as the blade number is increased from one to four and that the effects of these interactions create the key difference between the CFD and the BET code results.

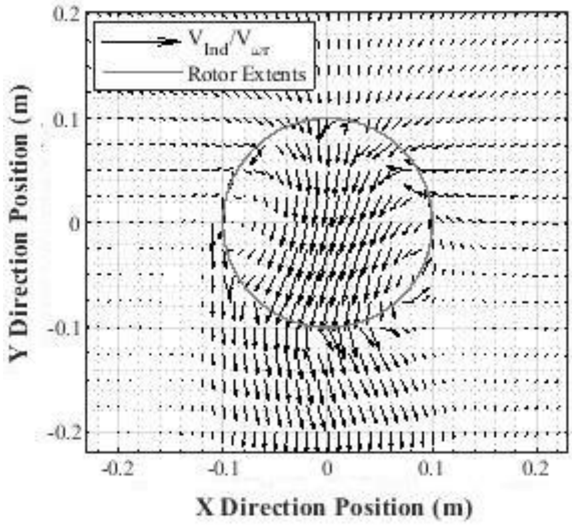

Figure 7.11 – Phase averaged non-dimensional rotor resultant velocity vector plot at a blade cyclic pitch angle of θ_{BL} = 20°

Although blade vortex interaction is not considered in the BET code, at a blade cyclic pitch amplitude of 20°and below, good agreement is seen between the predicted CFD and BET code 4/Rev response. This would indicate that the strength of the vortices generated is weaker at low cyclic pitch amplitudes. Therefore, their influence on force generation is reduced, justifying the use of a reduced-order model at low cyclic pitch amplitudes.

Instantaneous blade forces are shown in figure 7.12 for a blade cyclic pitch amplitude of 40° to establish the change in blade loading with blade cyclic pitch amplitude increase in the X and Y direction. Significant differences between the four-blade CFD model and BET code exist in both directions, particularly in the fourth quadrant between Ψ = 270° and Ψ = 360°. Figure 7.12 (b) identifies a double peak in the Y-direction force generation, which is not replicated by either the one-blade CFD model or BET code. Figure 7.13 shows a rotor inflow velocity plot, identifying a flow recirculation region in the lower right-hand corner of the rotor, corresponding to Ψ = 270° and Ψ = 360°, indicating a significant change in flow physics between the blade cyclic pitch amplitude of 20° and 40°.

7.7. Instantaneous Flow Field Comparison

Q-criterion contours are shown in figure 7.14 for a blade cyclic pitch amplitude of 20° and 40° to quantify the difference between the two pitch amplitudes and understand the changes in blade force generation in figure 7.12. In figure 7.14 (e), for a blade cyclic pitch amplitude of 40° following Ψ = 270°, a shed vortex from blade B1 in figure 7.14 (d) attaches to the boundary layer of blade B4 in figure 7.14 (e). This attachment on the suction side forms part of the LEV formation and growth on the suction side of the blade. As the rotor rotates, the LEV vortex is shed into the wake, as shown in figure 7.14 (f), where the flow is then fully separated on the inner suction surface of the blade. This is confirmed in figure 7.15 (a) and figure 7.15 (b) for C_P and Skin Friction coefficient SF. The leading edge (LE) separation can be seen in figure 7.15 (b), as the SF approaches zero, accompanied by the prominent C_P suction peak in figure 7.15 (a), showing that the magnitude of pressure variation decreases away from the LE edge.

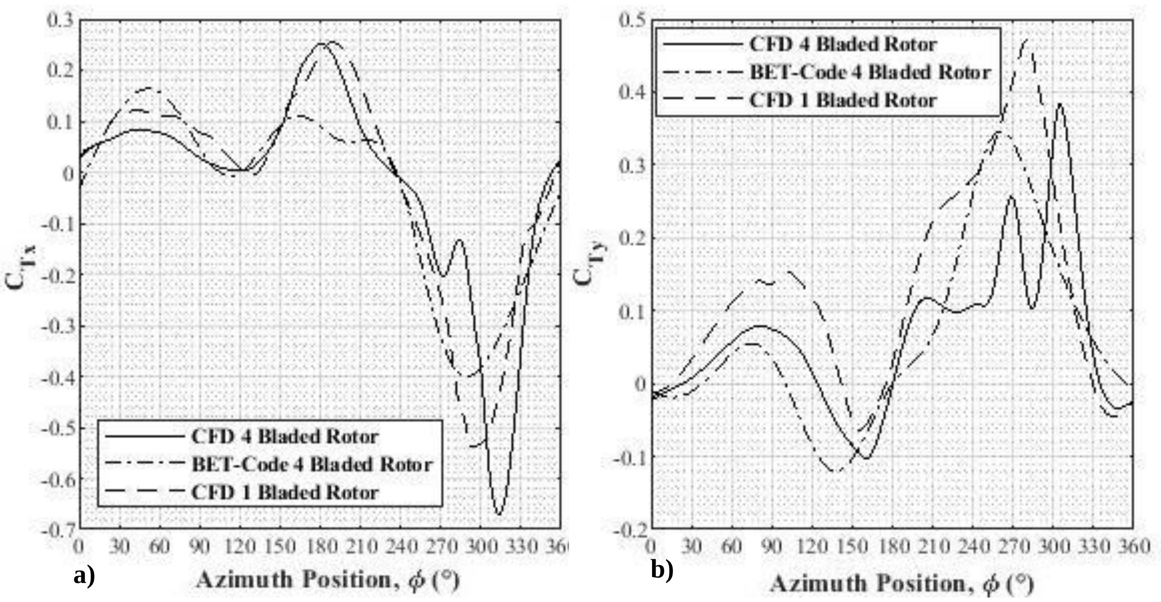

Figure 7.12 – Blade instantaneous Coefficient of Thrust at a blade cyclic pitch angle of θ_{BL} = 40° (a) Rotor X Direction and (b) Rotor Y Direction

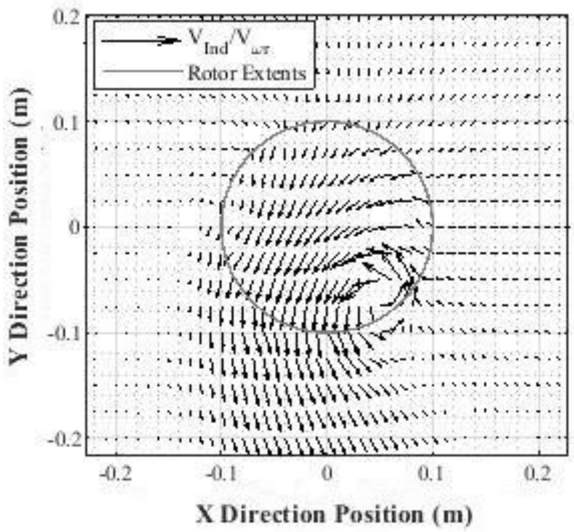

Figure 7.13 – Phase Averaged Non-dimensional Rotor Resultant Velocity Vector Plot at blade cyclic pitch angle of θ_{BL} = 40°

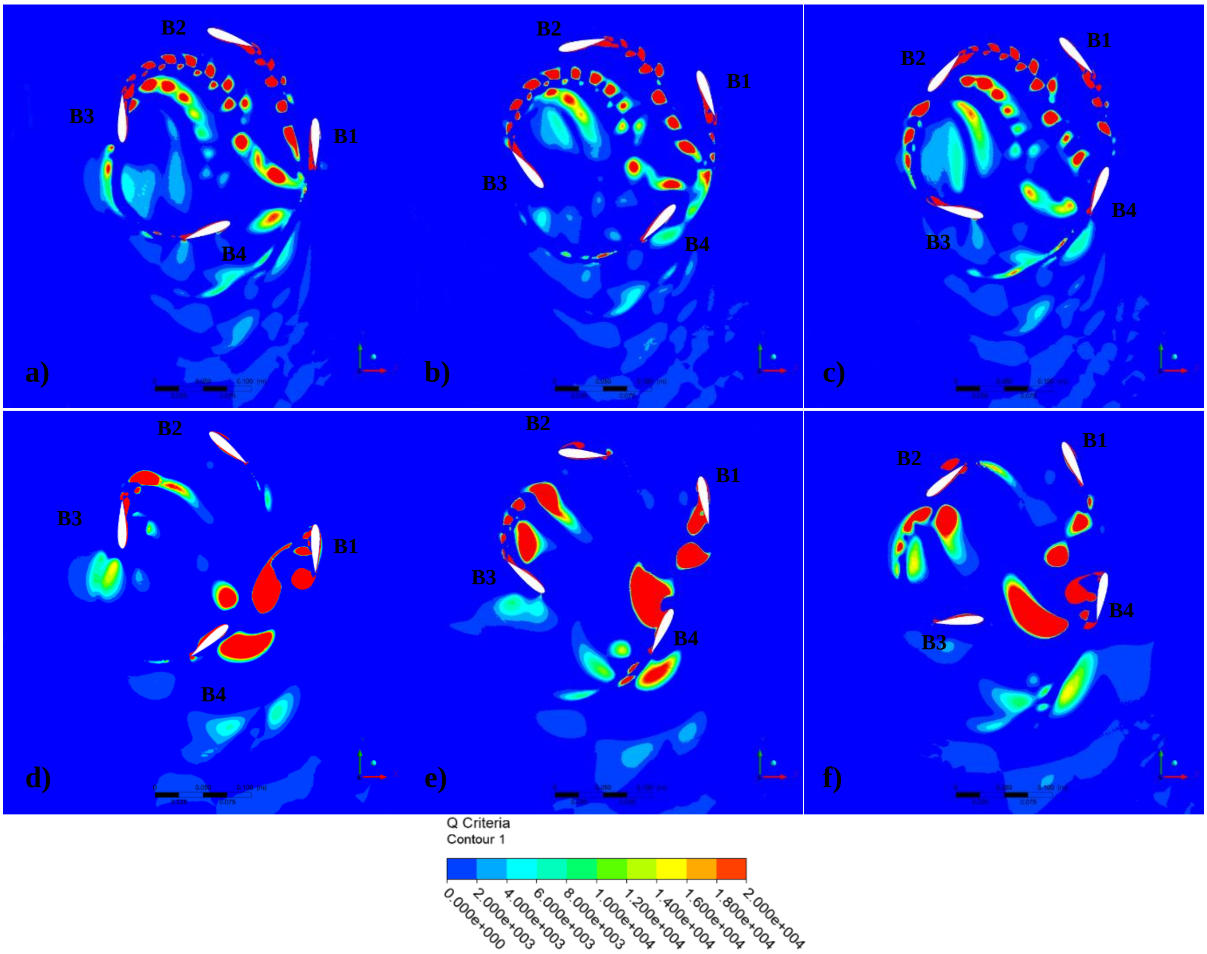

Figure 7.14 – 2D CFD analysis instantaneous contours of Q criteria for a blade cyclic pitch angle θ_{BL} = 20° (a-c) and θ_{BL} = 40° (d-f)

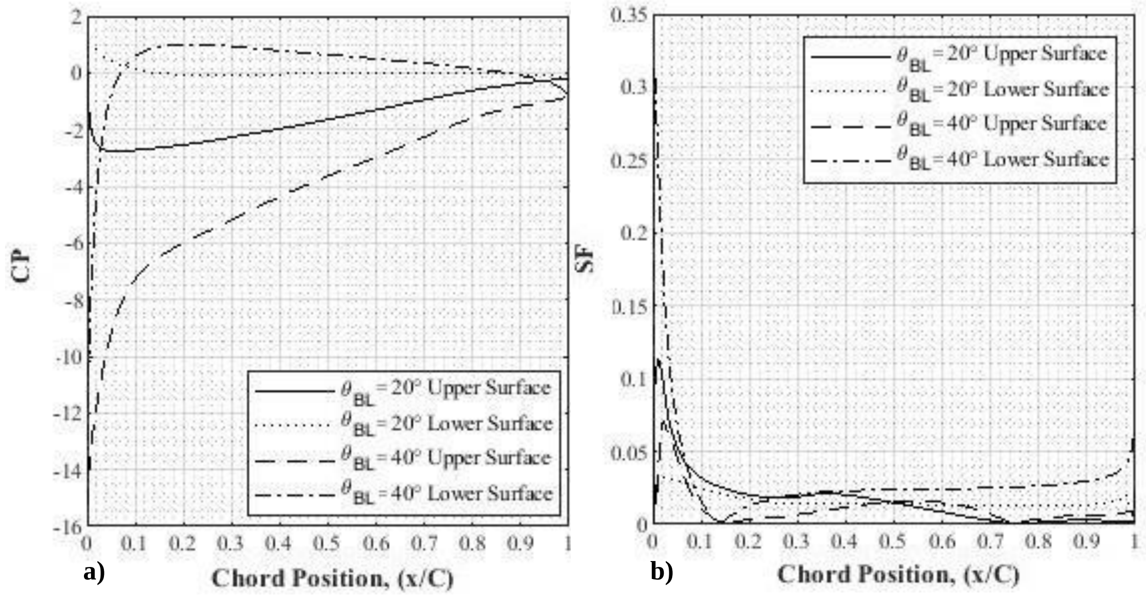

Figure 7.15 – CFD analysis for blade 4 at Ψ = +330° for a blade cyclic pitch angle of θ_{BL} = 20° and 40° (a) C_P and (b) SF Coefficient

The vortex attachment at this position coincides with the negative spike in the X-direction force in figure 7.12 (a) and a corresponding loss of Y-direction force in figure 7.12 (b), confirming the overall effect of blade vortex interaction is significant as blade cyclic pitch amplitude increases up to 40°. With an increase in blade cyclic pitch amplitude, the effect of vortex interaction on force generation becomes more significant. The main reason differences are identified between the CFD and BET-code results at high blade cyclic pitch amplitudes. Figure 7.14 (a-c) outlines the vortex shedding behavior at a blade cyclic amplitude of 20° and identifies reduced blade vortex interaction, validating the justification of using a reduced-order model only at low cyclic pitch amplitudes.

7.8. Rotor Wake Vortex Shedding

Section 7.7 identified qualitative changes in the rotor behavior with an increase in blade cyclic pitch amplitude and assumed that the strength of the shed vortices increased with blade cyclic pitch amplitude. A frequency analysis of the shed wake behind a blade was undertaken for one rotor revolution to quantify this. Velocity magnitude data was extracted from the instantaneous CFD analysis flow field at azimuth position increments of 1° one chord downstream of the blade pitch axis position, as shown in figure 7.16. The data was extracted along a line from 0.25c to 1.75c, using 1000 uniformly distributed points, where c is the blade chord. The analysis was based on a blade chord of 50 mm and a rotor radius of 100 mm.

The blade shedding frequencies are shown in figure 7.17 (a) for a blade cyclic pitch amplitude of 20°. Two distinct peaks are identified at frequencies of 7/Rev and 8/Rev. The vortex shedding frequency varies with non-dimensional radius, with the majority of the vortices being shed between 1.4c and 2.0c, representing a 70 and 100 mm radius, respectively. This confirms that the shed vortices are kept within the rotor at reduced blade cyclic pitch amplitude and not shed into the wake, as shown in figure 7.14 (a).

As the blade cyclic pitch amplitude is increased to 40°, the peak amplitude is observed at a lower frequency, notably 5/Rev and 6/Rev from figure 7.17 (b). The lower frequencies correspond to the vortices shed near to and during blade stall, which are typically larger. From figure 7.17 (b), the frequency content and fluctuation with a non-dimensional radius are much larger at 40° compared to the 20° case signifying that the flow field is more turbulent within and surrounding the rotor. Consistent with [18] for a NACA 0012 blade profile.

The analysis confirms that as the blade cyclic pitch amplitude reduces, the frequency of the shed vortices increases, consistent with the qualitative changes identified. It also confirms the original hypothesis that as blade cyclic pitch amplitude reduces, it is accompanied by a reduction in vortex strength.

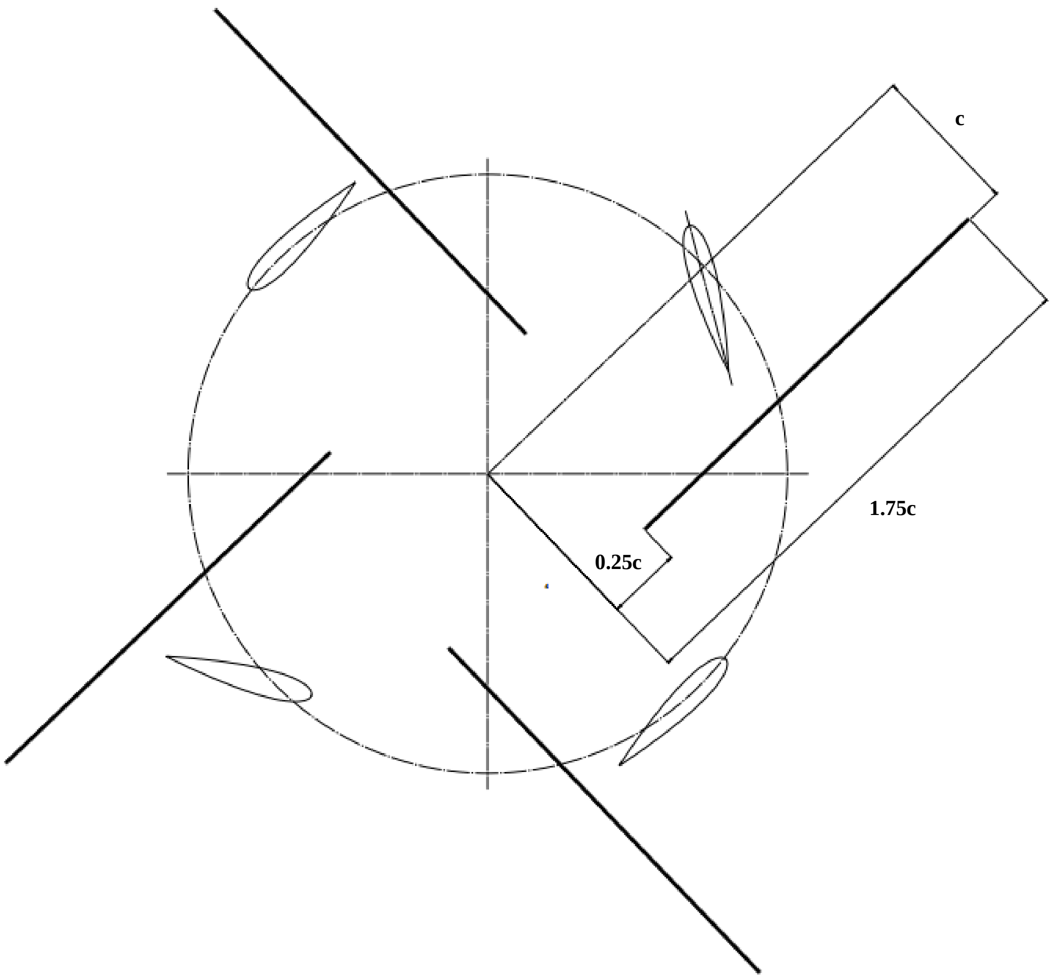

Figure 7.16 – Positional data used to extra velocity magnitude data in CFD flowfield

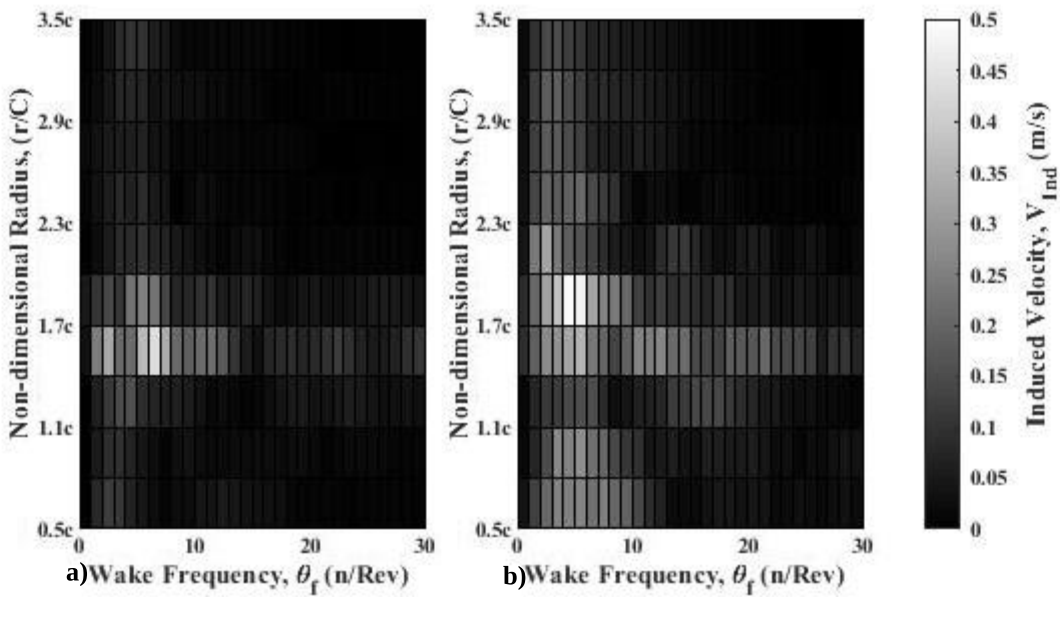

Figure 7.17 – Rotor wake frequency with changing non-dimensional radius (a) θ_{BL} = 20° and (b) θ_{BL} = 40°

7.9. Chapter Review

This chapter has presented the first numerical and experimental investigation of the cycloidal rotor and vibratory response with blade cyclic pitch amplitude and rotor speed changes. It was found that the dominant rotor harmonic related to thrust generation is 4/Rev, which represents the fundamental blade pass frequency. The 4/Rev response was found to be strongly related to blade cyclic pitch amplitude, with increased modulation with increasing blade cyclic pitch amplitude. Higher harmonic components of blade pass frequency are significantly lower than the N_b/Rev response at high blade cyclic pitch angles and can be treated as negligible when operating in these regions in the analysis of rotor systems. This finding aligns with typical independent studies [85].

Blade wake interaction and blade stall play a crucial part in the overall rotor response and blade unsteady loading. The CFD modeling illustrates that this is particularly dominant in the lower half of the rotor at a blade cyclic pitch amplitude of 40°, but blade wake interaction becomes weaker as blade cyclic pitch amplitude reduces. The difficulties associated with modeling these events highlight the challenge in the quantitative numerical analysis of the behavior, but for anything more than cursory design sizing, the modeling of this phenomenon is critical to accurate results.

Qualitatively the CFD model corroborated the behaviors seen in the experimental results for the 4/Rev response and was able to capture the flow features relevant to higher-order dynamics with improved accuracy that the BET model cannot capture,

Accurate calculation of rotor vibratory loading plays a vital role in cycloidal rotor development and is a key driver in component design. This work confirms that high-order computational models are required to accurately model the rotor vibratory response and form a basis for additional experimental and computational analysis.

Chapter 8 – Higher Harmonic Control of Cycloidal Rotor Vibration

8.1. Introduction

In contrast to conventional rotorcraft, little data exists on analyzing and understanding the vibratory response for cycloidal rotors. Vibration reduction using active control approaches such as HHC has received much attention over recent decades. The present chapter presents the first known comprehensive experimental and computational implementation of HHC on a cycloidal rotor for vibratory load suppression, describing the significant contributions and novelty of the current research.

The study first uses a linearised optimization method through computational modeling at a single input harmonic. A non-linear optimization follows this. The optimal HHC input amplitude and phase were determined for each modeling approach. Finally, experiments using the same linearised optimization assumptions were undertaken to demonstrate HHC application for vibration suppression. Comparison with CFD and reduced-order modeling approaches allows conclusions to be drawn as to the important characteristics of the unsteady flow field and identifies the key flow physics responsible for the changes in dynamic loading.

Challenges behind the analysis of vibration suppression are analyzed, and a rigorous demonstration of the efficacy of HHC for cycloidal rotor vibration suppression is provided. The work highlights the importance of vibration control techniques for this nascent thrust technology.

In this chapter, two computational approaches are evaluated for their prediction of rotor behavior: a simple BET code and a 2D CFD model, as described in Chapters 5 and 6, respectively. Tests were conducted on a 4-blade cycloidal rotor as developed in Chapter 4 for rotor hover testing. The supporting theory behind HHC and the methods behind the single step and non-linear optimization used to calculate the optimal HHC input are detailed, assuming a baseline blade cyclic pitch amplitude of 40° in all cases. The chapter culminates in an experimental HHC input optimization informed by the computational models.

8.2. Higher Harmonic Control Fundamentals

HHC is implemented in two ways in conventional rotorcraft applications: firstly, using actuators below the swashplate in the non-rotating frame, and secondly, in the rotating frame, with actuators between the swashplate and rotor blade [80]. The rotating frame actuation approach is more commonly known as Individual Blade Control (IBC). IBC can be extended by implementing actively controlled full or partial trailing edge flaps and using active twist rotor blades where the entire rotor blade is twisted by embedded piezoelectric fibers [14].

The HHC response input generates higher harmonic air loads to reduce the rotor oscillatory blade loads [89]. Vibration reduction using HHC has been shown in flight [135,136] and wind tunnel tests [88], and it is typically implemented via closed-loop control. During closed-loop control, the vibratory output is measured, and control inputs are updated at set time intervals when steady-state outputs are achieved. When the system reaches a steady-state vibratory response, amplitude and phase are measured and used to update the amplitude and phase of the HHC inputs for vibration suppression. The closed-loop control effectively acts as an online optimization process to find the optimal HHC input operating point.

HHC implementation typically assumes that the system can be represented by a linear model relating the rotor vibratory loads to the HHC control inputs within a single HHC loop cycle based on the transfer or sensitivity matrix method [86]. In a physical system, HHC modifies the cyclic pitch of the blades with the addition of higher harmonic frequencies. During HHC, the swashplate is typically excited at N_b/Rev, where N_b is the blade number, which results in blade pitch oscillations of (N_b – 1)/Rev and (N_b + 1)/Rev in the rotating frame [85]. Typical conventional rotorcraft require a small HHC input amplitude of between 0.5° to 1.5° [86], with small angle approximations justifying the assumption of a linear control response adopted in some of the present work.

During HHC, the blade's total pitch angle in the rotating frame is

$$\theta_s = \theta_{BL} + \sum_n \theta_n \tag{8.1}$$

It consists of two contributions: firstly, the baseline blade cyclic pitch input, θ_{BL} and secondly, the higher harmonic pitch inputs, θ_n where

$$\theta_n = \theta_{ns} \sin(n\Psi) + \theta_{nc} \cos(n\Psi) \tag{8.2}$$

θ_n is made up of HHC control input sine and cosine components θ_{ns} and θ_{nc}, defined as

$$\theta_{ns} = A_n \cos(n\phi_n) \tag{8.3}$$

and

$$\theta_{nc} = A_n \sin(n\phi_n) \tag{8.4}$$

where ϕ_n and A_n represent the phase angle and amplitude of the HHC control input, respectively, and Ψ the rotor azimuth angle. The respective blade azimuth angle of the q^th blade, Ψ_q is

$$\Psi_q = \Psi + \frac{2\pi}{N_b}(q-1) \qquad q = 1,2,\dots.N_b \tag{8.5}$$

The 0° azimuth position is defined in figure 8.1.

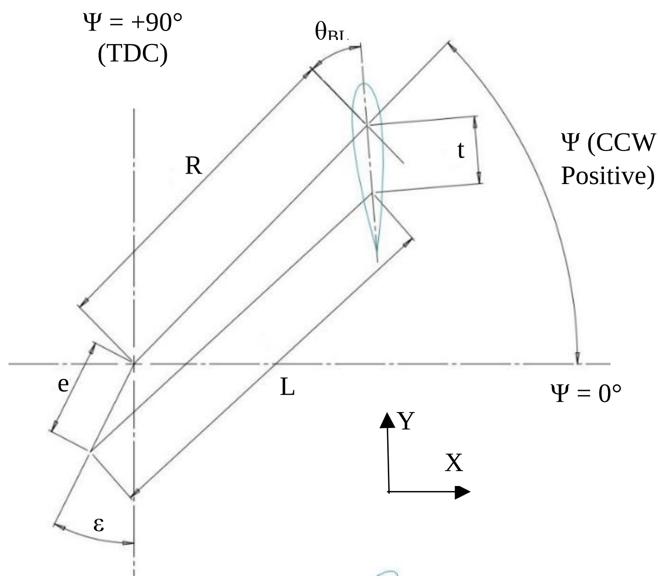

Figure 8.1 – Cycloidal rotor analysis coordinate system.

Rotorcraft blade dynamic loads contain many frequencies, but generally, for a correctly tracked rotor, only frequencies that are integer multiples of the blade passage frequency at kN_b/Rev transmit to the non-rotating frame; all other harmonics cancel at the hub [85,137] as summarised in Chapter 7. The case where k is zero represents the steady-state hub load components. For conventional rotorcraft with a four-blade rotor, the 4/Rev harmonic is the dominant unsteady component [137]. The hub loads associated with higher harmonics of blade pass frequency at $2N_b$, $3N_b$, and $4N_b$/Rev are typically much smaller than the N_b/Rev components and often neglected for conventional rotors.

In order to reduce the 4/Rev harmonic in the stationary frame for the current 4-blade rotor would be expected to require the superposition of a 3 or 5/Rev blade pitch excitation in the rotating frame based on known rotorcraft HHC theory, proven by the analysis outlined in Chapter 7, section 7.2. The results of the current study will be seen to corroborate this expectation.

8.3. Cycloidal Rotor HHC Implementation

Rotorcraft assume a sinusoidal cyclic pitch profile provided by a swashplate. An approximate sinusoidal cyclic pitch input is also commonly used for a cycloidal rotor, achieved via a passive mechanism or cam, although it is difficult to achieve an exact sinusoidal profile. For example, the motion produced by a typical four-bar mechanism [116], as adopted here, is shown in figure 8.1. The exact baseline blade cyclic pitch input θ_{BL} for this system is given by

$$\theta_{BL} = \frac{\pi}{2} - \cos^{-1}\left(\frac{a^2 - L^2 + t^2}{2at}\right) - \sin^{-1}\left(\frac{e}{a}\cos(\Psi + \varepsilon)\right) \tag{8.6}$$

where

$$a = \sqrt{e^2 + R^2 + 2eR\sin(\Psi + \varepsilon)} \tag{8.7}$$

The exact θ_{BL} value is used throughout the computational and experimental studies presented here and used in the calculation of θ_s. R represents the rotor radius, and L is the theoretical distance between the eccentric offset position and the blade pitch pin. e represents the distance between the eccentric offset position and the rotor spindle centreline. Finally, t is the distance between the blade pitching axis and the blade pitch pin for connection to the four-bar mechanism.

This study has made a number of adaptations to conventional HHC methods for the cycloidal rotor HHC proof of concept. Firstly, the adoption of a fixed passive cam profile, as shown in figure 8.2, to define the blade pitching profile described above has not been extended to permit on-the-fly adjustment of the HHC pitch input components. For this reason, the scope of the experimental study does not cover fully closed-loop HHC and instead uses a single-step optimization-based approach to determine suitable harmonic pitch inputs for the hover condition.

Secondly, initial computational studies use the same open-loop adjustments of the control inputs based on a measured global sensitivity matrix, similar to the single-step convergence property of HHC demonstrated in [138]. The more advanced computational studies in this paper substitute the feedback control loop of conventional HHC with a conceptually-similar non-linear optimization algorithm, achieving the same aim of minimizing the vibration response with an iterative convergence behavior. This approach lends itself naturally to comparisons between the vibration reduction achieved in the full non-linear iterative optimization and the simplified single-step optimization process adopted to enable experimental validation. Finally, the present study focuses on only a single HHC input harmonic to make the experimental process tractable.

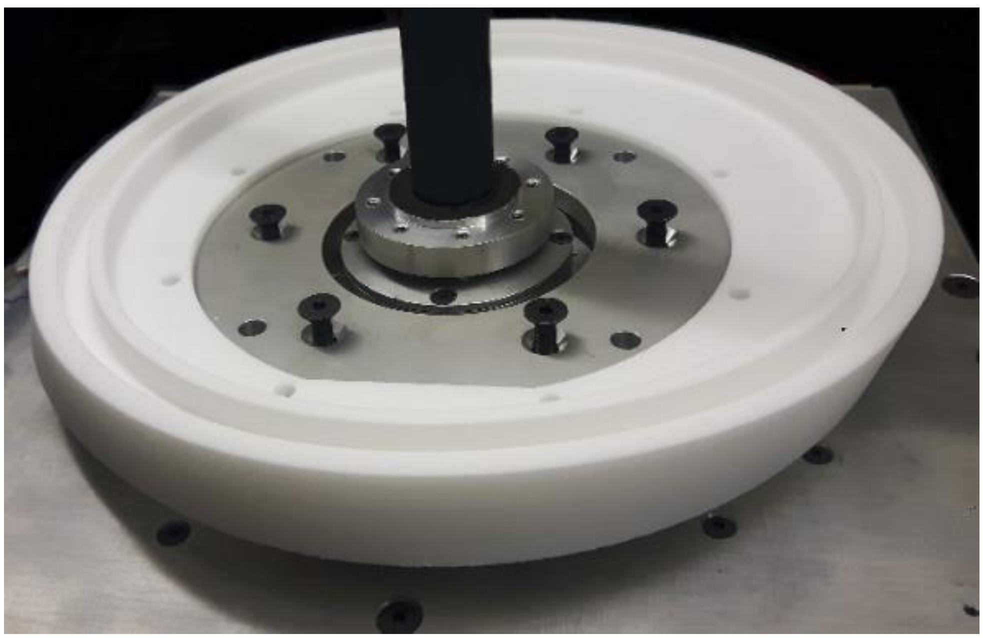

Figure 8.2 – SLS cycloidal rotor passive cam ring mechanism

8.4. HHC Input Optimisation Methodology

8.4.1. Sensitivity Analysis

The rotor periodic vibratory response can be represented by the superposition of sine and cosine components at multiples of the blade pass frequency, the kN_b/Rev harmonics in the X and Y directions. The optimization, whether performed directly in a computational optimization algorithm or achieved through iterative HHC feedback loops, aims to minimize the rotor vibratory response associated with the blade pass harmonics. After optimization, the theoretically achievable system sine and cosine harmonic outputs $\mathbf{z_c}$ are given by

$$\{\mathbf{z_c}\} = [\mathbf{T}]\{\mathbf{u}\} \tag{8.8}$$

where $\mathbf{u}$ is comprised of the HHC control inputs θ_{ns} and θ_{nc} as used in equation. 8.12, and $\mathbf{T}$ is the sensitivity matrix.

The starting point for optimization is the calculation of the sensitivity matrix, which contains one row for each of the response harmonics and one column for each of the control inputs. If only one harmonic frequency n is used for the inputs, then the sensitivity matrix $\mathbf{T}$ is given by

$$[\mathbf{T}] = [\mathbf{t_1}\ \mathbf{t_2}] \tag{8.9}$$

where $\mathbf{t_1}$ and $\mathbf{t_2}$ are column vectors that represent the change in the system's overall harmonic output, $\mathbf{z_c}$, in response to the input perturbations θ_{ns} and θ_{nc} respectively. The inputs $\mathbf{u}$ are then given by

$$\{\mathbf{u}\} = \begin{Bmatrix} \theta_{ns} \\ \theta_{nc} \end{Bmatrix} \tag{8.10}$$

The present study focuses on HHC in a simplified form, using only one HHC input harmonic frequency, corresponding to two HHC control inputs comprised of the sine and cosine components at that frequency. A full and systematic analysis of the influence of all harmonics between 1 and 16/Rev was investigated to aid with the choice of a suitable input harmonic. This was done by calculating full sensitivity matrices utilizing the BET code and CFD models. The sensitivity matrix was evaluated one column at a time, making small perturbations to each of the inputs in turn.

The input perturbations were considered as two independent HHC inputs θ_{ns} and θ_{nc} for each higher harmonic considered, with each input superimposed onto θ_{BL} and analyzed. Two components at each of the sixteen frequencies gave a total of 32 input harmonics for the calculation of each sensitivity matrix. All test conditions for investigation take a peak amplitude of θ_{BL} of 40°.

A range of input perturbation sizes was considered for the BET code and CFD models to evaluate the linearity of the input-output relationship and guide the choice of perturbation size for use in the experiments. In the experiment, it was important to balance the nonlinearities introduced by large input perturbations with the lower accuracy achieved using perturbations that are too small.

Following the calculation of the sensitivity matrices, a deeper numerical investigation of the HHC inputs was undertaken to establish the dominant HHC input harmonic affecting the rotor vibratory response, to corroborate the sensitivity matrix accuracy, and understand the underlying rotor physics. BET code and CFD computational studies were used to fully explore the problem space by varying the HHC input amplitude and phase over the range of harmonic of interest.

8.4.2. Single-Step Linearised Optimisation

The first method used in both the computational and the experimental studies is a single-step optimization, representing one iteration of an HHC control loop. A single-step optimization will find the exact optimal operating point for a linear system and can approximate it for a nearly linear system. This approach was the only method used for the experiment due to the limitations of the available pitch control mechanisms (described in section 8.3). Therefore, this method was used in CFD simulation as a basis for comparison.

The objective of the optimization was to minimize the rotor vibratory response $\mathbf{z_c}$ associated with the blade pass harmonics. A reference response $\mathbf{z_r}$ is defined as the target for the optimization and is typically a zero vector for zero vibratory output. The vector $\mathbf{z_{bl}}$ represents the baseline system harmonic response outputs with an HHC control input vector of zeros. The initial error that the optimization seeks to eliminate is $\mathbf{z_e}$, given by

$$\{\mathbf{z_e}\} = \{\mathbf{z_r}\} - \{\mathbf{z_{bl}}\} \tag{8.11}$$

The HHC cyclic pitch inputs are then calculated from

$$\{\mathbf{u}\} = [\mathbf{T}]^{+}\{\mathbf{z_e}\} \tag{8.12}$$

where $\mathbf{T}^{+}$ is the Moore-Penrose inverse of $\mathbf{T}$. The input $\mathbf{u}$ is used to calculate θ_n and superimposed onto θ_{BL} to give θ_s. The computational models and experiments are then rerun with θ_s defining the pitching schedule. The resulting measured/computed harmonic outputs $\mathbf{z_a}$ are used to calculate the residual error after optimization $\mathbf{U}$ to complete the analysis, where

$$\{\mathbf{U}\} = \{\mathbf{z_r}\} - \{\mathbf{z_a}\} \tag{8.13}$$

The starting point for the single-step optimization is the calculation of the system output vibration levels with the baseline cyclic pitch angle θ_{BL} only. During this initial stage, no HHC input is applied for each modeling approach. The vibratory response considers the vibration associated with the blade pass frequency N_b and higher harmonics of blade pass frequency at $2N_b$, $3N_b$, and $4N_b$/Rev. Utilizing the appropriate sensitivity matrix, the optimal inputs $\mathbf{u}$ for vibration suppression are calculated from equation 8.12, assuming a zero rotor vibratory response target. The calculated values of $\mathbf{u}$ are superimposed onto θ_{BL} to produce the optimized pitch schedule θ_s and the respective models rerun. The vibratory response of the optimized system with θ_s included is calculated, and the residual error after optimization $\mathbf{U}$ is determined. In order to check the validity of the calculated optimum, the system's vibratory response at multiple HHC input amplitudes at constant phase was undertaken, where the amplitudes straddled those calculated in the optimization.

8.4.3. Non-linear Optimisation

Following the single-step optimization, an iterative non-linear optimization was performed to evaluate the efficacy of the single-step optimization approach. A constrained non-linear optimization was undertaken within a reduced-order BET code model using the Fmincon() MATLAB function to validate the linear optimization approach assumption. Fmincon is a solver-based non-linear optimization used for constrained minimization of a scalar objective function of several variables. The squared ℓ^2 norm of the residual error $\mathbf{U}$ is used as the objective function in the full non-linear optimization:

$$\mathrm{J} = \{\mathbf{U}\}^{\mathrm{T}}\{\mathbf{U}\} \tag{8.14}$$

Comparison of J for θ_{BL} and θ_{s} the cases with and without HHC control input enable a direct comparison between the optimized and baseline pitch schedule case to be used as a metric to quantify the overall vibration improvement, D.

The non-linear optimization aims to reduce the rotor vibratory response associated with N_b and higher harmonics of blade pass frequency at $2N_b$, 3Nb, and 4Nb/Rev, by reducing the objective function J. A single higher harmonic input was used in the constrained optimization to replicate the experimental approach.

8.4.4. Single-step Experimental Optimisation

Following the preceding computational studies, the single-step optimization method was used based on the dominant HHC input for vibration suppression identified in the experimental study. Initial experimental runs were undertaken with a blade cyclic pitch angle of θ_{BL} to calculate the baseline system vibratory response. Informed by the computational models, a range of HHC input perturbations was considered from 1.5° to 9° for both the sine and cosine perturbed inputs to calculate the sensitivity matrix. Where each perturbed input utilized a separate cam profile. The optimal inputs **u** for vibration suppression were then calculated, and a new cam was produced with the optimal HHC input superimposed onto θ_{BL} and the test rerun.

Finally, a series of further tests utilizing cams at varying HHC input amplitude at constant phase on either side of the calculated optimum amplitude was undertaken to confirm the experimentally calculated optimum and evaluate the HHC approach's efficacy.

8.5. Computational Modeling Results

8.5.1. Sensitivity Analysis

Figure 8.3 and figure 8.4 show the sensitivity matrices from the BET code and CFD analysis with a higher harmonic input up to 16/Rev, using perturbations of 1.0° for both studies. The only output harmonics to show non-negligible response are at integer multiples of the blade pass frequency, as expected due to the analysis making the assumption of a tracked rotor. The sensitivities are greatest in general with respect to the kN_b+/-1 input components for both the BET code and CFD modeling. For example, a 4/Rev output has the greatest sensitivity to a 3/Rev, and 5/Rev HHC input; an 8/Rev output is most susceptible to a 7/Rev and 9/Rev input. The vibratory response of the four-blade cycloidal rotor is dominated by the 4/Rev sine and cosine harmonic output, θ_{4s} and θ_{4c} respectively in both the rotor X and Y measurement directions. Interrogation of the two sensitivity matrices shows that the 3/Rev sine and cosine HHC input, θ_{3s} and θ_{3c} have the greatest influence with respect to the sine and cosine components of the 4/Rev harmonic output in the X and Y direction.

Although the magnitudes of the respective 3/Rev input sensitivity components are different for the two modeling approaches. This suggests that the phase of the calculated

4/Rev rotor response with the baseline cyclic pitch profile θ_{BL}, varies between the BET code and CFD modeling. The BET code 3/REV input sensitivity is dominated by the sine component, where the CFD sensitivity matrix shows the requirement of a combination of a sine and cosine 3/Rev input. As expected, the sensitivity matrices show that the rotor harmonics are modulated by +1 from the rotating to the non-rotating frame, with a 3/Rev input harmonic being required for maximum vibration suppression.

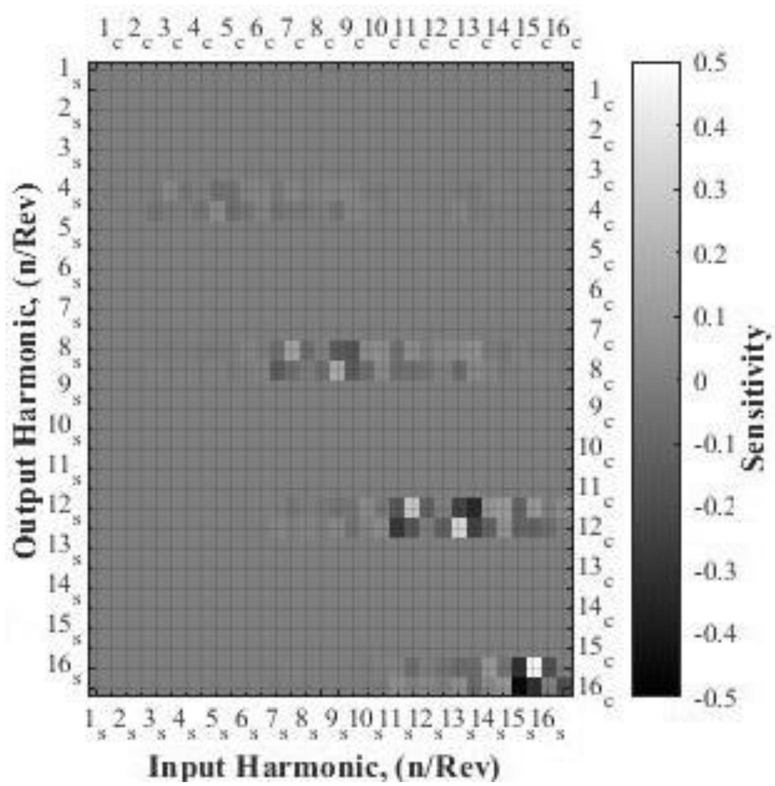

Figure 8.3 – Calculated BET code sensitivity matrix with an input harmonic from 1/Rev to 16/Rev using an input perturbation of 1.0° using a baseline cyclic pitch profile θ_{BL} of 40°

A parameter sweep of HHC input phase and amplitude was undertaken at single harmonics from 1/Rev to 16/Rev, as shown in figure 8.5, using the two computational modeling approaches to calculate the maximum estimated reduction in rotor vibratory response to test the validity of the sensitivity matrices. The BET code and CFD models predict that the 3/Rev HHC input harmonic potentially has the most significant impact on the rotor vibratory response, in agreement with the sensitivity matrices, calculating a vibration reduction between 74 and 78%. The vibration reduction associated with the 1/Rev HHC input harmonic from figure 8.5 is not seen in the sensitivity matrix data. Interrogation of the resulting pitching schedule θ_s with the 1/Rev input included shows that the HHC input is 180° out of phase with θ_{BL}, which has the effect of reducing the overall cyclic pitch angle to a lower level, as opposed to reducing the vibration level for the θ_{BL} analyzed.

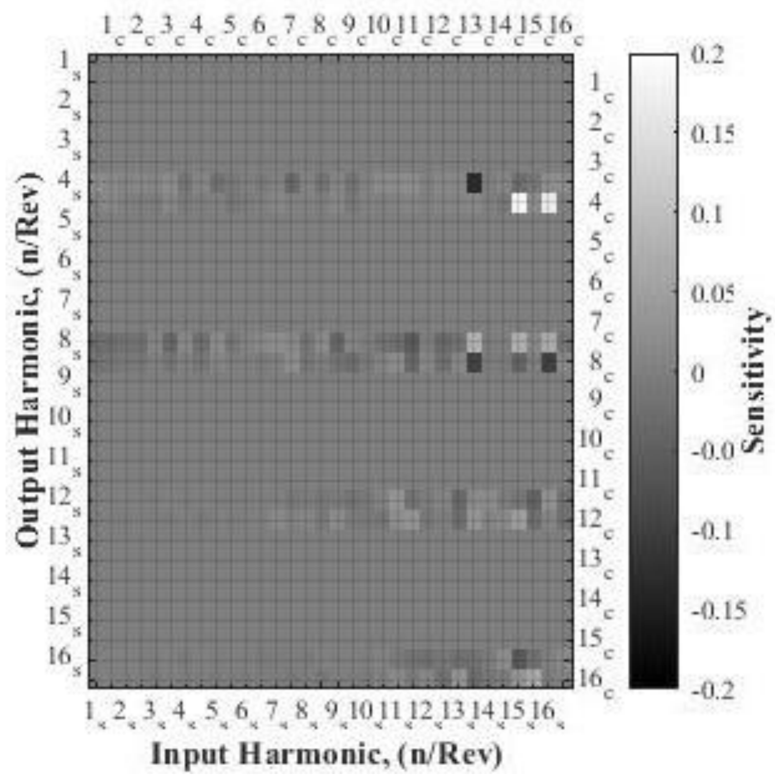

Figure 8.4 – Calculated 2D CFD model sensitivity matrix with an input harmonic from 1/Rev to 16/Rev using an input perturbation of 1.0° using a baseline cyclic pitch profile θ_{BL} of 40°

Based on this, all subsequent computational and experimental optimization studies presented assume a 3/Rev HHC input only. Figure 8.6 shows the resulting experimental variation in the rotor 4/Rev output harmonic in the X direction for a range of HHC 3/Rev cosine, θ_{3c} input perturbations for the calculation of the sensitivity matrix. Of note is that the response across the full range of inputs considered is a reasonable linear approximation. Similar behavior was observed for the higher-order kN_b/Rev harmonics.

The implication is that a one-step approach for determining appropriate HHC control inputs holds promise for producing a good approximation to the optimal operating point.

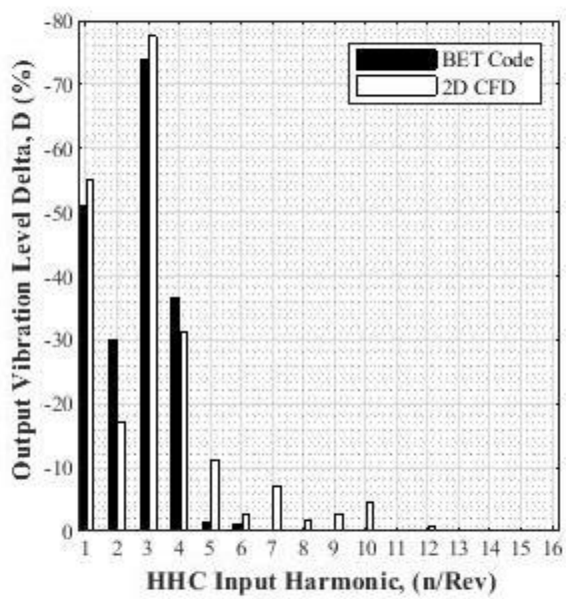

Figure 8.5 – Rotor kN_b/Rev rotor vibratory response change with HHC input

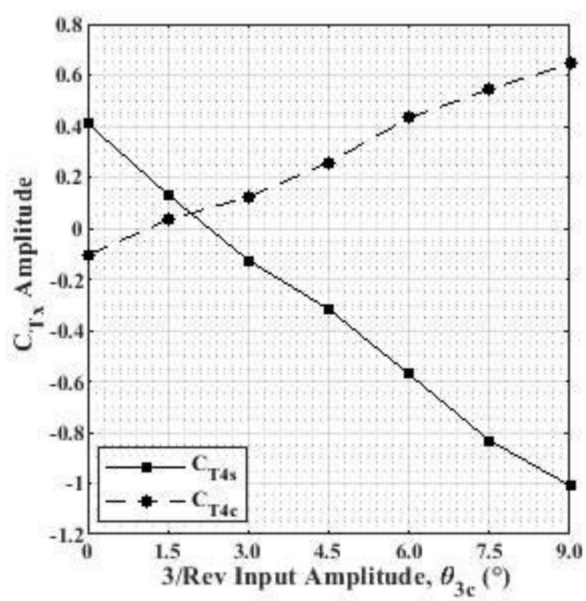

Figure 8.6 – Experimental 4/Rev X direction Sine and Cosine thrust coefficient change with increasing θ_{3c} HHC input

8.5.2. HHC Input Optimisation

The following section discusses the results from all of the optimization methods described in section 8.4 for both the BET code and CFD computational models, with a 3/Rev HHC input. The single-step BET code optimization calculated a 74.5% reduction in the rotor vibratory response, with a 3/Rev HHC input amplitude of 2.785° and phase of 2.940°. Comparison with the BET code iterative non-linear optimization calculated a 74.8% reduction in the rotor vibratory response, with a 3/Rev HHC input amplitude of 2.786° and phase of 2.877°. The BET code single-step and interactive optimization analyses are in very good agreement with one another in terms of both calculated vibration reduction and HHC input, further supporting the decision to use a single-step experimental optimization for the present investigation.

The CFD model single-step optimization calculated a 78.5% reduction in the rotor vibratory response, with a 3/Rev HHC input amplitude of 8.657° and phase of 67.519°. Individual CFD cases were run with varying HHC input amplitudes from 0 to 10° and phase angles from 0° to 120° to cover the full rotor azimuth with a 3/Rev input to provide additional validation to the single-step optimization assumption and determine if the calculated point was optimal. The calculated vibration reduction for the parameter sweeps is shown in figure 8.7. Examination of figure 8.7 confirms that the optimal point calculated in the single-step optimization is optimal and agrees with the full parameter sweep HHC input optimum of 8.5° amplitude and 67.5° phase, further validating the single-step optimization approach.

A comparison of the BET code single-step optimal HHC input to that calculated in the CFD single-step shows that both the BET code and CFD models give very different outcomes in terms of optimal HHC input amplitude and phase but a similar overall vibration level reduction. The CFD optimal profile is counter-intuitive, with a higher peak blade AOA generating lower vibration than the baseline pitch profile; section 8.8 analyzes this further to understand the mechanisms behind vibratory response generation and the differences between the BET code and CFD modeling approaches.

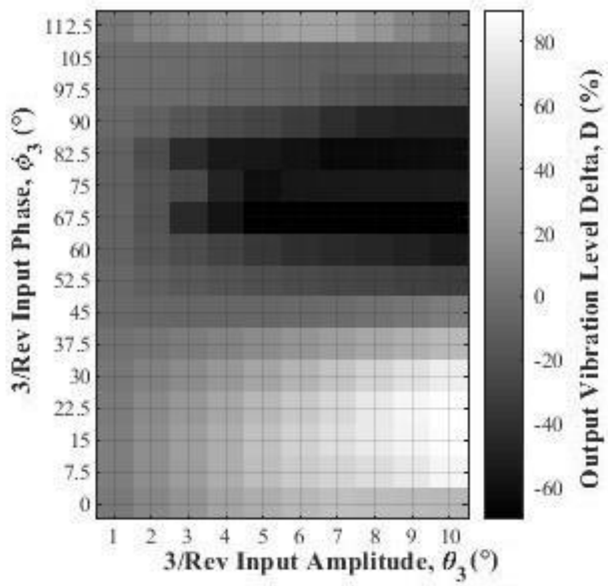

Figure 8.7 – 2D CFD rotor vibratory load change as a function of 3/Rev HHC input amplitude and phase

8.6. Single-step Experimental Optimisation

Following validation of the single-step optimization with computational models, a single-step experimental optimization was undertaken, and a 67.5% reduction in the rotor vibratory response was measured, with a 3/rev HHC input amplitude of 2.616° and phase of 35.6°. A series of further tests at varying HHC input amplitude at constant phase on either side of the experimental optimum was undertaken, as illustrated in figure 8.8. Figure 8.8 confirmed that the calculated experimental HHC input is an optimal point as the change in vibratory response on either side of the HHC input amplitude of 2.616° is lower when compared to the baseline configuration without HHC input.

Figure 8.9 (a) and figure 8.9 (b) show the experimental change in rotor vibration due to the HHC input from the baseline case for each kN_b/Rev harmonic considered in the X and Y measurement directions. It confirms that the 4/Rev harmonics dominate the rotor vibratory response in the X and Y directions. The experimental HHC input reduces all output harmonics except the θ_{8c} output in the X direction and the θ_{4s} and θ_{12s} component in the Y direction. The increase in the amplitude of these three components is small compared to the reduction in amplitude of the dominant 4/Rev components with HHC input inclusion, which yields that these small-amplitude increases will have little impact on the calculated optimal HHC input result. Added to this, there will also be greater intrinsic attenuation of high-frequency components in the load transfer pathway.

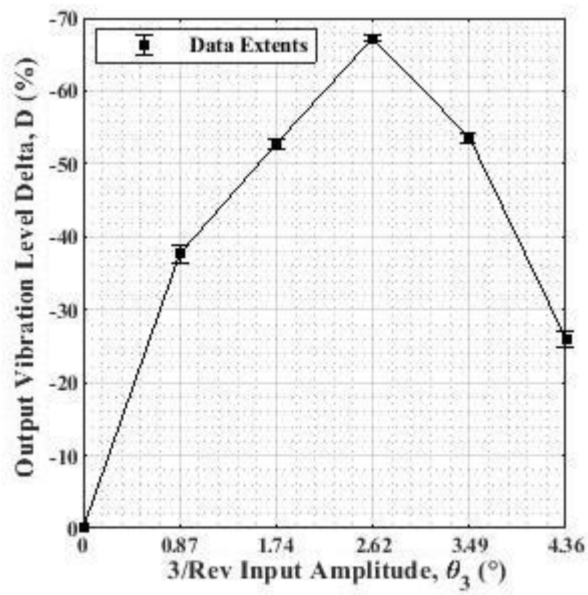

Figure 8.8 – Experimental kN$_b$/Rev rotor vibratory load change as a function of 3/Rev HHC input amplitude

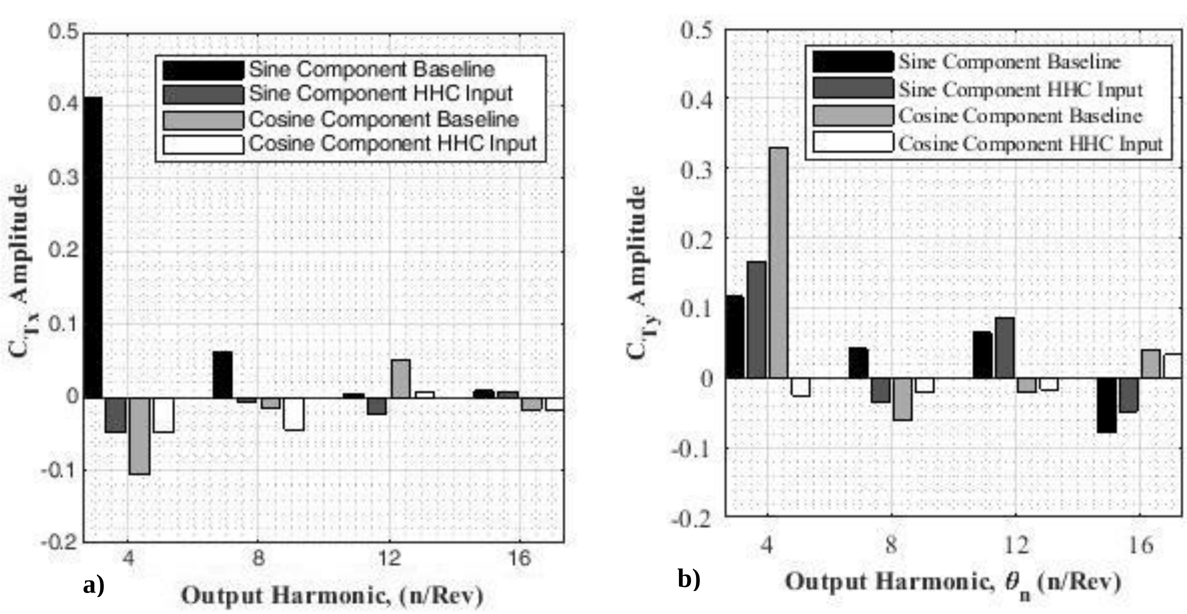

Figure 8.9 – Experimental kN$_b$/Rev rotor harmonic coefficients (a) X Direction and (b) Y Direction

8.7. Optimal Computational Model and Experimental HHC Input Comparison

A comparison of the calculated HHC input optimal points from each of the computational models and experimentation is shown in table 8.1. The amplitude of the single-step experimental 3/Rev input is in very good agreement with the two BET code modeling approaches. The 2D CFD single-step model predicts a 3/Rev HHC input amplitude of 8.657°, which is approximately a factor of three greater than the BET code and experimentally calculated amplitudes. The experimentally HHC input phase angle of 35.600° is halfway between that predicted by the BET code and CFD modeling. While the computational approaches provide a quantitative numerical analysis of the rotor vibratory response's underlying behavior, it also highlights the challenges and limitations in modeling the rotor vortex shedding behavior.

Table 8.1. Calculated optimum 3/Rev HHC input

Optimization Method	HHC 3/Rev Input Amplitude, θ_3 (°)	HHC 3/Rev Input Phase Φ_3 (°)
BET code single-step optimization	2.785	2.940
BET code full non-linear optimization	2.786	2.877
2D CFD single-step optimization	8.657	67.519
Experimental single-step optimization	2.616	35.600

8.8. Computational Model Unsteady Blade Force and Instantaneous Flow Field Analysis at Optimal HHC Input

Section 8.5 highlighted considerable differences in the calculated optimal HHC input amplitude and phase between the BET code and CFD modeling and a reduction in vibratory response with a higher peak AOA in the CFD model. The ability to model blade vortex interactions with the CFD is a key difference between the two modeling approaches. The CFD model of the baseline cyclic pitch and HHC input case is considered in more detail to understand the sensitivity of the blade loadings and rotor response to blade vortex interactions and flow separation.

Individual blade forces were plotted against changing azimuth for the CFD analysis, as shown in figure 8.10 (a) and figure 8.10 (b), for the baseline pitch and HHC input case to understand the effect of the HHC input on blade force generation. The HHC input changes the blade force generation in a few areas. In order to understand the mechanisms behind the changes in blade loading, a qualitative analysis of the instantaneous global contours of vorticity plots was initially undertaken for the baseline pitch and HHC input case, as shown in figure 8.11 (a-c) and figure 8.11 (d-f), respectively. The baseline pitch case is considered first.

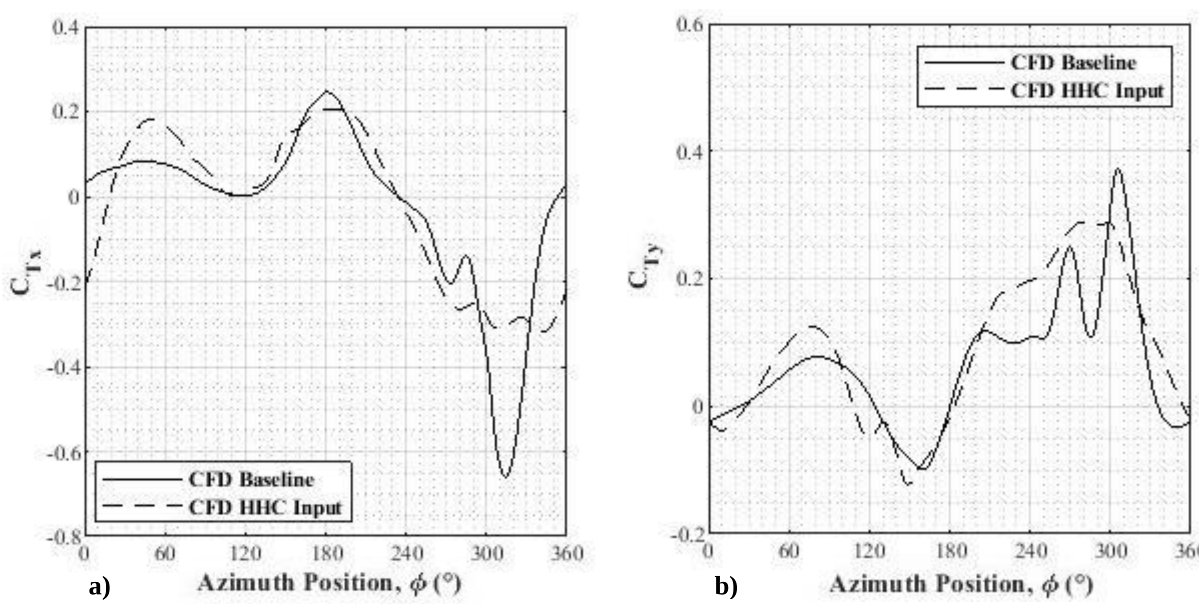

Figure 8.10 – CFD blade instantaneous blade load change with azimuth position (a) X Direction (b) Y Direction

At Ψ = 0°, a vortex is being shed from the leading edge of blade B1 in figure 8.11 (a). As the rotor rotates to Ψ = 30°, the shed vortex attaches to the boundary layer of blade B4 in figure 8.11 (b). This attachment on the suction side forms part of the LEV formation and growth on the suction side of the blade. As the rotor rotates to Ψ = 60°,

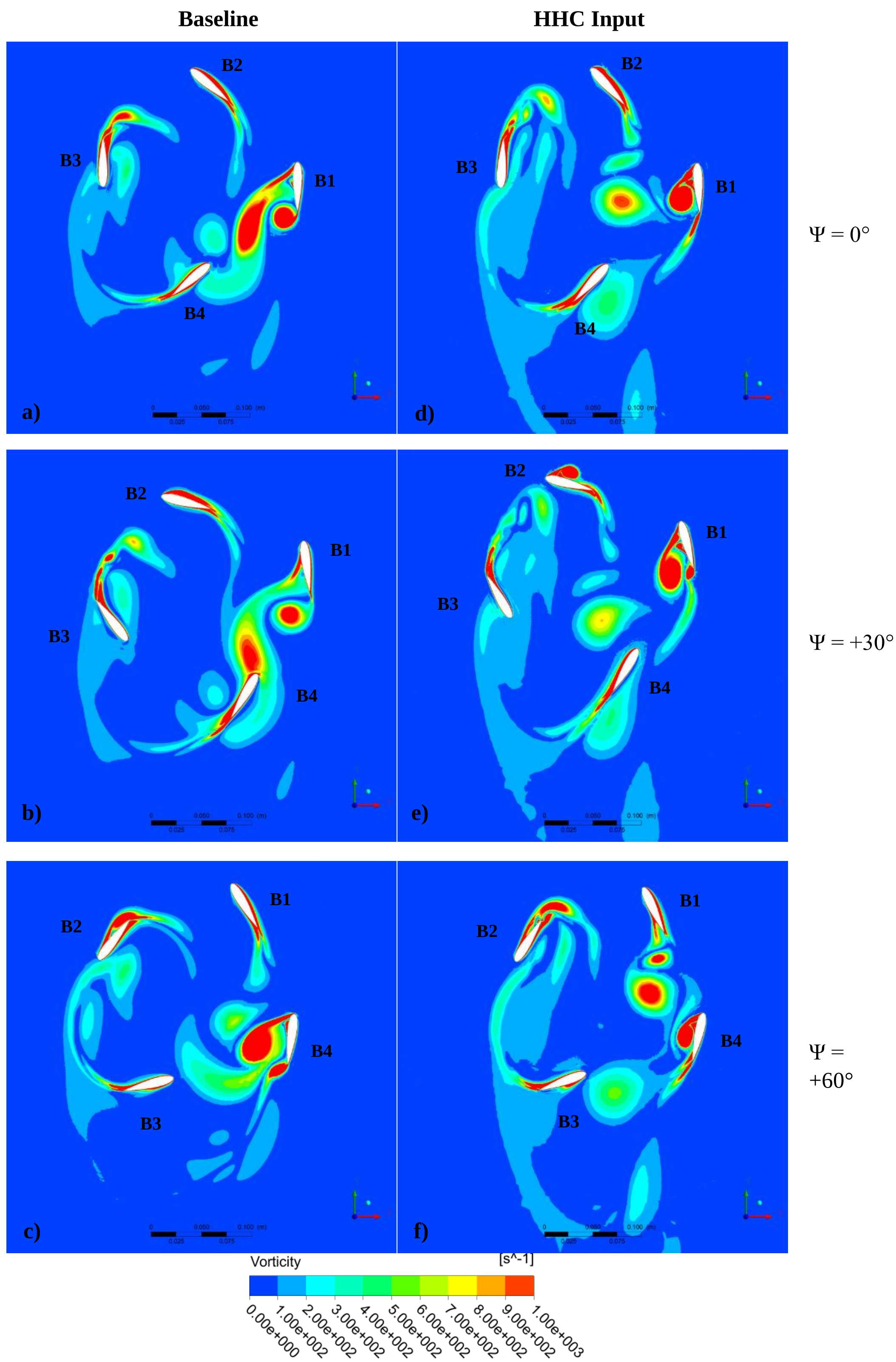

Figure 8.11 – Instantaneous CFD vorticity flow fields. (a to c) Baseline and (d to f) HHC input configuration

the LEV vortex on blade B4 begins to shed into the wake, as shown in figure 8.11 (c), where the flow is then fully separated on the inner suction surface of the blade. The vortex attachment in figure 8.11 (b) generates a negative spike in the X direction in 8.10 (a) and a corresponding loss of Y-direction force in figure 8.10 (b) at approximately Ψ = 300°. This is confirmed in figures 8.12 (a) and 8.12 (b) for C_P and skin friction coefficient (SF) for blade B4 at an azimuth position of Ψ = +30°, as depicted in figure 8.11 (e). The LE separation can be seen in figure 8.12 (b) as the SF approaches zero, accompanied by the prominent C_P suction peak in figure 8.12 (a), showing that the magnitude of pressure variation decreases away from the LE edge. At this point, the blade is on the downstroke, and a secondary LEV vortex forms, producing an increase in secondary lift, resulting in the distinctive double Y-direction force peak. The delay in the LEV detachment and convection into the wake provides an increase in dynamic lift

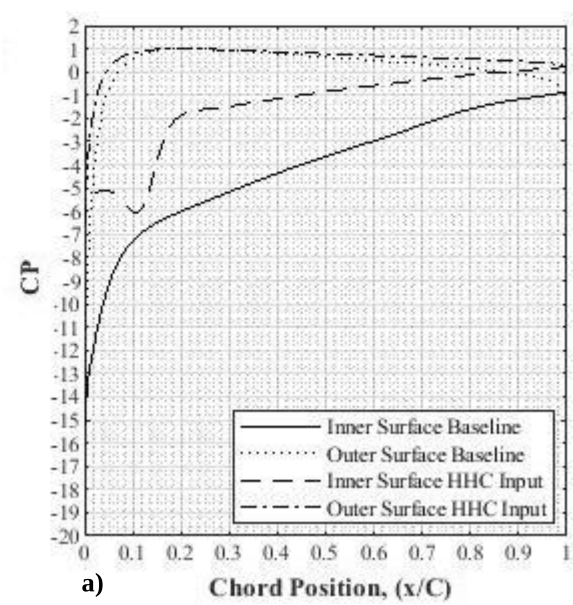

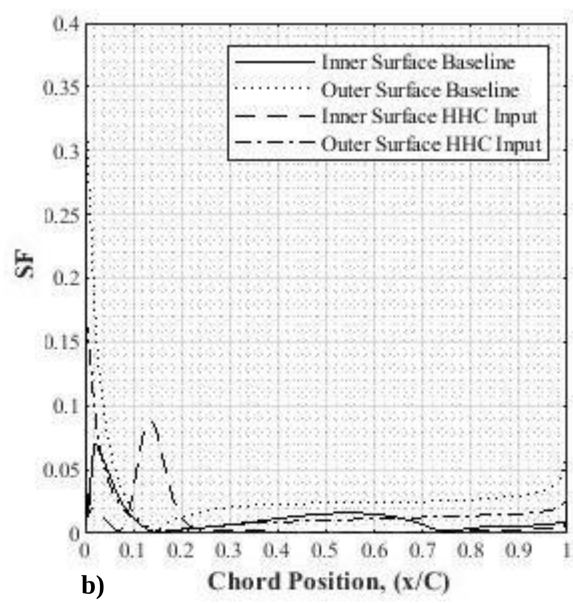

Figure 8.12 – CFD Analysis instantaneous data for blade 4 at Ψ = +30° (a) C_P and (b) SF Coefficient

For the HHC input case at Ψ = 0° azimuth, a strong leading-edge vortex (LEV) is produced at blade B1 due to the blade clockwise (CW) pitching motion generating increased X and Y force components, as shown in figure 8.11 (d). At the same time, a trailing edge vortex (TEV) is created but still attached. Comparison to figure 8.11 (a) indicates that the HHC input adds a phase delay to the generation and shedding of LEV and TEV as the baseline case blade B1 shows the vortices already shed. At $\Psi = 30°$, figure 8.11 (d) blade B1 shows laminar separation, transition, turbulent separation, and reattachment regions. These are attributable to multiple vortices being shed and created at the LE and interacting with the blade boundary layer. Between $\Psi = 0°$ and 30°, the X-direction HHC input blade force lags behind the baseline case from figure 8.10 (a). Thus, indicating an increase in effective AOA with HHC input despite operating at a reduced geometric pitch angle, highlighting a change in rotor inflow.

At $\Psi = 120$ to 130°azimuth position, figure 8.10 (a) shows a local minimum that corresponds to a reduction in Y direction force figure 8.10 (b). this reduction is attributable to a leading-edge separation bubble (LESB), as seen in figure 8.11 (e), blade B2. As the bubble begins to break down past this point, stall occurs, reducing the Y force component shown in figure 10 (b). This feature cannot be seen in the baseline case. The blade pitching in a counter-clockwise manner (CCW) coupled with the rotor inflow reduces blade AOA. Reattachment occurs with recovery as the AOA is decreased sufficiently, which is seen in the Y force generation at the $\Psi = 150°$ position.

The HHC input changes the blade force generation significantly in the fourth quadrant, between the $\Psi = 270°$ and 360°, where the baseline case is undergoing blade wake interaction and ultimately dynamic stall. With HHC input, the large X direction force overshoots and sudden reduction in Y direction force are not experienced. The introduction of the HHC input changes the trajectory and phasing of the shed vortices, and a comparison of figure 8.11 (b) and 8.11 (e) shows that there is limited BVI. This is confirmed in figure 8.12 (a), where there is a significant change in the C_p profile of blade B4, and no pressure peak at the blade LE is experienced. However, a region of flow separation and reattachment behind the LE corresponds to the 'dip' in the C_p profile between 0.1 and 0.2C, shown further by the SF profile in figure 8.12 (b) on the inner surface with HHC input at the same chordwise positions are reduced to zero. This indicates that the HHC input manipulates the blade separation and vortex-shedding events to change the rotor vibratory response.

The analysis shows that accurately modeling the interaction between blade wakes and shed vortices is key to calculating rotor vibration. This is the main reason why considerable differences in the calculated optimal HHC input amplitude and phase between the BET code and CFD modeling exist in section 8.5. The BET code is not able to consider blade interaction and assumes each blade is independent.

Whilst operating at higher geometric AOA with the CFD model with HHC input, the phase change in vortex shedding between $\Psi = 270°$ and $360°$ results in weaker blade vortex interactions and a reduction in force amplitude in this area. Interrogation of the pitch profile between the baseline and HHC input case shows that between approximately $\Psi = 290°$ and $350°$, the geometric AOA for the HHC input case is lower than the baseline, and this will also have an effect on vortex shedding behavior.

8.9. Cycloidal Rotor Performance with HHC Input

Yielding vibration reduction through HHC is one aspect of rotor optimization and is the aspect considered in detail in the current research. The Rotor power loading (PL) was calculated to establish how the inclusion of an HHC input changes rotor performance based on the experimental test results. For increased rotor efficiency, a higher value of PL is typically required. The inclusion of the optimal experimental HHC input at a single HHC input of 3/Rev reduces the PL by approximately 12%, as illustrated in figure 8.13, highlighting the importance of considering multiple areas of rotor optimization to progress the cycloidal rotor further.

8.10. Chapter Review

This chapter has presented the first numerical and experimental investigation of HHC control of cycloidal rotor vibratory loading. It was found that HHC is an effective vibratory load reduction technique for cycloidal rotors, with the 3/Rev HHC input reducing kN_b/Rev harmonics in all instances, with experimental reduction up to 67.5%.

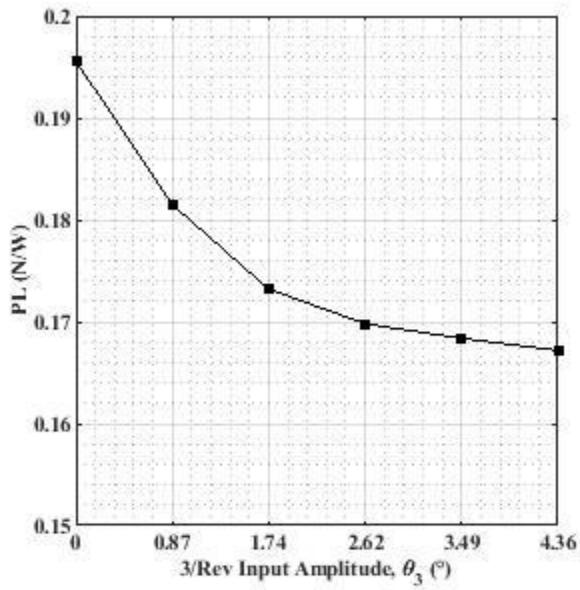

Figure 8.13 – Rotor Power Loading (PL) as a function of 3/Rev HHC input amplitude based on experimental data

The optimal operating point showed large variability between analysis techniques. In particular, the optimal amplitude and phasing of the input harmonic were found to be closely linked with flow separation events caused by the cyclic pitch motion. The interaction between blade wakes and shed vortices plays a vital role in the individual blade loading and subsequent rotor vibration. CFD modeling illustrates that this is particularly dominant in the lower half of the rotor. The difficulties associated with modeling these events highlight the challenge in the quantitative numerical analysis of the behavior. Qualitatively the experiment corroborated the behaviors seen in the simulations and validated the efficacy of the HHC approach.

Rotor vibratory loading plays a vital role in cycloidal rotor development and is a key driver in component design. This work confirms HHC control as a viable means of rotor vibration suppression and provides the necessary foundations for the development of a full closed-loop HHC implementation on a cycloidal rotor, which would develop the proof of concept HHC implemented into a system that is capable of flight and use in a wide range of operational maneuvers.

9. Conclusion

9.1. Introduction

The current thesis has analyzed the possibility of modeling and optimizing the cycloidal rotor vibratory response using a combination of reduced-order computational models, high-order computational models (CFD), and experimentation. A review of rotorcraft literature identified several sources of craft vibration, with the main rotor being a key driver in overall vibration levels. With a relatively large rotating structure and highly unsteady blade loads, cycloidal rotor vibratory response optimization was identified as a critical area for rotor advancement. Higher harmonic control (HHC) is proposed for the first time on a cycloidal rotor as a means of rotor vibration reduction.

The thesis has proposed, designed, developed, and validated methodologies to provide new insight into the operation of the cycloidal rotor and confirmed the use of HHC as a highly effective means of vibration suppression. The present chapter draws the thesis to a close, providing a summary of the research and the key findings. This is followed by an overview of the significant contributions of the research, and finally, future avenues of research are proposed.

9.2. Summary

A comprehensive review of cycloidal rotor independent research in Chapter 2 informed the design of the current test rig, outlined in Chapter 3. Chapter 3 began with an overarching design methodology followed by test rig construction and assembly. Much effort was spent developing the current experiment design to ensure the quality of the results. A method of sensor dynamic calibration typically used in standard rotorcraft research was modified for use with the cycloidal rotor based on previous studies reviewed in Chapter 2 to account for test rig dynamics. Limitations of the existing dynamic calibration test approaches were identified, and the 1D dynamic calibration transfer function approach was shown to be satisfactory in assessing vibratory loads. Similarly, as in standard rotorcraft research, rotor vibratory loads are intrinsically challenging to model and measure accurately due to uncertainties in blade aerodynamic loads and rotor flow physics, often driven by modeling assumptions and experimental limitations.

The experiments confirmed that mean thrust and power coefficients remain constant with changing blade cyclic pitch amplitude for varying rotor speeds, in line with independent rotor studies. High levels of experimental repeatability were identified, confirming the reliability of the test setup. Despite the mean coefficients remaining constant with changing rotational speed, this was not the case experimentally for the calculated 4/Rev rotor harmonics.

Experimental studies with the current test rig confirmed the finding of standard rotorcraft research. The cycloidal rotor vibratory response is defined by the blade pass frequency harmonics. The fundamental 4/Rev vibratory component is dominant for a 4-blade rotor and the main harmonic associated with thrust generation. The modulation of the vibratory response increased with increasing blade cyclic pitch angle up to the maximum amplitude of 40° considered. Higher harmonics of blade pass frequency magnitude are significantly lower than the 4/Rev response and were measured to be almost constant with changes in blade cyclic pitch amplitude from the experimental data.

An unsteady aerodynamic model was developed based on a uniform rotor inflow model and indicial response aerodynamics as outlined in Chapter 5 to account for the blade pitching kinematics. The model predicted the mean performance of the cycloidal rotor with good accuracy across the range of cyclic pitch amplitudes considered and aided preliminary test rig validation. However, the results showed only qualitative agreement in the 4/Rev rotor vibratory response compared with experimental data. This is discussed in Chapter 7.

The CFD model predicted the mean performance of the cycloidal rotor with good accuracy and showed an improved correlation with experimental results compared to the BET code. A comparison of the computational models highlighted differences between the BET code and 2D CFD models and subsequent BET code limitations. Overall, the applicability of reduced-order computational models in initial preliminary rotor design studies has been confirmed. But if greater detail is required to capture the rotor flow physics with improved accuracy, higher-order modeling approaches such as CFD is required.

In line with experimental results, the computational models show that the variation in the predicted 4/Rev response is strongly related to blade cyclic pitch amplitude, with increased modulation with increasing blade cyclic pitch amplitude. The CFD models discussed in Chapters 6 and 7 identified that as the blade cyclic pitch amplitude increases, the blade wake interaction and blade stall have a significant bearing on the overall vibratory response of the rotor. This is particularly evident in the final quadrant of the rotor between 270° and 360° azimuth. Based on this, further experimental development is recommended, as outlined in section 9.4 further work, to understand the cycloidal rotor flow physics in even more detail.

This leads to the data presented in Chapter 8 to study the effect of using HHC on the cycloidal rotor vibratory response, using modified versions of the computational models and test rig already developed. Following a systematic HHC parameter sweep to develop sensitivity matrices utilizing the computational models, the 4/Rev rotor response was found to be highly susceptible to a 3/Rev HHC input when used in conjunction with the developed linear and non-linear optimization strategies. Furthermore, the inclusion of HHC saw an experimental reduction in rotor vibratory response of up to 67.5%.

The optimal HHC input operating point showed large variability between analysis techniques. The HHC input amplitude and phasing of the input harmonic were closely linked with blade wake interaction events caused by the blade pitching motion. The difficulties associated with modeling the rotor flow physics highlighted the challenges in analyzing cycloidal rotor behavior. The experimental results corroborated the behaviors seen in the computational models and validated the efficacy of the HHC approach.

The work presented in this thesis has proven the hypothesis that HHC can be used for cycloidal rotor vibration control and demonstrated two computational modeling approaches for its implementation, to varying degrees of success. In addition, the research provides the foundations for further studies to implement full closed-loop HHC on a cycloidal rotor, as outlined in section 9.4 future work. This would develop the HHC explored here into a system that is capable of flight.

9.3. Principle Contributions

The main contributions of the work presented to the body of knowledge in the field are:

1. Undertook the first known systematic experimental study of the cycloidal rotor in hover to measure both the rotor mean and vibratory response over a range of blade cyclic pitch amplitudes and rotor speeds.

2. Development of a reduced-order unsteady BET code computational model validated against experimental data that provided new insight into cycloidal rotor operation and vibratory response.

3. A 2D CFD model was developed to calculate the rotor mean and vibratory response to undertake the first known computational model analysis to analyze a hovering rotor vibratory response over a range of blade cyclic pitch amplitudes and rotor speeds for comparison with experimental data. A systematic analysis of instantaneous blade loads and flow fields was undertaken to gain new insight into the mechanisms behind the cycloidal rotor vibratory response.

4. A computational optimization methodology was developed and validated to verify the feasibility of using HHC input as a cycloidal rotor vibration suppression method.

5. Undertook an experimental study implementing the optimization methodology by using novel cam profiles to validate and confirm the efficacy of the optimization approach and computational models.

9.4. Future Work

The current thesis has presented a systematic analysis of a hovering cycloidal rotor in its baseline form and with HHC implemented and highlighted some of the challenges associated with cycloidal rotor research. In reality, cycloidal rotor understanding and optimization are still in their infancy, with much scope for further assessment and improvement in many areas, vibration reduction being one.

Additional experimentation could also investigate the use of HHC feedback control through a bespoke controller and modified test rig cam actuation arrangement as a natural progression of the current research to enable in-flight changes to be made to HHC input. This would move the use of HHC closer to a system that could be used in actual flight and could be implemented via the use of individual blade actuation.

To gain a deeper understanding of the blade aerodynamic and inertial loading to guide future analysis methods, the instrumentation of a single blade or blade attachment point would be a worthwhile endeavor. While this would not be easily implemented due to measured data needing to be transferred from the rotating to stationary parts without the use of wires, it has the potential to provide insight that is not possible in other methods of analysis or experimentation.

Bibliography

[1] Anderson, S B. "Historical Overview of V/STOL Aircraft Technology," NASA Technical Memorandum 81280. Ames Research Center, California.

[2] "European Aeronautics: A Vision for 2020." Advisory Council for Aviation Research, and Innovation in Europe, European Commission, Luxembourg, 2001.

[3] "Flightpath 2050-Europe's Vision for Aviation." Directorate-General for Research and Innovation and Directorate-General for Mobility and Transport, Luxembourg, 2011.

[4] Benedict, M. "Fundamental Understanding of the Cycloidal Rotor Concept for Micro Air Vehicle Applications" (Thesis).

[5] Bacchini, A. Cestino, E. 2019. "Electric VTOL Configurations Comparison," Aerospace, Volume 6, Number 26.

[6] Kirsten, F K. "Cycloidal Propulsion in Air Part 1 Cycloidal Propulsion Theory," Engineering Experiment Station Series Bulletin No. 79.

[7] Kirsten, F K. "Cycloidal Propulsion in Air Part 2 Cycloidal Propellor Development," at the University of Washington Engineering Experiment Station Series Bulletin No. 79.

[8] Wheatley, J B., and Windler, R. "Wind Tunnel Tests of a Cyclogiro Rotor," Langley Memorial Aeronautical Laboratory NACA 528.

[9] Andrisani, A et al. 2016. "Optimal pitching schedules for a cycloidal rotor in hovering." Aircraft Engineering and Aerospace Technology An International Journal. Volume 88, Number 5, Pages 623 – 635.

[10] Daizong, L. "Design of a New VTOL by Combining Cycloidal Blades and Fan Wing Propellers," Department of Flight Vehicle Nanchang Hangkong University (Thesis).

[11] Nozaki, H., and Sekiguchi, Y. Matsuuchi, K. "Research and Development on Cycloidal Propellers for Airships. 18th AIAA Lighter Than Air Systems Technology," Conference, Seattle, Washington, 4 - 7 May 2009.

[12] Yun, C Y. et al. "The Cyclocopter: A New Type of UAV." ICAST 2003 14th International Conference on Adaptive Structures and Technologies. Seoul, Korea, October 7 – 9, 2003.

[13] Pines, D J., and Bohorquez, F. 2006. "Challenges Facing Future Micro-Air-Vehicle Development," Journal of Aircraft, Volume 43, Number 2, pages 290-305.

[14] Adams, Z. et al. 2013. "Design, Development, and Flight Test of a Small-Scale Cyclogyro UAV Utilizing a Novel Cam-Based Passive Blade Pitching Mechanism."

[15] Benedict, M. et al. 2014. “Effect of Flow Curvature on Forward Flight Performance of a Micro-Air-Vehicle-Scale Cycloidal Rotor.” AIAA JOURNAL, Volume 52, Number 6, Pages 1159-1169.

[16] Andrew, H. et al. 2014. “Flow Field Studies on a Micro Air Vehicle Scale Cycloidal Rotor in Forward Flight.” Exp Fluids, Volume 55, Page 1826.

[17] Strandgren, C B. 1933. “The Theory of The Strandgren Cyclogiro.” L’Aerophile, Volume 41, Number 7.

[18] Boschma, J H. “Final Report – Cycloidal Propulsion for UAV VTOL Applications SBIR Topic Number N98-022.” Bosch Aerospace, Inc.

[19] Iosilevskii, G. Levy, Y. 2006. “Experimental and Numerical Study of Cyclogiro Aerodynamics.” AIAA JOURNAL. Volume 44, Number 12, Pages 2866-2870.

[20] Xisto, C M et al. “Numerical Modelling of Geometrical Effects in the Performance of a Cycloidal Rotor,” 11th World Congress on Computational Mechanics (WCCM XI).

[21] Adams, Z. et al. 2013. “Design, Development, and Flight Test of a Small-Scale Cyclogyro UAV Utilizing a Novel Cam-Based Passive Blade Pitching Mechanism.”

[22] Foshag, W F., and Boehler, G D. “Review and Preliminary Evaluation of Lifting Horizontal Axis Rotating Wing Aeronautical Systems (HARWAS).”

[23] Pascoa, J., and Monteiro, J A L. “Effects of Harmonic Vibration on Cycloidal Rotor Performace.” Proceedings of the ASME 2018 International Mechanical Engineering Congress and Exposition IMECE2018. Pittsburgh, PA, USA. November 9-15, 2018.

[24] Habibnia, M., and Páscoa, J. 2021. “A Coupled Active Control Technique for Oscillating Blades in a Cycloidal Rotor Using CFD and ANN Analysis by Including 3D Endwall Effects.” Journal of Aerospace Engineering. Volume 18, Number 10.

[25] Xisto, C M et al. “PECyT - Plasma Enhanced Cycloidal Thruster.” Propulsion and Energy Forum, Cleveland, OH, USA. July 28-30, 2014.

[26] Leger, J A., Pascoa, J C., and Xisto, C M. 2015. “Analytical Modeling of a Cyclorotor in Hovering State.” Proc IMechE Part G: J Aerospace Engineering, Volume 0, Number 0, Pages 1–15.

[27] Yun, C H., and Park, I. “A New VTOL UAV Cyclocopter with Cycloidal Blades System.”

[28] Kim, S J. et al. “Design and Performance Tests of Cycloidal Propulsion Systems.”

[29] Jarugumilli, T., Benedict, M., and Chopra, I. "Experimental Optimization and Performance Analysis of a MAV Scale Cycloidal Rotor." 49th AIAA Aerospace Sciences Meeting including the New Horizons Forum and Aerospace Exposition, Orlando, Florida, 4 - 7 January 2011.

[30] Tang, J., Hu, Y., and Song, B. 2015. "Investigation on the Unsteady Aerodynamics of Cycloidal Propeller in Hovering Flight." Proc IMechE Part G: J Aerospace Engineering, Volume 229, Number 13, Pages 2519–2536.

[31] Squire, A., "Cyclocopter: Predicting The Generation of Lift from a Cyclorotor using a Cycloidal Blade System (Dissertation)."

[32] Monteiro, J., Pascoa, J C., and Xisto, C. 2013. "Analytical Modeling of a Cyclorotor in Forward Flight. SAE International."

[33] Yun, C H. et al. 2005. "Thrust Control Mechanism of VTOL UAV Cyclocopter with Cycloidal Blades System." Journal of Intelligent Material Systems and Structures. Volume 16, Pages 937 – 943.

[34] McNabb, M L. "Development of a Cycloidal Propulsion Computer Model and Comparison with Experiment." (Thesis)

[35] Yun, C H., and Park, I. "A New VTOL UAV Cyclocopter with Cycloidal Blades System."

[36] Benedict, M., Chopra, I., Mattaboni, M., and Masarati, P. "Aeroelastic Analysis of a MAV-Scale Cycloidal Rotor."

[37] Maine, R. "SBIR A02.07: VTOL to Transonic Aircraft. Acuity Technologies Inc."

[38] Benedict, M. et al. 2011. "Aeroelastic Analysis of a Micro-Air-Vehicle-Scale Cycloidal Rotor in Hover." AIAA JOURNAL, Volume 49, Number 11, Pages 2430-2443.

[39] Benedict, M., Jarugumilli, T., and Chopra, I. 2013. "Effect of Rotor Geometry and Blade Kinematics on Cycloidal Rotor Hover Performance." Journal of Aircraft, Volume 50, Number 5, Pages 1340-1352

[40] Yang, K. "Aerodynamic Analysis of an MAV Scale Cycloidal Rotor System Using a Structured Overset RANS Solver (Thesis)."

[41] Yu, H., Beng, T W., and Bin, L K. "The Investigation of Cyclogiro Design and the Performance. 25th International Congress of the Aeronautical Sciences."

[42] Ferreira, C. J. "The near wake of the VAWT2D and 3D views of the VAWT aerodynamics. (Thesis)."

[43] Hwang, I S., Hwang, C S., and Kim, S J. “Structural Design of Cyclocopter Blade System Seoul National University.”

[44] Houghton, E L., and Carpenter, P W. Fifth Edition. “Aerodynamics for Engineering Students.”

[45] Gosselin, R., Dumas, G., and Boudreau, M. “Parametric study of H-Darrieus vertical-axis turbines using uRANS simulations.” 21st Annual Conference of the CFD Society of Canada, Sherbrooke, Canada, 6 – 9 May 2013.

[46] Hu, Y., Zhang, H L., and Tan, C. 2015. “The Effect of the Aerofoil Thickness on the Performance of the MAV Scale Cycloidal Rotor.” The Aeronautical Journal, Volume 119, Number 1213.

[47] Beri, H., and Yao, Y. 2011. “Effect of Camber Airfoil on Self Starting of Vertical Axis Wind Turbine.” Journal of Environmental Science and Technology, Volume 4, Number 3, Pages 302-312.

[48] Hwang, I S. et al. “Multidisciplinary Optimal Design of Cyclocopter Blade System.”

[49] Jarugumilli, T. “An Experimental Investigation of a Micro Air Vehicle-Scale Cycloidal Rotor in Forward Flight (Thesis).”

[50] Hwang, I S., and Kim, S J. “Aerodynamic Performance Enhancment of Cycloidal Rotor According to Blade pivot Point Movement and Preset Angle Adjustment.” Seoul National University.”

[51] Prandtl, L., and Tietjens, O G. 1934. “Applied Hydro and Aeromechanics.” United Engineering Trustees Inc.

[52] Anderson, J D. Sixth Edition. “Fundamentals of Aerodynamics.” McGraw-Hill Education.

[53] Seifert, J. 2012. “A review of the Magnus effect in aeronautics.” Progress in Aerospace Sciences, Volume 55, Pages 17-45.

[54] Badalamenti, C., and Prince, S. “Effects of endplates on a rotating cylinder in crossflow.” 26th AIAA applied aerodynamics conference, Honolulu, Hawaii. 18 – 21 August 2008.

[55] Swanson, W M., 1961. “The Magnus effect: a summary of investigations to date.” Journal of Basic Engineering Transactions of ASME, Volume 83, Number 3, Pages 461-470.

[56] Prandtl, L. 1925. “Application of the ‘‘Magnus Effect’’ to the wind propulsion of ships.” NACA Technical Memorandum TM-367, Pages 93-108

[57] Ung, S K. et al. 2022. "Investigation into the Aerodynamic Performance of a Vertical Axis Wind Turbine with Endplate Design." Energies , Volume 15, 6925.

[58] Miao, W. et al. 2022. "A comprehensive analysis of blade tip for vertical axis wind turbine: Aerodynamics and the tip loss effect." Energy Conversion and Management, Volume 253, 115140.

[59] Jung, J H. et al. 2012. "Endplate effect on aerodynamic characteristics of three-dimensional wings in close free surface proximity." International Journal of Naval Architecture and Ocean Engineering, Volume 4, Number 4, Pages 477-487.

[60] Amato, F. et al. 2013. "Numerical Analysis of the Influence of Tip Devices on the Power Coefficient of a VAWT." International Conference on Mechanical, Industrial, and Manufacturing Engineering, Copenhagen, Denmark, Volume: 78, Pages 387-394.

[61] Gosselin, R., Dumas, G., and Boudreau, M. 2016. "Parametric study of H-Darrieus vertical-axis turbines using CFD simulations. Journal of Renewable and Sustainable Energy, Volume 8, 053301.

[62] Ramkissoon, R., and Manohar, K. 2016. "Experimental Investigation of End Plate Effects on the Vertical Axis Wind Turbine Airfoil Blade." International Journal of Innovative Research in Science, Engineering and Technology, Volume 5, Number 2.

[63] Shrestha, E. et al. "Flight Dynamics Modeling and System Identification of a Cyclocopter in Forward Flight." AHS 71st Annual Forum, Virginia Beach, VA, 5–7 May 2015.

[64] Migliore, P. G., Wolfe, W. P., and Fanuccif, J. B., 1980. "Flow Curvature Effects on Darrieus Turbine Blade Aerodynamics." Journal of Energy, Volume 4, Number 2, Pages 49-55.

[65] King, S. P. 1988. "The minimisation of helicopter vibration through blade design and active control." Aeronautical Journal, Volume. 92, Number 917, Pages 247–263.

[66] Yeo, H., and Chopra, I. 2001. "Coupled Rotor/Fuselage Vibration Analysis Using Detailed 3-D Airframe Models." Mathematical and Computer Modelling, Volume 4, Number 33, Pages 1035-1054.

[67] Friedmann, P. P., and Millott, T.A. 1995. "Vibration Reduction in Rotorcraft Using Active Control: A Comparison of Various Approaches." JOURNAL OF GUIDANCE, CONTROL, AND DYNAMICS, Volume 18, Number 4.

[68] Loewy, R. G. 1984. "Helicopter vibrations- a technological perspective." American Helicopter Society, Journal, Volume 29, Pages 4–30.

[69] Ellis, C. W., and Jones, R. 1963. "Application of an Absorber to Reduce Helicopter Vibration Levels," Journal of the American Helicopter Society. Volume 8, Number 3, Pages 30–39.

[70] Sun, J., Jolly, Q., and Norris, M. A. 1995. "Passive, adaptive and active tuned vibration absorbers survey," Journal of mechanical design, Volume 117, B, Pages 234–242.

[71] Han, D., and Smith, E. C. 2009. "Lagwise loads analysis of a rotor blade with an embedded chordwise absorber." Journal of Aircraft, Volume 46, Number 4, Pages 1280–1290.

[72] Hanouva, M. N. H., and Pierce, G. A. 2009. "Helicopter Vibration Suppression Using Simple Pendulum Absorbers on the Rotor Blade." Journal of the American Helicopter Society, Volume 29, Number 3, Pages 19–29.

[73] Austruy, J. "ROTOR HUB VIBRATION AND BLADE LOADS REDUCTION, AND ENERGY HARVESTING VIA EMBEDDED RADIAL OSCILLATOR" (Thesis).

[74] Reichert, G. 1981. "Helicopter vibration control – a survey", Vertica, Volume 5, Pages 1-20.

[75] Bramwell, A. R. S., Balmford, D., and Done, G., Second Edition. "Bramwell's Helicopter Dynamics."

[76] Moffatt, S., and Griffiths, N. 2009. "Structural Optimisation and Aeroelastic Tailoring of the BERP IV Demonstrator Blade." American Helicopter Society 65th Annual Forum.

[77] Pritchard, J. I., and Adelman, H. M. 2008. "Optimal placement of tuning masses for vibration reduction in helicopter rotor blades." AIAA Journal, Volume 28, Number 2, Pages 309–315.

[78] Markievicz, R. H. 1990. "A study of the aeroelastic behaviour of helicopter rotor blades featuring swept tips." (Thesis).

[79] Phuriwat, A. I., and Gandhi, F. 2002. "Semi-Active Control of Helicopter Vibration Using Controllable Stiffness and Damping Devices." (Thesis).

[80] Papavassiliou, I., Friedmann, P. P., and Venkatesan, C. 1993. "Coupled Rotor-Fuselage Vibration Reduction Using Open-Loop Blade Pitch Control." Mathl. Comput. Modeling, Volume 18, Number 3/4, Pages 131–156.

[81] Jacklin, S. A., Haber, A., de Simone, G. Norman, T. R., and Shinoda, P. 2002. "FULL-SCALE WIND TUNNEL TEST OF AN INDIVIDUAL BLADE CONTROL SYSTEM FOR A UH-60 HELICOPTER." American Helicopter Society 58th Annual Forum, Montréal, Canada, June 11-13.

[82] Straub, F., Anand, V.R., Birchette, T., and Lau, B. "SMART Rotor Development and Wind-Tunnel Test."

[83] Millott, T. A. 1993. "Vibration reduction in helicopter rotors using an actively controlled partial span trailing edge flap located on the blade." (Thesis).

[84] Milgram, J. H. 1997 "A Comprehensive Aeroelastic Analysis of Helicopter Main Rotors with Trailing Edge Flaps for Vibration Reduction." (Thesis).

[85] Nguyen, K. Q. 1994. "Higher Harmonic Control Analysis for Vibration Reduction of Helicopter Rotor Systems." NASA TM-103855.

[86] Johnson, W. 1992. "Self-Tuning Regulators for Multicyclic Control of Helicopter Vibration." NASA Technical Paper 1996.

[87] Robinson, L. H. 1989. "Aeroelastic Simulation of Higher Harmonic Control." (Thesis).

[88] Hammond, C. E. 1983. "Wind Tunnel Results Showing Rotor Vibratory Loads Reduction Using Higher Harmonic Blade Pitch." Journal of the American Helicopter Society, Volume 28, Number 1, Pages 10-15.

[89] Nguyen, K., Betzina, M., and Kitaplioglu, C. 2000. "Full-Scale Demonstration of Higher Harmonic Control for Noise and Vibration Reduction on the XV-15 Rotor." American Helicopter Society 56th Annual Forum, Virginia Beach, VA, May 2-4.

[90] Cheng, R. P., Theodore, C. R., and Celi, R. 2000. "EFFECTS OF HIGHER HARMONIC CONTROL ON ROTOR PERFORMANCE." 56th Annual Forum of the American Helicopter Society, Virginia Beach, Virginia, USA, May 2-4.

[91] Nixon, M. W., Kvaternik, R. G., and Settle T. B. "HIGHER HARMONIC CONTROL FOR TILTROTOR VIBRATION REDUCTION."

[92] Kottapalli, S, and Leyland, J. "Analysis of Open Loop Higher Harmonic Control at High Airspeeds on a Modern FourBladed Articulated Rotor." NASA Technical Memorandum 103876.

[93] Payne, P. R. "Higher Harmonic Rotor Control The Possibilities of Third and Higher Harmonic Feathering for Delaying the Stall Limit in Helicopters." Journal of Rotorcraft

[94] Welsh, W. A. Von Hardenberg, P. C. Von Hardenberg, P. W., and Staple, A. E. 1990. "Test and Evaluation of Fuselage Vibration Utilizing Active Control of Structural Response (ACSR) Optimized to ADS-27." Proceedings of the 46th Annual Forum of the American Helicopter Society, Washington, DC, USA.

[95] Pearson, J. T., and Goodall, R. M. 1994. "Adaptive Schemes for the Active Control of Helicopter Structural Response." IEEE TRANSACTIONS ON CONTROL SYSTEMS TECHNOLOGY, Volume 2, Number 2.

[96] Kreshock, A. R., Thornburgh, R. P., and Wilbur, M. L. "A Dynamic Calibration Method for Experimental and Analytical Hub Load Comparison." NASA/TM–2017-219601. ARL-RP-0592.

[97] Nguyen, K., and Lau, B. “Dynamics of the McDonnell Douglas Large Scale Dynamic Rig and Dynamic Calibration of the Rotor Balance.” NASA Technical Memorandum 108855. Ames Research Center, California.

[98] Norman, T. R. et al. 2002. “Low-Speed Wind Tunnel Investigation of a Full-Scale UH-60 Rotor System.” American Helicopter Society 58th Annual Forum, Montreal, Canada, June 11-13.

[99] Peterson, R. L., and van Aken, J. M. “Dynamic Calibration of the NASA Ames Rotor Test Apparatus Steady/Dynamic Rotor Balance.” NASA Technical Memorandum 110393

[100] Russell, C. 2014. “Shake Test Results and Dynamic Calibration Efforts for the Large Rotor Test Apparatus.” Presented at the Fifth Decennial AHS Aeromechanics Specialists’ Conference, San Francisco, CA, January 22-24.

[101] Russell, C. “Shake Test Results and Dynamic Calibration Efforts for the Large Rotor Test Apparatus.”

[102] Lehmann, G., and Fu. K. H. “Theoretical and Experimental Investigations on a six-component Rotor Balance.” Eleventh European Rotorcraft Forum, Paper Number 102, The City University, London, England

[103] Pope, A., Barlow, J.B., and Rae, W. H. Third Edition. “Low-speed Wind Tunnel Testing.”

[104] Belkherchouche, A., Boudiaf. A., and Belouchrani, M. E. L. 2014. “Contribution to the Life Prediction of Aluminium Alloys Parts under Isothermal Fatigue.” Key Engineering Materials, Volume 592-593, Pages 233-236.

[105] Changyou Li, C., Dai, W., Duan, F., Zhang, Y., and He, D. 2017. “Fatigue Life Estimation of Medium-Carbon-Steel with Different Surface Roughness.” Appl. Sci., Volume 7, Number 338.

[106] Chambers, J. A. “Preloaded Joint Analysis Methodology for Space Flight Systems.” NASA Technical Memorandum 106943. Lewis Research Center Cleveland, Ohio

[107] Murthy1, S. 2018. “Verification of Over-Speed and Burst Margin Limits Inaero Engine Rotor Coupling Along with Estimation of Low Cycle Fatigue Life.” International Journal of Applied Engineering Research. Volume 13, Number 20, Pages 14498-14504.

[108] Gibson, R. F. 2016 “Principles of Composite Material Mechanics.”

[109] Moffat, R. J. 1988. “Describing the Uncertainties in Experimental Results.” Experimental Thermal and Fluid Science, Volume 1, Pages 3-17.

[110] Ewins, D. J. Second Edition. “Modal Testing: Theory, Practice and Application.”

[111] Heathcote, D. J., 2017. "Aerodynamic Loads Alleviation Using Mini-Tabs." University of Bath. Thesis

[112] Benedict, M., Ramasamy, M., and Chorpra, I. 2010. "Performance of a cycloidal rotor concept for micro-air-vehicle applications." Journal American Helicopter Society." Volume 55, Pages 22002–1–22002-14.

[113] Yousefi1, K., and Razeghi, A. "Determination of the Critical Reynolds Number for Flow over Symmetric NACA Airfoils." 2018 AIAA Aerospace Sciences Meeting, Kissimmee, Florida, January 8–12.

[114] Garrick, I. E., 1936. "Propulsion of a flapping and oscillating airfoil," NACA Report No. 567, Pages 419-427.

[115] Tang, J., Hu, Y, Song, B., and Yang, H. 2018. "An unsteady free wake model for aerodynamic performance of cycloidal propellers." Proc IMechE Part G: J Aerospace Engineering, Volume 232, Number 2, pages 290–307.

[116] Yun, C. Y., and Park, I. 2004. "A New VTOL UAV Cyclocopter with Cycloidal Blades System," American Helicopter Society 60th Annual Forum, Baltimore, MD.

[117] Leishman, J. G. 2016. Second Edition. "Principles of Helicopter Aerodynamics."

[118] Leishman, J. G., and Beddoes, T. T. 1986. "A Generalised Model for Airfoil Unsteady Aerodyanmic Behaviour and Dynamic Stall Using the Indicial Method." 42nd Annual Form of the Americal Helicopter Society, Washington, D.C., USA, June 1986.

[119] Leishman, J. G., and Beddoes, T. T. 1986. "A Semi-Empirical Model For Dynamic Stall." 42nd Annual Form of the Americal Helicopter Society, Washington, D.C., USA, June 1986.

[120] Childs, P. R. N., 2011. First Edition. "Rotating Flow."

[121] Hu. Y., Lang, Z. H., and Qi, W. G. 2018. "Two-dimensional and three-dimensional numerical simulations of cycloidal propellers in hover." Proc IMechE Part G: J Aerospace Engineering, Volume 232, Number 7, Pages 1223–1234.

[122] Ferrier, L. 2020. "Investigation on the Aerodynamic Performance of Cycloidal Rotors with Active Leading-Edge Morphing." Thesis

[123] www.engineering.com/story/choosing-the-right-turbulence-model-for-your-cfd-simulation. Accessed 15/04/2022

[124] Wilcox, D. 1998. Second Edition. "Turbulence Modeling for CFD."

[125] Singh, K., and Pascoa, J. C. 2019. "Numerical Modeling of Stall and Poststall Events of a Single Pitching Blade of a Cycloidal Rotor." Journal of Fluids Engineering, Volume 141.

[126] Patankar, S. V., 1990, Numerical Heat Transfer and Fluid Flow, Hemisphere, Washington, DC.

[127] Lee, T., and Gerontakos, P., 2004, "Investigation of Flow Over an Oscillating Airfoil," Journal Fluid Mech., Volume 512, Pages 313–341.

[128] McNaughton, J., Billard, F., and Revell, A. 2014. "Turbulence modeling of low Reynolds number flow effects around a vertical axis turbine at a range of tip-sped ratios." Journal Fluids Structures, Volume 47, Pages 124–138.

[129] Ansys FLUENT, I. Fluent 6.3 User's Guide, Fluent Documentation.

[130] Xisto, C. M., Leger, J., and Pascoa, J. C. 2016. "Parametric Analysis of a Large-scale Cycloidal Rotor in Hovering Conditions," ASCEs Journal of Aerospace Engineering, Volume 30, Number 1, Pages 1–14.

[131] Hand, B., Kelly, G., and Cashman, A. 2017. "Numerical simulation of a vertical axis wind turbine airfoil experiencing dynamic stall at high Reynolds numbers," Computers and Fluids, Volume 149, Pages 12–30.

[132] Bangga, G., Hutomo, G., Wiranegara, R., and Sasongko, H. 2017. "Numerical study on a single bladed vertical axis wind turbine under dynamic stall," Journal of Mechanical Science and Technology, Volume 31, Number 1, Pages 261–267.

[133] Gessow, A., and Myers, G.C. 1985. Eighth Edition. "Aerodynamics of the Helicopter."

[134] Todorov, M., Dobrev, I., Massouh, F., and Velkova, C. 2012. "AN INVESTiGATION OF THE MOTION OF A HELICOPTER ROTOR WITH FLAPPING AND LEAD/LAG HINGES IN HOVER." BulTrans-2012 Proceedings, Sozopol, September 26-28.

[135] Wood, E., Powers, R., Cline, J., and Hammond, C., "On Developing and Flight Testing a Higher Harmonic Control System," Journal of the American Helicopter Society, Vol. 30, No. 1, 1985.

[136] Miao, W., Kottapalli, S., and Frye, H. "Flight Demonstration of Higher Harmonic Control on the S-76 Rotor," American Helicopter Society 42nd Annual Forum Proceedings, Washington, D.C., 1986.

[137] Castillo-Rivera, S., and Tomas-Rodriguez, M., "Hover Flight Helicopter Modelling and Vibrations Analysis," XXXVI Automatics Conference, Bilbao, 2015, pp. 473-480.

[138] Patt, D., Liu, L., Chandrasekar, J., Bernstein, D. S., and Friedmann, P. P., "Higher-Harmonic-Control Algorithm for Helicopter Vibration Reduction Revisited," Journal of Guidance, Control, and Dynamics, Vol. 28, No. 5, 2005, pp. 918 – 930.

Appendix A – Cycloidal Rotor Detail Drawings

The following appendix contains a general arrangement and detailed component drawings of the cycloidal rotor and component parts used throughout the current research.

Drawings specific to the current test rig due to test facility interface requirements are not provided as these will be different at each research establishment.

ITEM NUMBER	PART NUMBER	DESCRIPTION	QUANTITY
1	RW-00-01	OVERALL BLADE ASSEBLY	4
2	RW-00-02	ROTOR OUTER END PLATE ASSEMBLY	1
3	RW-00-03	ROTOR INNER END PLATE ASEMBLY	1
4	RW-20-07	ROTOR SHAFT	1
5	-	M3 x 5 COUNTERSUNK HEAD CAP SCREW	4
6	-	M2.5 x 2.5 BUTTON HEAD CAP SCREW	12
7	-	SELF ALIGNING BEARING	4

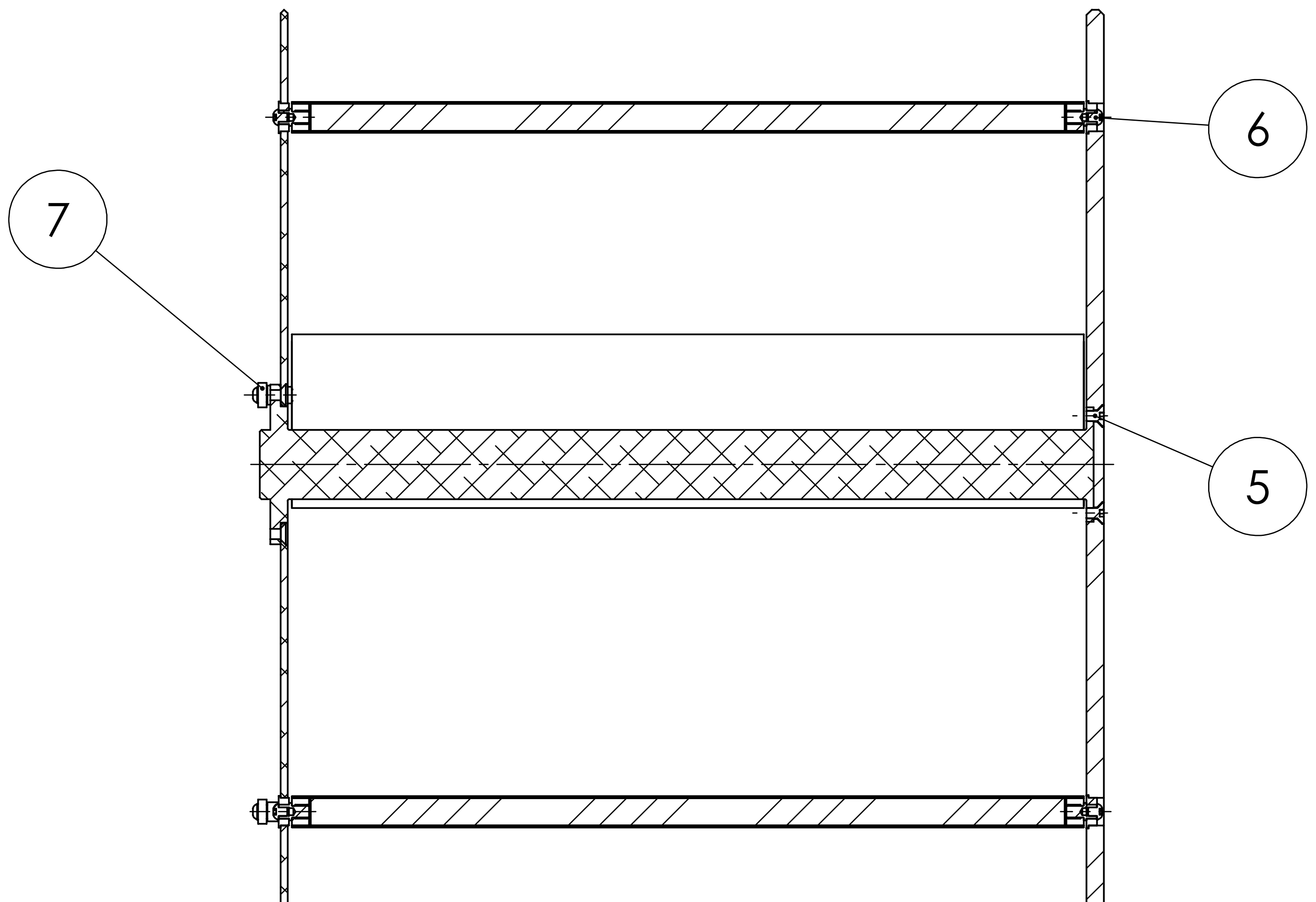

SECTION A-A

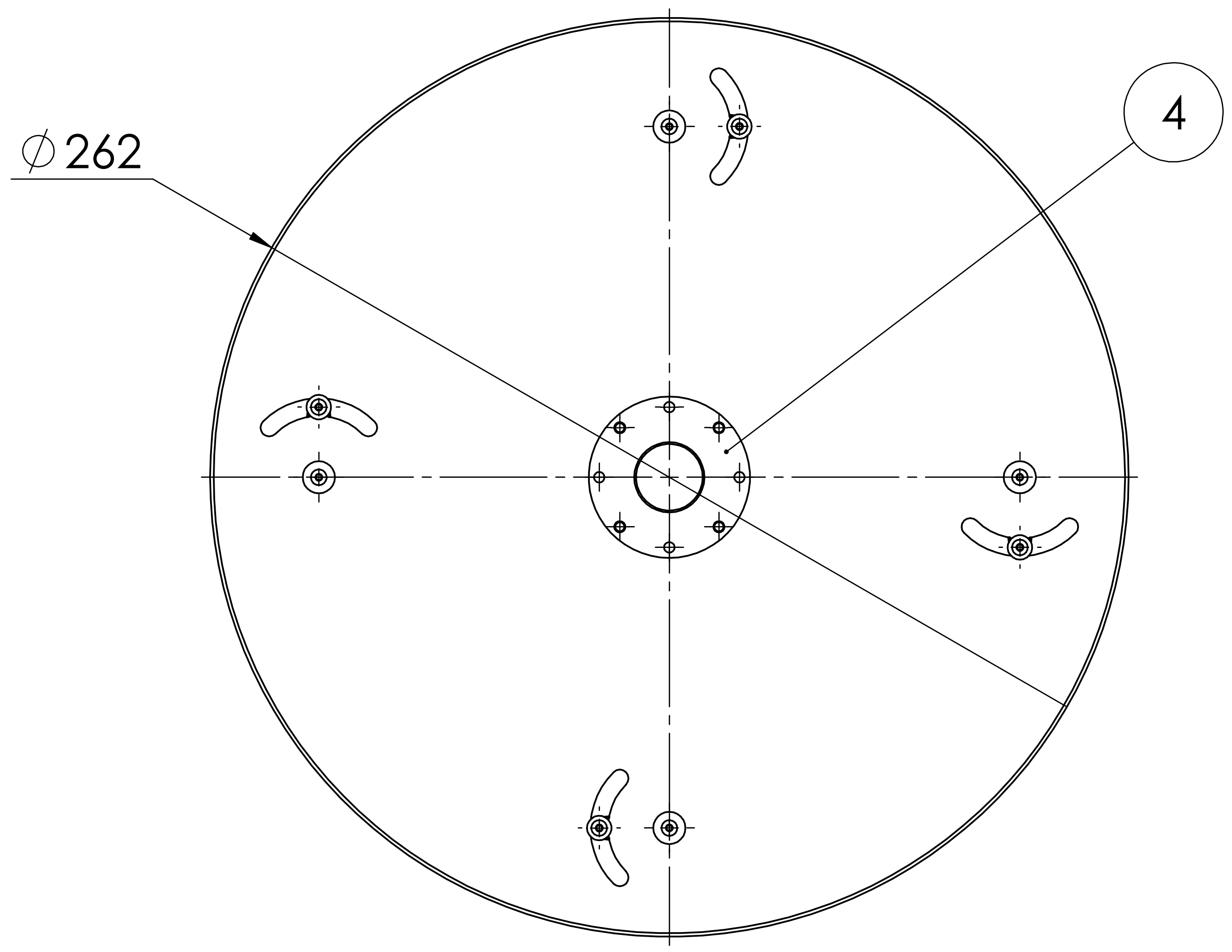

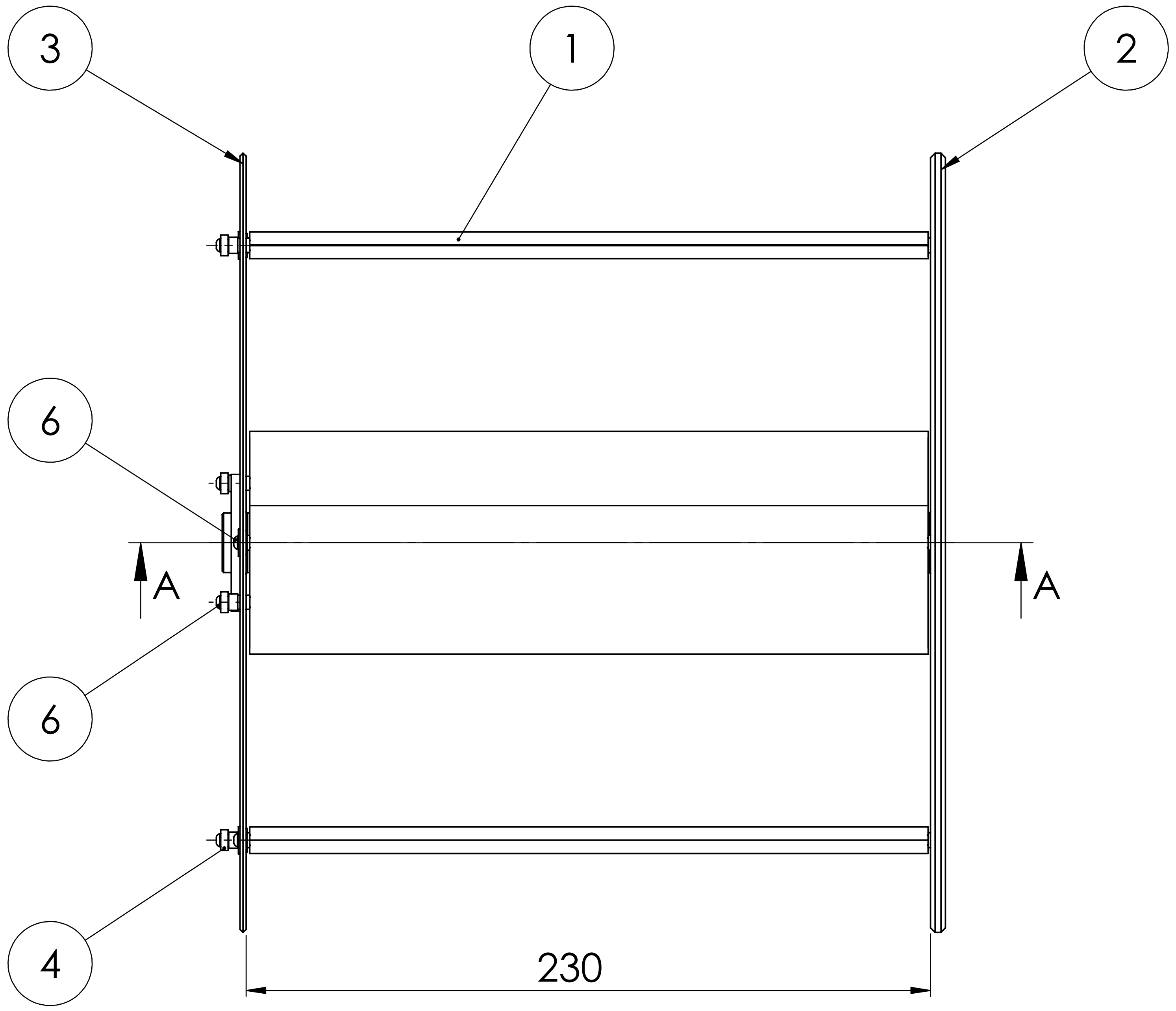

DO NOT SCALE DRAWING

REVISION: 01

DIMENSIONS IN mm U.O.S.
DIM. TOLERANCES: +/- 0.2 mm U.O.S.
ANGLE TOL.: +/- 0.25 DEGREES U.O.S.
SURFACE FINISH: 3.2 MICRONS U.O.S
UNSPECIFIED RADII: 0.8 mm
REMOVE ALL BURRS & SHARP EDGES

	NAME	DATE
DRAWN	RW	01/2022
CHK'D		
APPV'D		

MATERIAL: SEE NOTES

FINISH: SEE NOTES

THIRD ANGLE

UNIVERSITY OF BATH

WEIGHT:

TITLE: CYCLOIDAL ROTOR ASSEMBLY

SCALE:1:2

DWG NO. RW-00-00

SHEET 1 OF 1

A2

ITEM NUMBER	PART NUMBER	DESCRIPTION	QUANTITY
1	RW-10-01	NACA-0018 BLADE ASSEMBLY	1
2	RW-20-01	REAR BLADE PITCH PIN	1
3	RW-20-02	FRONT BLADE PITCH PIN	2

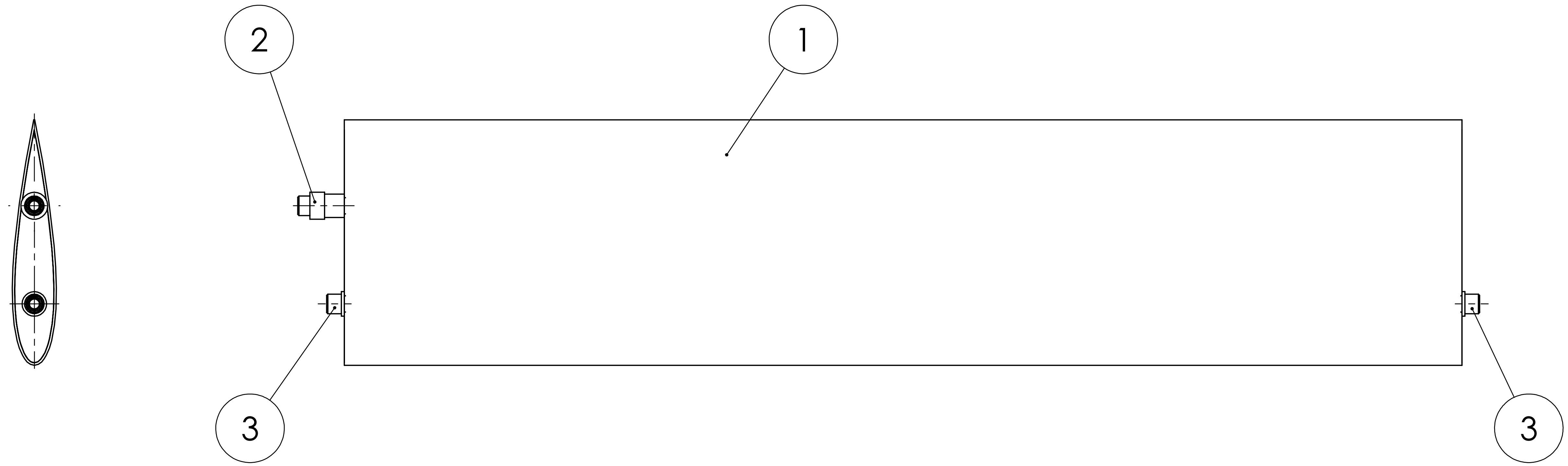

NOTES:

ITEM 2 AND 3 TO BE HELD IN POSITION WITH
LOCTITE 243 MEDIUM STRENGTH THREAD LOCKER

DO NOT SCALE DRAWING

REVISION: 01

DIMENSIONS IN mm U.O.S.
DIM. TOLERANCES: +/- 0.2 mm U.O.S.
ANGLE TOL.: +/- 0.25 DEGREES U.O.S.
SURFACE FINISH: 3.2 MICRONS U.O.S
UNSPECIFIED RADII: 0.8 mm
REMOVE ALL BURRS & SHARP EDGES

	NAME	DATE
DRAWN	RW	01/2022
CHK'D		
APPV'D		

MATERIAL: SEE NOTES

FINISH: SE NOTES

THIRD ANGLE

WEIGHT:

UNIVERSITY OF BATH

TITLE: OVERALL BLADE ASSEMBLY

SCALE:1:1

DWG NO. RW-00-01

SHEET 1 OF 1

A3

ITEM NUMBER	PART NUMBER	DESCRIPTION	QUANTITY
1	RW-20-06	ROTOR OUTER END PLATE	1
2	MF34 ZZ	FLANGED BEARING	4

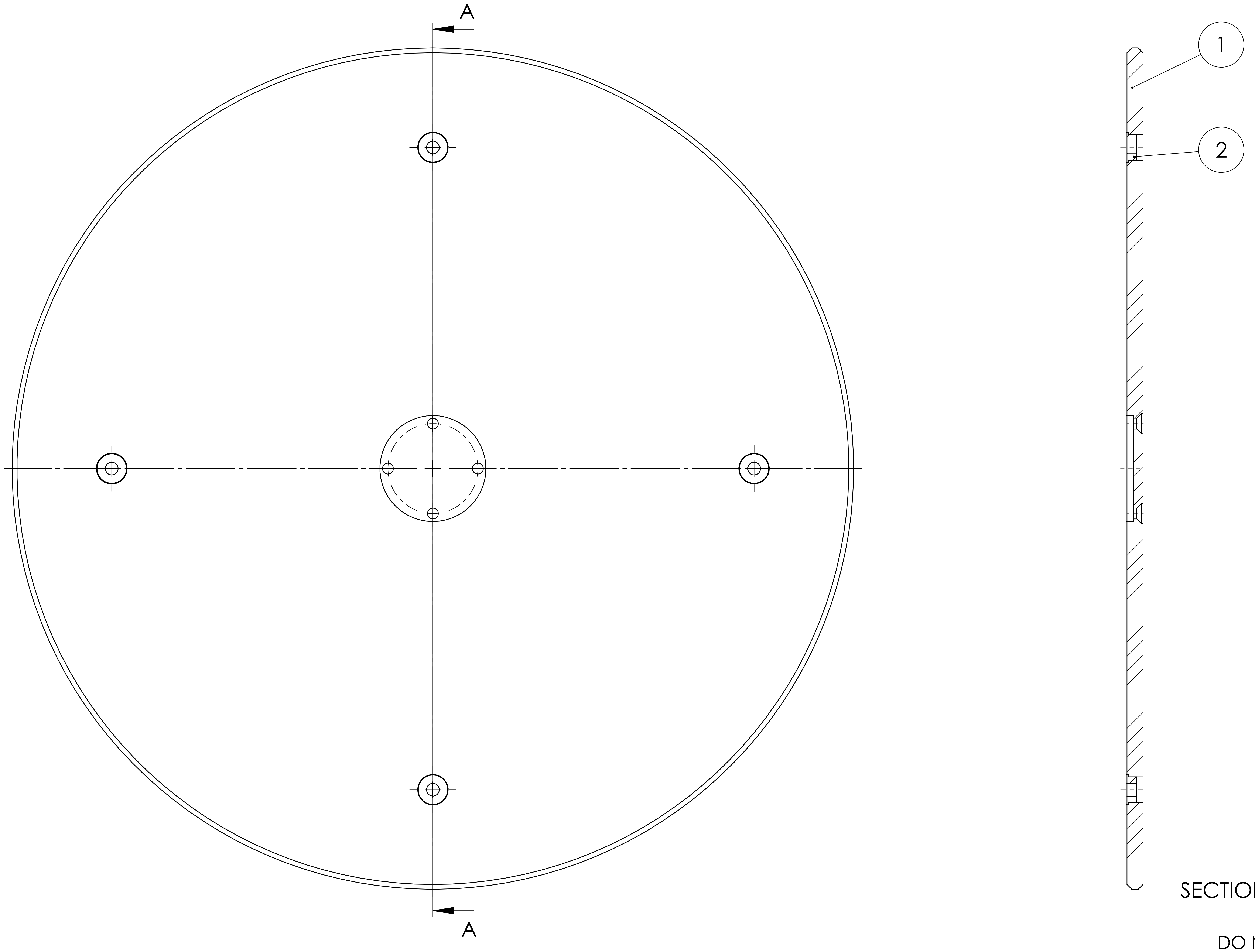

SECTION A-A

DO NOT SCALE DRAWING

REVISION: 01

DIMENSIONS IN mm U.O.S.
DIM. TOLERANCES: +/- 0.2 mm U.O.S.
ANGLE TOL.: +/- 0.25 DEGREES U.O.S.
SURFACE FINISH: 3.2 MICRONS U.O.S
UNSPECIFIED RADII: 0.8 mm
REMOVE ALL BURRS & SHARP EDGES

	NAME	DATE
DRAWN	RW	01/2022
CHK'D		
APPV'D		

MATERIAL: SEE NOTES

FINISH: SEE NOTES

THIRD ANGLE

WEIGHT:

SCALE:1:1

UNIVERSITY OF BATH

TITLE: ROTOR OUTER END PLATE ASSEMBLY

DWG NO. RW-00-02

SHEET 1 OF 1

A2

ITEM NUMBER	PART NUMBER	DESCRIPTION	QUANTITY
1	RW-20-05	ROTOR INNER END PLATE	1
2	MF34 ZZ	FLANGED BEARING	4

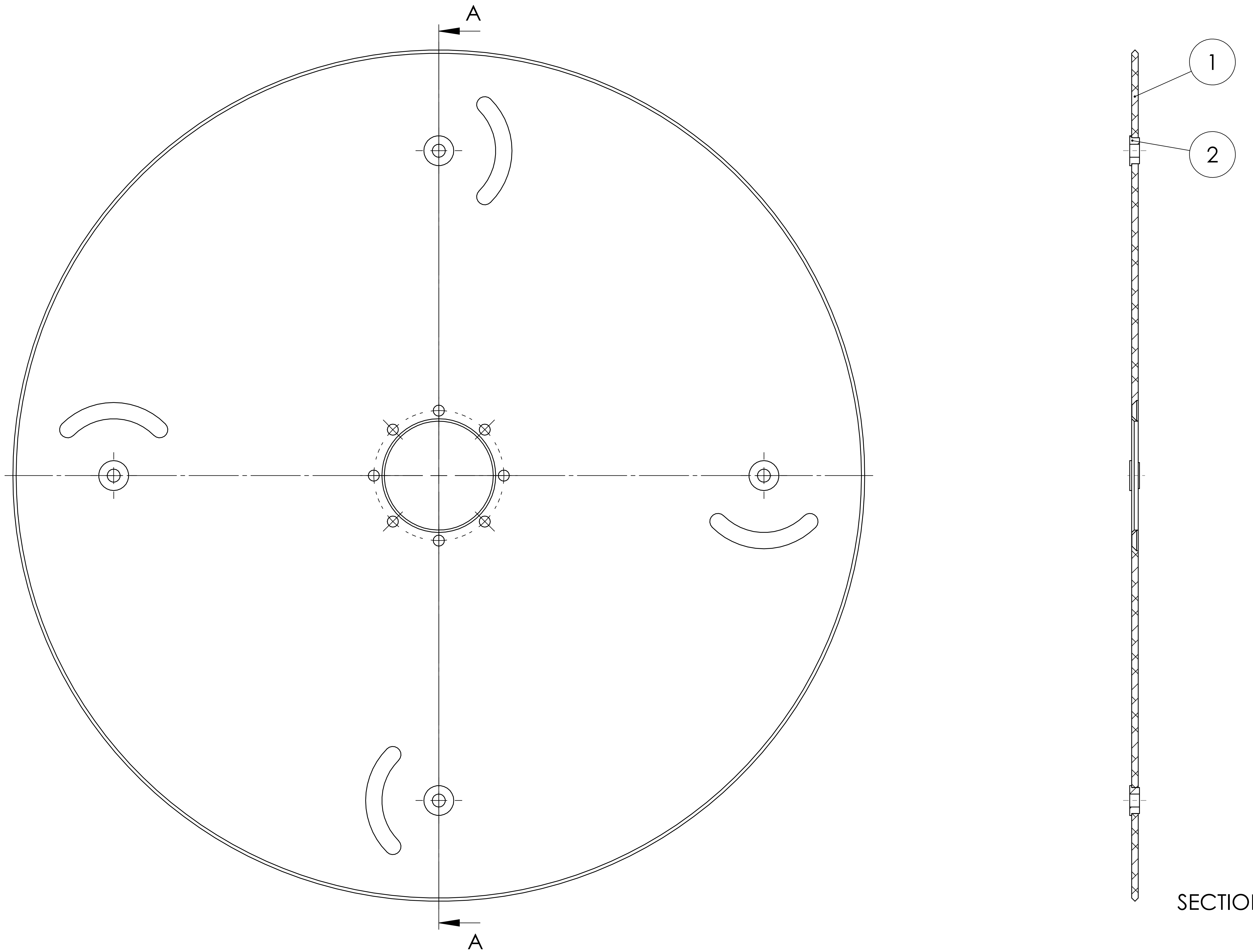

SECTION A-A

DO NOT SCALE DRAWING

REVISION: 01

DIMENSIONS IN mm U.O.S.
DIM. TOLERANCES: +/- 0.2 mm U.O.S.
ANGLE TOL.: +/- 0.25 DEGREES U.O.S.
SURFACE FINISH: 3.2 MICRONS U.O.S
UNSPECIFIED RADII: 0.8 mm
REMOVE ALL BURRS & SHARP EDGES

	NAME	DATE
DRAWN	RW	01/2022
CHK'D		
APPV'D		

MATERIAL: SEE NOTES

FINISH: SEE NOTES

THIRD ANGLE

UNIVERSITY OF BATH

WEIGHT:

TITLE: ROTOR INNER END PLATE ASSEMBLY

SCALE:1:1

DWG NO. RW-00-03

SHEET 1 OF 1

A2

ITEM NUMBER	PART NUMBER	DESCRIPTION	QUANTITY
1	RW-20-04	NACA 0018 BLADE LAYUP	1
2	RW-20-03	BLADE END PLATE	2

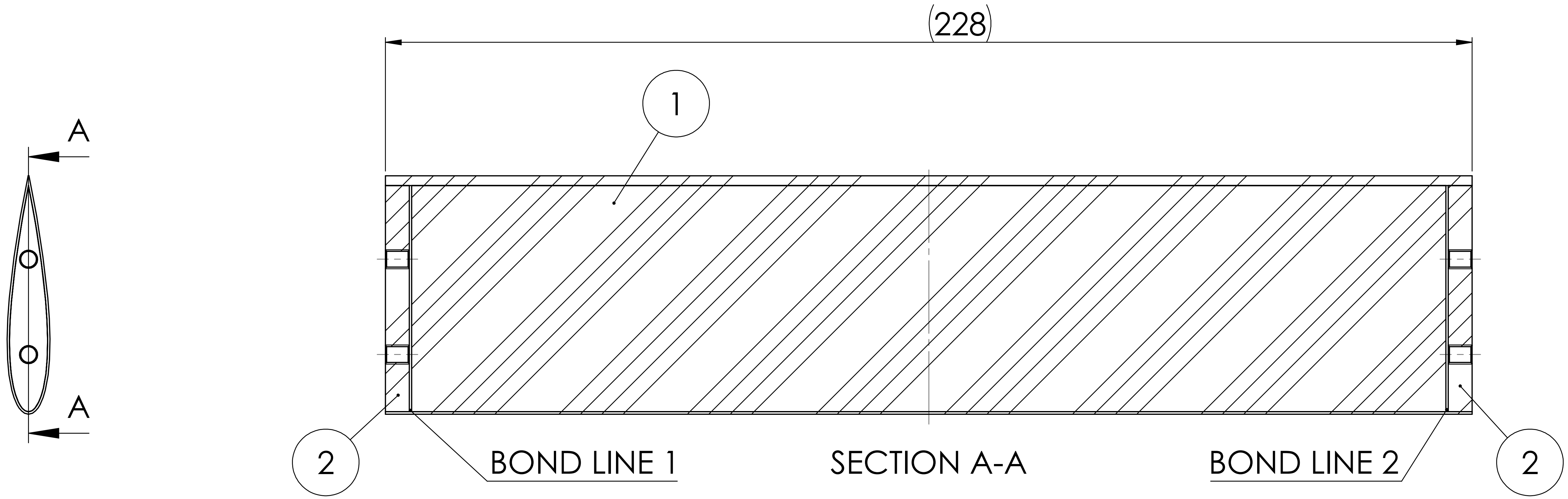

NOTES:

ET515 SEMI FLEXIBLE EPOXY ADHESIVE
TO BE USED TO ASSEMBLE ITEMS 1 AND 2.

DO NOT SCALE DRAWING

REVISION: 01

DIMENSIONS IN mm U.O.S.
DIM. TOLERANCES: +/- 0.2 mm U.O.S.
ANGLE TOL.: +/- 0.25 DEGREES U.O.S.
SURFACE FINISH: 3.2 MICRONS U.O.S
UNSPECIFIED RADII: 0.8 mm
REMOVE ALL BURRS & SHARP EDGES

	NAME	DATE
DRAWN	RW	01/2022
CHK'D		
APPV'D		

MATERIAL: SEE NOTES

FINISH: SEE NOTES

THIRD ANGLE

WEIGHT:

UNIVERSITY OF BATH

TITLE: NACA 0018 BLADE ASSEMBLY

SCALE:1:1

DWG NO. RW-10-01

SHEET 1 OF 1

A3

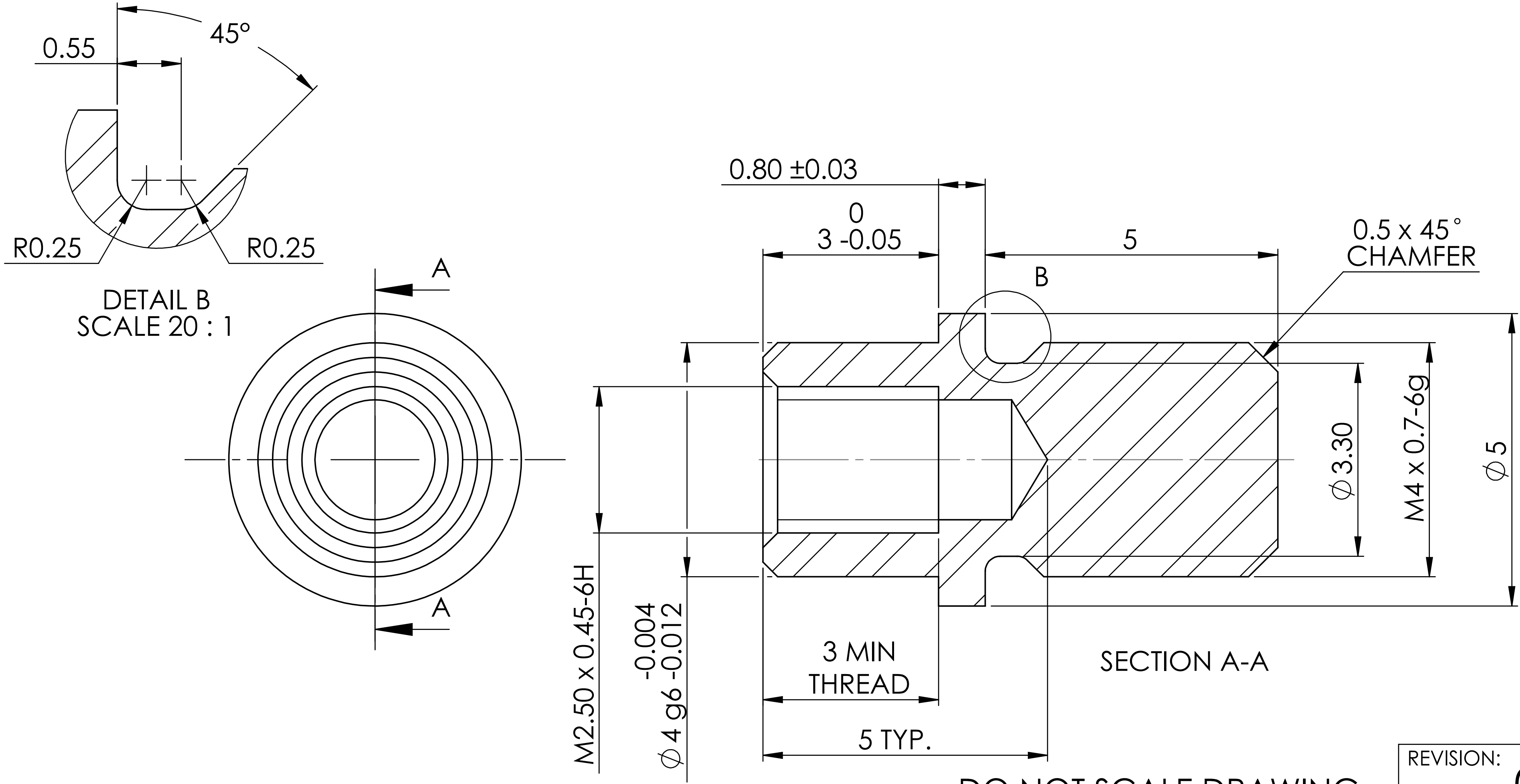

ALL UNSPECIFIED CHAMFERS 0.25 mm

DO NOT SCALE DRAWING

REVISION: 01

DIMENSIONS IN mm U.O.S.
DIM. TOLERANCES: +/- 0.2 mm U.O.S.
ANGLE TOL.: +/- 0.25 DEGREES U.O.S.
SURFACE FINISH: 3.2 MICRONS U.O.S
UNSPECIFIED RADII: 0.8 mm
REMOVE ALL BURRS & SHARP EDGES

	NAME	DATE
DRAWN	RW	01/2022
CHK'D		
APPV'D		

MATERIAL: EN24T

FINISH: NATURAL

THIRD ANGLE

UNIVERSITY OF BATH

WEIGHT:

TITLE: FRONT BLADE PITCH PIN

SCALE:10:1

DWG NO. RW-20-01

SHEET 1 OF 1

A4

ALL UNSPECIFIED CHAMFERS 0.25 mm

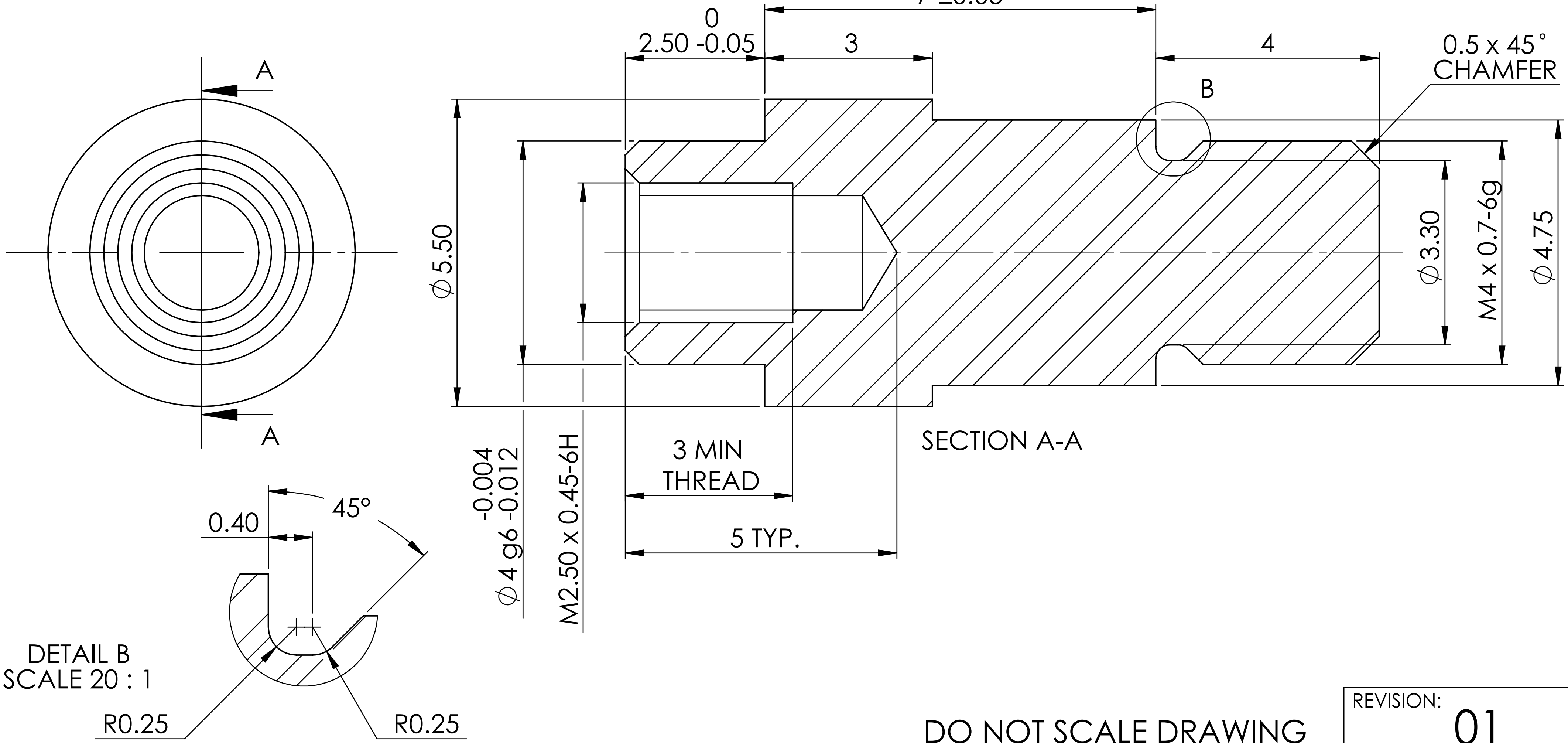

DO NOT SCALE DRAWING

REVISION: 01

DIMENSIONS IN mm U.O.S.
DIM. TOLERANCES: +/- 0.2 mm U.O.S.
ANGLE TOL.: +/- 0.25 DEGREES U.O.S.
SURFACE FINISH: 3.2 MICRONS U.O.S
UNSPECIFIED RADII: 0.8 mm
REMOVE ALL BURRS & SHARP EDGES

	NAME	DATE
DRAWN	RW	01/2022
CHK'D		
APPV'D		

MATERIAL: EN24T

FINISH: NATURAL

THIRD ANGLE

UNIVERSITY OF BATH

WEIGHT:

TITLE: REAR BLADE PITCH PIN

SCALE:10:1

DWG NO. RW-20-02

SHEET 1 OF 1

A4

NOTE 1:

COMPONENT OUTER PROFILE TO BE DETERMINED
FROM 3D GEOMETRY RW-20-03.STEP LATEST ISSUE.

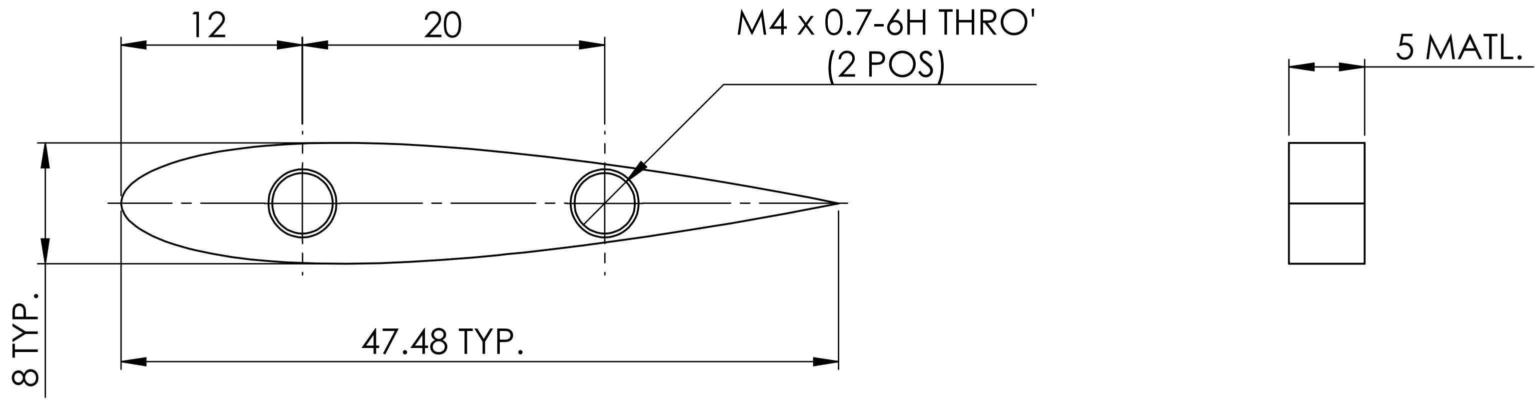

DO NOT SCALE DRAWING

REVISION: 01

DIMENSIONS IN mm U.O.S.
DIM. TOLERANCES: +/- 0.2 mm U.O.S.
ANGLE TOL.: +/- 0.25 DEGREES U.O.S.
SURFACE FINISH: 3.2 MICRONS U.O.S
UNSPECIFIED RADII: 0.8 mm
REMOVE ALL BURRS & SHARP EDGES

	NAME	DATE
DRAWN	RW	01/2022
CHK'D		
APPV'D		

MATERIAL:
ALUMINIUM ALLOY
6082 T6

FINISH:
NATURAL

THIRD ANGLE

UNIVERSITY OF BATH

WEIGHT:

TITLE:
BLADE END PLATE

SCALE:2:1

DWG NO.
RW-20-03

SHEET 1 OF 1

A4

NOTES:

1. COMPONENT SYMMETRIC ABOUT THE CENTRELINE.
2. BLADE CORE FORMED BY HAND TO SUIT MOULD FROM AIREX C70 STRUCTURAL FOAM.
3. BLADE OUTER SKIN MANUFACTURED FROM CARBON FIBER OF THREE LAYERS. 200g CLOTH 0-90°/100g UD 0°/200g CLOTH 0-90°.
4. LAYERS BONDED WITH E12 HIGH PERFORMANCE LAMINATING RESIN.

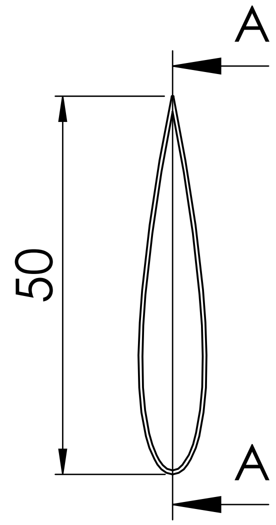

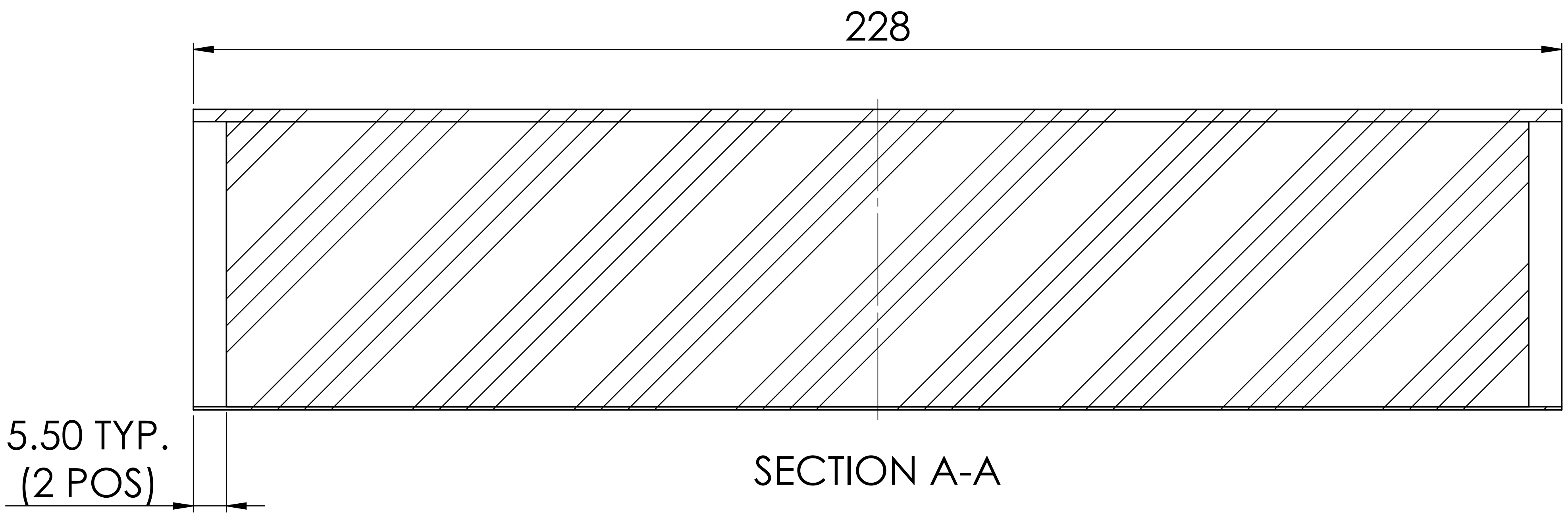

SECTION A-A

DO NOT SCALE DRAWING

REVISION: 01

DIMENSIONS IN mm U.O.S.
DIM. TOLERANCES: +/- 0.2 mm U.O.S.
ANGLE TOL.: +/- 0.25 DEGREES U.O.S.
SURFACE FINISH: 3.2 MICRONS U.O.S
UNSPECIFIED RADII: 0.8 mm
REMOVE ALL BURRS & SHARP EDGES

	NAME	DATE
DRAWN	RW	01/2022
CHK'D		
APPV'D		

MATERIAL: SEE NOTES

FINISH: NATURAL

THIRD ANGLE

WEIGHT:

SCALE:1:1

UNIVERSITY OF BATH

TITLE: NACA 0018 BLADE LAYUP

DWG NO. RW-20-04

SHEET 1 OF 1

A3

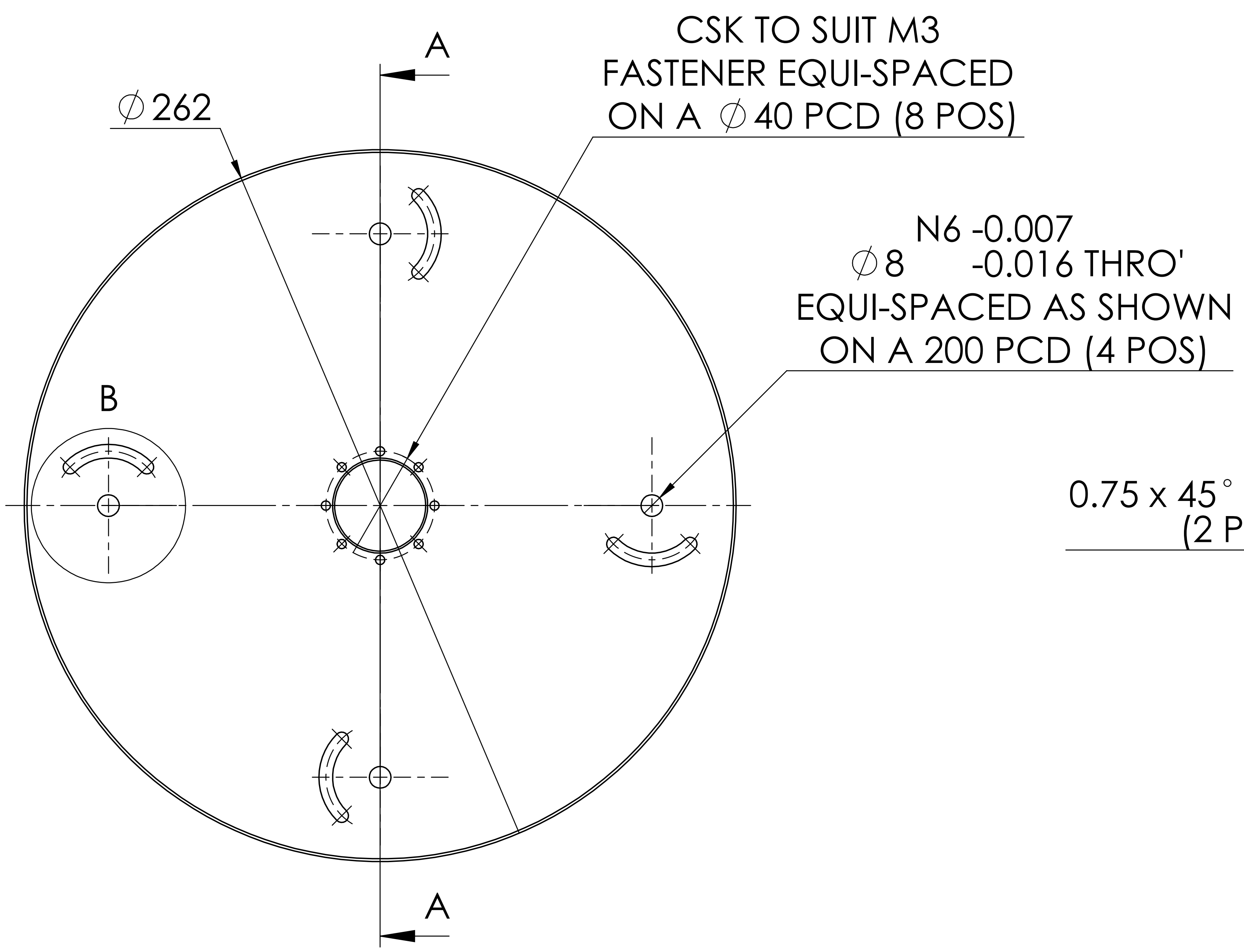

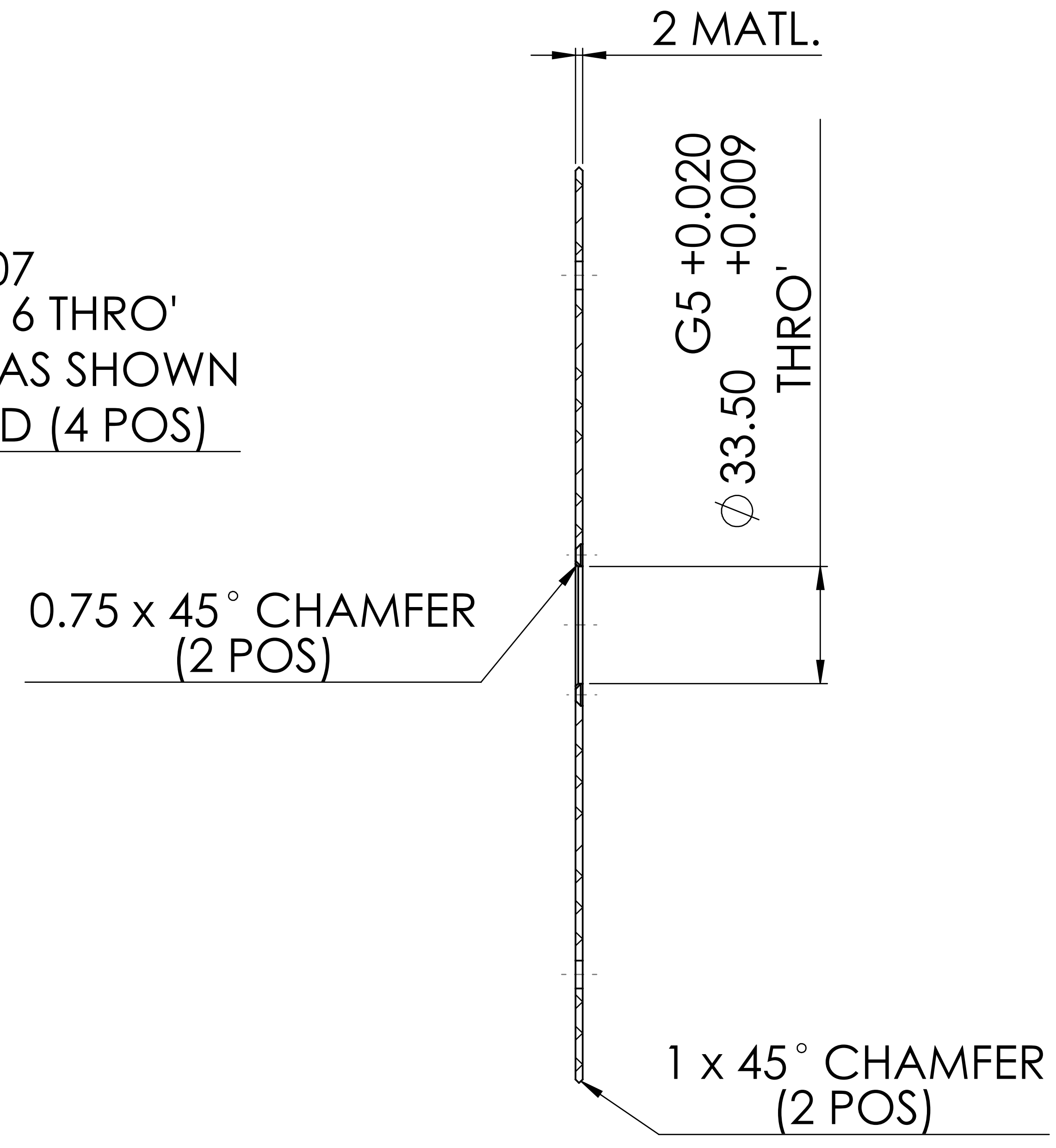

SECTION A-A

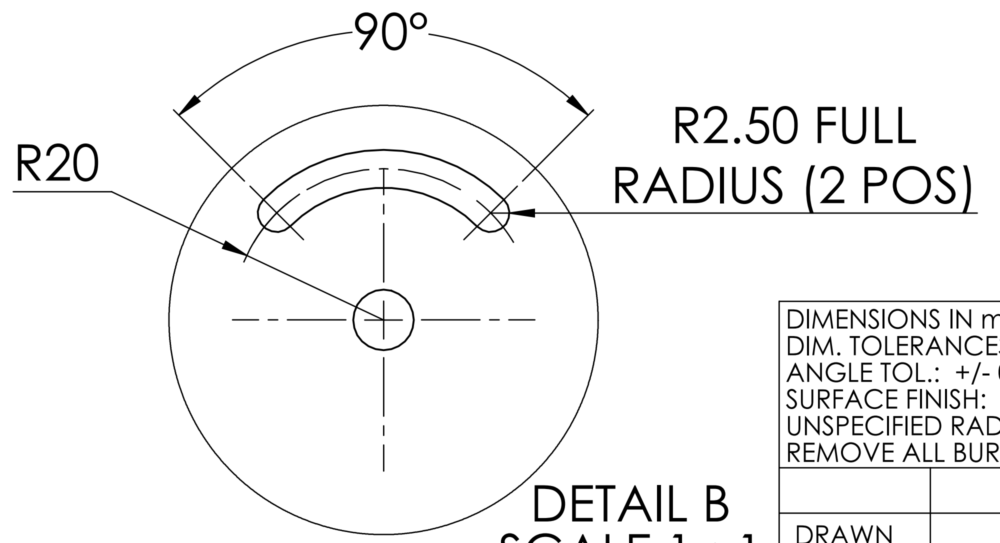

DETAIL B
SCALE 1 : 1
(4 POS)

DO NOT SCALE DRAWING

REVISION: 01

DIMENSIONS IN mm U.O.S.
DIM. TOLERANCES: +/- 0.2 mm U.O.S.
ANGLE TOL.: +/- 0.25 DEGREES U.O.S.
SURFACE FINISH: 3.2 MICRONS U.O.S
UNSPECIFIED RADII: 0.8 mm
REMOVE ALL BURRS & SHARP EDGES

	NAME	DATE
DRAWN	RW	01/2022
CHK'D		
APPV'D		

MATERIAL: ALUMINIUM ALLOY 6082 T6

FINISH: NATURAL

THIRD ANGLE

UNIVERSITY OF BATH

WEIGHT:

TITLE: ROTOR INNER END PLATE

SCALE:1:2

DWG NO. RW-20-05

SHEET 1 OF 1

A3

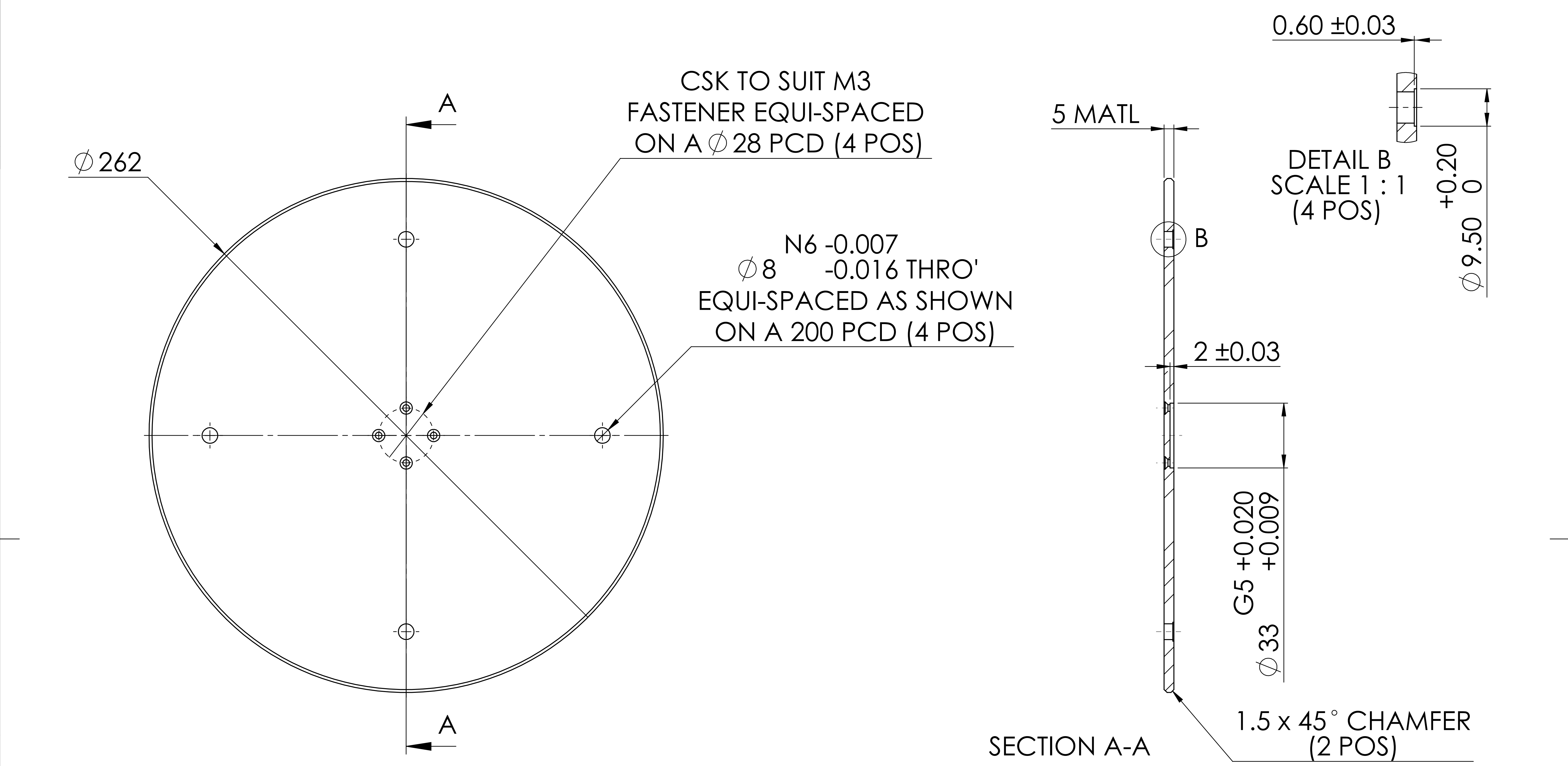

DO NOT SCALE DRAWING

REVISION: 01

DIMENSIONS IN mm U.O.S.
DIM. TOLERANCES: +/- 0.2 mm U.O.S.
ANGLE TOL.: +/- 0.25 DEGREES U.O.S.
SURFACE FINISH: 3.2 MICRONS U.O.S
UNSPECIFIED RADII: 0.8 mm
REMOVE ALL BURRS & SHARP EDGES

	NAME	DATE
DRAWN	RW	01/2022
CHK'D		
APPV'D		

MATERIAL: NYLON 6 CLEAR

FINISH: NATURAL

THIRD ANGLE

UNIVERSITY OF BATH

WEIGHT:

TITLE: ROTOR OUTER END PLATE

SCALE:1:2

DWG NO. RW-20-06

SHEET 1 OF 1

A3

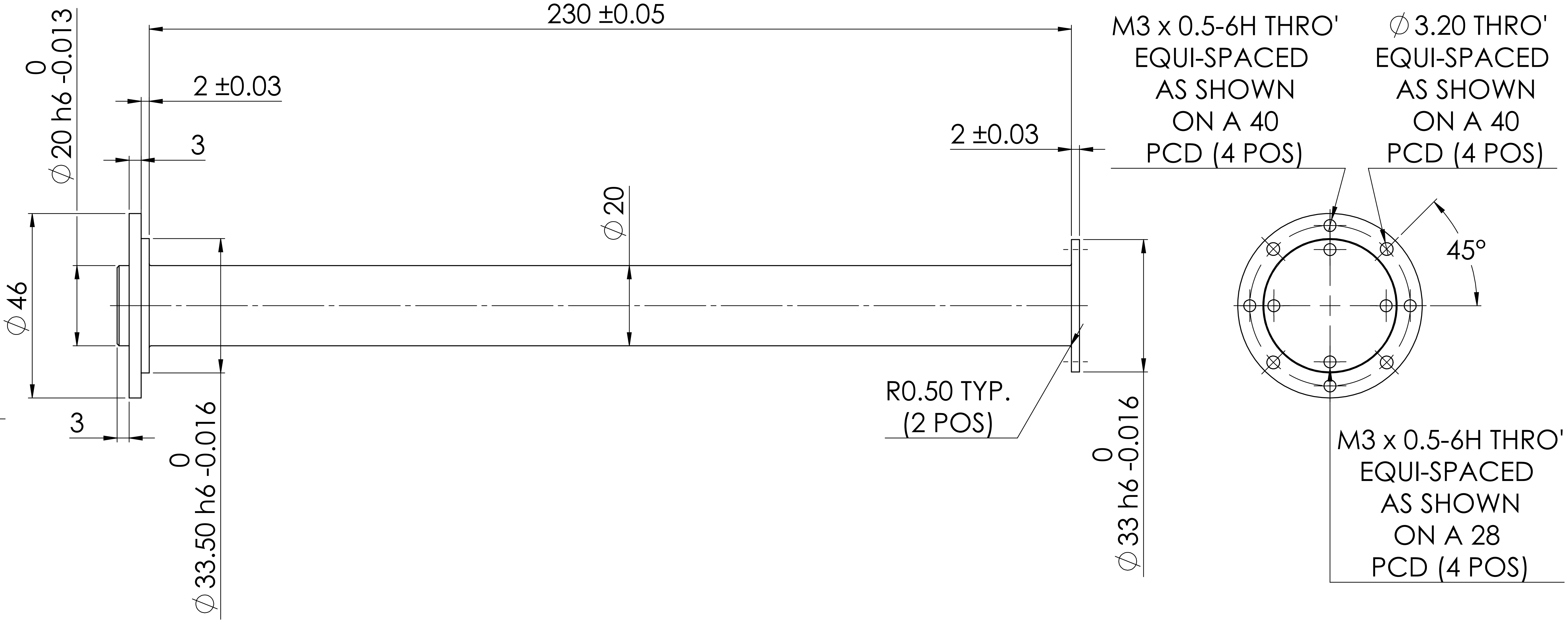

ALL UNSPECIFIED CHAMFERS 0.5 x 45°

DO NOT SCALE DRAWING

REVISION: 01

DIMENSIONS IN mm U.O.S.
DIM. TOLERANCES: +/- 0.2 mm U.O.S.
ANGLE TOL.: +/- 0.25 DEGREES U.O.S.
SURFACE FINISH: 3.2 MICRONS U.O.S
UNSPECIFIED RADII: 0.8 mm
REMOVE ALL BURRS & SHARP EDGES

	NAME	DATE
DRAWN	RW	01/2022
CHK'D		
APPV'D		

MATERIAL: ALUMINIUM ALLOY 6082 T6

FINISH: NATURAL

THIRD ANGLE

WEIGHT:

SCALE:1:1

UNIVERSITY OF BATH

TITLE: ROTOR SHAFT

DWG NO. RW-20-07

SHEET 1 OF 1

A3

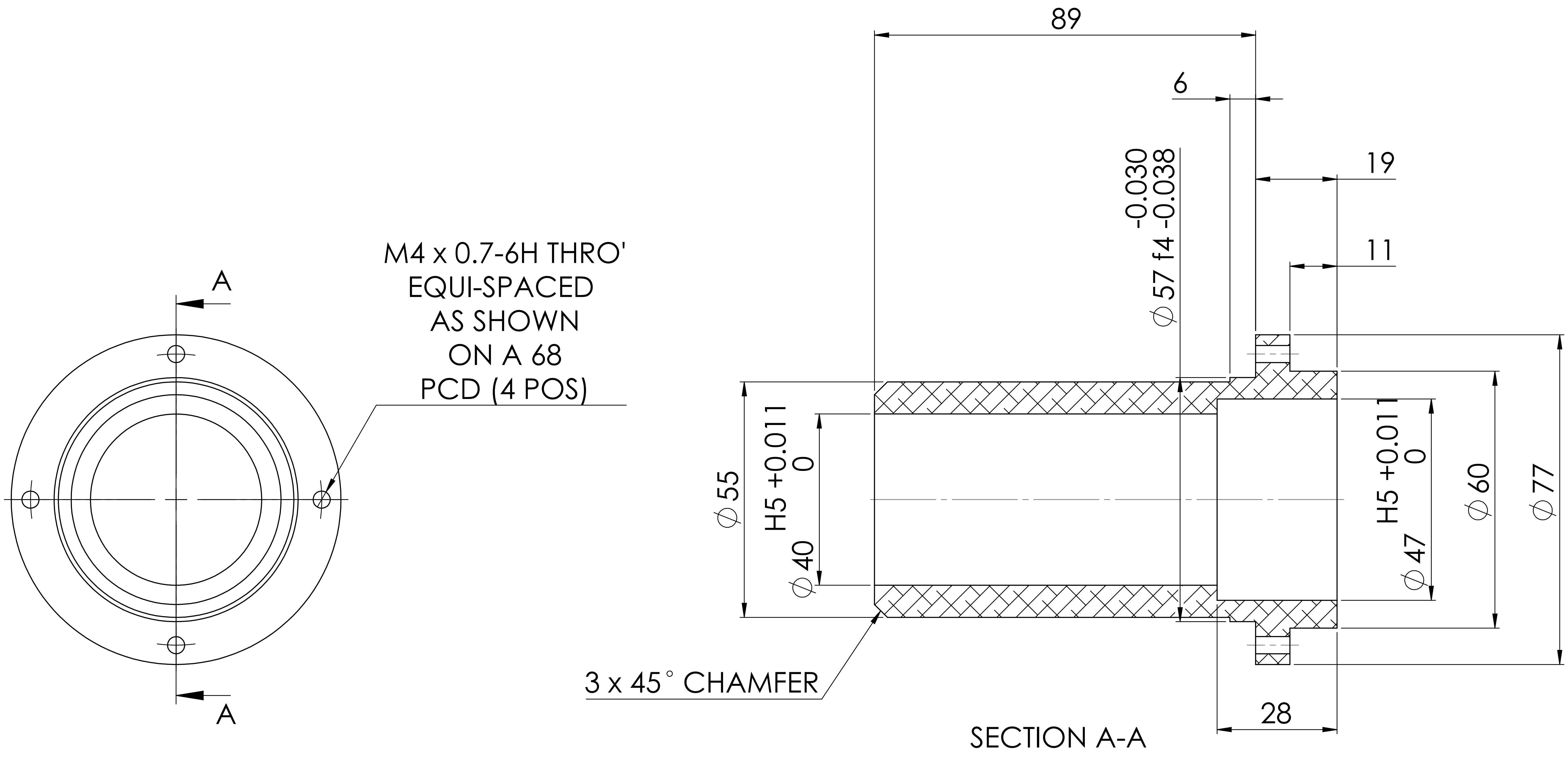

DO NOT SCALE DRAWING

REVISION: 01

DIMENSIONS IN mm U.O.S.
DIM. TOLERANCES: +/- 0.2 mm U.O.S.
ANGLE TOL.: +/- 0.25 DEGREES U.O.S.
SURFACE FINISH: 3.2 MICRONS U.O.S
UNSPECIFIED RADII: 0.8 mm
REMOVE ALL BURRS & SHARP EDGES

	NAME	DATE
DRAWN	RW	01/2022
CHK'D		
APPV'D		

MATERIAL: ALUMINIUM ALLOY 6082 T6

FINISH: NATURAL

THIRD ANGLE

WEIGHT:

SCALE:1:1

UNIVERSITY OF BATH

TITLE: BEARING HOUSING

DWG NO. RW-20-08

SHEET 1 OF 1

A3

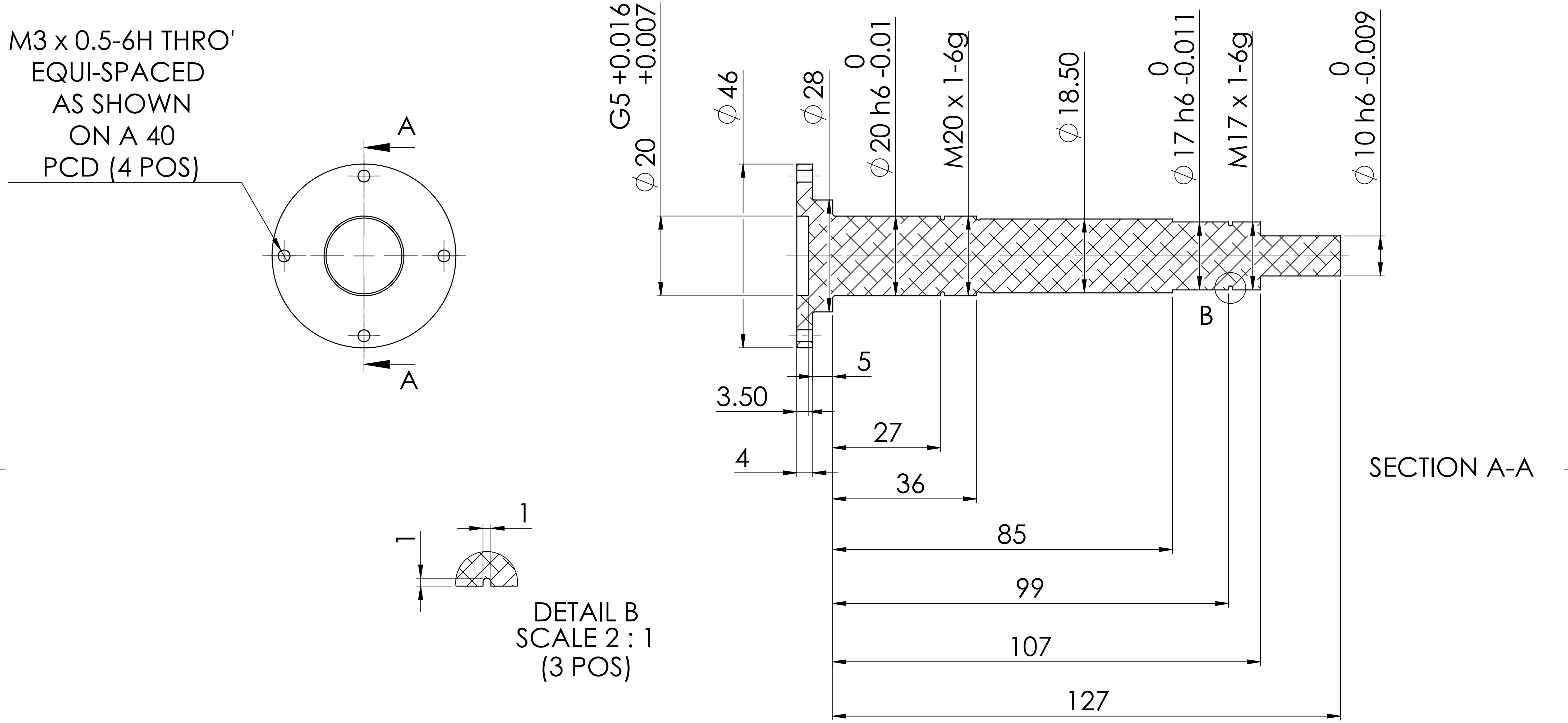

ALL UNSPECIFIED RADII 0.5 mm

DO NOT SCALE DRAWING

REVISION: 01

DIMENSIONS IN mm U.O.S.
DIM. TOLERANCES: +/- 0.2 mm U.O.S.
ANGLE TOL.: +/- 0.25 DEGREES U.O.S.
SURFACE FINISH: 3.2 MICRONS U.O.S
UNSPECIFIED RADII: 0.8 mm
REMOVE ALL BURRS & SHARP EDGES

	NAME	DATE
DRAWN	RW	01/2022
CHK'D		
APPV'D		

MATERIAL: EN8

FINISH: NATURAL

THIRD ANGLE

WEIGHT:

SCALE:1:1

UNIVERSITY OF BATH

TITLE: BEARING SHAFT

DWG NO. RW-20-09

SHEET 1 OF 1

A3

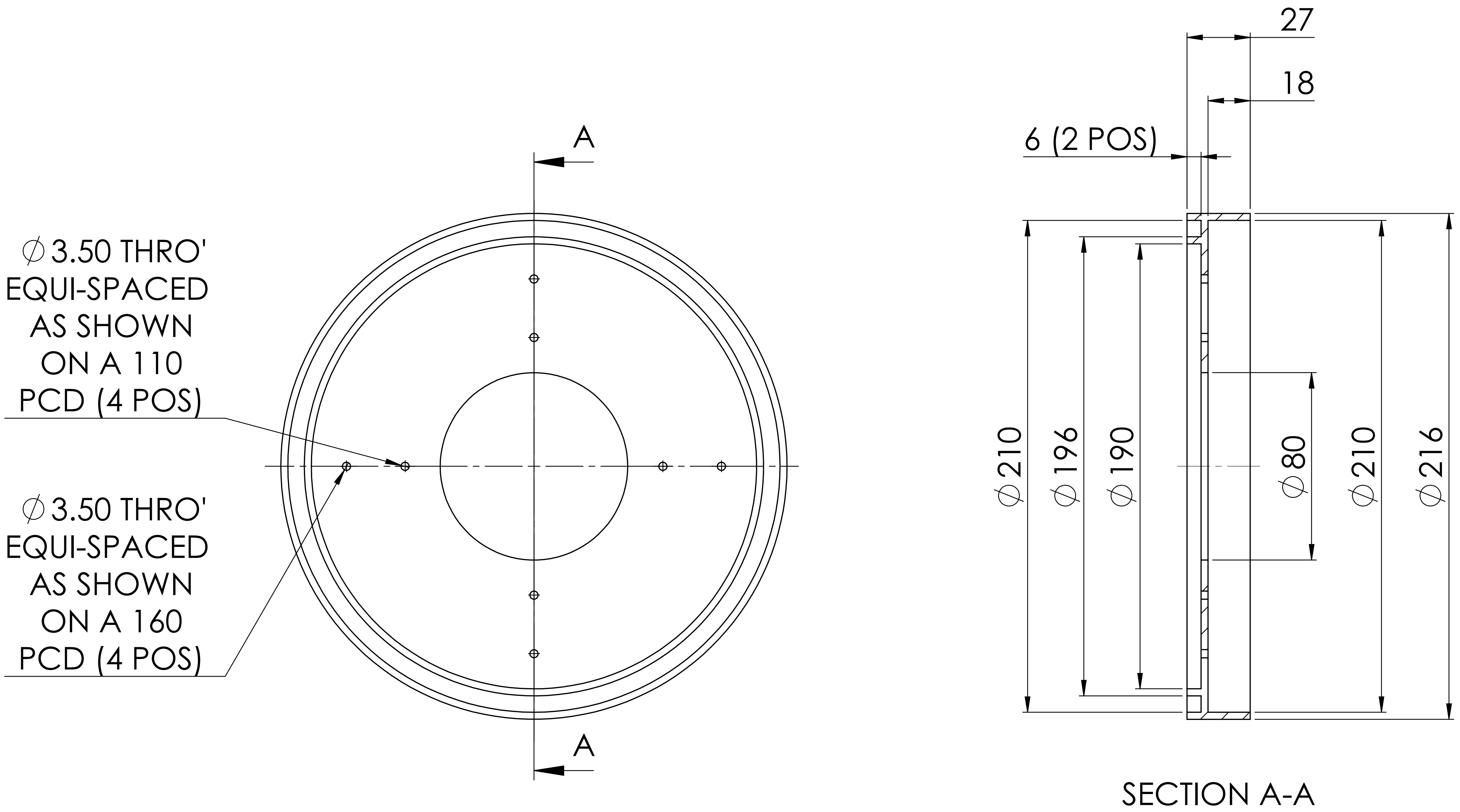

DO NOT SCALE DRAWING

REVISION: 01

DIMENSIONS IN mm U.O.S.
DIM. TOLERANCES: +/- 0.2 mm U.O.S.
ANGLE TOL.: +/- 0.25 DEGREES U.O.S.
SURFACE FINISH: 3.2 MICRONS U.O.S
UNSPECIFIED RADII: 0.8 mm
REMOVE ALL BURRS & SHARP EDGES

	NAME	DATE
DRAWN	RW	01/2022
CHK'D		
APPV'D		

MATERIAL: NYLON 6 BLACK

FINISH: NATURAL

THIRD ANGLE

UNIVERSITY OF BATH

WEIGHT:

TITLE: CAM RING

SCALE:1:2

DWG NO. RW-20-10

SHEET 1 OF 1

A3

Appendix B – Test Rig Reaction Force Equations

In operation, the cycloidal rotor is subject to inertial and aerodynamic loading. Equations were developed, as summarised below, to calculate the reaction loads at the blade pitch pins, rotor end discs, and spindle bearings to aid with the rotor system's design and support the overall test rig design in chapter 3.

Nomenclature

$\omega =$ Rotor angular velocity $(\mathrm{rad/s})$

$\Psi =$ Blade azimuth position (rad)

$\theta_{BL} =$ Blade cyclic pitch angle (rad)

$\omega_b =$ Blade angular velocity $(\mathrm{rad/s})$

$\alpha =$ Blade angular acceleration $(\mathrm{rad/s^2})$

$L =$ Geometric link length (m)

$P =$ Blade pitch point offset (m)

$e =$ Eccentric point offset (m)

$\varepsilon =$ Eccentric point phase angle (rad)

1. Blade Angular Velocity and Angular Velocity Calculation

The blade pitches with rotor rotation, and the blade angular velocity is given by

$$\omega_b = \frac{d\theta_{BL}}{d\Psi} \cdot \omega \tag{B1}$$

where

$$\omega = \frac{d\Psi}{dt} \tag{B2}$$

Substituting equation B2 into B1 gives

$$\omega_b = \frac{d\theta_{BL}}{dt} = \frac{d\theta_{BL}}{d\Psi} \cdot \frac{d\Psi}{dt} \tag{B3}$$

The blade angular acceleration α, from the second derivative chain rule is given by

$$\alpha = \frac{d^2\theta_{BL}}{dt^2} = \frac{d^2\theta_{BL}}{d\Psi^2} \cdot \left(\frac{d\Psi}{dt}\right)^2 + \frac{d\theta_{BL}}{d\Psi} \cdot \frac{d^2\Psi}{dt^2} \tag{B4}$$

In this case $\frac{d^2\Psi}{dt^2} = 0$, therefore

$$\alpha = \frac{d^2\theta_{BL}}{dt^2} = \frac{d^2\theta_{BL}}{d\Psi^2} \cdot \left(\frac{d\Psi}{dt}\right)^2 \tag{B5}$$

The blade cyclic pitch angle θ_{BL} as shown in Figure B1, is

$$\theta_{BL} = \frac{\pi}{2} - cos^{-1}\left(\frac{a^2 - L^2 + p^2}{2ap}\right) - sin^{-1}\left(\frac{e}{a} cos(\Psi + \varepsilon)\right) \tag{B6}$$

where

$$a = \sqrt{e^2 + R^2 + 2eRsin(\Psi + \varepsilon)} \tag{B7}$$

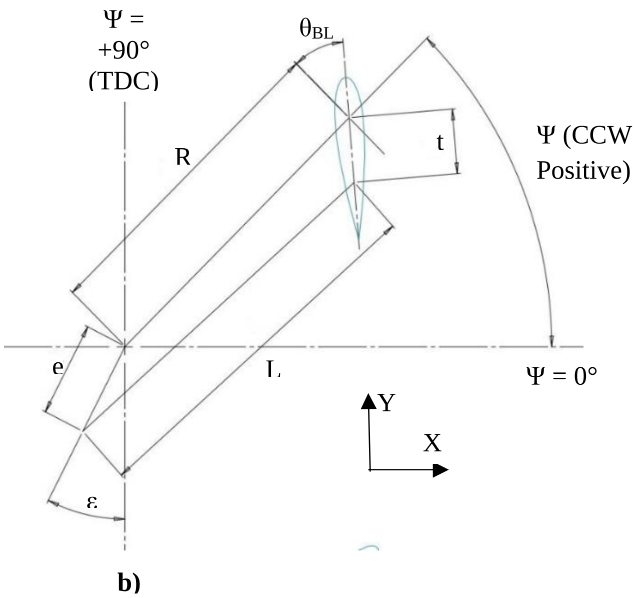

Figure B1 – Rotor geometric parameters

2. Blade Pitch Pin Force Reaction Calculation

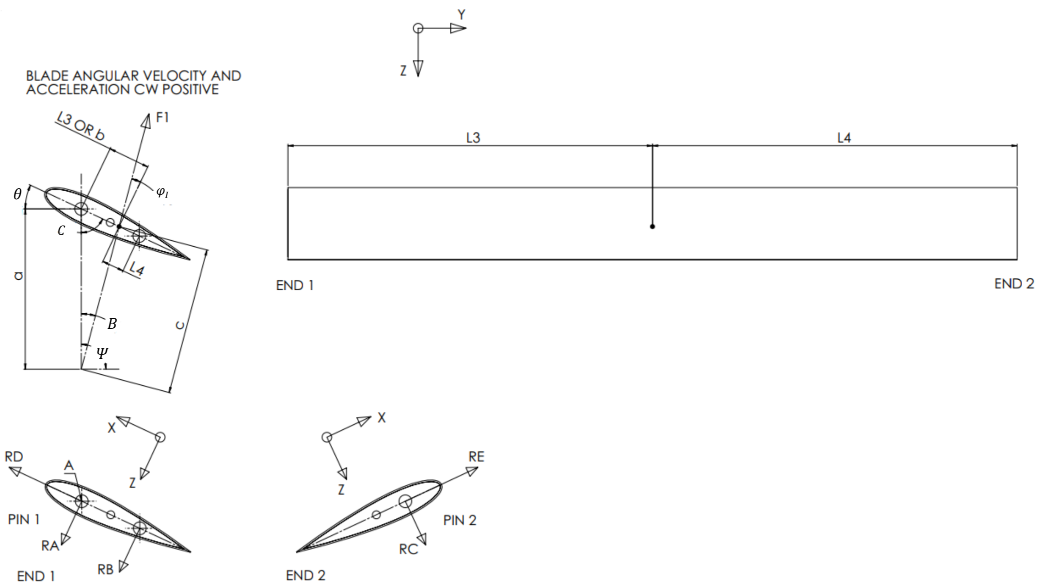

Figure B2 – Rotor blade-free body diagram

From Figure B2

$$c = \sqrt{a^2 + b^2 - 2ab \cdot \cos(C)} \tag{B8}$$

where

$$B = sin^{-1}\left[\frac{b \cdot \sin(C)}{c}\right] \tag{B9}$$

and

$$\varphi_I = \theta - B \tag{B10}$$

2.1. Blade Inertial Loading due to Centripetal Acceleration from Rotor Rotation

$$F_1 = m_b \omega^2 \mathrm{c} \tag{B12}$$

Resolving forces in the X-direction

$$R_{A_I} + R_{B_I} + R_{C_I} - F_1 \cos(\varphi_I) = 0 \tag{B13}$$

Resolving forces in the Y-direction

$$R_{D_I} + R_{E_I} + F_1 \sin(\varphi_I) = 0 \tag{B14}$$

Taking moments about point A XZ plane (clockwise Positive)

$$-F_1L_3\cos(\varphi_I)+R_{B_I}(L_3+L_4)=0 \tag{A15}$$

Taking moments about point A YZ plane (clockwise Positive)

$$-F_1L_1\cos(\varphi_I)+R_{C_I}(L_1+L_2)=0 \tag{A16}$$

Taking moments about point A XY plane (clockwise Positive)

$$-F_1L_1\sin(\varphi_I)-R_{E_I}(L_1+L_2)=0 \tag{A17}$$

Reaction Forces

Rearranging equation A15

$$R_{B_I}=\frac{(F_1L_3\cos(\varphi_I))}{(L_3+L_4)} \tag{A18}$$

Rearranging equation A16

$$R_{C_I}=\frac{(F_1L_1\cos(\varphi_I))}{(L_1+L_2)} \tag{A19}$$

Rearranging equation A17

$$R_{E_I}=\frac{-(F_1L_1\sin(\varphi_I))}{(L_1+L_2)} \tag{A20}$$

Rearranging equation B13

$$R_{A_I} = F_1 \cos(\varphi_I) - R_{B_I} - R_{C_I} \tag{B21}$$

Substituting equations B18 and B19 into equation B21

$$R_{A_I} = F_1 \cos(\varphi_I) - \frac{(F_1 L_3 \cos(\varphi_I))}{(L_3 + L_4)} - \frac{(F_1 L_1 \cos(\varphi_I))}{(L_1 + L_2)} \tag{B22}$$

Rearranging equation B14

$$R_{D_I} = -F_1 \sin(\varphi_I) - R_{E_I} \tag{B23}$$

Substituting equation B20 into equation B23

$$R_{D_I} = -F_1 \sin(\varphi_I) + \frac{(F_1 L_1 \sin(\varphi_I))}{(L_1 + L_2)} \tag{B24}$$

2.2. Blade Inertial Loading due to Centripetal Acceleration from Blade Oscillation

Resolving forces in the X direction

$$R_{D_P} + R_{E_P} - m_b \omega_b^2 L_3 = 0 \tag{B25}$$

Resolving forces in the Y direction

$$R_{A_P} + R_{C_P} + m_b \alpha L_3 = 0 \tag{B26}$$

Taking moments about point A XZ plane (clockwise positive)

$$T + R_{B_P}(L_3 + L_4) = 0 \tag{B27}$$

Taking moments about point A YZ plane (clockwise positive)

$$m_b \alpha L_3 L_1 + R_{C_P}(L_1 + L_2) = 0 \tag{B28}$$

Taking moments about point A XY plane (clockwise positive)

$$m_b \omega_b^2 L_3 L_1 - R_{E_P}(L_1 + L_2) = 0 \tag{B29}$$

Reaction Forces

Rearranging equation B29

$$R_{E_P} = \frac{m_b \omega_b^2 L_3 L_1}{(L_1 + L_2)} \tag{B30}$$

Substituting B30 into B25 and rearranging

$$R_{D_P} = m_b \omega_b^2 L_3 \left(\frac{L_2}{L_1 + L_2}\right) \tag{B31}$$

Rearranging equation B28

$$R_{C_P} = -\frac{m_b \alpha L_3 L_1}{(L_1 + L_2)} \tag{B32}$$

Substituting B32 into B26 and rearranging

$$R_{A_P} = -m_b \alpha L_3 \left(\frac{L_2}{L_1+L_2}\right) \tag{B33}$$

Rearranging equation B27

$$R_{B_P} = -\frac{T}{(L_3+L_4)} \tag{B34}$$

2.3. Blade Aerodynamic Loading

The aerodynamic analysis was based on the superposition of the aerodynamic loads from the BET-code developed in chapter 5 as a function of rotor azimuth position. A simplifying assumption has been made in the aerodynamic load analysis. The aerodynamic center is assumed to act at the same position as the blade center of gravity (CoG).

Resolving forces in the X direction

$$R_{A_a} + R_{B_a} + R_{C_a} - F_y \sin(\varphi_I) - F_x \sin(\theta_{BL}) = 0 \tag{B35}$$

Resolving forces in the Y direction

$$R_{D_a} + R_{E_a} + F_y \cos(\varphi_I) - F_x \cos(\theta_{BL}) = 0 \tag{B36}$$

Taking moments about point A XZ plane (clockwise positive)

$$-F_x L_3 \sin(\theta_{BL}) - F_y L_3 \sin(\varphi_I) + R_{B_a}(L_3 + L_4) = 0 \tag{B37}$$

Taking moments about point A YZ plane (clockwise positive)

$$-F_x L_1 \sin(\theta_{BL}) - F_y L_1 \sin(\varphi_I) + R_{C_a}(L_1 + L_2) = 0 \quad \text{(B38)}$$

Taking moments about point A XY plane (clockwise positive)

$$F_x L_1 \cos(\theta_{BL}) - F_y L_1 \cos(\varphi_I) - R_{E_a}(L_1 + L_2) = 0 \quad \text{(B39)}$$

Reaction Forces

Rearranging equation B37

$$R_{B_a} = \frac{\left(F_x L_3 \sin(\theta_{BL}) + F_y L_3 \sin(\varphi_I)\right)}{(L_3 + L_4)} \quad \text{(B40)}$$

Rearranging equation B38

$$R_{C_a} = \frac{\left(F_x L_1 \sin(\theta_{BL}) + F_y L_1 \sin(\varphi_I)\right)}{(L_1 + L_2)} \quad \text{(B41)}$$

Rearranging equation B39

$$R_{E_a} = \frac{\left(F_y L_1 \cos(\varphi_I) - F_x L_1 \cos(\theta_{BL})\right)}{(L_1 + L_2)} \quad \text{(B42)}$$

Rearranging equation B35

$$R_{A_a} = F_y \sin(\varphi_I) + F_x \sin(\theta_{BL}) - R_{B_a} - R_{C_a} \quad \text{(B43)}$$

And substituting B40 and B41 into equation B43

$$R_{A_a} = F_y \sin(\varphi_I) + F_x \sin(\theta_{BL}) - \frac{\left(F_y L_1 \cos(\varphi_I) - F_x L_1 \cos(\theta_{BL})\right)}{(L_1 + L_2)} - \frac{\left(F_x L_1 \sin(\theta_{BL}) + F_y L_1 \sin(\varphi_I)\right)}{(L_1 + L_2)} \tag{B44}$$

Rearranging equation B36

$$R_{D_a} = F_x \cos(\theta_{BL}) - F_y \cos(\varphi_I) - R_{E_a} \tag{B45}$$

And substituting B42 into equation B45

$$R_{D_a} = F_x \cos(\theta_{BL}) - F_y \cos(\varphi_I) - \frac{\left(F_y L_1 \cos(\varphi_I) - F_x L_1 \cos(\theta_{BL})\right)}{(L_1 + L_2)} \tag{B46}$$

2.4. Resultant Blade Pitch Pin Reaction Forces

The overall resultant blade pitch pin loads are the summation of the inertial and aerodynamic loads in the preceding sections. Each is outlined below

$$R_A = R_{A_I} + R_{A_P} - R_{A_a} \tag{B47}$$

$$R_B = R_{B_I} + R_{B_P} - R_{B_a} \tag{B48}$$

$$R_C = R_{C_I} + R_{C_P} - R_{C_a} \tag{B49}$$

$$R_D = R_{D_I} + R_{D_P} - R_{D_a} \tag{B50}$$

$$R_E = R_{E_I} + R_{E_P} - R_{E_a} \tag{B51}$$

Pin 1 Resultant

$$R_{Pin1} = \sqrt{R_A^2 + R_D^2} \tag{B52}$$

Pin 2 Resultant

$$R_{Pin2} = \sqrt{R_C^2 + R_E^2} \tag{B53}$$

2.5. Rotor-Disc Tangential and Radial Loads

The design of the upper and lower rotor disc requires a stress analysis and high cycle fatigue (HCF) life calculation to be undertaken. The blade pitch pin reaction forces have been converted into radial and tangential force components for convenience, as shown below.

Pin1

$$R_{Pin1_{rad}} = R_A \cos(\theta) - R_D \cos(\varphi_I) \tag{B54}$$

$$R_{Pin1_{tan}} = R_A \sin(\theta) + R_D \sin(\varphi_I) \tag{B55}$$

Pin2

$$R_{Pin2_{rad}} = R_C \cos(\theta) - R_E \cos(\varphi_I) \tag{B56}$$

$$R_{Pin2_{tan}} = R_C \sin(\theta) + R_E \sin(\varphi_I) \tag{B57}$$

3. Bearing Reaction Forces

Bearing reaction forces were calculated based on the residual out-of-balance loads calculated in section 2. A worst-case failure condition was also considered where a blade failure resulted in a ‘blade off’ condition. The main criteria under this scenario are for the test rig to remain together

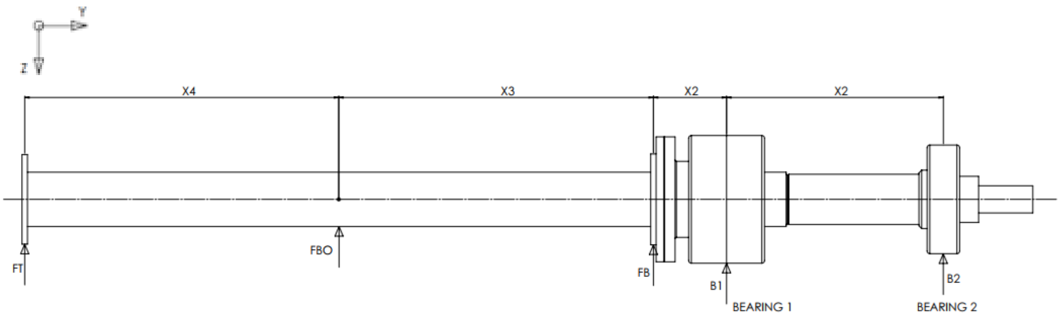

Figure B3 – Rotor spindle free body diagram

From Figure B3

Resolving forces in the X direction

$$F_T + F_{BO} + F_B - B_1 - B_2 = 0 \quad \text{(B58)}$$

Taking moments about point A XY plane (clockwise positive)

$$F_T(X_1 + X_3 + X_4) + F_{BO}(X_1 + X_3) + F_B(X_1) + B_2(X_2) = 0 \quad \text{(B59)}$$

Reaction Forces

Rearranging equation A58

$$B_1 = F_T + F_{BO} + F_B - B_2 = 0 \quad \text{(B60)}$$

Rearranging equation A59

$$B_2 = \frac{-F_T(X_1+X_3+X_4)-F_{BO}(X_1+X_3)-F_B(X_1)}{X_2} \tag{B61}$$

Appendix C – iCUB Six Degree of Freedom Force Torque Sensor Specification

The test rig was mounted onto a six-degree-of-freedom force torque sensor during testing and characterization. A sensor specification is included in the current section to define the instrumentation limitations and supporting documentation.

F/T Sensors

The F/T sensor (6-dof) has also been specially designed to fit the iCub. However, the size of the sensor has been made compatible with an existing commercial product. On the other hand the signal conditioning electronics has been made to fit the sensor itself, consequently reducing the space required. The F/T sensor is based on a classical Wheatstone bridge design employing 12 semiconductor strain gauges arranged in a 6 half-bridges configuration.ed robots

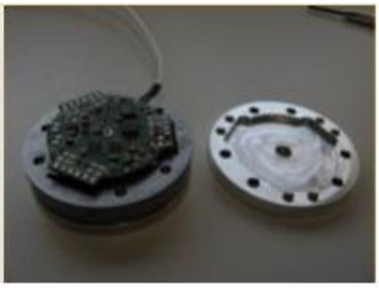

Mechanical specifications

Physical specifications

The physical specifications of the sensor are reported in Table 1:

Weight	0.122[kg]
Diameter	45[mm]
Height	18.4[mm]

Table 1: Physical specifications of the sensor

Measurement frame specifications

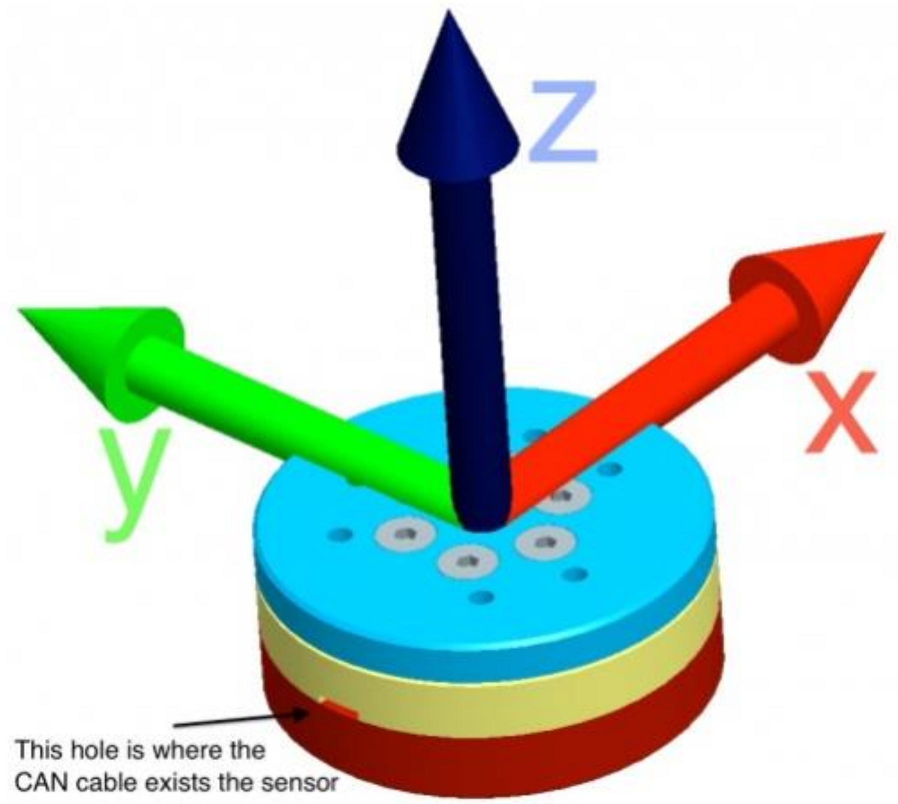

The F/T sensor reference frame

Please notice that key elements to localize the reference frame on the sensor are two: 1. the hole where the CAN exits the sensor; 2. the thick VS the thin sensor cover.

The sensor is calibrated to measure the Force/Torque applied by the upper (blue) part of the sensor on the lower (red) part of sensor, and express it on the F/T sensor reference frame.

Calibration specifications

The sensors are calibrated in order to obtain high resolution in typical operating regions. Typical values of the range and resolution for a sensor after the calibration procedure are reported in Table

2. The resolution is typical for most applications and can be improved with filtering. Resolutions quoted are the effective resolution after dropping three counts of noise.

	Fx, Fy [N]	Fz [N]	Tx, Ty [Nm]	Tz [Nm]
Range	1500	2000	35	25
Resolution	0.25	0.25	0.005	0.004

Table 2: typical values after sensor calibration

Appendix D – Uncertainty Analysis

An uncertainty analysis was undertaken on all experimental measurements, utilizing the method developed by Moffat [94]. The method combines all bias and precision errors to produce an uncertainty with a 95% confidence level. The calculation method is defined as:

$$\delta\mathrm{R} = \left\{\left(\frac{\partial \mathrm{R}}{\partial \mathrm{x}_1}\delta \mathrm{x}_1\right)^2 + \left(\frac{\partial \mathrm{R}}{\partial \mathrm{x}_2}\delta \mathrm{x}_2\right)^2 + \cdots \left(\frac{\partial \mathrm{R}}{\partial \mathrm{x}_3}\delta \mathrm{x}_3\right)^2\right\}^{\frac{1}{2}} \quad \text{(D1)}$$

Where x is the contributing variable and R is the required quantity, C_{Tx}, C_{Ty}, and C_P in the current study

1.1. Rotor Mean Force Measurements – Non-Dimensional Coefficients C_{Tx}, and C_{Ty}

For the X direction mean Thrust Coefficient C_{Tx} and C_{Tx} (Only C_{Tx} shown to avoid repetition), where,

$$\mathrm{C_{Tx}} = \frac{\mathrm{F_x}}{\rho_a \mathrm{A}_R (\omega \mathrm{R})^2} = \frac{\mathrm{F_x}}{Z_\mathrm{x}} \quad \text{(D2)}$$

The uncertainty in C_{Tx} is defined as:

$$\delta\mathrm{C_{Tx}} = \left\{\left(\frac{\partial \mathrm{C_{Tx}}}{\partial \mathrm{F_x}}\delta \mathrm{F_x}\right)^2 + \left(\frac{\partial \mathrm{C_{Tx}}}{\partial \mathrm{Z_x}}\delta \mathrm{Z_x}\right)^2\right\}^{\frac{1}{2}} \quad \text{(D3)}$$

Giving,

$$\delta\mathrm{C_{Tx}} = \left\{\left(\frac{1}{\mathrm{Z_x}}\delta \mathrm{F_x}\right)^2 + \left(\frac{-\mathrm{F_x}}{\mathrm{Z_x^2}}\delta \mathrm{Z}_x\right)^2\right\}^{\frac{1}{2}} \quad \text{(D4)}$$

F_X is the rotor mean force in the X measurement direction, and Z_x represents an aerodynamic constant assumed for ease of calculation.

Force Uncertainty – δF_x

The rotor force component F_x is calculated from the average of 45,000 force sensor samples, using sensor manufacturer calibration data. Based on this, there are three uncertainties identified.

Force sensor measurement uncertainty

a result of sensor calibration defined as

$$\delta S = \frac{\pm 0.025}{F_x} \tag{D5}$$

Force F_x averaging uncertainty

The rotor force components are presented as average values, approximating the mean value. The measurement uncertainty is given by

$$\delta N_A = \frac{1.96\sigma(F_x)}{N^{0.5}} \tag{D6}$$

F_x is the rotor mean force in the X measurement direction as previously defined, N represents the number of samples in the data set, and σ is the standard deviation. A value of 1.96 was used to provide a 95% confidence level.

Force sensor drift uncertainty

Drift uncertainty was accounted for by performing a static test before and after each experimental run. An estimate of the uncertainty due to sensor drift was calculated from

$$\delta D_x = \frac{F_{x_2} - F_{x_1}}{2} \tag{D7}$$

The above three uncertainties then combine to give the overall uncertainty in force, F_x

$$\delta F_x = \left\{\left(\frac{\partial F_x}{\partial S}\delta S\right)^2 + \left(\frac{\partial F_x}{\partial N_A}\delta N_A\right)^2 + \left(\frac{\partial F_x}{\partial D_x}\delta D_x\right)^2\right\}^{\frac{1}{2}} \quad \text{(D8)}$$

This gives

$$\delta F_x = \left\{\left(\frac{0.025}{F_x}\right)^2 + \left(\frac{1.96\sigma(F_x)}{N^{0.5}}\right)^2 + \left(\frac{F_{x_2} - F_{x_1}}{2}\right)^2\right\}^{\frac{1}{2}} \quad \text{(D9)}$$

Aerodynamic Constant Uncertainty - δZ_x

The aerodynamic constant Z_x is calculated from measured data for each variable, with each variable having its own uncertainty, summarised below.

Density uncertainty

$$\rho_a = \frac{p}{Rt} \quad \text{(D10)}$$

Where p is the static pressure, R the Universal Gas Constant, and t is the static temperature. The uncertainty associated with the density calculation is

$$\delta\rho = \left\{\left(\frac{\partial \rho_a}{\partial p}\delta p\right)^2 + \left(\frac{\partial \rho_a}{\partial t}\delta t\right)^2\right\}^{\frac{1}{2}} \quad \text{(D11)}$$

Pressure measurement uncertainty

This is measured to be within 0.05 bar, and the uncertainty is given by $\delta p = \pm 0.05$ bar.

Temperature measurement uncertainty

The temperature is measured to be within 0.5°C, where $\delta t = \pm 0.5$°C defines the uncertainty. Therefore the uncertainties combine to give the overall uncertainty in density, ρ

$$\delta\rho = \left\{\left(\frac{0.05}{\mathrm{Rt}}\right)^2 + \left(\frac{-0.5pR}{(Rt)^2}\right)^2\right\}^{\frac{1}{2}} \tag{D12}$$

Planform area uncertainty

The planform area is made up of two measured variables; the uncertainty for each variable is

Span height, $\delta \mathrm{H_R} = \pm 0.5$mm and Rotor diameter, $\delta \mathrm{D_R} = \pm 0.5$mm

The uncertainty associated with the planform area calculation is then

$$\delta \mathrm{A} = \left\{\left(\frac{\partial \mathrm{A}_R}{\partial \mathrm{H_R}}\delta \mathrm{H_R}\right)^2 + \left(\frac{\partial \mathrm{A}_R}{\partial \mathrm{D_R}}\delta \mathrm{D_R}\right)^2\right\}^{\frac{1}{2}} \tag{D13}$$

Therefore the uncertainties combine to give the overall uncertainty in the planform area, A_R, where

$$\delta \mathrm{A}_R = \{(0.0005\mathrm{D_R})^2 + (0.0005\mathrm{H_R})^2\}^{\frac{1}{2}} \tag{D14}$$

Rotor rotational speed uncertainty

Rotor rotational speed was measured with a 360 Pulse Per Revolution (PPR) encoder and controlled via a PID controller loop. The PID control loop parameters were tuned, and the speed was always found to be within 1% of the required set point across the full speed range. The rotor speed uncertainty is, therefore, given by $\delta\omega = \pm 0.01\omega$.

Where ω is the rotor rotational speed. The uncertainty associated with the aerodynamic constant Z_x calculation is

$$\delta Z_x = \left\{ \left(\frac{\partial Z_x}{\partial A_R} \delta A_R \right)^2 + \left(\frac{\partial Z_x}{\partial \rho_a} \delta \rho_a \right)^2 + \left(\frac{\partial Z_x}{\partial \omega} \delta \omega \right)^2 + \left(\frac{\partial Z_x}{\partial R} \delta R \right)^2 \right\}^{\frac{1}{2}} \qquad \text{(D15)}$$

The uncertainties combine to give the overall uncertainty in the aerodynamic constant, Z_x, which is given by

$$\delta Z_x = \left\{ \left(\rho_a \omega^2 r^2 \{(0.0005 D_R)^2 + (0.0005 H_R)^2\}^{\frac{1}{2}} \right)^2 + \left(A_R \omega^2 r^2 \left\{ \left(\frac{0.05}{Rt} \right)^2 + \left(\frac{-0.5pR}{(Rt)^2} \right)^2 \right\}^{\frac{1}{2}} \right)^2 + (0.02 \rho_a A_R \omega^2 r^2)^2 + (0.001 \rho_a A_R \omega^2 r)^2 \right\}^{\frac{1}{2}} \qquad \text{(D16)}$$

1.2. Rotor Mean Resultant Force – Non-Dimensional Coefficients C_T

The orthogonal X and Y force components in the test measurement directions are combined to calculate the overall thrust coefficient C_T, defined as

$$C_T = \sqrt{C_{T_x}^2 + C_{T_y}^2} \qquad \text{(D17)}$$

The uncertainty in C_T is calculated from

$$\delta C_T = \left\{ \left(\frac{\partial C_T}{\partial C_{Tx}} \delta C_{Tx} \right)^2 + \left(\frac{\partial C_T}{\partial C_{Ty}} \delta C_{Ty} \right)^2 \right\}^{\frac{1}{2}} \qquad \text{(D18)}$$

Giving,

$$\delta C_T = \left\{\left(\frac{C_{Tx}}{\sqrt{C_{Tx}^2 + C_{Ty}^2}}\delta C_{Tx}\right)^2 + \left(\frac{C_{Ty}}{\sqrt{C_{Tx}^2 + C_{Ty}^2}}\delta C_{Ty}\right)^2\right\}^{\frac{1}{2}} \quad \text{(D19)}$$

1.3. Rotor Mean Power Measurements – Non-Dimensional Coefficients C_P

For the Rotor Power Coefficient C_P, where

$$C_P = \frac{P}{\rho_a A_R (\omega R)^3} = \frac{P}{Z_P} \quad \text{(D20)}$$

The uncertainty in C_P is defined as

$$\delta C_P = \left\{\left(\frac{\partial C_P}{\partial P}\delta P\right)^2 + \left(\frac{\partial C_P}{\partial Z_P}\delta Z_P\right)^2\right\}^{\frac{1}{2}} \quad \text{(D21)}$$

Giving,

$$\delta C_P = \left\{\left(\frac{1}{Z_P}\delta P\right)^2 + \left(\frac{-P}{Z_P^2}\delta Z_P\right)^2\right\}^{\frac{1}{2}} \quad \text{(D22)}$$

P is the rotor power, and Z_P represents an aerodynamic constant assumed for ease of calculation.

Power Uncertainty – δP

The rotor power is calculated from

$$P = Q\omega \quad \text{(D23)}$$

Where Q is the rotor torque and ω is the rotor rotational speed. The uncertainty associated with the rotor power calculation is

$$\delta P = \left\{\left(\frac{\partial P}{\partial Q}\delta Q\right)^2 + \left(\frac{\partial P}{\partial \omega}\delta\omega\right)^2\right\}^{\frac{1}{2}} \quad \text{(D24)}$$

The rotor power P is calculated using sensor manufacturer calibration data from the average of 45,000 force sensor samples measuring torque. Based on this, there are three uncertainties identified in the torque measurement.

Force sensor measurement uncertainty

Force sensor measurement uncertainty is a result of sensor calibration and is defined as

$$\delta S_P = \frac{\pm 0.05}{Q} \tag{D25}$$

Power averaging uncertainty

The rotor power is presented as average values, approximating the actual mean value. The measurement uncertainty is defined as

$$\delta N_{AP} = \frac{1.96\sigma(Q)}{N^{0.5}} \tag{D26}$$

Q is the rotor torque as previously defined, N represents the number of samples in the data set, and σ is the standard deviation. A value of 1.96 was used to provide a 95% confidence level.

Sensor drift uncertainty

Uncertainty due to sensor drift was accounted for by performing a static test before and after each experimental run. An estimate of the uncertainty due to sensor drift is calculated from

$$\delta D_P = \frac{Q_2 - Q_1}{2} \tag{D27}$$

The above three uncertainties combine to give the overall uncertainty in Torque, Q:

$$\delta Q = \left\{\left(\frac{\partial Q}{\partial S_P}\delta S_P\right)^2 + \left(\frac{\partial Q}{\partial N_{AP}}\delta N_{AP}\right)^2 + \left(\frac{\partial Q}{\partial D_P}\delta D_P\right)^2\right\}^{\frac{1}{2}} \qquad (D28)$$

This gives

$$\delta Q = \left\{\left(\frac{0.05}{Q}\right)^2 + \left(\frac{1.96\sigma(Q)}{N^{0.5}}\right)^2 + \left(\frac{Q_2 - Q_1}{2}\right)^2\right\}^{\frac{1}{2}} \qquad (D29)$$

Rotor rotational speed uncertainty

The rotor speed uncertainty is estimated from $\delta\omega = \pm 0.01 N_R$

The above uncertainties combine to give the overall uncertainty in Power, P:

$$\delta P = \left\{\left(\omega\left\{\left(\frac{0.05}{Q}\right)^2 + \left(\frac{1.96\sigma(Q)}{N^{0.5}}\right)^2 + \left(\frac{Q_2 - Q}{2}\right)^2\right\}^{\frac{1}{2}}\right)^2 + (0.01 N_R Q)^2\right\}^{\frac{1}{2}}$$

(D30)

Aerodynamic Constant Uncertainty - δZ_P

The aerodynamic constant is calculated from measured experimental data for each variable. Each variable has its own uncertainty. Many of the variables have been defined in the calculation of δZ_X. The uncertainty associated with the aerodynamic constant Z_P calculation is

$$\delta Z_P = \left\{\left(\frac{\partial Z_P}{\partial A_R}\delta A_R\right)^2 + \left(\frac{\partial Z_P}{\partial \rho}\delta\rho\right)^2 + \left(\frac{\partial Z_P}{\partial \omega}\delta\omega\right)^2 + \left(\frac{\partial Z_P}{\partial R}\delta R\right)^2\right\}^{\frac{1}{2}} \qquad (D31)$$

The uncertainties combine to give the overall uncertainty in the aerodynamic constant, Z_P, where

$$\delta Z_P = \left\{ \left(\rho_a \omega^3 r^3 \{(0.0005D_R)^2 + (0.0005H_R)^2\}^{\frac{1}{2}} \right)^2 + \left(A_R \omega^3 r^3 \left\{ \left(\frac{0.05}{Rt} \right)^2 + \left(\frac{-0.5pR}{(Rt)^2} \right)^2 \right\}^{\frac{1}{2}} \right)^2 + (0.03\rho_a A_R \omega^3 r^3)^2 + (0.0015\rho_a A_R \omega^3 r^2)^2 \right\}^{\frac{1}{2}} \quad \text{(D32)}$$

D1.4. Rotor Cyclic Pitch Angle Input, θ_{BL} Uncertainty Level

The blade cyclic pitch angle θ_{BL} is dependent on the rotor geometry itself, defined by

$$\theta_{BL} = \frac{\pi}{2} - \cos^{-1}\left(\frac{a^2 - L^2 + P^2}{2aP}\right) - \sin^{-1}\left(\frac{e}{a} \cdot \cos(\Psi + \varepsilon)\right) \quad \text{(D33)}$$

The uncertainty in θ_{BL} is defined as

$$\delta\theta_{BL} = \left\{ \left(\frac{\partial\theta_{BL}}{\partial a}\delta a\right)^2 + \left(\frac{\partial\theta_{BL}}{\partial L}\delta L\right)^2 + \left(\frac{\partial\theta_{BL}}{\partial P}\delta P\right)^2 + \left(\frac{\partial\theta_{BL}}{\partial e}\delta e\right)^2 + \left(\frac{\partial\theta_{BL}}{\partial \Psi}\delta \Psi\right)^2 + \left(\frac{\partial\theta_{BL}}{\partial \varepsilon}\delta \varepsilon\right)^2 \right\}^{\frac{1}{2}} \quad \text{(D34)}$$

Where,

$$\frac{\partial\theta_{BL}}{\partial a} = \frac{4a^2P - 2P(a^2 - L^2 + P^2)}{(2aP)^2\sqrt{1 - \left(\frac{a^2 - L^2 + P^2}{2aP}\right)^2}} + \frac{e\cos(\Psi + \varepsilon)}{a^2\sqrt{1 - \left(\frac{e}{a}\cos(\Psi + \varepsilon)\right)^2}} \quad \text{(D35)}$$

$$\frac{\partial\theta_{BL}}{\partial L} = \frac{-L}{aP\sqrt{1 - \left(\frac{a^2 - L^2 + P^2}{2aP}\right)^2}} \quad \text{(D36)}$$

$$\frac{\partial\theta_{BL}}{\partial P} = \frac{4P^2a - 2a(a^2 - L^2 + P^2)}{(2aP)^2\sqrt{1 - \left(\frac{a^2 - L^2 + P^2}{2aP}\right)^2}} \quad \text{(D37)}$$

$$\frac{\partial\theta_{BL}}{\partial e} = \frac{-\cos(\Psi+\varepsilon)}{a\sqrt{1-\left(\frac{e}{a}\cos(\Psi+\varepsilon)\right)^2}} \tag{D38}$$

$$\frac{\partial\theta_{BL}}{\partial\Psi} = \frac{\partial\theta_{BL}}{\partial\varepsilon} = \frac{e\sin(\Psi+\varepsilon)}{a\sqrt{1-\left(\frac{e}{a}\cos(\Psi+\varepsilon)\right)^2}} \tag{D39}$$

Where a is a geometric parameter defined by

$$a = \sqrt{e^2 + R^2 + 2eR\cdot\sin(\Psi+\varepsilon)} \tag{D40}$$

The uncertainty in 'a' is defined as

$$\delta a = \left\{\left(\frac{\partial a}{\partial e}\delta e\right)^2 + \left(\frac{\partial a}{\partial R}\delta R\right)^2 + \left(\frac{\partial a}{\partial\psi}\delta\psi\right)^2 + \left(\frac{\partial a}{\partial\varepsilon}\delta\varepsilon\right)^2\right\}^{\frac{1}{2}} \tag{D41}$$

Where,

$$\frac{\partial a}{\partial e} = \frac{e+R\sin(\Psi+\varepsilon)}{\sqrt{e^2+R^2+2eR\sin(\Psi+\varepsilon)}} \tag{D42}$$

$$\frac{\partial a}{\partial R} = \frac{R+e\sin(\Psi+\varepsilon)}{\sqrt{e^2+R^2+2eR\sin(\Psi+\varepsilon)}} \tag{D43}$$

$$\frac{\partial a}{\partial\psi} = \frac{\partial a}{\partial\varepsilon} = \frac{2eR\cos(\Psi+\varepsilon)}{\sqrt{e^2+R^2+2eR\sin(\Psi+\varepsilon)}} \tag{D44}$$

The geometric parameter 'a' is made up of four measured variables that can be measured directly with measuring equipment. The uncertainty for each variable is

- Eccentric Point offset, e, $\delta e = \pm 0.05$mm,
- Rotor Radius, R, $\delta R \pm 0.25$mm,
- Azimuth Angle, ψ, $\delta\psi \pm 0.25°$,

And

- Eccentric Point Phase Angle, ε, $\delta\varepsilon \pm 0.25°$

The length of the control rod L is:

$$L = \sqrt{P^2 + R^2} \tag{D45}$$

The uncertainty in L is defined as

$$\delta L = \left\{\left(\frac{\partial L}{\partial P}\delta P\right)^2 + \left(\frac{\partial L}{\partial R}\delta R\right)^2\right\}^{\frac{1}{2}} \tag{D46}$$

Giving,

$$\delta L = \left\{\left(\frac{P}{\sqrt{P^2+R^2}}\delta P\right)^2 + \left(\frac{R}{\sqrt{P^2+R^2}}\delta R\right)^2\right\}^{\frac{1}{2}} \tag{D47}$$

The pitch link length, P, is made up of a measured variable, where the uncertainty is:

Pitch Link Length, P, $\delta P = \pm 0.5\text{mm}$

Appendix E – ICP PCB Force Sensor Specification

An additional single-axis force sensor was used during shaker testing and dynamic calibration, a PCB 208C02. A sensor specification is included in the current section to define the instrumentation limitations and leading dimensions.

Appendix E – ICP PCB Force Sensor Specification

Model Number 208C02	ICP® FORCE SENSOR	Revision: K ECN #: 46791

Performance	ENGLISH	SI	
Sensitivity(± 15 %)	50 mV/lb	11.241 mV/kN	
Measurement Range(Compression)	100 lb	0.4448 kN	
Measurement Range(Tension)	100 lb	0.4448 kN	
Maximum Static Force(Compression)	600 lb	2.669 kN	
Maximum Static Force(Tension)	500 lb	2.224 kN	
Broadband Resolution(1 to 10,000 Hz)	0.001 lb-rms	0.004 N-rms	[1]
Low Frequency Response(-5 %)	0.001 Hz	0.001 Hz	[2]
Upper Frequency Limit	36 kHz	36 kHz	[3]
Non-Linearity	≤ 1 % FS	≤ 1 % FS	[4]
Environmental			
Temperature Range	-65 to +250 °F	-54 to +121 °C	
Temperature Coefficient of Sensitivity	≤ 0.05 %/°F	≤ 0.09 %/°C	
Electrical			
Discharge Time Constant(at room temp)	≥ 500 sec	≥ 500 sec	
Excitation Voltage	20 to 30 VDC	20 to 30 VDC	
Constant Current Excitation	2 to 20 mA	2 to 20 mA	
Output Impedance	≤ 100 Ohm	≤ 100 Ohm	
Output Bias Voltage	8 to 14 VDC	8 to 14 VDC	
Spectral Noise(1 Hz)	0.000135 lb/√Hz	0.000603 N/√Hz	[1]
Spectral Noise(10 Hz)	0.0000276 lb/√Hz	0.000123 N/√Hz	[1]
Spectral Noise(100 Hz)	0.0000096 lb/√Hz	0.0000427 N/√Hz	[1]
Spectral Noise(1 kHz)	0.0000021 lb/√Hz	0.0000095 N/√Hz	[1]
Output Polarity(Compression)	Positive	Positive	
Physical			
Stiffness	6 lb/µin	1.05 kN/µm	[1]
Size (Hex x Height x Sensing Surface)	0.625 in x 0.625 in x 0.500 in	15.88 mm x 15.88 mm x 12.7 mm	
Weight	0.80 oz	22.7 gm	
Housing Material	Stainless Steel	Stainless Steel	
Sealing	Hermetic	Hermetic	
Electrical Connector	10-32 Coaxial Jack	10-32 Coaxial Jack	
Electrical Connection Position	Side	Side	
Mounting Thread	10-32 Female	10-32 Female	

CE [5]

All specifications are at room temperature unless otherwise specified.
In the interest of constant product improvement, we reserve the right to change specifications without notice.

ICP® is a registered trademark of PCB Group, Inc.

OPTIONAL VERSIONS

Optional versions have identical specifications and accessories as listed for the standard model except where noted below. More than one option may be used.

N - Negative Output Polarity

Output Polarity(Compression)	Negative	Negative

TLD - TEDS Capable of Digital Memory and Communication Compliant with IEEE 1451.4

Output Bias Voltage	8 to 15 VDC	8 to 15 VDC

W - Water Resistant Cable

NOTES:

[1] Typical.
[2] Calculated from discharge time constant.
[3] Estimated using rigid body dynamics calculations.
[4] Zero-based, least-squares, straight line method.
[5] See PCB Declaration of Conformance PS023 for details.

SUPPLIED ACCESSORIES:

Model 080A81 Thread Locker (1)
Model 081B05 Mounting Stud (10-32 to 10-32) (2)
Model 084A03 Impact Cap (1)
Model M081A62 Mounting stud, 10-32 to M6 x 1, BeCu with shoulder (2)

Entered: LK	Engineer: DK	Sales: RM	Approved: BAM	Spec Number:
Date: 5/11/2017	Date: 5/11/2017	Date: 5/11/2017	Date: 5/11/2017	8467

PCB PIEZOTRONICS
3425 Walden Avenue, Depew, NY 14043

Phone: 716-684-0001
Fax: 716-684-0987
E-Mail: info@pcb.com

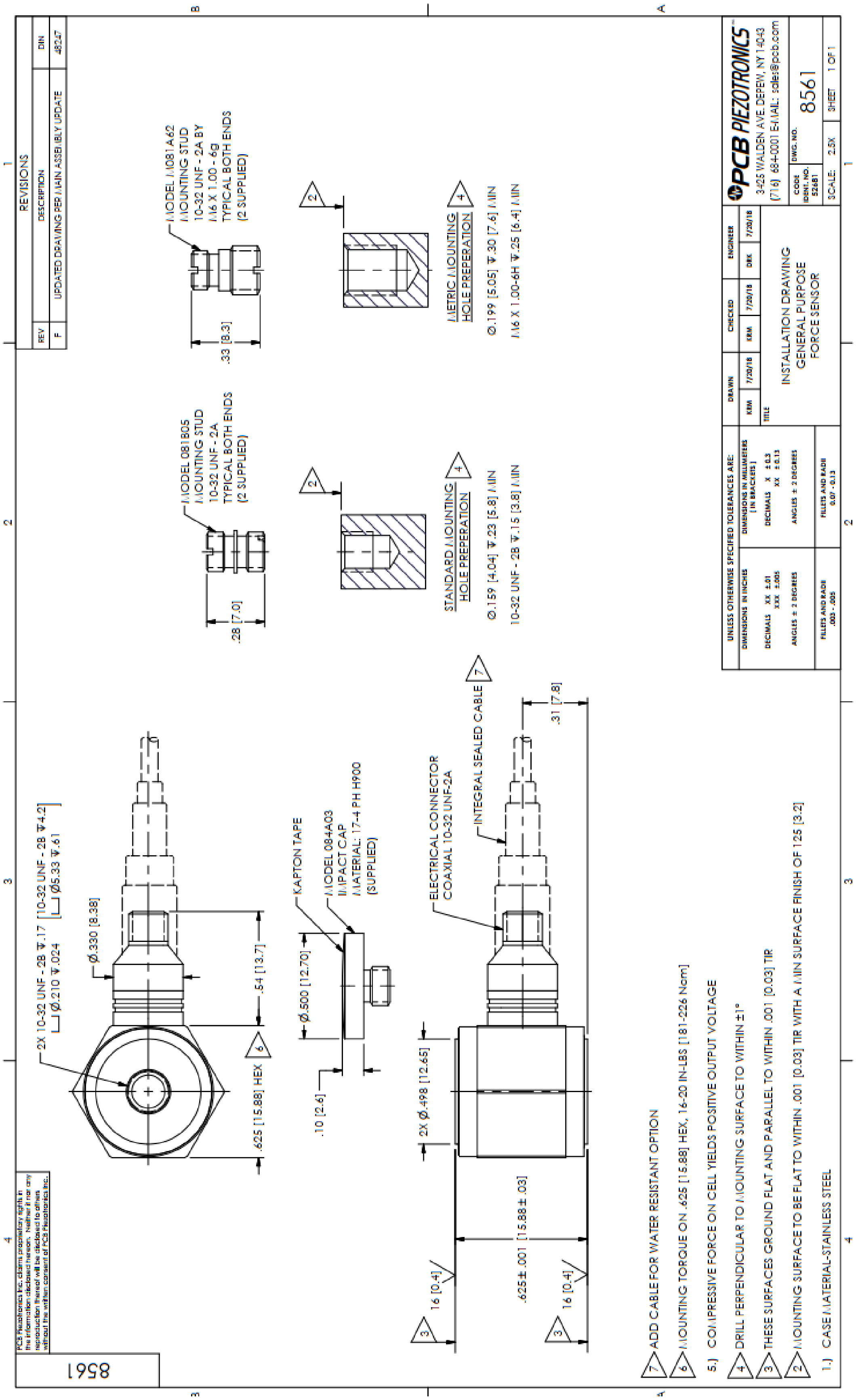

REVISIONS
REV
DESCRIPTION
DIN
F
UPDATED DRAWING PER MAIN ASSEMBLY UPDATE
48247
MODEL M081A62 MOUNTING STUD 10-32 UNF - 2A BY M6 X 1.00 - 6g TYPICAL BOTH ENDS (2 SUPPLIED)
MODEL 081B05 MOUNTING STUD 10-32 UNF - 2A TYPICAL BOTH ENDS (2 SUPPLIED)
.33 [8.3]
.28 [7.0]
METRIC MOUNTING HOLE PREPERATION
Ø.199 [5.05] ⊽.30 [7.6] MIN
M6 X 1.00-6H ⊽.25 [6.4] MIN
STANDARD MOUNTING HOLE PREPERATION
Ø.159 [4.04] ⊽.23 [5.8] MIN
10-32 UNF - 2B ⊽.15 [3.8] MIN
2X 10-32 UNF - 2B ⊽.17 [10-32 UNF - 2B ⊽4.2]
Ø.210 ⊽.024 [Ø5.33 ⊽.61]
Ø.330 [8.38]
.54 [13.7]
.625 [15.88] HEX
KAPTON TAPE
MODEL 084A03 IMPACT CAP MATERIAL: 17-4 PH H900 (SUPPLIED)
Ø.500 [12.70]
.10 [2.6]
ELECTRICAL CONNECTOR COAXIAL 10-32 UNF-2A
INTEGRAL SEALED CABLE
.31 [7.8]
2X Ø.498 [12.65]
.625±.001 [15.88±.03]
16 [0.4]
ADD CABLE FOR WATER RESISTANT OPTION
MOUNTING TORQUE ON .625 [15.88] HEX, 16-20 IN-LBS [181-226 Ncm]
5.) COMPRESSIVE FORCE ON CELL YIELDS POSITIVE OUTPUT VOLTAGE
DRILL PERPENDICULAR TO MOUNTING SURFACE TO WITHIN ±1°
THESE SURFACES GROUND FLAT AND PARALLEL TO WITHIN .001 [0.03] TIR
MOUNTING SURFACE TO BE FLAT TO WITHIN .001 [0.03] TIR WITH A MIN SURFACE FINISH OF 125 [3.2]
1.) CASE MATERIAL-STAINLESS STEEL
UNLESS OTHERWISE SPECIFIED TOLERANCES ARE:
DRAWN KRM 7/20/18
CHECKED KRM 7/20/18
ENGINEER DRK 7/20/18
TITLE
INSTALLATION DRAWING GENERAL PURPOSE FORCE SENSOR
PCB PIEZOTRONICS
3425 WALDEN AVE. DEPEW, NY 14043
(716) 684-0001 EMAIL: sales@pcb.com
CODE IDENT. NO. 52681
DWG. NO. 8561
SCALE: 2.5X
SHEET 1 OF 1
8561